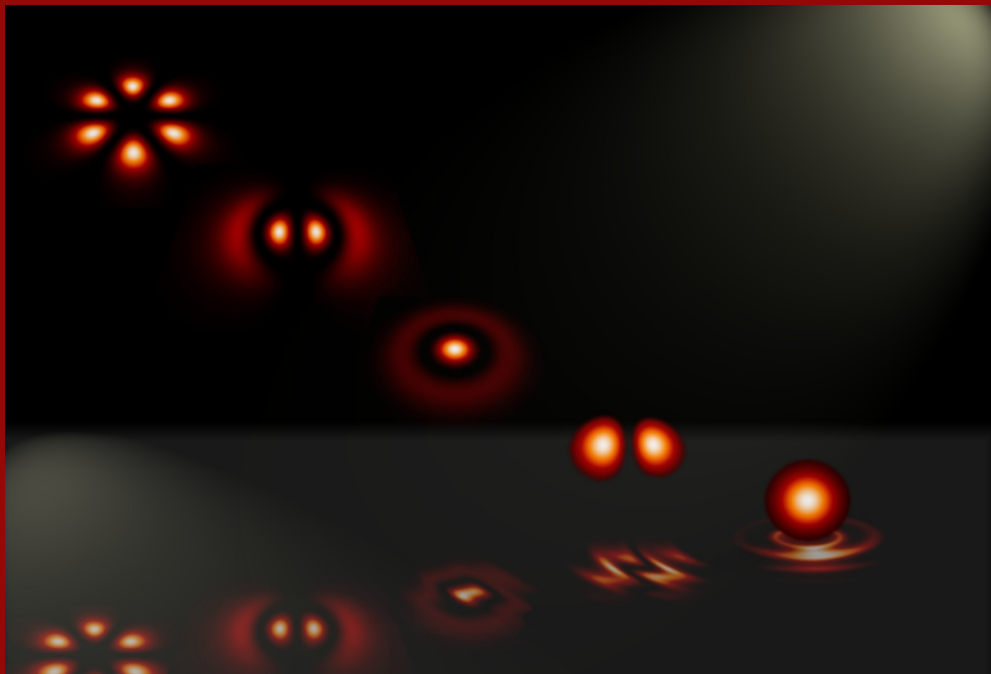


SEMICONDUCTOR LASER DYNAMICS

*Compound-cavity, polarization and
transverse modes*

José Mulet Pol



PhD Thesis

Semiconductor Laser Dynamics:

Compound-cavity, polarization and transverse modes

Tesis presentada per José Mulet Pol, en el Departament de Física de la Universitat de les Illes Balears, per optar al grau de Doctor en ciències Físiques.

Els directors de tesis Maxi San Miguel Ruibal catedràtic de la universitat de les Illes Balears i Claudio Mirasso Santos professor titular de la mateixa universitat certifiquen que aquesta tesis doctoral ha estat realitzada pel Sr. José Mulet Pol, i perquè quedi constància escrita firmen

a Palma 25 de Novembre de 2002.

Maxi San Miguel Ruibal

Claudio Mirasso Santos

Agraïments

L'objectiu d'aquesta tesi és el de resumir del treball realitzat durant els quatre anys de doctorat i que és fruit dels coneixements adquirits mitjançant l'assistència a conferències, escoles, estances, seminaris, i discussions entre cafè i cafè.

La investigació ha estat realitzada en l'Instituto Mediterráneo de Estudios Avanzados (IMEDEA) de la Universitat de les Illes Balears, finançada per la beca del Ministerio de Educación y Cultura AP99-78215109K, i per tota una sèrie de projectes: Accions integrades Hispano-Alemanes HA98-29, VISTA Research Training Network HPRN-CT-2000-00034, MCyT TIC99-0645-C05-02 i BFM2000-1108, i OCCULT No. IST-2000-29683.

En primer lloc vull agrair tot el suport i confiança dipositada per part dels meus directors de tesis el Prof. Maxi San Miguel i el Dr. Claudio Mirasso. També al Dr. Salvador Bal-le persona sense la qual gran part d'aquesta tesi no hagués estat possible. A tots als vells i nous companys de l'EFE amb qui he compartit aquests quatre anys. Per tots els bons moments i per la comprensió en els més difícils, gràcies a tots!

La primera part del treball s'ha realitzat en col.laboració amb el Dr. Tilmann Heil, Dr. Ingo Fischer, i Michael Peil de la Universitat de Darmstadt d'Alemanya. Vull agrair tota la seva atenció durant la meva visita a Darmstadt. Al Dr. Jorge Rocca, a Dr. Carmen Menoni i família per la fantàstica hospitalitat durant la meva estada a la Colorado State University. Als Dr. Angel Valle i Luis Pesquera per totes les estimulants discussions sobre làsers de semiconductor que tinguérem a Santander. També vull donar gràcies per totes les discussions en la Universitat amb els Dr. Alessandro Scirè, Jan Danckaert, Cristina Masoller, Thorsten Ackemann, Massimo Guidici, Stephane Barland, ... Gràcies també a n'en Juanjo i en Pere per solucionar ràpidament els problemes informàtics.

Finalment com a bon Mallorquí del Raiguer no puc oblidar agrair primerament a n'en Jordi Perelló (àlies tres caires) i a n'en J. Daniels per activar l'inspiració en els moments difícils. Al bar de Sa Plaça de Sineu pel frit-callos-llengo-ensaladilla dels dissabtes. Pels inoblidables moments amb els integrants de l'associació gastronòmica i club de "Gorans", a n'en "Stayakitú" pels vuit-cents litres de vinagre i moltes altres històries que no puc mencionar aquí...

Contents

Resum	ix
1 Introduction	1
1.1 Semiconductor Lasers	1
1.2 Edge-Emitting Semiconductor Lasers	4
1.3 Surface-Emitting Semiconductor Lasers	7
1.4 Common Features in the Modeling of Semiconductor Lasers	10
1.4.1 Maxwell's equations	11
1.4.2 Semiconductor dynamics	12
1.5 Overview	15
I Compound-Cavity Edge-Emitting Semiconductor Lasers	19
Preface to the First Part	21
2 Semiconductor Lasers with Optical Feedback	23
2.1 Introduction	23
2.2 The Model	25
2.2.1 The Lang-Kobayashi model	31
2.3 Operation Regimes	36
2.4 Statistics of Power Dropouts	39
2.4.1 Statistics of the time between dropouts	41
2.5 Entraining Power Dropouts	48
2.6 Discussion	51
3 Bidirectionally Coupled Semiconductor Lasers	53
3.1 Introduction	53
3.2 The Model	56
3.3 Monochromatic Steady-State Solutions	63

3.3.1	Symmetric operation	65
3.3.2	General case	68
3.4	Phenomenological Rate Equation Model	71
3.5	Experimental Setup	75
3.6	Results Under Symmetric Operation	77
3.6.1	Coupling-induced instabilities	77
3.6.2	Synchronization properties	78
3.6.3	Phase dynamics	83
3.7	Dynamical Model Including Higher-Order Terms	85
3.8	Summary	89
4	Conclusions to Part One	93
II	Polarization and Transverse Mode Dynamics in Vertical-Cavity Surface-Emitting Lasers	97
	Preface to the Second Part	99
5	Intensity and Polarization Noise in VCSELs	101
5.1	Introduction	101
5.2	Spin Dynamics and Light Polarization State	104
5.3	Spin-Flip Model	107
5.4	Regimes of Operation	112
5.5	Fluctuation of the Intensity Components	114
5.5.1	Fluctuations of the circular components	117
5.5.2	Fluctuation of the linear components	118
5.6	Fluctuation of the Polarization Angles	120
5.7	Role of the Spin-Flip and Birefringence	124
5.8	Polarization Anticorrelations	127
5.9	Summary, Discussion and Perspectives	129
6	Spatiotemporal Modeling of the Optical Properties of VCSELs	133
6.1	Introduction	133
6.2	Optical model	136
6.3	Material model	142
6.4	Dimensionless model	147
6.5	Polarization Mode Selection in the Fundamental Transverse Mode	149
6.6	Transverse Mode Selection at Threshold	151
6.6.1	Numerical simulations	158

6.7 Subnanosecond Electrical Excitation	161
6.8 Summary and Discussion	169
7 Transverse Mode Dynamics: Spatiotemporal versus modal expansion descriptions	171
7.1 Introduction	171
7.2 Optical Modal Expansion	172
7.3 Results	176
7.3.1 Single-mode operation	176
7.3.2 Multimode operation	182
7.4 Conclusions	184
8 Conclusion to Part Two	187
Concluding Remarks	189
Appendix A: Stability Analysis of LK Model	191
Appendix B: Regimes of Operation	193
Appendix C: Langevin Equations	197
Appendix D: RIN Expressions	201
Appendix E: Optical Modes	203
Appendix F: Integration Scheme	207
Notation	209
Bibliography	211
List of Figures	221
Curriculum Vitae	i

Resum

Actualment les aplicacions tecnològiques requereixen la integració de dispositius optoelectrònics de baix consum, de cada vegada més petits i més ràpids. Els làsers de semiconductor (SCL) són uns bons candidats per aquestes tecnologies degut al seu baix cost, petit tamany, i la possibilitat d'esser modulats a gran velocitat. Els làsers de semiconductor s'empren habitualment en la vida moderna. En sistemes de telecomunicacions, els làsers envien senyals a milers de quilòmetres per fibres òptiques. En aplicacions electròniques, els làsers de semiconductor s'empren per llegir/escriure dades sobre discs compactes, CD-ROMs i DVDs. Altres aplicacions habituals són les impressores i fotocopiadores làser, punters làser, sensors de pol·lució, *displays*, etc.

Aquesta tesi és una contribució a l'estudi de les propietats dinàmiques dels làsers de semiconductor. Ens centram en la discussió de les inestabilitats òptiques que tenen lloc en aquests dispositius. El treball de modelat considera dues configuracions distintes. Depenent de la geometria de la cavitat làser tenim: i) làsers d'emissió lateral de cavitat composta, ii) làsers de cavitat vertical i emissió per superfície. Un dels majors reptes de la tesi és la comprensió i identificació dels processos físics que governen les inestabilitats. Vull fer notar que l'estructura dels capítols és bastant autocontinguda així com una sèrie d'aspectes metodològics. Cada tema inclou el plantejament del problema, formulació del model, anàlisis, resultats experimentals en cas que n'hi hagi, i conclusions. La formulació electromagnètica del làser és formalment equivalent al d'una guia d'ones dèbilment pertorbada.

En la primera part de la tesi tractem amb làsers d'emissió lateral amb graus de llibertat afegits. L'anàlisi teòric està acompanyat amb discussions i resultats experimentals. L'estudi comença en el **capítol 2** amb la dinàmica de modes de cavitat externa en làsers de semiconductor amb retroalimentació òptica retrasada. Així com es comenta en la secció 1.2, els SCL amb retroalimentació òptica mostren una dinàmica molt complexa, i a la vegada interessant, que ha estat objecte d'un intens estudi. Avui en dia, aquests sistemes són de gran interès en la generació de sortides caòtiques. El caos òptic d'alta dimensió té aplicacions en sistemes de comunicació codificada d'alta velocitat [46]. Llavors, la caracterització dels règims caòtics és essencial. Po-

dem forçar el làser amb retroalimentació òptica a operar en un règim caòtic considerant nivells de reinjecció de llum moderats i cavitats externes llargues. Aquí empram el model de Lang-Kobayashi per descriure l'evolució d'un únic mode longitudinal en làsers tipus distributed-feedback (DFB). En aquest treball estudiem les propietats estadístiques de les sortides òptiques caòtiques així com les lleis d'escala associades amb les transicions entre distints règims d'operació. Encara que les senyals òptiques mostrin una gran irregularitat, trobam que algunes propietats estadístiques segueixen regles específiques. En el **capítol 3**, consideram l'acoblament mutu de dos làsers de semiconductor idèntics. El cas de dos SCL acoblats unidireccionalment ha estat estudiat previament, demostrant que sota certes condicions els làsers poden sincronitzar-se [47]. Curiosament, existeixen escassos treballs sobre l'acoblament bidireccional de làsers, els quals suggereixen que nous escenaris de sincronització són possibles [48]. La deducció de les equacions comença de principis bàsics, tot reprenent el problema electromagnètic del sistema acoblat. Trobam que les mínimes equacions necessaris per descriure el sistema corresponen a un problema d'injecció bidireccional amb retràs. En aquest treball estam interessats en descriure les inestabilitats induïdes per l'acoblament mutu i les propietats de sincronització. Especialment, comentam la importància del paper del retràs en l'acoblament mutu dels oscil·ladors. El **capítol 4** presenta les conclusions de la primera part de la tesis. El resum de les tasques de modelat en la primera part són

- Simulació numèrica del model de Lang-Kobayashi sobre intervals de temps llargs (\sim ms) i escombrant el co-espai de paràmetres. Caracterització estadística dels SCL amb retroalimentació òptica.
- Modelat electromagnètic de dos SCL idèntics acoblats mútuament. Estudi de la validesa de models senzills.
- Implementació numèrica dels models anteriors: Interpretació de les inestabilitats induïdes per l'acoblament i la sincronització dels làsers, observades experimentalment.

Dels resultats numèrics i experimentals que hem obtingut podem concloure

1. Evidència experimental i numèrica de l'alternància entre emissió estable (en un mode de cavitat externa) i fluctuacions de baixa freqüència (LFF). La distribució de temps de caiguda de la intensitat òptica en un làser monomode amb retroalimentació òptica mostra una gran dispersió de temps. Llei de escala tipus $\langle T \rangle \sim (p/p_c - 1)^{-1}$ pel temps entre caigudes T , associada a la transició d'operació estable a LFF.
2. Existència de solucions monochromàtiques *phase-locked* per a l'acoblament de dos SCL. Aquest tipus d'operació sembla inestable sota condicions dinàmiques conduint el sistema a solució de sincronització àcrona (a distint temps).

En la segona part de la tesi, descrivim les inestabilitats òptiques que ocorren en làsers de cavitat vertical i emissió per superfície (VCSELS). En primer cas, estudiem les propietats de polarització de la llum emesa. Insistim en la importància de la dinàmica d'espí sobre les propietats de renou i la selecció de modes de polarització. En segon lloc considerem l'excitació de modes transversals en dispositius guiats per guany. La segona part de la tesi està organitzada de la manera següent. Començem en el **capítol 5** descrivint la dinàmica de petita senyal amb el conegut model Spin-Flip per dispositius monomodes. En particular calculam l'espectre de les fluctuacions d'intensitat resolt en polarització. Donam una interpretació de les evidències experimentals d'anticorrelació entre les fluctuacions de les components de polarització. En el **capítol 6**, es presenta una generalització del model spin-flip mitjançant la incorporació de graus de llibertat espacials i una funció susceptibilitat òptica depenent de la freqüència. El model que resulta combina els efectes de polarització i transversals i és adequat per descriure la dinàmica de gran senyal. En l'absència de modes transversals, la selecció de modes de polarització resulta d'un efecte conjunt de la dinàmica d'espí, la posició relativa sobre la corba de guany i efectes tèrmics. En segon lloc, es mantenen els graus de llibertat espacials i el model espai-temporal que resulta s'empra per estudiar la selecció de modes transversals. En aquest cas, considerem dispositius guiats per guany que presenten una petita distribució d'índex de refracció que prové d'una lent tèrmica feble. Analitzam els efectes de la lent tèrmica sobre les característiques dels dispositius. En primer lloc desenvolupam un mètode semi-analític per determinar la selecció de modes transversals devora de la corrent lliard del làser associat amb distintes estructures. En segon lloc considerem la dinàmica de modes transversals que ocorre sota una excitació de gran amplitud de la corrent elèctrica. Aquesta darrera situació és la que generalment s'utilitza en sistemes de comunicacions òptiques amb esquema digital. El **capítol 7** també considera modulació de corrent de gran amplitud, però en aquest cas estudiem dispositius més petits. En aquest cas, la difusió espacial de portadors en dispositius monomodes origina l'aparició de pulsacions secundàries de la intensitat òptica durant els transitoris d'apagat. Comparant la descripció espai-temporal amb la seva corresponent expansió modal, discutim els límits de validesa i l'ús pràctic d'una expansió modal per descriure la dinàmica de gran senyal en VCSELS guiats per guany. Podem concretar amb més detall les tasques de modelat de la segona part de la tesi

- Modelat bàsic del temps de coherència d'espí en estructures de semiconductor de pou quàntic i la seva rellevància sobre les propietats de polarització en VCSELS. Implementació numèrica del model spin-flip incloent fonts estocàstiques de renou.
- Anàlisi de petita senyal i de fluctuacions. Càlcul analític de l'espectre de fluc-

tuacions de potència de la intensitat total i de les components de polarització. Interpretació de l'anticorrelació entre les fluctuacions de les components de polarització.

- Modelat bàsic. Recerca de descripcions simples per la susceptibilitat òptica a un nivell mesoscòpic incloent efectes de polarització, interacció a molts de cossos i efectes tèrmics.
- Desenvolupament de còdigs numèrics, que incorporin la susceptibilitat òptica, per estudiar la dinàmica de modes de polarització i transversals en dispositius guiats per guany: mecanismes de selecció de modes, i efectes d'anti-guiat per portadors sota modulació de gran amplitud.

Les conclusions que treim de la segona part de la tesis són

1. Els mecanismes de selecció de modes transversals depenen tant de les característiques del material (freqüència d'operació, guany material, etc.) com de les geomètriques mitjançant la lent tèrmica (guany modal). Llavors dependent de les característiques del dispositiu distints modes transversals poden ser seleccionats devora de la corrent llindar. Sota excitació de gran amplitud hi ha altres mecanismes dinàmics que intervenen (cremat espacial de portadors, omplida de bandes, etc.).
2. La necessitat de models espai-temporals en dispositius guiats per guany està justificada en el cas de guiats febles (gradents tèrmics menors de 8 K). En tal cas les descripcions modals donen lloc a errors quantitius.

Finalment, en el **capítol 8** es donen les conclusions de la segona part de la tesis.

La comprensió dels mecanismes físics que governen les inestabilitats ha de permetre, més que procediments per evitar-les, la possibilitat d'una lliure manipulació i per tant, donar sortida a nous graus de llibertat.

Palma, 25 Novembre 2002

José Mulet Pol

Chapter 1

Introduction

1.1 Semiconductor Lasers

The origins of the laser¹ can be traced back to the Einstein's concept of stimulated emission. The presence of a photon, with appropriate frequency, can stimulate an excited atom to emit a photon with identical phase, frequency and propagation direction that the incident one [1]. Three ingredients are fundamental in any laser: a medium providing gain/amplification, a pump generating population inversion, and a cavity confining the optical field. The first population inversion was attained in ammonia molecules passing through an electrostatic focuser by Townes and Shawlow [2] in 1954. The constructed device, originally called MASER, emitted light in the microwave range. The first successfully laser, operating in the visible spectrum, was constructed by Maiman [3] and consisted of a ruby crystal surrounded by a helicoidal flash tube. This advent was followed, at the ends of the same year, by the experimental demonstration of working He-Ne gas lasers.

Semiconductors were too different to an "atomic" system, and too poorly understood, to profit much from the success with ruby and gas lasers. The feasibility of stimulated emission in semiconductors was considered by the early 60's but there was no motivation to explore the possibilities as it was believed that the emission would be weak. However in 1962 a group from MIT Lincoln Labs reported emission of radiation, using Zn-diffused GaAs p-n junction, and transmission of the light over a considerable distance. This report sparked great interest and before the year was out, four groups reported working semiconductor lasers (SCL) [4].

Current technological applications demand the miniaturization and integration of low-consume optoelectronic devices. At the same time, faster devices are needed to process the information. Semiconductor lasers have become the technology of

¹LASER is the acronym of light amplification by stimulated emission of radiation.

choice for many important applications because of their small size, low cost, high reliability, spectral and modulation characteristics. Semiconductor lasers are widely used in modern life. In telecommunications they send signals for thousands of kilometers along optical fibers. In consumer electronics, semiconductor lasers are used to read/write data on compact disks, CD-ROMs and DVDs. Other applications include laser printers, laser pointers, pollution monitoring, displays, etc.

Working principles

The energy separation between the valence and conduction bands of a semiconductor material is of the order of $E_g \sim 1$ eV, thus being comparable with the thermal excitation energy and the photon energy in the visible spectrum. This fact converts semiconductors in very interesting elements for optical applications. The concept of a carrier in a SCL is associated with an electron in the conduction band and hole in the valence band that actually

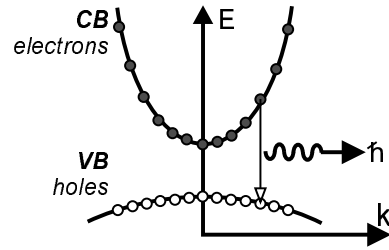


Figure 1.1. Band structure of a semiconductor, (CB) conduction band, and (VB) valence band.

represents the vacancy of an electron. Under thermodynamic equilibrium, electrons and holes are distributed over a range of energies according to Fermi-Dirac statistics. Hence, electrons predominantly occupy the bottom of the conduction band whereas holes are at the top of the valence band [Fig. 1.1]. Photons are generated by the radiative recombination of electron-hole pairs. Since this process requires the conservation of electron wavenumber k , it will be more efficient in direct band-gap semiconductors. Under thermal equilibrium, the rate of radiative recombination is extremely small, only ~ 100 photons are emitted per cm^3s providing an insignificant output power. In order to generate light, population inversion in the semiconductor must be achieved by localizing in a spatial region, known as active region, a large number of electrons and holes. Let us see how to reach these conditions.

Semiconductor lasers are based on p-n junctions of semiconductor materials – *diode lasers*. The confinement of carriers is accomplished by means a heterostructure, i.e., by inserting the active region between two semiconductor materials of wider band-gap. The working principles of a $p^+ - p - n$ structure are sketched in Fig. 1.2. Electrons and holes can move freely to the active layer under forward bias $V > 0$. Once there, they cannot cross to the cladding regions because the potential barrier resulting from the band-gap differences. The resulting energy structure is able to trap a large number of electrons and holes inside the active region, where they can radiatively recombine. In turn, this heterostructure provides lateral confinement

of the electric field due to the higher refractive index in the central region. The most important class of semiconductor diode lasers are based on III-V compounds, for instance² GaAlAs/GaAs and InGaAsP for longer wavelength communication windows. The development of blue semiconductor lasers on the basis of GaN [5] opens the way for a host of new applications of semiconductor lasers: the light is emitted at shorter wavelengths and thus can be more tightly focused, e.g. increasing the density of data stored.

Advances in quantum-mechanically designed materials have led to new low-threshold and high-power semiconductor lasers that are suitable for a broad range of applications. The thin layer of GaAs bounded on either side by GaAlAs, confine electrons and holes. In present devices, the thickness of the GaAs layer is typically smaller than $\sim 200 \text{ \AA}$, thus the confinement energies become quantified. The resulting heterostructure is known as quantum well laser [6] in order to differentiate from bulk structures. Further confinement of the electron's motion to one and zero dimensions have lead to quantum wire and quantum dot lasers. Intrinsic properties of quantum dot lasers include low threshold current, higher temperature operation range, higher modulation bandwidth and narrower linewidth [7]. More recently, the development of quantum-cascade lasers [8] has provided excellent devices for applications requiring high power, tunability and pulsed operation at room temperature.

²The notation $\text{Ga}_{1-x}\text{Al}_x\text{As}/\text{GaAs}$, with x the molar fraction of Al, represents the nature of the materials forming the heterostructure, i.e., a “sandwich” of GaAlAs/GaAs/GaAlAs.

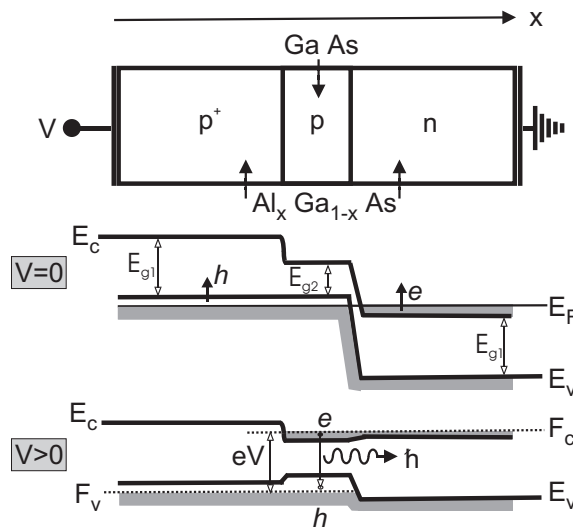


Figure 1.2. Energy band diagram of a heterostructure semiconductor laser under thermodynamic equilibrium ($V = 0$), and forward bias ($V > 0$).

The optical gain is accomplished by electric injection of minority carriers into the thin active layer. However, optical gain alone is not enough to operate a laser. The polished facets perpendicular to the junction plane provides the optical feedback by forming a Fabry-Perot cavity, whose role is twofold. First, it selects a preferred direction for stimulated emission and second, it introduces a frequency-selective mechanism that defines the longitudinal cavity modes. Since the mirrors are partially reflecting, a fraction of photons escape through the mirrors leading to a decay of the electric field within the cavity. Moreover, the electric field is absorbed by the different material layers constituting the laser. Thus, the optical intensity decays at a rate [9]

$$\kappa = \frac{c}{n_g} \left[\alpha_{int} + \frac{1}{2L} \ln \frac{1}{R_1 R_2} \right], \quad (1.1)$$

where $R_{1,2}$ represents the internal reflectivities of the facets, L the cavity length, n_g the group refractive index, c the speed of light in vacuum, and α_{int} the internal losses. From the above expression, we conclude that there exists a compromise between the cavity length and the facet reflectivities to ensure moderate losses. In order to achieve laser operation the injected current has to exceed a certain threshold value, a point where the optical gain equals the total losses.

Standing waves in a Fabry-Perot cavity are only possible for a discrete number of frequencies that define the longitudinal cavity modes. The frequency mode spacing reads [9]

$$\Delta\nu_L = \frac{c}{2n_g L}. \quad (1.2)$$

For an effective width of the gain spectrum $\Delta\nu_G$, the ratio $\Delta\nu_G/\Delta\nu_L$ provides an estimation of the number of longitudinal modes that may become active. It is well known that multimode emission affects the performance of the device in data-transmission applications because of an enhanced pulse dispersion during fiber propagation. In order to achieve singlemode operation is preferable to enhance the mode separation $\Delta\nu_L$, by reducing the cavity length L . However, in this case the losses in Eq. (1.1) dramatically increase unless the facet reflectivity is enhanced by some means.

Depending on the dimensions and geometry of the cavity, lasers can be classified into edge-emitting lasers (EELs) and vertical-cavity surface-emitting lasers (VCSELs). The dynamics of these devices will be investigated in the two parts of the thesis.

1.2 Edge-Emitting Semiconductor Lasers

In an EEL, sketched in Fig. 1.3, the light propagates in a rectangular waveguide whose longitudinal extent coincides with the active layer. The mirrors are formed by cleav-

ing the semiconductor wafer along the crystal planes to form smooth facets. No external mirrors are in general required, since cleaved facets of semiconductor already provide sufficient reflectivity to allow the laser operation. If necessary, dielectric materials are subsequently deposited to reach the desired reflectivity. The typical cavity length in EELs is of the order of $L \sim 300 \mu\text{m}$, the facet reflectivities of $R \approx 0.3$, and longitudinal mode frequency spacing of $\Delta\nu_L \sim 100 \text{ GHz}$. Thus a large number of longitudinal modes can participate in the laser action. In spite of the advantages over conventional gas lasers, edge-emitting SCL have several shortcomings: divergent beams, elliptical beam profiles, multimode emission, etc. As a consequence new semiconductor structures have been developed in order to improve the characteristics of EELs: distributed feedback (DFB) and distributed Bragg reflectors (DBR) lasers [10], cleaved compound-cavity lasers [11], and more recently microcavity lasers [12]. The polarization direction of the electric field in an EEL is imposed by the structure, being transverse electric (TE) or transverse magnetic (TM) depending whether the electric or the magnetic field is linearly-polarized along the heterojunction plane.

A proper design of the laser structure is essential to achieve continuous wave (cw) operation at room temperature and low threshold currents. The heterostructure already provides confinement of the optical mode perpendicular to the junction plane. However, additional confinement along the junction plane is required. The laser structures can be classified into gain-guided and index-guided depending the way in which the optical mode is confined. In gain-guided devices the optical mode along the junction plane is determined by the spatial distribution of gain, which in turn depends on the distribution of injection current. In index-guided a spatial variation of the index of refraction creates a waveguide that defines the modes. The typical threshold currents of gain-guided lasers is about $\sim 100 \text{ mA}$, whereas only $\sim 10 \text{ mA}$ in index-guided devices [10]. The localization of the current along the active region improves the device characteristics. Gain-guided structures use proton implantation

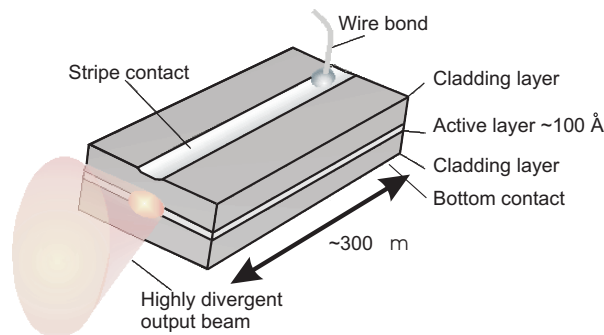


Figure 1.3: Sketch of a heterostructure edge-emitting semiconductor laser.

that create a region of high resistivity that restricts the flow of the current. Broad-area lasers obtain substantial output powers, however they do not use any scheme of current confinement and exhibit high threshold current densities and filamentation of the optical profiles.

In this work, we are concerned with some aspects of the nonlinear dynamics of SCL. Previous studies [14, 15] investigated a variety of problems: the switch-on time and time-jitter of the optical pulses during gain-switching [16], self-pulsing due to Q-switching via a saturable absorber [17], ultrashort pulses via mode locking [18], period doubling and route to chaos in direct current modulated lasers [19], injection locking [20, 21], etc. Semiconductor lasers are quite sensitive to external perturbations due to the low reflectivity of the mirrors. Considerable attention was devoted to investigating the effects of optical feedback on the static, dynamic, spectral, noise and modulation characteristics [22, 23], and on selfpulsing lasers [24]. Even a relatively small amount of external optical feedback can significantly affect the performance of the laser: a dramatic increase in the emission linewidth was found [25]. These findings motivated the understanding of the nonlinear dynamical processes originating these instabilities [26]. A striking behavior of the optical intensity appears: the appearance of power dropouts at irregular time intervals, *low frequency fluctuations* (LFF), as can be seen in Fig. 1.4(a). The first experimental evidence of such a behavior was already reported in the 70's [27]. The debate about the origin of the LFF have been very intense: stochastic, deterministic, and the importance of multilongitudinal emission [See Chapter 2]. Looking at faster time scales in Fig. 1.4(b), the optical intensity displays a highly irregular behavior with pulsations at the \sim ns time scale. The first part of the thesis is intended to modeling and characterizing the feedback-induced instabilities. We perform a statistical description of the LFFs by means an extensive numerical simulation of the Lang-Kobayashi model [28]. We will briefly mention the applications of these systems in encoded optical communications.

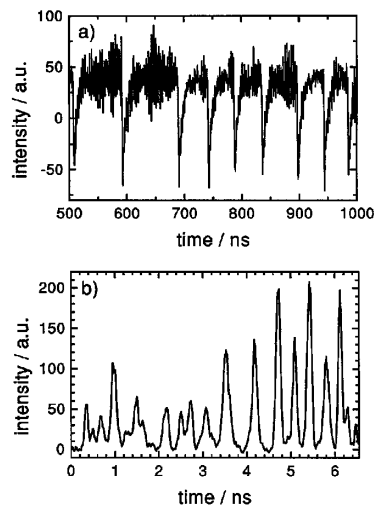


Figure 1.4. Experimental time traces of a semiconductor laser with optical feedback measured with (a) photodiode and (b) a streak camera. After Ref. [13].

1.3 Surface-Emitting Semiconductor Lasers

VCSELs are a particular type of SCL in which the resonating cavity is perpendicular to a thin active layer. The typical dimensions, length \times width \times thickness, in a VCSEL are $\sim 1 \times 10 \times 10 \mu\text{m}^3$, considerably different than an EEL. An important consequence is that VCSELs emit in a single-longitudinal mode. In contrast to conventional EELs, the optical beam is guided and emitted in the vertical direction. The thin active layer ($\sim 10 - 30 \text{ nm}$) is usually composed by one or several quantum wells providing high optical gain, low threshold current, high relaxation oscillation frequency, and improved temperature characteristics. More recently, VCSELs based on quantum dot active material have been developed [7]. It is worth noting that the single gain-path length in a VCSEL is extremely small, typically of 1% of the cavity length, i.e., four orders of magnitude shorter than an EEL. Therefore, the active layer has to be placed at an antinode of the electric field to enhance the optical confinement. Secondly, it is imperative to fabricate mirrors with very high reflectivities, active regions with high optical gain, and cavities with very low optical losses. The VCSEL's mirrors are created by growing a stack of quarter-wavelength layers of semiconductor materials with alternating refractive indexes, forming a distributed Bragg reflector (DBR). The order of 20–40 pairs are necessary to achieve high reflectivities.

Carrier transport between the electric contacts along the different layers determines the lateral distribution of current density at the active layer, that in turn delimits the lateral extension of the active region. The electric contact is disk-shaped or ring-shaped in bottom-emitter and top-emitter devices as shown in Fig. 1.5. Gain-guided VCSELs use proton implantation to localize the current close to the cavity axis. In weakly index-guided VCSELs, an oxide-layer is placed close to an antinode of the electric field. The lower refractive index of the oxidized region, typically a change of $\sim 10^{-2}$, provides a lateral confinement of the electric field. The central aperture

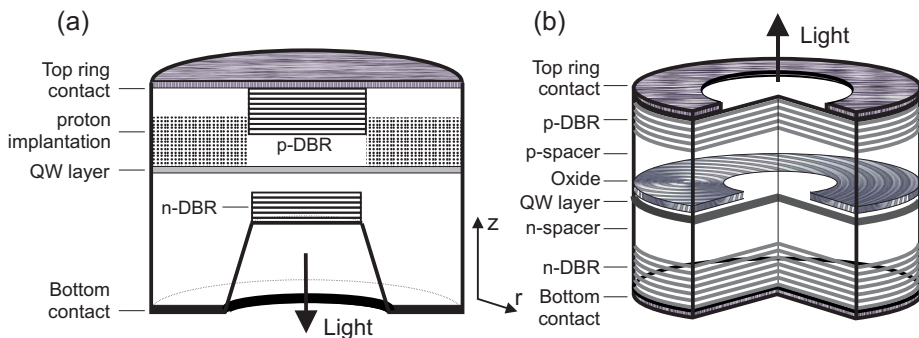


Figure 1.5. Sketch of a bottom-emitting (a) and top-emitting (b) vertical-cavity surface-emitting semiconductor laser.

of the oxide restricts the current flow and thus the extension of the active region. Strongly index-guided devices, such as airpost VCSELs, have an abrupt separation between semiconductor air that provides a large refractive-index contrast, $\Delta n \sim 1$.

In contrast to EELs, the geometry of the VCSEL's cavity is cylindrical. For this reason, the output beam is circular reducing the coupling losses with fibers. The vertical structure allows for an easy integration in two-dimensional (2D) arrays, and more recently in photonic band gap lasers. Further, it allows for a direct testing without necessity of cleaving and separating the devices. The careful design of the active material provides ultra-low threshold currents $\sim \mu\text{A}$.

Development of VCSELs

Certainly, VCSELs that are currently commercially available, have been the fruit of the continuous development of the semiconductor technology and growth techniques. The first surface emitting (SE) laser was experimentally demonstrated by Melngailis already in 1965. The active material consisted in a piece of bulk InSb, refrigerated at 10 K and immersed in an intense magnetic field in order to confine the carriers. The concept of heterostructure in SE laser was introduced by K. Iga (1977) as an alternative method to improve the carrier confinement. Exploiting this idea, H. Soda in 1979 obtained pulsed operation of GaInAsP/InP SE with threshold current of 900 mA operating at 70 K. The threshold current of these initial SE devices was so high because the reflectivity of the metallic mirrors was insufficient. In 1984, K. Iga replaced them by semiconductor mirrors obtaining pulsed operation of GaAlAs/GaAs VCSEL at room temperature. Important improvements were achieved after the introduction of multilayer mirrors and also when replacing the bulk active material by quantum wells. With this new technology, Jewell et al. (1989) grew VCSELs with threshold currents as low as 1-2 mA operating cw at room temperature.

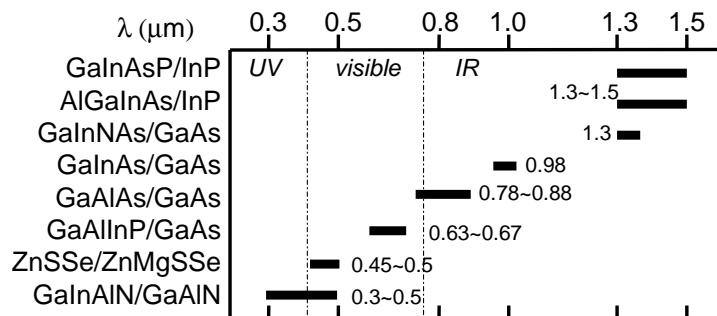


Figure 1.6: Materials for VCSELs in a wide spectral band. After Ref. [29].

The first commercial applications of VCSELs started to appear since 1996, being suitable for local area networks (LANs), optical interconnects, and for future applications in the gigabit Ethernet as well. By a proper combination of materials it is possible to construct devices emitting at different wavelengths [See Fig. 1.6]. The importance of GaInAsP/InP VCSELs operating at 1.3 or 1.55 μm is increasing, since their potential application in parallel lightwave systems and parallel optical interconnects. Some commercial links are also available with AlGaAs/GaAs VCSELs emitting near 0.85 μm . Red emitting VCSELs, based on GaAlInP/GaAs materials, are also attractive for their applications in CD players and plastic optical fiber systems. Green-blue and blue VCSELs are, in general, more difficult to obtain displaying high threshold currents, short lifetimes and in many cases only pulsed operation. The applications of blue VCSELs is huge, for instance, in storage and information retrieval, full color displays, and high efficiency illumination together with green and red devices.

Instabilities

In spite of these very attractive advantages, several instabilities have been identified in VCSELs. The polarization of the electric field in an EEL is defined by the structure, however polarization in VCSELs is not as well stabilized due to their circularly symmetric cavity. A common instability, known since long time ago, is the *polarization switching* among two orthogonal linearly-polarized states as shown in Fig. 1.7. This fact motivates the understanding, characterization and control of polarization in VCSELs. Since in many descriptions of EELs the polarization degrees of freedom are disregarded, the description of polarization effects requires of a thorough revision of the microscopic processes involved [30]. The relative contribution of thermal [31] and nonthermal [32] effects has been broadly discussed [33, 34]. Moreover, the rela-

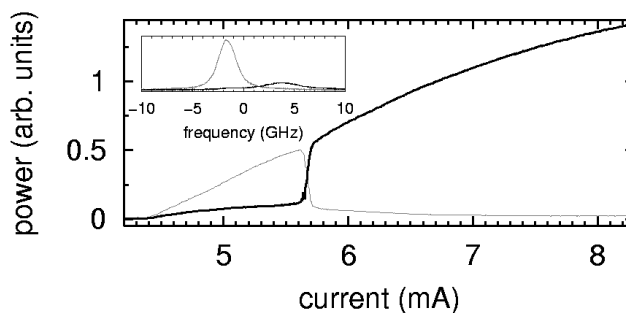


Figure 1.7. LI curve after projection on linear polarization states for a 8 μm proton-implanted VCSEL. The black (grey) lines correspond to high (low) frequency mode. The inset shows the optical spectrum at a current 4.3 mA. After T. Ackemann and M. Sondermann, Appl. Phys. Lett. **78**, 3574 (2001).

tively large Fresnel number allows for the formation of spatial structures [35, 36]. Figure 1.8 shows that although the laser onset is initiated in a Gaussian transverse mode, more complicated structures develop for higher injection currents. The understanding of polarization and transverse modes in VCSELs requires of a unified description. These issues will be treated in the second part of the thesis. We will show how the dynamics of the electron's spin, described by the spin-flip model [37], naturally enters into the description of the light polarization of quantum well VCSELs. Finally, the behavior of VCSELs is sensitive to thermal effects mainly through two mechanisms: a global increase of the temperature (device heating), and the development of transverse gradients of temperature (thermal lensing). The former leads to a reversible switch-off of the output power when increasing the current injection through thermal roll-off [Fig. 1.8], while the latter affects to the transverse mode properties of the device. The modeling of the transverse mode structure of gain-guided VCSELs requires of the simultaneous consideration of gain-guiding, carrier antiguiding and thermal mechanisms [38].

1.4 Common Features in the Modeling of Semiconductor Lasers

The modeling of semiconductor lasers requires a trade-off between comprehensibility, accuracy and complexity. In this thesis, we aim to understand the optical processes occurring in semiconductor lasers. The challenge involves two aspects i) the formulation of the physical models and ii) their analysis and numerical solution. Strictly speaking, the dynamical properties of semiconductor laser are the result of a complex interplay of diverse physical mechanisms; namely, optical, thermal, and electrical effects. The interdependence of these effects should require of self-consistent solutions [39]. Then, in order to develop the simplest theoretical de-

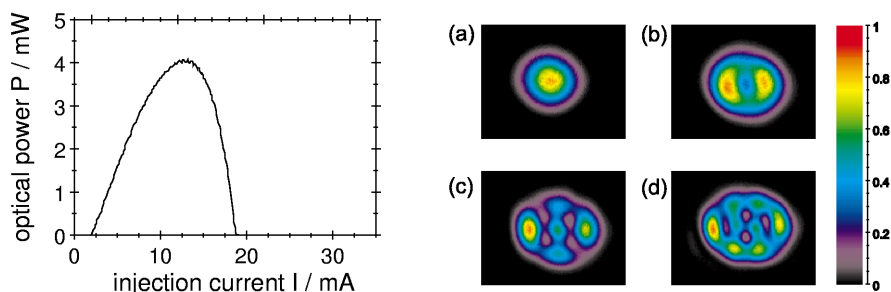


Figure 1.8. Optical power versus injection current for a 6 μm oxide aperture VCSEL (left). Nearfield images at injection currents 3.0 mA (a), 6.2 mA (b), 14.7 mA (c), and 18 mA (d). After C. Degen et al., *Opt. Express* 5, 38 (1999).

scription, it is essential to identify the relevant mechanisms for each problem. Next, we summarize the basic equations that govern the evolution of the optical variables and the light-matter interaction.

1.4.1 Maxwell's equations

The electromagnetic analysis of the fields within a laser cavity starts from Maxwell's equations [40]. For a nonmagnetic medium ($\mu_\omega \approx 1$) and in the absence of free charges, at optical frequencies ($\rho_\omega \approx 0$), the Maxwell's equations [40] expressed in frequency domain read

$$\vec{\nabla} \cdot \vec{\mathcal{D}}_\omega \approx 0, \quad (1.3a)$$

$$\vec{\nabla} \cdot \vec{\mathcal{B}}_\omega = 0, \quad (1.3b)$$

$$\vec{\nabla} \times \vec{\mathcal{E}}_\omega = i\omega \vec{\mathcal{B}}_\omega, \quad (1.3c)$$

$$\vec{\nabla} \times \vec{\mathcal{H}}_\omega = \vec{\mathcal{J}}_\omega - i\omega \vec{\mathcal{D}}_\omega, \quad (1.3d)$$

where $\vec{\mathcal{E}}_\omega$ and $\vec{\mathcal{H}}_\omega$ are the electric and magnetic fields, $\vec{\mathcal{D}}_\omega$ and $\vec{\mathcal{B}}_\omega$ are the respective flux densities, and $\vec{\mathcal{J}}_\omega$ is the current density vector. Note that we have used

$$\tilde{F}_\omega \equiv \int_{-\infty}^{\infty} dt e^{i\omega t} F(t),$$

for the direct Fourier transform, a definition that will be used all through the thesis. Eqs. (1.3a)–(1.3d) are complemented with the constitutive relationships in semiconductor media

$$\vec{\mathcal{D}}_\omega = \epsilon_0 \vec{\mathcal{E}}_\omega + \vec{\mathcal{P}}_\omega, \quad (1.4a)$$

$$\vec{\mathcal{B}}_\omega = \mu_0 \vec{\mathcal{H}}_\omega, \quad (1.4b)$$

$$\vec{\mathcal{J}}_\omega = \sigma_\omega \vec{\mathcal{E}}_\omega, \quad (1.4c)$$

with ϵ_0 the vacuum permittivity, μ_0 the vacuum permeability, and σ_ω the electrical conductivity of the medium. The induced material polarization $\vec{\mathcal{P}}_\omega$ has two contributions: the linear $\vec{\mathcal{P}}_\omega^l$ and nonlinear $\vec{\mathcal{P}}_\omega^{nl}$ polarization

$$\vec{\mathcal{P}}_\omega = \vec{\mathcal{P}}_\omega^l + \vec{\mathcal{P}}_\omega^{nl}. \quad (1.5)$$

The linear contribution takes into account the dielectric nature of the passive semiconductor medium, and can be expressed in terms of the linear susceptibility χ_ω^l through $\vec{\mathcal{P}}_\omega^l = \epsilon_0 \chi_\omega^l \vec{\mathcal{E}}_\omega$, that in turn defines the background refractive index

$$n_{e\omega} \equiv \sqrt{1 + \chi_\omega^l}.$$

On the other hand, the nonlinear polarization describes both the gain/absorption and dispersion of the semiconductor medium as a function of the carrier density N induced by electrical injection.

Taking the $(\vec{\nabla} \times)$ of the Eq. (1.3c) and assuming that $\vec{\nabla} \cdot \vec{\mathcal{E}}_\omega \approx 0$, we obtain a wave equation for the electric field

$$\vec{\nabla}^2 \vec{\mathcal{E}}_\omega + i\omega \frac{\sigma_\omega(\vec{r})}{\epsilon_0 c^2} \vec{\mathcal{E}}_\omega + \left(\frac{\omega}{c}\right)^2 n_{e\omega}^2(\vec{r}) \vec{\mathcal{E}}_\omega = -\frac{1}{\epsilon_0} \left(\frac{\omega}{c}\right)^2 \vec{\mathcal{P}}_\omega^{nl}(\vec{r}), \quad (1.6)$$

where $n_{e\omega}(\vec{r})$ represents the distribution in passive refractive-index.

1.4.2 Semiconductor dynamics

In the semiclassical laser theory, the light-matter interaction is described by the material polarization \mathcal{P}^{nl} that appears in the wave equation (1.6) of the electric field \mathcal{E} . Next we enumerate the ingredients required for determining the dynamics of the semiconductor material.

1. *Band structure*: The energy-dispersion relationships $E_i(\mathbf{k})$ and dipole-matrix elements $\vec{\mu}_{\mathbf{k}}$ can be determined by solving the Schrödinger equation for the Bloch function at wavevector \mathbf{k} . The Hamiltonian must include i) interaction of the electron with the periodic lattice H_0 , ii) $\mathbf{k} \cdot \mathbf{p}$ interaction, and iii) deformation potentials H_{strain} in the case of strain.
2. *Interaction Hamiltonian*: It includes kinetic energy from electrons and holes at different Bloch wavenumbers \mathbf{k} , dipole interaction of the light with the electric field, and many-body effects.
3. *Heisenberg equations of motion*: Evolution of the electronic occupation number $n_{e\mathbf{k}}$, hole occupation $n_{h\mathbf{k}}$, and microscopic polarization $p_{\mathbf{k}}$ at wavevector \mathbf{k} .
4. *Bloch semiconductor equations*: The Hartree-Fock contribution of the Coulomb interaction is expressed as screening terms. Each transition at fixed \mathbf{k} is conceptually equivalent to a two-level system, although with renormalized transition energies and Rabi frequencies.

When the Coulomb interaction is neglected, the Bloch semiconductor equations reduce to the *free-carrier model*. In this case, the semiconductor behaves as an ensemble of inhomogeneously broadened two-level systems. A transition to fixed \mathbf{k} is equivalent to the density-matrix ρ formulation of a two-level system, i.e., the diagonal terms of ρ stand for $n_{e\mathbf{k}}$ and $(1 - n_{h\mathbf{k}})$, whereas the cross-terms represent $p_{\mathbf{k}}$. The

free-carrier model reads [14, 41, 42]

$$\frac{dp_{\mathbf{k}}}{dt} = -(\gamma_{\perp} + i\omega_{\mathbf{k}})p_{\mathbf{k}} - i\Omega_{\mathbf{k}} [n_{e\mathbf{k}} - (1 - n_{h\mathbf{k}})], \quad (1.7a)$$

$$\frac{dn_{i\mathbf{k}}}{dt} = i [\Omega_{\mathbf{k}} p_{\mathbf{k}}^* - \Omega_{\mathbf{k}}^* p_{\mathbf{k}}] + \Lambda_{i\mathbf{k}} + \left. \frac{dn_{i\mathbf{k}}}{dt} \right|_{decay}, \quad (1.7b)$$

where

$$\Omega_{\mathbf{k}} \equiv \frac{\mu_{\mathbf{k}} \mathcal{E}}{\hbar}, \quad \omega_{\mathbf{k}} \equiv \frac{E_e(\mathbf{k}) - E_h(\mathbf{k})}{\hbar},$$

are the Rabi and transition frequencies respectively. In the relaxation rate approximation, the carrier-carrier collisions introduce a dephasing of the material polarization γ_{\perp} (linewidth of the optical transitions), and more important, tend to drive the population distributions to quasi-equilibrium Fermi-Dirac functions [43]. The term $\Lambda_{i\mathbf{k}}$ represents the generation of carriers due to pumping, whereas the last term in Eq. (1.7b) includes radiative/nonradiative decay. The free-carrier model provides compact expressions for the macroscopic material polarization \mathcal{P}^{nl} , at a monochromatic field at frequency ω , starting from the microscopic $p_{\mathbf{k}}$

$$\mathcal{P}_{\omega}^{nl} = \frac{1}{V} \sum_{\mathbf{k}} \mu_{\mathbf{k}}^* p_{\mathbf{k}}, \quad (1.8a)$$

$$p_{\mathbf{k}} = -\frac{i}{\hbar} \mu_{\mathbf{k}} \mathcal{E}_{\omega} [n_{e\mathbf{k}} - (1 - n_{h\mathbf{k}})] \frac{1}{i(\omega_{\mathbf{k}} - \omega) + \gamma_{\perp}}. \quad (1.8b)$$

with $i = e, h$ and V the active crystal volume. Under quasi-equilibrium conditions the carrier distributions $n_{i\mathbf{k}}$ are equivalent to the Fermi-Dirac distributions $f^i(E_i(\mathbf{k}))$

$$f^i(E_i(\mathbf{k})) = \frac{1}{1 + e^{(E_i(\mathbf{k}) - F^i)/k_B T}}, \quad (1.9)$$

with F^i the quasi-Fermi levels for electrons and holes, k_B the Boltzmann constant and T the temperature absolute. The material polarization can be alternatively described through the optical susceptibility χ

$$\mathcal{P}_{\omega}^{nl} = \varepsilon_0 \chi(\omega, \{n_{e\mathbf{k}}, n_{h\mathbf{k}}\}) \mathcal{E}_{\omega}.$$

The optical susceptibility reads

$$\chi(\omega, N) = -\frac{i}{\varepsilon_0} \frac{1}{V\hbar} \sum_{\mathbf{k}} |\mu_{\mathbf{k}}|^2 \frac{f_{\mathbf{k}}^e + f_{\mathbf{k}}^h - 1}{i[\omega_{\mathbf{k}}(N) - \hbar\omega] + \gamma_{\perp}(k)} Q_{\mathbf{k}}. \quad (1.10)$$

Proceeding in a phenomenological way, many body effects can be taken into account through the renormalization of the band-gap with the carrier density $\omega_{\mathbf{k}}(N)$ and the

Coulomb-enhancement factor $Q_{\mathbf{k}}$. The real and imaginary parts of $\chi = \chi' + i\chi''$ provide the index of refraction and gain induced by carriers. The Kramers-Krönig relations [44] connect χ' and χ''

$$\chi'(\omega) = -\frac{1}{\pi} \mathbb{P} \int_{-\infty}^{\infty} d\nu \frac{\chi''(\nu)}{\nu - \omega}, \quad (1.11a)$$

$$\chi''(\omega) = \frac{1}{\pi} \mathbb{P} \int_{-\infty}^{\infty} d\nu \frac{\chi'(\nu)}{\nu - \omega}, \quad (1.11b)$$

where \mathbb{P} stands for the Cauchy principal value of the integral. Microscopic theories including collision terms and screening of the Coulomb interaction provides a very good description of the absorption/gain spectra as can be seen in Fig. 1.9. However, the inclusion of these theories into the laser dynamics is very time consuming, even without considering spatial effects [43]. In chapter 6 we will develop analytical approximations to Eq. (1.10) for the circular polarization components of the electric field. The concept of spin sub-bands will be introduced there.

The evolution of the macroscopic carrier densities can be obtained from the microscopic quantities $n_{e\mathbf{k}}$ and $n_{h\mathbf{k}}$

$$N = \frac{1}{V} \sum_{\mathbf{k}} n_{i\mathbf{k}}, \quad (1.12)$$

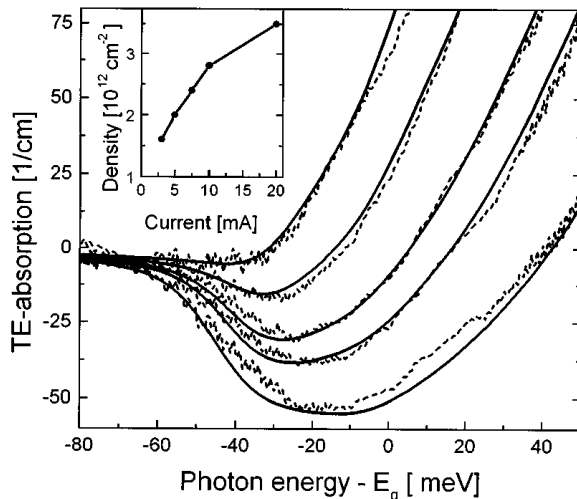


Figure 1.9. Experimental (dashed lines) TE absorption spectra of a single quantum well (GaIn)As/(AlGa)As laser diode. From top to bottom, the injection currents are $I = (0, 1, 3, 5, 7.5, 10, 12.5, 20)$ mA. The solid lines correspond to the predictions of the microscopic theory. After C. Ellmers et al., Appl. Phys. Lett. **72**, 1647 (1998).

Using Eqs. (1.12) and (1.7b) we obtain the evolution of the macroscopic carrier density

$$\frac{\partial N}{\partial t} = \frac{\eta I}{eV} - R(N) + \mathcal{D}\nabla^2 N - \frac{i}{\hbar} [\mathcal{P}^{nl}\mathcal{E}^* - \mathcal{P}^{nl*}\mathcal{E}], \quad (1.13)$$

I injection current, η the injection efficiency³, \mathcal{D} carrier diffusion. The carrier recombination $R(N)$ contains a nonradiative term AN , spontaneous radiative recombination BN^2 , etc. The last term in Eq. (1.13) accounts for stimulated recombination of carriers. Carrier transport and capture from the bulk material to the quantum well [6, 12, 45] have been disregarded, considering sufficiently slow variations of the carrier distributions.

1.5 Overview

In this thesis we aim to investigate the dynamical properties of both edge-emitting and vertical-cavity surface-emitting semiconductor lasers. We center the discussion on the optical processes occurring in these devices. We notice that the structure of each chapter is somehow self-contained, including a description of the problem, formulation of the model, analysis, experimental results if they apply, and conclusions.

In the first part of the thesis we deal with edge-emitting semiconductor lasers with added degrees of freedom. The theoretical studies are accompanied and discussed with experimental results. The study begins in chapter 2 with the dynamics of external-cavity modes in semiconductor lasers with delayed optical feedback. As commented in Sec. 1.2, the fascinating nonlinear dynamics exhibited by SCL with optical feedback has been matter of an intense research. Nowadays these systems are of increasing interest for the generation of chaotic outputs. High dimensional optical chaos has practical applications in high-speed encoded communication systems [46]. The characterization of the chaotic regimes is essential. We force the system to operate in a chaotic regime, by considering moderate feedback levels and long external-cavities. The single-longitudinal mode Lang-Kobayashi model is used to describe experiments with distributed-feedback semiconductor lasers. In this work we investigate the statistical properties of the chaotic outputs as well as the scaling laws associated with the transitions between different regimes. In spite of the apparent irregularity in the time signals, the statistical quantities follow quite generic rules. In chapter 3 we consider the bidirectional coupling of two twin SCL. Unidirectionally coupled semiconductor lasers has been extensively characterized in the past, demonstrating that under proper conditions they may synchronize [47]. Remarkably, only few studies focused on the bidirectional coupling among the lasers,

³For the sake of simplicity we skip the factor η in the rest of the thesis, assuming that it is included into the definition of I .

providing new scenarios of synchronization [48]. Starting from basic principles, we retake the electromagnetic modeling of the coupled system. We find that the minimal governing equations correspond to a bidirectional injection problem with delay. In this work, we are interested in characterizing the instabilities induced by the mutual coupling of the lasers and the synchronization properties. We address the importance of the delay in the mutual coupling of the oscillators. Chapter 4 presents the conclusions of part one of the thesis. The summary of the modeling tasks developed in the part one is

- Long-time interval (\sim ms) numerical simulation of the Lang-Kobayashi model. Statistical characterization of singlemode semiconductor lasers with delayed optical feedback.
- Electromagnetic modeling of the bidirectional coupling of two twin semiconductor lasers. Study of the validity of simple models.
- Numerical implementation of the above model: Interpretation of the experimentally observed coupling-induced instabilities and synchronization.

In the second part of the thesis, we describe the optical instabilities displayed by vertical-cavity surface-emitting lasers. We investigate the polarization properties of the light emitted. We stress the importance of the electron's spin dynamics on the noise characteristics and selection of polarization modes. In a second place, the excitation of transverse modes in gain-guided devices is considered. The second part is organized according to a hierarchy of models. We begin in chapter 5 describing the small-signal dynamics with the so-called Spin-Flip model. In particular we compute the polarization resolved intensity noise spectra in singlemode VCSELs. We interpret the origin of the experimentally observed correlated fluctuations between polarization components. In chapter 6, we present a generalization of the spin-flip model by incorporating spatial degrees of freedom and a frequency-dependent optical susceptibility. The resulting model is suitable for the study of large-signal dynamics. In the absence of spatial effects, the selection of polarization modes results from a joint interplay of spin dynamics, nonlinear semiconductor dynamics and thermal effects. In a second step, the spatial degrees of freedom are maintained and the resulting spatiotemporal model is used for investigating the selection of transverse modes. We consider gain-guided devices that include a weak passive distribution of index of refraction that arise from a thermally-induced lens. We analyze the effects of thermal lensing on the device characteristics. Firstly, we develop a semi-analytical method for determining the transverse mode selection at threshold associated with different device structures. Secondly, we consider the transverse mode dynamics under large-signal excitation of the injection current. This last situation occurs in optical communication systems using a digital encoding. Chapter 7 also considers large-signal

current modulation, but in this case smaller active-region VCSELs are analyzed. Spatial carrier diffusion in singlemode devices originates secondary pulsations of the optical intensity during the turn-off transients. By comparing the spatiotemporal description with its optical modal expansion, we discuss the validity and feasibility of an optical modal expansion when describing transverse mode dynamics in gain-guided VCSELs. To be more specific, the modeling tasks that we are considering include

- Basic modeling of the spin coherence in quantum-well semiconductors and its relevance on the polarization properties of VCSELs. Numerical implementation of the spin-flip model including stochastic terms.
- Noise and small-signal analysis: Analytical calculation of the relative intensity-noise spectra of the total intensity and polarization components. Physical understanding of anticorrelated fluctuations of the polarization components.
- Fundamental modeling: Search for accurate and simple descriptions of the full optical susceptibility at a mesoscopic level incorporating polarization, many body and thermal effects.
- Development of numerical codes, incorporating the frequency-dependent susceptibility, to study of the dynamical behavior of polarization and transverse modes in gain-guided VCSELs: mode selection mechanisms, and carrier anti-guiding effects under large current modulation.

Chapter 8 describes the conclusions of the second part of this thesis.

Part I

**Compound-Cavity
Edge-Emitting Semiconductor
Lasers**

Preface to the First Part

In this first part, we investigate the dynamical properties of edge-emitting semiconductor lasers with added degrees of freedom. We consider two examples: delayed optical feedback and bidirectionally coupled semiconductor lasers. The study of these systems is motivated by experimental evidences of a highly complex dynamics. We perform a direct comparison between numerical predictions and experimental results. We find that in both cases the optical coherence of the electric fields is of high relevance. These configurations can generate a variety of output signals, from short optical pulses to high-dimensional optical chaos, with important applications in communication systems. Before these technologic applications become fully functional, two aspects require to be analyzed. Firstly, robust and practical means of generating optical chaos have to be developed and characterized. Secondly, the feasibility of encoded communications also depends on the robustness and facility of the receiver system to synchronize to the chaotic signal of the transmitter.

This part is divided in two chapters. Firstly, we consider the effect of delayed optical feedback in edge-emitting semiconductor lasers. We focus on the chaotic regimes that appear for low to moderate levels of light re-injection, and long external cavities. We perform extensive numerical simulation of the Lang-Kobayashi equations over long time intervals. A statistical characterization of the low-frequency fluctuation regime, where the optical intensity exhibits irregular power dropouts, is carried out. Secondly, we consider the mutual coupling of two distant semiconductor lasers. In this case we investigate the instabilities induced by the delayed mutual coupling, and specially the synchronization properties. The modeling tasks concentrate in determining the evolution of the longitudinal mode amplitude of the electric field. So far multilongitudinal mode emission, light polarization and transverse spatial effects are disregarded.

Chapter 2

Semiconductor Lasers with Optical Feedback

2.1 Introduction

Systems¹ containing feedback loops appear very commonly in a wide variety of fields, including biology, ecology and physics. In biology they occur in regulation and stabilization processes, e.g., blood cell-production, neural control, and respiratory physiology. A fundamental characteristic of many of these dynamical systems is that their behavior depend on time delays [49]. Time delays appear due to the fact that most of the processes are not instantaneous, but take place in a finite time (production, conduction, transmission, diffusion, etc.). For instance, the control of physiological systems (heart rate, blood pressure, motor activity) is performed by negative feedback loops that are in general delayed.

In Chapter 1 we emphasized the relevance of semiconductor lasers (SCL) in many modern applications owing to their various interesting properties: low consume, small size, integrability, etc. However the performance of these devices can be affected by the presence of environmental perturbations. One of this effects is the re-injection of a fraction of light into the laser diode after a time τ later –*delayed optical feedback*. This effect may occur, for instance, due to unwanted reflections at the end of a fiber, on compact disc surfaces, or intentionally due to the presence of an external mirror. The finite distance between the laser and the external mirror introduces a delay owing to the light propagation-time. Optical feedback can be classified into two sub-classes, coherent and incoherent feedback, depending whether the coherence time of the laser light is larger or smaller than the delay time τ respec-

¹ This chapter is based on the papers:

J. Mulet and C. R. Mirasso, Phys. Rev. E **59**, 5400 (1999);

T. Heil, I. Fischer, W. Elsässer, J. Mulet and C. R. Mirasso, Opt. Lett. **18**, 1275 (1999).

tively. In this work we focus the study on the coherent case, where the optical phase of the electric field plays a crucial role introducing constructive and destructive interferometric effects. Other feedback configurations, where the optical phases do not directly affect the properties of the system have been studied in the literature, e.g., incoherent optical feedback [50, 51] and optoelectronic feedback [52]. During the early 80s feedback in SCL sparked a great interest owing to the capability of stabilizing a particular longitudinal mode, thus improving the noise characteristics. This interest, however, progressively drifted towards the fascinating nonlinear behavior exhibited by this system.

From the mathematical point of view a delay term in a differential equation yield an infinite dimensional phase-space, since a function, defined over a continuous interval $[0, \tau[$, has to be specified as initial condition. The understanding of delayed feedback systems has been boosted during the last years using semiconductor lasers. Fundamental nonlinear dynamical phenomena, such as, period doubling and quasi-periodic route to chaos have been characterized in these systems. Also high-dimensional chaotic attractors have been identified. Furthermore the analogy between delay differential equations and 1D spatial extended systems (coupled maps) have been established [53] and exploited for the characterization of the chaotic regimes [54].

This chapter is devoted to introducing the physics of compound-cavity SCL. Firstly, we study the effect of a passive external cavity on the laser dynamics. In Sec. 2.2 we present a systematic derivation of the laser equations with optical feedback. We sequentially introduce fundamental concepts that will be useful in the following chapters of the thesis: Boundary conditions at reflecting interfaces are treated using the Fourier domain representation, whereas the dynamical properties are accessible through the slowly-varying approximation. In Sec. 2.2.1 we present a modern review of the Lang-Kobayashi model for lasers with optical feedback, paying special attention to the different regimes of operation [Sec. 2.3]. Next we focus the discussion to the statistical properties governing the low frequency fluctuation dynamics [Sec. 2.4]. Scaling laws associated with the transition from stable operation to low frequency fluctuations (LFF) are numerically and experimentally analyzed. In most of the experiments Fabry-Perot lasers, which exhibit multimode operation when they are subject to delayed optical feedback, are used (e.g. Hitachi LP1400, Sharp LT015 or Spectral Diode SDL-5401-G1). Therefore, even though singlemode theory and multimode experiments may agree, the mismatch between theoretical assumptions and experimental conditions has yield considerable controversies [55, 56]. In Sec. 2.4.1 we use distributed feedback lasers (DFB) to obtain an optimum match between experimental and theoretical conditions to provide an experimental system in which the results of numerical investigations can be realized straightforwardly in experi-

ments. The statistical properties of low frequency fluctuations under modulation of the injection current are discussed in Sec. 2.5 and finally Sec. 2.6 is devoted to concluding and summarizing the chapter.

2.2 The Model

In a semiclassical framework, the electromagnetic fields are described through the Maxwell's equations while the matter (semiconductor medium) is characterized using the Quantum Mechanical theory [See Sec. 1.4]. A semiclassical description of the spontaneous emission processes, neglecting the quantification of the electric fields, is also performed. In this chapter we restrict ourselves to give an operational definition of noise, although we will return to this concept in Chapter 5 and Appendix C.

Field equations and boundary conditions

The Maxwell's equations (1.3a)–(1.3d), expressed in frequency domain, lead to a wave equation for the electric field

$$\vec{\nabla}^2 \vec{\mathcal{E}}_\omega + i\omega \frac{\sigma_\omega(x)}{\epsilon_0 c^2} \vec{\mathcal{E}}_\omega + \left(\frac{\omega}{c}\right)^2 n_{e\omega}^2(x) \vec{\mathcal{E}}_\omega = -\frac{1}{\epsilon_0} \left(\frac{\omega}{c}\right)^2 \vec{\mathcal{P}}_\omega^{nl}(\vec{r}), \quad (2.1)$$

σ_ω is the conductivity of the medium, $n_{e\omega}(x)$ the built-in refraction index step that defines the active region, and $\vec{\mathcal{P}}_\omega^{nl}$ the nonlinear contribution to the material polarization.

We consider a Fabry-Perot cavity as the one depicted in Fig. 2.1. The nonlinear polarization $\vec{\mathcal{P}}_\omega^{nl}(\vec{r})$ is nonvanishing in the active region, i.e., $-W/2 \leq x \leq W/2$, W being the active-region thickness. Due to the geometry of the device, the electric field can be assumed to be linearly polarized along the heterojunction plane

$$\vec{\mathcal{E}}_\omega(\vec{r}) = \tilde{\mathcal{E}}_\omega(z) \Phi_\omega(x) \hat{y}. \quad (2.2)$$

$\Phi(x)$ defines the profile associated with the transverse electric (TE) mode whereas the longitudinal dependence is described by $\tilde{\mathcal{E}}_\omega(z)$. The transverse magnetic (TM) modes will be neglected in the analysis, because they typically have higher threshold currents due to the lower mirror reflectivities for this polarization orientation. The modification of the propagation constants due to the presence of a finite distribution of field, i.e. transverse modes, is accounted through the effective refractive-index approximation. Introducing the ansatz (2.2) into (2.1), taking $n_{\text{eff}}(\omega)$ as a separation variable, and projecting onto a mode $\Phi_\omega^*(x)$ we arrive at

$$d_z^2 \tilde{\mathcal{E}}_\omega(z) + \beta_\omega^2 \tilde{\mathcal{E}}_\omega(z) + \frac{i\omega \bar{\sigma}_\omega}{\epsilon_0 c^2} \tilde{\mathcal{E}}_\omega(z) = -\left(\frac{\omega}{c}\right)^2 \Gamma_x \chi^{nl}(N) \tilde{\mathcal{E}}_\omega(z), \quad (2.3a)$$

$$\nabla_\perp^2 \Phi_\omega(x) + \left(\frac{\omega}{c}\right)^2 [n_{e\omega}^2(x) - n_{\text{eff}}^2(\omega)] \Phi_\omega(x) = 0, \quad (2.3b)$$

where the average electric conductivity $\bar{\sigma}_\omega$ and transverse confinement factor Γ_x read

$$\bar{\sigma}_\omega = \frac{\int_{-\infty}^{\infty} \sigma_\omega(x) |\Phi_\omega(x)|^2 dx}{\int_{-\infty}^{\infty} |\Phi_\omega(x)|^2 dx}, \quad \Gamma_x = \frac{\int_{-W/2}^{W/2} |\Phi_\omega(x)|^2 dx}{\int_{-\infty}^{\infty} |\Phi_\omega(x)|^2 dx}. \quad (2.4)$$

$\beta_\omega \equiv (\omega/c)n_{\text{eff}}(\omega)$ stands for the propagation constant associated with the longitudinal mode and has to be determined from Eq. (2.3b) complemented with adequate boundary conditions. In the case of a flat distribution of refractive index with $\bar{n}_{e\omega}$, the propagation constant reduces to $\beta_\omega = (\omega/c)\bar{n}_{e\omega}$.

We consider the situation depicted in the Fig. 2.1, that consists in a Fabry-Perot cavity with length L arranged in tandem with an external mirror separated by a distance L_e . The external cavity is defined by the physical separation between the right laser facet and the external mirror. The longitudinal dependence of the electric field, within both the laser cavity and the external cavity, is expressed as the superposition of two counter-propagating waves

$$\tilde{\mathcal{E}}_\omega(z) = \begin{cases} \tilde{\mathcal{E}}^+ e^{iqz} + \tilde{\mathcal{E}}^- e^{-iqz} + c.c. & -L \leq z \leq 0 \\ \tilde{\mathcal{E}}_0^+ e^{iq_0 z} + \tilde{\mathcal{E}}_0^- e^{-iq_0 z} + c.c. & 0 < z \leq L_e \end{cases}. \quad (2.5)$$

This form takes implicit the hypothesis of perfect mode matching between the TE laser mode $\Phi(x)$ and the incoming feedback field. $\tilde{\mathcal{E}}^\pm$ and $\tilde{\mathcal{E}}_0^\pm$ stand for the amplitudes, at frequency ω , of the counter-propagating waves inside the laser section and in the external cavity, respectively. The associated propagation constants are q and q_0 . Upon substitution of Eq. (2.5) into Eq. (2.3a) we have

$$[\beta_\omega^2 - q_\omega^2] \tilde{\mathcal{E}}_\omega(z) + \frac{i\omega\bar{\sigma}_\omega}{\epsilon_0 c^2} \tilde{\mathcal{E}}_\omega(z) = -\left(\frac{\omega}{c}\right)^2 \Gamma_x \chi^{nl}(N) \tilde{\mathcal{E}}_\omega(z), \quad (2.6)$$

for $-L \leq z \leq 0$.

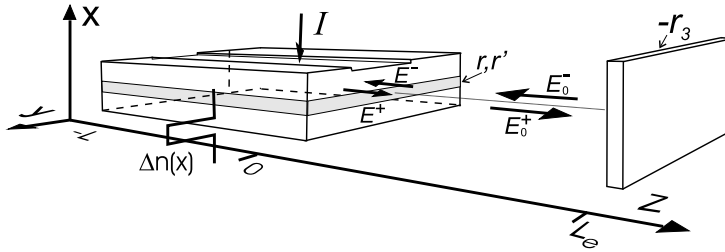


Figure 2.1. Edge-emitting laser with optical feedback from a distant reflector. Counter-propagating waves verify boundary conditions. Light propagates in the longitudinal z -direction while the polarization of the field is transverse electric.

We consider that all the laser facets are carefully cleaved, giving rise to dielectric-dielectric interfaces. They have an internal (external) real reflectivity and transitivity $r', t' (r, t)$. The Stokes' relationships [40] lead to $r = -r'$ and $tt' = 1 - r^2$. The electric field and its z -derivative must be continuous at each laser facet. We arrive to the following boundary conditions for the amplitudes of the counter-propagating waves

$$z = -L, \quad e^{-iqL} \tilde{\mathcal{E}}^+ = r' e^{iqL} \tilde{\mathcal{E}}^-. \quad (2.7a)$$

$$z = 0, \quad \tilde{\mathcal{E}}_0^+ = t' \tilde{\mathcal{E}}^+ + r \tilde{\mathcal{E}}_0^-, \quad (2.7b)$$

$$\tilde{\mathcal{E}}^- = r' \tilde{\mathcal{E}}^+ + t \tilde{\mathcal{E}}_0^-. \quad (2.7c)$$

$$z = L_e, \quad e^{-iq_0 L_e} \tilde{\mathcal{E}}_0^- = -r_3 e^{iq_0 L_e} \tilde{\mathcal{E}}_0^+. \quad (2.7d)$$

For convenience, we have taken the origin of the z -axis at the right laser facet. In first approximation, we consider the reflection and transmission coefficients independent on propagation constants, i.e., independent on both ω and N . The only assumption is that the external metallic mirror introduces a reflection phase of π under normal incidence, negative sign in Eq. (2.7d). The propagation constant in the external cavity reads

$$q_0 = \frac{\omega}{c} + \frac{i}{2} \alpha_\omega^{ext}, \quad (2.8)$$

where α_ω^{ext} stands for the total accrued coupling losses. Alternatively, we can express

$$e^{i2q_0 L_e} \equiv \xi e^{i\omega\tau}, \quad (2.9)$$

with $\tau \equiv 2L_e/c$ the round-trip delay time while ξ^2 is the total power attenuation, due to e.g., diffraction or coupling losses with other optical elements.

By using Eqs. (2.7b)–(2.7d) we can express the amplitude $\tilde{\mathcal{E}}^-$ propagating in the left direction as

$$\begin{aligned} \tilde{\mathcal{E}}^- &= r_{\text{eff}}(\omega) \tilde{\mathcal{E}}^+, \\ r_{\text{eff}}(\omega) &\equiv r' \left[1 + \frac{(1-r^2)}{r} \frac{r_3 \xi e^{i\omega\tau}}{(1+r r_3 \xi e^{i\omega\tau})} \right]. \end{aligned} \quad (2.10)$$

From the above expression, we deduce that the effect of the external cavity can be substituted by an effective frequency-dependent mirror with reflectivity $r_{\text{eff}}(\omega)$. By also using Eq. (2.7a), we arrive at the following relationship between the two counter-propagating waves within the laser section

$$\begin{bmatrix} 1 & -r' e^{i2qL} \\ -r_{\text{eff}}(\omega) & 1 \end{bmatrix} \begin{bmatrix} \tilde{\mathcal{E}}^+ \\ \tilde{\mathcal{E}}^- \end{bmatrix} = \begin{bmatrix} 0 \\ 0 \end{bmatrix}. \quad (2.11)$$

The boundary conditions impose a relationship between the counter-propagating wave amplitudes. Thus the longitudinal dependence of the electric field can be solely described, e.g., by the field amplitude propagating in the left direction $\tilde{\mathcal{E}}^-$

$$\begin{aligned}\tilde{\mathcal{E}}_\omega(z) &= \tilde{\mathcal{E}}^- f(z), \\ f(z) &\equiv r' e^{i2kL} e^{iqz} + e^{-iqz},\end{aligned}\quad (2.12)$$

$f(z)$ being the standing wave within the laser cavity.

A nontrivial solution of Eq. (2.11) must verify the secular condition of vanishing determinant

$$r' r_{\text{eff}}(\omega) e^{i2qL} = 1, \quad (2.13)$$

from which we deduce the propagation constant of the laser with optical feedback

$$q_{M\omega} = \frac{M\pi}{L} + \frac{i}{2L} \ln r^2 + \frac{i}{2L} \ln \left(1 + \frac{(1-r^2)}{r} \frac{r_3 \xi e^{i\omega\tau}}{(1+r r_3 \xi e^{i\omega\tau})} \right). \quad (2.14)$$

In Eq. (2.14), M is an integer number that labels the order of the longitudinal mode, the second term describes the losses through the laser facets, while the last one accounts for the interferometric effect of the external cavity, thus introducing frequency dependent losses with the periodicity of a free-spectral range ($1/\tau$). It is worth mentioning that the variation in propagation constant with respect to the solitary laser operation reads

$$\Delta\theta_\omega \equiv 2L(q_\omega - q_\omega^{\text{sol}}) = i \ln \left(1 + \frac{(1-r^2)}{r} \frac{r_3 \xi e^{i\omega\tau}}{(1+r r_3 \xi e^{i\omega\tau})} \right). \quad (2.15)$$

The slowly varying approximation

Simultaneous emission in several longitudinal modes is very common in edge emitting lasers. For this reason, many strategies have been devised in order to guaranty single-longitudinal mode operation. Large side-mode suppression ratio can be achieved using distributed feedback reflector (DFB) lasers, distributed Bragg reflector (DBR) lasers, and vertical-cavity surface-emitting lasers (VCSELs). Even though the single longitudinal mode approximation is questionable in edge-emitting lasers (EELs), we can imagine that by means one of the aforementioned methods², emission close to a longitudinal mode (with order M_0) can be achieved. Inasmuch as the

²The rigorous demonstration requires of the reformulation of the propagation problem. For instance in the DFB laser, we need to impose compatible boundary conditions accounting for the grating structure. For DFB laser diodes, the feedback rate κ_f becomes in general complex and is given by some complicated expression [26, 57] which depends on the details of the grating.

electric field is nearly monochromatic around the longitudinal mode resonance frequency Ω , fully determined from $q_\Omega = \frac{\Omega}{c} n_{\text{eff}}(\Omega) = M_0 \pi / L$, it is useful to expand all the frequency dependent quantities in Eq. (2.6) around Ω

$$\beta_\omega^2 = \beta_\Omega^2 + 2\beta_\Omega \beta'_\Omega (\omega - \Omega) + \dots, \quad (2.16)$$

where $\beta'_\Omega = d[(\omega/c) n_{\text{eff}}(\omega)]/d\omega|_\Omega$ accounts for the dispersion of the mode M_0 that in turn defines its group velocity $v_g = 1/\beta'_\Omega$. Now we take advantage that $\text{Re } q \gg \text{Im } q$ and that $\text{Re } q_\omega$ is close to β_Ω

$$\begin{aligned} \beta_\Omega^2 - q_\omega^2 &= [\beta_\Omega + q_\omega][\beta_\Omega - q_\omega] \\ &\approx -2\beta_\Omega \frac{i}{2L} [\ln r^2 + \ln(r_{\text{eff}}(\omega)/r')] . \end{aligned} \quad (2.17)$$

Next, we introduce Eq. (2.12) and Eqs. (2.16)–(2.17) into the wave equation (2.6) and we project onto the longitudinal mode $f^*(z)$. A further simplification consists in neglecting the z -dependence of $\chi_\Omega^{nl}(N)$ that arises from inhomogeneities in the carrier variables by introducing the total number of carriers

$$\mathcal{N} = \int_{\text{active}} N(\vec{r}) d^3 \vec{r}, \quad (2.18)$$

where the integral extends over the active region. In such a case, we arrive to the following equation for the field amplitude

$$\begin{aligned} -i(\omega - \Omega) \tilde{\mathcal{E}}^- &= \\ -\frac{\kappa}{2} \tilde{\mathcal{E}}^- + i \frac{\Omega^2}{c^2} \frac{\Gamma_x}{2\beta_\Omega \beta'_\Omega} \chi_\Omega^{nl}(\mathcal{N}) \tilde{\mathcal{E}}^- + \frac{1}{\tau_{in}} \ln \left[\frac{r_{\text{eff}}(\omega)}{r'} \right] \tilde{\mathcal{E}}^-, \end{aligned} \quad (2.19)$$

where $\tau_{in} = 2L v_g^{-1}$ is the internal round-trip time, and κ the total cavity decay rate³ that have two contributions: internal α^{int} and facet α^m losses

$$\kappa = v_g \left(\frac{\Omega \bar{\sigma}_\Omega}{\epsilon_0 c^2 \beta_\Omega} + \frac{1}{L} \ln \frac{1}{r^2} \right) \equiv v_g (\alpha^{int} + \alpha^m). \quad (2.20)$$

A final step consists in Fourier transforming back to time domain Eq. (2.19). One of the major difficulty in finding close expressions in time domain is the presence of the logarithmic term. In a VCSEL, while operating within the stop-band, $(1 - r^2)$ is a small parameter because the high reflectivity of the DBR mirrors, regardless the magnitude of ξr_3 [58]. Unfortunately this approximation does not hold in an EEL in

³Note that with this definition of κ , the electric field decays at a rate $\kappa/2$, whereas the photon number at a rate κ .

which the facets are simply cleaved. A possible way to proceed is to assume small external reflectivity and coupling transmission, and take $\xi r_3 \ll 1$ as a small expansion parameter

$$\ln \left[\frac{r_{\text{eff}}(\omega)}{r'} \right] = \sum_{n=1}^{\infty} (-1)^n \frac{(r^{2n} - 1)}{nr^n} (r_3 \xi)^n e^{i\omega n \tau}. \quad (2.21)$$

Next we define the slowly-varying envelope (SVE) of the electric field by means

$$\mathcal{E}^-(t) = E(t)e^{-i\Omega t}. \quad (2.22)$$

In frequency domain the above expression reads $\tilde{\mathcal{E}}^-(\omega) = \tilde{E}(u)$, with $u \equiv \omega - \Omega$ being the slow frequency reference frame. The field equation in frequency domain neglecting higher-order terms in (ξr_3) reads

$$-iu\tilde{E}_u = -\frac{\kappa}{2}\tilde{E}_u + i\frac{\Omega^2}{c^2} \frac{1}{2\beta_\Omega \beta'_\Omega} \Gamma_x \chi_\Omega^{nl}(N)\tilde{E}_u + \kappa_f e^{i\Omega\tau} e^{iu\tau} \tilde{E}_u, \quad (2.23)$$

$\kappa_f \equiv (1-r^2)\xi r_3/(r\tau_{in})$ being the feedback rate. The above equation can be straightforwardly transformed to time domain ($-iu \rightarrow d_t$)

$$d_t E(t) = -\frac{\kappa}{2}E(t) + \frac{1}{2}(1-i\alpha)G(t)E(t) + \kappa_f e^{i\Omega\tau} E(t-\tau). \quad (2.24)$$

We have substituted the susceptibility of the bulk active material by the approximation

$$G(t) = \frac{G_N(\mathcal{N}(t) - \mathcal{N}_t)}{1 + \varepsilon|E(t)|^2}, \quad (2.25)$$

with $G_N \equiv -v_g \Gamma_x \Omega^2 / (c^2 \beta_\Omega) (\partial \text{Im} \chi^{nl} / \partial \mathcal{N})|_\Omega$ the differential gain, \mathcal{N}_t the total carrier number at transparency, and ε phenomenologically describes gain saturation due to, e.g., spectral hole-burning effects. A crucial parameter that describes phase-amplitude coupling mechanisms in semiconductor lasers is the linewidth enhancement factor

$$\alpha \equiv \frac{\partial_N \text{Re} \chi^{nl}|_\Omega}{\partial_N \text{Im} \chi^{nl}|_\Omega}. \quad (2.26)$$

In gas lasers, α measures the relative detuning between the longitudinal mode resonance and the gain peak being negligible when comparing with SCL.

It is worth remarking that the emission frequency (close to threshold and in the absence of noise) is $\Omega + \alpha\kappa$. For convenience, we compensate for this frequency shift by moving to the free-running reference frame $E(t) \rightarrow E(t)e^{-i\kappa\alpha t}$. The resulting equation reads

$$d_t E(t) = \frac{1}{2}(1-i\alpha)[G(t) - \kappa]E(t) + \hat{\kappa}_f E(t-\tau). \quad (2.27)$$

where $\hat{\kappa}_f \equiv \kappa_f e^{i\Omega_0\tau}$ and $\Omega_0 \equiv \Omega + \kappa\alpha$ being the free-running emission frequency. The feedback phase $\phi_0 \equiv \Omega_0\tau \bmod (2\pi)$ varies from $[0, 2\pi]$ when the external cavity length is varied within an emission wavelength. The stability properties of the fixed points is sensible to this parameter, specially in the short cavity regime [59].

2.2.1 The Lang-Kobayashi model

The evolution of the longitudinal mode amplitude has been described by means a time-delayed rate equation. This field equation has to be complemented by specifying the evolution of the total carrier population \mathcal{N} . The carrier equation does not need any modification with respect to the free-running case. The detailed derivation of these equations can be found elsewhere [10, 60]. In the case of single-longitudinal mode operation and weak feedback, $(r_3\xi) \rightarrow 0$, the evolution of the field and carrier variables is governed by

$$\frac{dE(t)}{dt} = \frac{1}{2}(1 - i\alpha)[G(t) - \kappa]E(t) + \hat{\kappa}_f E(t - \tau) + F_E(t), \quad (2.28a)$$

$$\frac{d\mathcal{N}(t)}{dt} = \frac{I}{e} - \gamma_e \mathcal{N}(t) - G(t)|E(t)|^2 + F_N(t). \quad (2.28b)$$

The physical meaning of the different terms in Eq. (2.28b) is: I/e is the number of injected electron-hole pairs, γ_e is the rate of spontaneous recombination, and $G(t)|E(t)|^2$ describes the processes of stimulated recombination. These basic equations describing SCL with optical feedback were introduced by Lang and Kobayashi (LK) [28] in 1980. Clear restrictions are the single longitudinal mode hypothesis as well as the weak feedback conditions: only one reflection in the external cavity is accounted for. We have phenomenologically added gain suppression effects through the parameter ε , and Langevin noise sources $F_E(t), F_N(t)$. Spontaneous emission processes are described by white Gaussian random numbers [61] with zero mean $\langle F_E(t) \rangle = 0$, and delta-correlation in time $\langle F_E(t) F_E^*(t') \rangle = 4\gamma_e \beta_{sp} \mathcal{N} \delta(t - t')$. The spontaneous emission factor β_{sp} , represents the number of spontaneous emission events that couples with the lasing mode. The noise term in the carrier equation $F_N(t)$, coming from spontaneous emission as well as shot noise contribution, is generally small and it will be neglected all through this chapter. A better characterization of stochastic processes can be found in the Appendix C.

In the absence of optical feedback, the usual gain-clamping condition $G = \kappa$ determines the solitary inversion $\mathcal{N}_{th}^{sol} = \mathcal{N}_t + \kappa/G_N$, and the solitary threshold current $I_{th}^{sol} = e\gamma_e \mathcal{N}_{th}^{sol}$.

parameter	symbol	HLP1400	DFB	units
solitary laser threshold	I_{th}	55	27	mA
differential gain	G_N	2.76×10^{-6}	7.0×10^{-6}	ns^{-1}
cavity decay rate	κ	158	180	ns^{-1}
alpha factor	α	4	3.4	–
e-h pair decay rate	γ_e	1.66	2.22	ns^{-1}
carriers at transparency	\mathcal{N}_t	1.51×10^8	5.02×10^7	–
spontaneous emission	β_{sp}	5×10^{-7}	5×10^{-8}	–
nonlinear gain coeff.	ε	3×10^{-7}	8×10^{-8}	–

Table 2.1. Symbols and parameters corresponding to the experimental conditions of the HLP1400 and DFB lasers. The feedback conditions, τ and κ_f , and the injection currents are indicated in the text.

Dimensionless equations

From a numerical point of view it is more convenient to work with dimensionless variables scaled by

$$A(t) \equiv \sqrt{\frac{\kappa}{\gamma_e} \frac{1}{\mathcal{N}_t}} E(t), \quad D(t) \equiv \frac{\mathcal{N}(t)}{\mathcal{N}_t} - 1. \quad (2.29)$$

The LK model Eqs. (2.28a)–(2.28b) reduces to

$$\frac{dA(t)}{dt} = \frac{\kappa}{2}(1 - i\alpha)[\mathcal{G}(t) - 1]A(t) + \hat{\kappa}_f A(t - \tau) + F_A(t), \quad (2.30a)$$

$$\frac{dD(t)}{dt} = \gamma_e [\mu - D(t) - \mathcal{G}(t)|A(t)|^2], \quad (2.30b)$$

$$\mathcal{G}(t) = \frac{a D(t)}{1 + s|A(t)|^2}. \quad (2.30c)$$

We have introduced the following dimensionless parameters: the scaled gain factor $a \equiv G_N \mathcal{N}_t / \kappa$, the scaled injection current $\mu \equiv I / (e \mathcal{N}_t \gamma_e) - 1$, and the scaled gain suppression coefficient $s \equiv \epsilon \gamma_e \mathcal{N}_t / \kappa$. The current is usually given with respect the solitary threshold value $p \equiv I / I_{th}^{sol}$, so that $\mu = p(1 + 1/a) - 1$. The scaled noise source has a correlation $\langle F_A(t) F_A^*(t') \rangle = 4\kappa \beta_{sp} (D + 1) \delta(t - t')$.

Alternatively to the complex electric field representation, we can derive equa-

tions for its amplitude and phase by writing, $A(t) = \sqrt{P(t)} \exp[i\phi(t)]$, that read

$$\begin{aligned} \frac{dP(t)}{dt} &= \kappa[\mathcal{G}(t) - 1]P(t) + 2\kappa_f \sqrt{P(t)P(t-\tau)} \cos(\eta(t) + \phi_0) \\ &\quad + 4\kappa\beta_{sp}(D + 1) + F_P(t), \end{aligned} \quad (2.31a)$$

$$\frac{d\phi(t)}{dt} = -\alpha \frac{\kappa}{2} [\mathcal{G}(t) - 1] + \kappa_f \sqrt{\frac{P(t-\tau)}{P(t)}} \sin(\eta(t) + \phi_0) + F_\phi(t), \quad (2.31b)$$

$\eta(t) \equiv \phi(t-\tau) - \phi(t)$ being related with the mean optical frequency in a time τ . The real Langevin noise sources $F_P(t)$ and $F_\phi(t)$ are obtained by Itô transformation [62].

Fixed points

A monochromatic steady state solution of Eqs. (2.30a)–(2.30c) can be expressed as $A(t) = \sqrt{\bar{P}} \exp(-i\Delta\omega t)$, and $D(t) = \bar{D}$. The external cavity mode (ECM) frequency $\Delta\omega$ is obtained from the solutions of the transcendent equation [63]

$$\eta_s = -C \sin(\eta_s + \text{atan } \alpha + \Omega_0\tau), \quad (2.32)$$

with $\eta_s = \Delta\omega\tau$, and $C \equiv \kappa_f\tau\sqrt{1+\alpha^2}$ the effective feedback strength. The number of ECM is proportional to $C/(2\pi)$. The remaining steady-state quantities can be obtained from

$$\bar{\mathcal{G}} = 1 - \frac{2\kappa_f}{\kappa} \cos(\eta_s + \Omega_0\tau), \quad (2.33a)$$

$$\bar{P} = \frac{1}{(a+s)} \left(\frac{\mu a}{\bar{\mathcal{G}}} - 1 \right), \quad (2.33b)$$

$$\bar{D} = \frac{1}{a} (1 + s\bar{P})\bar{\mathcal{G}}. \quad (2.33c)$$

The fixed points are located on an ellipse in the $\bar{\mathcal{G}} - \eta_s$ plane, while the representation in the $\bar{P} - \eta_s$ plane is banana-shaped [63].

From Eq. (2.33a) we can define the maximum loss reduction due to the feed back light as $\mathcal{R}_\kappa \equiv 2\kappa_f/\kappa$. This effect manifest itself in a reduction in threshold current that can be determined from Eq. (2.33b) by imposing the condition $\bar{P} = 0$. We denote I_{th}^{sol} and I_{th}^{feed} as the threshold currents of the free-running and laser with feedback, respectively. Then the threshold reduction reads

$$\mathcal{R}_\mu \equiv 1 - \frac{I_{th}^{feed}}{I_{th}^{sol}} = \frac{2\kappa_f/\kappa}{1+a}. \quad (2.34)$$

As an alternative to κ_f , the feedback level can be quantified by providing the two extensively used figures of merit \mathcal{R}_μ and \mathcal{R}_κ .

Linear stability analysis

A fundamental step in the analysis of any dynamical system is the determination of the stability of their steady state solutions. A first attempt was put forward by Mørk and coworkers [64, 65] that, by neglecting power fluctuations, investigated the stability of the monochromatic solutions using the image of a “thermodynamic” potential. In order to obtain an expression for this potential, we take in Eq. (2.31a) $dP(t)/dt = 0$ and we arrive to an equation for the optical phase $\phi(t)$

$$\frac{d\phi(t)}{dt} = \kappa_f \sqrt{1 + \alpha^2} \sin(\phi(t - \tau) - \phi(t) + \text{atan } \alpha + \Omega_0 \tau). \quad (2.35)$$

In order to overcome the problem of the delayed term in the above equation, Mørk and Tromborg applied an additional approximation: small and slow variations of the phase during a round-trip time. Then the variable $\eta(t) \equiv \phi(t - \tau) - \phi(t)$ can be approximated by

$$\dot{\phi}(t) \approx -\frac{1}{\tau} \eta(t) - \frac{1}{2} \dot{\eta}(t). \quad (2.36)$$

Then the evolution of $\eta(t)$ can be expressed in a potential form

$$\dot{\eta}(t) = -\frac{1}{\tau} \frac{d}{d\eta} U(\eta) + 2F_\eta(t), \quad (2.37a)$$

$$U(\eta) \equiv \eta^2 - 2C \cos(\eta + \text{atan } \alpha + \Omega_0 \tau). \quad (2.37b)$$

The extrema of the potential $U(\eta)$ correspond to the fixed points given in Eq. (2.32). The local minima of the potential, $1 + C \cos(\eta + \text{atan } \alpha + \Omega_0 \tau) > 0$, are the stable fixed points. In the presence of noise, the phase drifts through the stable fixed points in such a way that the most stable mode is located at the bottom of the potential, with frequency $\eta \approx 0$ (minimum linewidth mode). However, this approximation is unrealistic for large feedback levels because the relaxation oscillations, associated with intensity fluctuations, can easily destabilize the modes.

The general linear stability analysis theory going beyond the constant intensity approximation [66] is summarized in Appendix A. The number of solutions in the complex plane of the equation (A.4) is infinite due to the infinite number of resonances. A fixed point is unstable if there exists at least one solution with $\text{Re } \lambda > 0$. A fixed point is stable if $\text{Re } \lambda < 0$ for all λ 's. In the absence of feedback, the solutions of Eq. (A.4) are $\lambda = 0$ describing the phase invariance of the solitary laser and two complex conjugated eigenvalues that neglecting gain saturation, read

$$\lambda_{\pm} = -\Gamma_R \pm i \sqrt{\Omega_R^2 - \Gamma_R^2}, \quad (2.38)$$

with $\Gamma_R \equiv T\mu/2$ the relaxation oscillations (ROs) damping and $\Omega_R \equiv [Ta(a\mu - 1)]^{1/2}$ the ROs frequency that increases with the square-root of the current.

A detailed analysis of the LSA of the fixed points can be found elsewhere [66, 67, 68]. Here, we restrict ourselves to summarize some of the most outstanding results. Depending on the stability properties, the fixed points are classified as follows:

- *Antimodes*: They are originated by the destructive interference among the cavity and the feed back field. They are unstable saddle modes that correspond to the local maxima of the thermodynamic potential. The values of κ_f where a saddle-node bifurcation takes place, giving rise to a new pair of fixed points, is approximately given by [70]

$$\kappa_f \approx \frac{\beta + \sqrt{\beta^2 - 2}}{2\tau\sqrt{1 + \alpha^2}}, \quad (2.39)$$

with $\beta = \phi_0 + \text{atan } \alpha + (2n - \frac{1}{2})\pi$, and $n = 1, 2, \dots$

- *External-Cavity Modes (ECM)*: They correspond to the local minima of the thermodynamical potential and can be destabilized through Hopf bifurcation. Two ECM are separated by an antimode. They can be regarded as the constructive interference among the cavity field and the delayed feedback field.
- *Maximum Gain Mode (MGM)*: This is the highest power or minimum threshold mode . The phase condition $\Omega_0\tau = \kappa\tau\alpha \pmod{2\pi}$ provides a solution at frequency $\eta_{m.g.m} = -\kappa\tau\alpha$. MGM corresponds to the most stable mode against

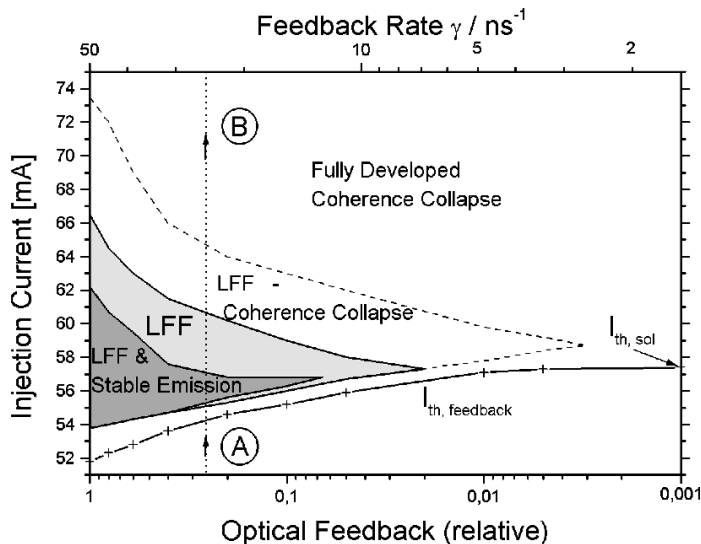


Figure 2.2: Operation regimes of a laser with optical feedback, after Ref. [69].

relaxation oscillations. It can be proved that the MGM is stable for arbitrarily large feedback strengths [67]. For sufficiently large feedback, modes in the neighborhood of the MGM can be also stable when the correct phase is used.

- *Minimum Linewidth Mode (MLM)*: In the potential framework, MLM (the mode with frequency closest to the one of the solitary laser) is the most stable mode. However, this solution can be destabilized through relaxation oscillations for relatively weak feedback levels. The phase defining this mode is $\Omega\tau = -\text{atan } \alpha \pmod{2\pi}$, which provides a solution at frequency $\eta = 0$.
- *Phase Condition for the Most Unstable State*: K. Wadda [68] found that with the phase $\phi_0 = \pi + \text{atan } \alpha$, the laser is brought into the most unstable state for a given value of α . It provides the largest suppression of stimulated emission due to the destructive interference with the delayed feedback field.

2.3 Operation Regimes

During the early 80s feedback in SCL sparked a great interest owing to their noise related properties. Under proper operation conditions, short external cavities and careful matching of the feedback phase $\Omega_0\tau$, the cw emission linewidth can be reduced by more than a factor of ten [71, 72]. In contrast, the cw operation can become unstable through Hopf bifurcation when deviating from these optimum conditions. This instability yield self-pulsation of the optical intensities with frequency locked to the external round-trip time. Further increase of the feedback level leads to multistability between the different ECM and hysteresis in the light-intensity (L-I) curve. The interest concerning noise characteristics gradually shifted toward the deterministic dynamics induced by the delayed optical feedback. The external cavity behavior has been classified into five different regimes (I-V) [73, 74]. In this work we focus on the region IV where two distinct regimes of chaotic operation occur, namely coherence collapse (CC) and low-frequency fluctuations (LFF). They are of special interest both for the reach nonlinear dynamics as well as for the potential application in encoded communication systems [47, 75, 76]. These two regimes appear in a wide range of parameters, injection current versus optical feedback strength co-space, as shown in Fig. 2.2.

Coherence collapse

Experimental measurements of the optical spectrum found a large increase in emission linewidth (from ~ 100 MHz to ~ 25 GHz) when the laser was subject to moderate amounts of feedback ($\sim 1\%$ injected light) from a reflector distanced by ~ 1 m. This effect, commonly referred as coherence collapse or regime IV [25], is a form of

deterministic chaos of high dimensionality that typically involves hundreds of unstable ECM. Period doubling route to chaos was found when the relaxation oscillations locked to an external cavity resonance [77], while quasi-periodic route was observed [78, 79] otherwise.

The optical intensity traces shown in Fig. 2.3(a), obtained from the LK model, display a sequence of irregular pulses at the nanosecond time scale. A two dimensional projection of the phase-space D versus η , where $D = \mathcal{N}/\mathcal{N}_t - 1$ is the scaled carrier number and $\eta(t) = \phi(t-\tau) - \phi(t)$ is the phase difference of the slowly-varying complex field in one external round-trip time, indicates that the $\eta(t)$ drifts back and forth through several unstable Hopf bifurcated ECM [Fig. 2.3(b)]. The implication of this highly complex dynamics is reflected in the time-averaged optical spectrum that shows a dramatic broad linewidth (~ 20 GHz) [Fig. 2.3(c)].

Low-frequency fluctuations

A low frequency peak (~ 10 MHz) in the power spectrum was reported by Risch et al. [27] when the laser, while operating in regime IV, was pumped close to the solitary threshold current. Such a low frequency fluctuation dynamics is characterized by sudden dropouts of the optical power followed by a gradual recovery process

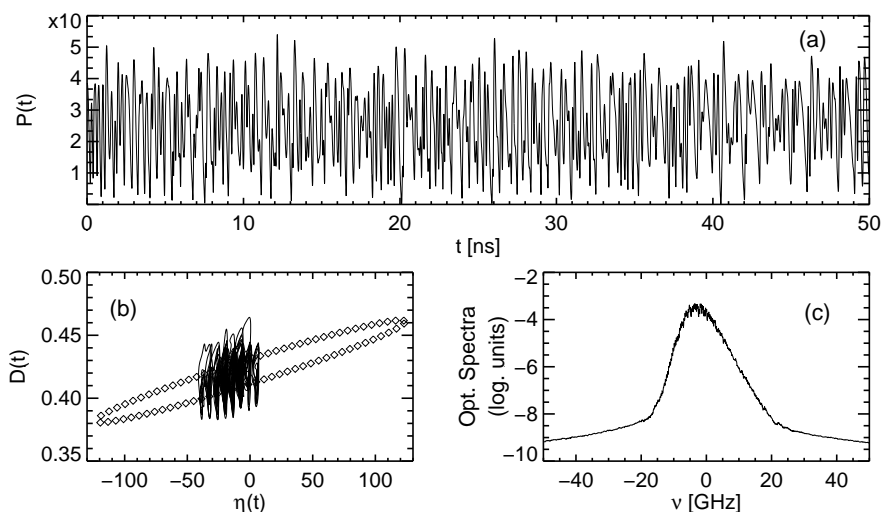


Figure 2.3. Characteristic dynamics of a laser with optical feedback operating within the CC regime: (a) evolution of the optical power, (b) two-dimensional phase-space projection, diamonds denote steady state solutions, (c) time-averaged optical spectrum. The parameters are given in Table 2.1-HLP1400 except for $p = 1.2$, $\tau = 2.3$ ns and $\kappa_f = 16.5$ ns $^{-1}$.

[Fig. 2.4(a)]. The typical time scale of power dropouts is of the order of ~ 100 ns, being much larger than any other time scale in the system. An interesting feature of this recovery process is that the laser intensity undergoes fast pulsations on a $\sim 20 - 100$ ps time scale. Interestingly these pulsations were predicted by the LK model [63] before the experimental verification [13, 55].

In Fig. 2.4(a), we illustrate the typical LFF obtained from the LK model when the laser operates at the solitary threshold current. In the $\eta - D$ phase space, the trajectory drifts toward negative η visiting different ECM and passing through the unstable manifold of a saddle generating a dropout event. The different time scales involved in the dynamics can be easily extracted when looking at the time averaged power spectrum [Fig. 2.4(c)]. A broad low frequency peak is present, as a consequence of power dropouts, followed by a sequence of external cavity resonances.

The work by Risch in 1977 motivated the understanding of the mechanisms that originate the LFF dynamics. Different explanations have been proposed, some of them rely with its deterministic origin while others have a stochastic basis. Henry and Kazarinov (HK) [80] proposed a first explanation studying the effect of spontaneous emission fluctuations. The presence of noise can force the system to escape from a stable fixed point, a minimum in a potential picture. Then the trajectory performs an excursion in the phase space until temporarily remains in some minimum

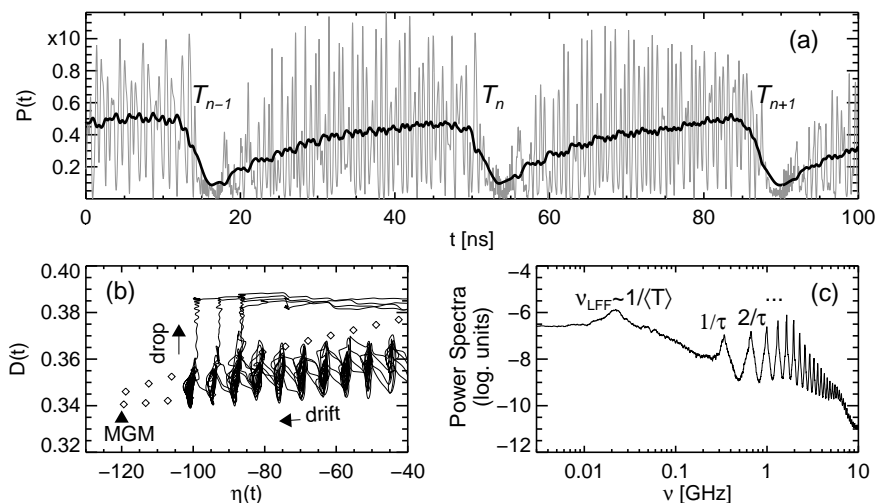
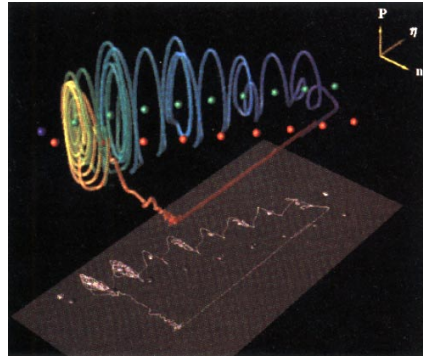


Figure 2.4. Characteristic dynamics of a laser with optical feedback under LFF operation: (a) evolution of the optical power, unfiltered (grey) and 250 MHz low pass filtering (black), (b) two-dimensional phase-space projection, diamonds denote steady state solutions, (c) time-averaged power spectrum. The time elapsed between dropouts is denoted by $T_n - T_{n-1}$. The same parameter than Fig. 2.3 except for $p = 1.0$.

Figure 2.5. Three dimensional representation of the LFF attractor (Sisyphus effect). After Ref. [84] with permission.



of the potential. Mørk [81] generalized the HK's framework by developing an iterative spectral method, where LFFs are understood as the result of bistability between the maximum gain mode and a low intensity state.

In contrast to the previous stochastic explanations, experimental evidences for a deterministic time-inverted type-II intermittency were reported by Sacher [82]. Only in 1994 Sano, [83] showed that the LK model exhibits LFFs as a result of a deterministic crisis of an attractor, that is to say, the trajectory in the phase space collides with an antimode at some point of the evolution. During the recovery process a chaotic itinerancy with a drift occurs, i.e., the trajectory visits different attractors created in the vicinity of each ECM. This process is commonly known as *Sisyphus effect* [63] because its analogy with the Sisyphus' labor in the Greek mythology⁴. The system evolves towards the MGM mode, whence the trajectory is repelled by the saddle towards the off-state [Fig. 2.5].

2.4 Statistics of Power Dropouts

In the previous section we have discussed different interpretations for the LFF onset. Refuting one of the deterministic or stochastic descriptions is not trivial, especially in semiconductor lasers that are intrinsically “noisy” systems. Further, power dropout events are irregularly distributed, both in time and intensity, and therefore a statistical description should be performed.

Many experiments dealt with the power statistics of the fast pulses that appear between power dropouts. Some of these experiments found an asymmetrically decreasing distribution with maximum probability near the mean value [85, 86], while

⁴The gods had condemned Sisyphus to ceaselessly rolling a rock to the top of a mountain, whence the stone would fall back of its own weight. Then Sisyphus watches the stone rush down in a few moments toward the plain whence he will have to push it up again toward the summit.

other ones reported intensity distributions with maximum at very low intensity levels with a monotonic decrease as the power increases [13, 69]. These discrepancies have been attributed to the multi-longitudinal mode operation [87], although gain suppression effects in the single mode LK model can also yield similar results [56]. The dispute about this fast pulsing statistics can be eluded when looking to longer time scale dynamics. Consequently, we investigate the statistics of the time elapsed between consecutive power dropouts. At least five experiments have been carried out this study in semiconductor lasers with optical feedback [82, 88]-[91]. All these works reported similar results, probability distribution functions with a dead region for short times and exponential decay for longer times. The mean time between dropouts decreases when the injection current increases.

Another interesting aspect associated with the transition from stable operation to LFFs is the existence of scaling laws for the time between dropouts with the injection current, that results to be an easy experimentally accessible control parameter. In the case of time-inverted type-II intermittency [92], reported by Sacher, the scaling law is $\langle T \rangle \sim |p - p_c|^{-1}$. p represents the normalized injection current while p_c stands for the critical value of the LFF onset. We note that this result is usually applicable to low dimensional systems, however it can be extended to a large class of chaotic systems exhibiting crisis-induced intermittency [93] where $\langle T \rangle \sim |p - p_c|^{-\gamma}$, γ being the critical exponent. On the other hand, Henry and Kazarinov provided an estimation of the mean time between dropouts $\langle T \rangle$ based on a stochastic theory. The time T has two contributions $T = T_0 + T_r$, where T_0 is the escape time from the stable mode and T_r is the recovery time (usually neglected). The mean time between dropouts reads [80]

$$\langle T \rangle \approx \frac{\pi}{a \left(1 + \frac{4P}{P_1}\right)} \exp \left[\frac{1}{3b} \mathcal{R}_\mu^3 \left(1 + \frac{P_1}{4P}\right)^3 \right], \quad (2.40)$$

where P_1 is the mean power for the current corresponding to the solitary laser threshold in the presence of feedback and P the mean power dependent on the injection current. \mathcal{R}_μ is the threshold reduction induced by the optical feedback in Eq. (2.34), and a , b are two laser-specific constants. It is worth recalling that spontaneous emission noise is essential in this model because the mean time diverges when $b \rightarrow 0$ ($\beta_{sp} \rightarrow 0$).

More recently, Eguía et al. [94, 95] have proposed a paradigmatic dynamical model in order to explain LFFs in SCL with optical feedback. This model combine both stochastic effects and the deterministic topological structure of the phase space. In this model, LFFs are induced by noise-driven events when operating below an Andronov bifurcation. In this excitable regime, drops are statistically distributed according to a Krammer's problem (exponential decay). Above the bifurcation point a

limit cycle is created and deterministic effects dominate, i.e., noise solely introduces an uncertainty in the number of twists around the unstable fixed point. Thus in this scenario, noise plays a crucial role in anticipating the appearance of LFFs before the bifurcation takes place.

Although many interpretations of LFFs have been discussed above, they are mainly based on some kind of reduction of the infinite dimensional delay-differential LK equations. To gain insight into the LFF regime, we undertake the study of the statistics of the time between dropouts by performing an extensive numerical simulation of the LK model over long time intervals.

2.4.1 Statistics of the time between dropouts

The LK model predicts that stable emission is obtained for injection currents below some critical value p_{LFF} . When the control parameter slightly exceeds this critical value, stable emission is interrupted by occasional power dropouts. We investigate the statistical properties of the time elapsed between consecutive dropouts while increasing the injection current from p_{LFF} . The value of p_{LFF} is numerically determined and has been estimated to be $p_{\text{LFF}} = 0.88 \pm 0.01$ for the actual choice of parameters [Table 2.1-HLP1400]. In addition, we have taken a feedback rate $\kappa_f = 35 \text{ ns}^{-1}$ and an external cavity length $\sim 50 \text{ cm}$ that provides a $\tau = 3.3 \text{ ns}$ delay time. The mean time between dropouts $\langle T \rangle$ and the probability distribution functions (PDF) are computed by taking time series longer than 1 ms (average over $\sim 10^4$ dropouts). A means of automatically determining whether a dropout event has occurred is a necessity when analyzing long time series. The criterion used in this work makes use of the fact that a dropout event manifests itself in the $\eta - D$ phase space, as a sudden large excursion of the trajectory towards positive values of η [See Fig. 2.4(b)]. A dropout event is assumed to occur when a sudden change of at least six modes ($\sim 6 \times 2\pi$ in η), towards the center of the ellipse, is observed. This detection scheme is somewhat arbitrary, but it has been found to be perfectly correlated with the occurrence of power dropouts and, more important, it allows us to distinguish between the chaotic back and forth changes in η (*inverse switching*) and a dropout event when approaching the CC regime.

Fig. 2.6 shows the PDF of the time T between dropouts for three different bias currents. These cases correspond to (a) the LFF regime below the solitary laser threshold, (b) the LFF regime above the solitary laser threshold, and (c) the CC regime. For sufficiently short times all the PDFs display a dead zone that shrinks when increasing the injection current. This dead zone is a consequence of the typical time scale associated with the recovery process connecting two consecutive power dropouts. Once the system reaches operation in the vicinity of the MGM, the mechanisms causing the dropout leads to a distribution of preferred time intervals revealed

in the PDFs. In the LFF regime the distributions display a dominant peak around the mean value in agreement with previous experimental results, obtained from lasers that typically operate with several longitudinal modes [89, 90]. When the system is biased just above the onset of LFFs, Fig. 2.6(a), a secondary peak appears in the PDF at shorter times. Simulations have been undertaken to check that this small peak also appears in the PDF for values of p between 0.88 – 0.92. An interpretation of such a two time scale dynamics stems from the interplay of stochastic and deterministic effects. The main peak is originated from the long residence times in the vicinity of the MGM. Then, noise ejects the system away and a train of fast optical bursts appear originating the secondary peak in the PDF. This bursting terminates as soon as operation close to the MGM is reached and the process restarts. When operating above the solitary threshold (b), the influence of the noise diminishes and power dropouts are distributed according the deterministic scenario. For bias currents within the CC regime, the PDF displays a weakly modulated flat structure at short times with an exponential decay for longer times, and hence in qualitatively agreement with experimental observations as outlined in [89, 90]. However, the amplitude of the os-

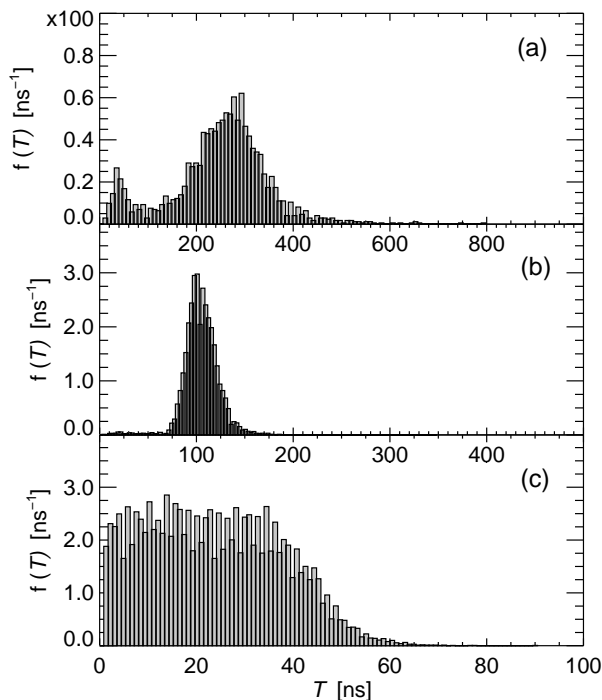


Figure 2.6. Probability distribution functions of the time between dropouts for three different bias currents. (a) $p = 0.92$, $\langle T \rangle = 312$ ns; (b) $p = 1.014$, $\langle T \rangle = 116$ ns; (c) $p = 1.18$, $\langle T \rangle = 25$ ns.

cillations in the PDF are very small when comparing with those in the experiments of Ref. [89].

Return maps T_{n+1} vs T_n for the same currents used in Fig. 2.6 are shown in Fig. 2.7. A rather uniform cloud of points in both the LFF and CC regimes can be seen, indicating a lack of periodicity in the dynamical evolution, with no correlation between dropouts. The same qualitatively return maps are obtained when the spontaneous emission noise term in Eq. (2.30a) is removed. For the actual choice of parameters, spontaneous emission noise seems to have a small influence on the statistical quantities describing the power dropouts. However, it is possible to find combinations of parameters, currents close to threshold and small facet reflectivities, where the time between dropouts considerably increases when an optimum noise level is used [88]. If this time increases, the system has more changes to reach the MGM and consequently it has to dropout due to noise effects. Our results are in good agreement with previously reported data [89], except for the correlation among the time intervals observed in the CC regime. It is worth noting that our explanation of the return maps is different from that given in Ref. [89]. The latter interprets LFFs as a consequence of the existence of an Andronov bifurcation in which noise is essential to anticipate the bifurcation and avoid a periodic regime.

As a final step, we look for scaling laws governing the transition from stable operation to the LFF regime. In Fig. 2.8, the mean time is plotted versus the bias current (a) scaled to the solitary threshold $\epsilon_1 = p - 1$ and (b) scaled to the onset of the LFFs $\epsilon_2 = p/p_{\text{LFF}} - 1$. The last points of Fig. 2.8(a), close to CC, can be fitted with $1/\epsilon_1$. This dependence was experimentally found by Sacher et al. [82]. However, this dependence bends for lower currents, in good agreement with more recent experimental results [88, 90]. The numerical results in the LFF regime scale very closely to

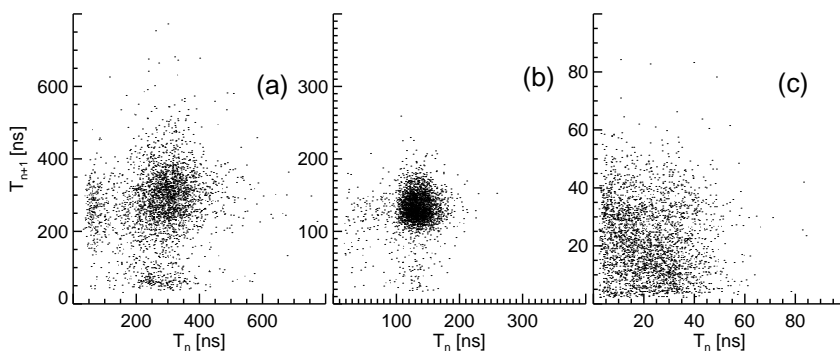


Figure 2.7. Return maps T_{n+1} versus T_n for the time between dropouts for the same currents as Fig. 2.6.

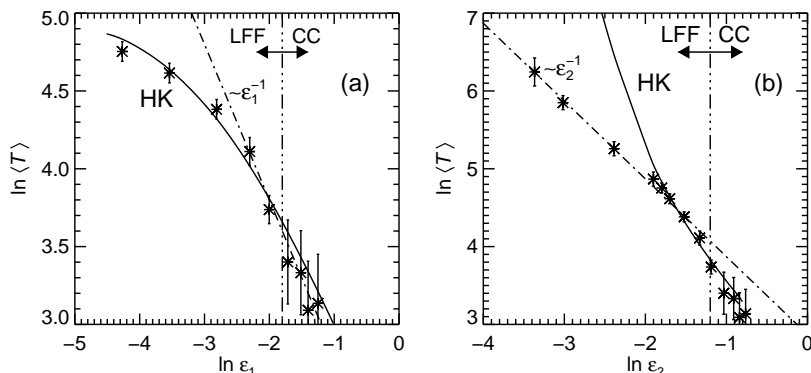


Figure 2.8. Mean time between dropouts versus normalized current (a) to the solitary laser threshold and (b) to the onset of LFFs (p_{LFF}). Points are calculated from numerical simulations of LK model. Solid-lines correspond to the Henry-Kazarinov approximation and dot-dashed lines are straight lines with slope -1 . The parameters that best fit our numerical results are $a = 25 \text{ ps}^{-1}$ and $b = 6.32 \times 10^{-3}$, but only for currents above the solitary laser threshold. Dot-dot-dashed lines roughly delimits the LFF and CC regimes.

$1/\epsilon_2$ [Fig. 2.8(b)] when replotted using $\ln \langle T \rangle$ vs $\ln \epsilon_2$. The predictions from the HK theory (solid line) are unable to fit this behavior. Hence, we have seen that the natural threshold required to understand the scaling properties of the system appears to be p_{LFF} and thus the data should be normalized to this value. The scaling law $\langle T \rangle \sim \epsilon_2^{-1.079}$ is obtained from the paradigmatic model proposed by Eguía et al. [94], being in qualitative agreement with our numerical results and those experimentally obtained in Refs. [88, 90], only when the system operates above the Andronov bifurcation. For lower values of ϵ_2 the system is within the excitable regime and the scaling follows a Krammer's law.

Statistics under single-mode operation of a DFB laser

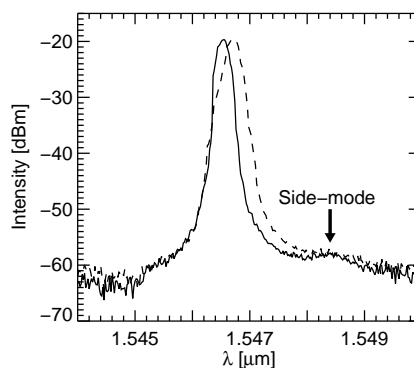
In the previous section, we have presented the most outstanding features of the time statistics between power dropouts resulting from an extensive numerical simulation of the LK model. Next, we present a detailed experimental and numerical comparison of the feedback-induced instabilities in DFB lasers subject to optical feedback demonstrating that only one longitudinal mode is sufficient to adequately describe the LFF instability.

We use a $1.55 \mu\text{m}$ single-mode DFB laser with a large side mode suppression ratio (SMSR) to fulfill the single-mode assumption of the LK model. Further, moderate amounts of optical feedback allow us to neglect multiple reflections. Fig. 2.9 depicts the optical spectra of the solitary laser and the laser with optical feedback. The spec-

tra have been recorded with a grating spectrometer with a resolution of 0.1 nm. The significant linewidth broadening towards longer wavelength corresponds to predictions of the LK model [67]. The laser persists in its single mode operation with a very large SMSR of 40 dB during LFF operation. Fig. 2.9 demonstrates that the single-mode operation holds even for fully developed coherence collapsed operation of the laser. Thus, multimode operation is not required for the occurrence of LFFs in semiconductor lasers.

In our numerical simulations, based on the LK model, we use parameters that are estimated from the experiment conditions [Table 2.1]: $\tau = 2.3$ ns, and $\kappa_f = 14.35$ ns⁻¹ reducing the threshold of the laser by 5.4%. DFB-specific effects (e.g., interaction between the DFB grating and the external cavity [57]) are neglected, as it is justified by the excellent agreement of our numerical and experimental results. Using the above parameters, the threshold current for the appearance of LFFs has been determined to be $p_{\text{LFF}} = 0.97$, in agreement with the experimental value. For bias currents close above p_{LFF} we observe both, experimentally and numerically, alternation between LFFs and stable operation on a single high-gain external-cavity mode (HGM) [67, 69]. This is the first time that LFF and stable emission are numerically obtained in such long time scales. Figures 2.10(a),(b) depict experimental and numerical time series, respectively, typical for this alternating behavior. Both time series have been obtained for $p = 0.98$. Within this regime, the system jumps back and forth between the LFF behavior and the stable HGM. This action is best demonstrated by the numerical simulations in $\eta - D$ space. The numerics in the inset Fig. 2.10(b) confirm that the system reaches the stable HGM. In noiseless numerical simulations, the trajectory first undergoes several power dropouts, then reaches the HGM and, finally, remains there. Only when the stochastic term is included in the equations the dynamical behavior depicted in Fig. 2.10(b) is observed. This can be understood as follows: Once the trajectory has reached the stable emission

Figure 2.9. Optical spectrum of the DFB laser. The solid line corresponds to the solitary laser, the dashed line to the laser with feedback under CC operation. $I = 1.18 I_{th}$.



state, noise is essential for ejecting the trajectory away from the HGM such that the LFF behavior can restart. In general, the stability of the external-cavity modes, i.e., their robustness against external perturbations or noise, is strongly dependent on the linewidth enhancement factor α [68]. Our numerical simulations demonstrate that the stability of the laser increases by decreasing α , a result that corresponds to recent experimental findings with Fabry-Perot lasers [96].

We have performed long time statistical investigations of the time intervals between subsequent power dropouts. Our extensive numerical simulations permit the first quantitative comparison of experiment and theory on such long time scales. Experimentally, we have recorded 50 time series, each of $5 \mu\text{s}$ length, covering several thousand power dropouts; numerically, we have considered of the order of 10^4 dropout events. From these time series we obtained PDFs of the time intervals between subsequent power dropouts. Figure 2.11 depicts the corresponding experimental and numerical PDFs for three different injection currents covering the whole LFF regime: (a) $p = 0.98$, (b) $p = 1.04$, and (c) $p = 1.08$. The agreement of theory and experiment is excellent. All PDFs display similar features: an exponential decay for long times, and a dead zone for short times specially for low bias currents. We point out that theoretically and experimentally obtained PDFs show an identical dependence on the injection current. In particular, the mean time interval between

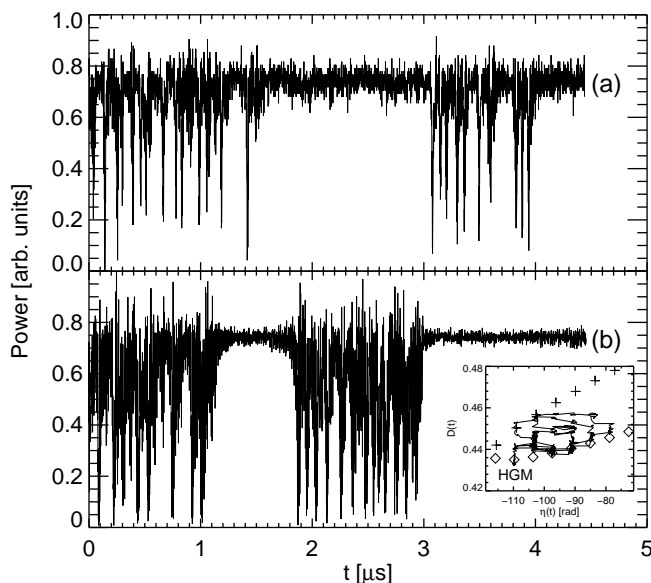


Figure 2.10. Time traces showing alternation between LFF and stable operation. (a) experiment and (b) numerical simulations. The inset of figure (b) shows in the $\eta - D$ space how the trajectory jumps from LFF behavior to the stable high-gain mode (HGM).

subsequent power dropouts $\langle T \rangle$ exhibits an interesting dependence on the injection current: Figure 2.12 depicts experimental and numerical data in a ln-ln plot of $\langle T \rangle$ versus $\varepsilon_2 = p/p_{\text{LFF}} - 1$, where the current is normalized with respect to the threshold current for the onset of the LFF. Both data sets demonstrate that, within the LFF regime, $\langle T \rangle$ scales as ε_2^{-1} , whereas the fit based on the predictions by Henry and Kazarinov [80] exhibits substantial deviations from the experimental and numerical results. The ε_2^{-1} scaling of $\langle T \rangle$ as well as the exponential decay and the dead time that are present in the PDFs have also been observed in experiments in which multimode Fabry-Perot lasers were used [90]. This fact indicates that these are general properties that are present in the dynamics of semiconductor lasers, and consequently are independent of the number of optical modes involved in the laser emission. However, the mechanism that underlies the scaling is not yet fully understood [88, 97].

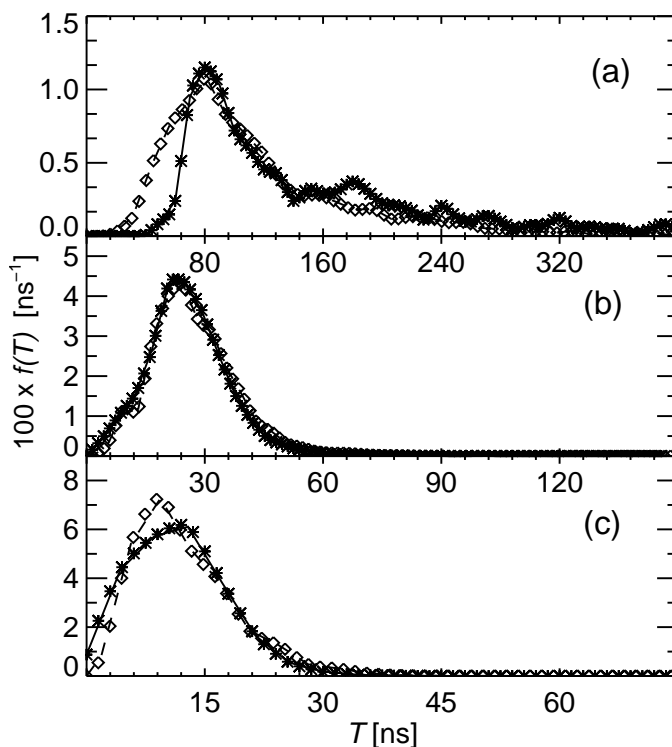


Figure 2.11. Probability density function $f(T)$ of the time interval T between subsequent power dropouts. (a) $p = 0.98$, (b) $p = 1.04$ and (c) $p = 1.08$. Diamonds and dashed line correspond to experimental data; stars and solid lines to numerical simulations. Note the different scales of $f(T)$ and T in (a)–(c). Parameters are given in the text.

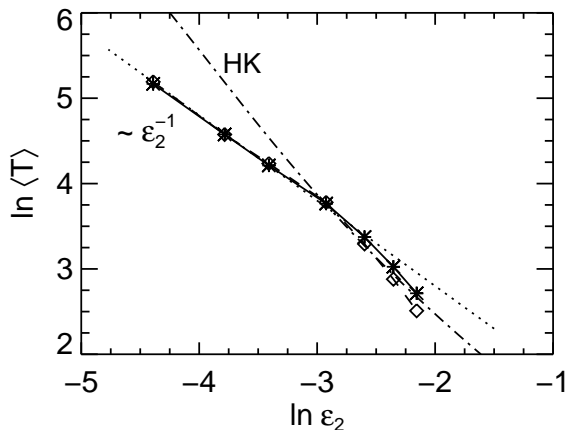


Figure 2.12. Ln-ln plot of the average time interval between subsequent dropouts $\langle T \rangle$ versus the normalized injection current $\epsilon_2 = p/p_{\text{LFF}} - 1$. Diamonds and dashed line correspond to experimental data; stars and solid lines to numerical simulations. The dotted line corresponds to a linear fit $\langle T \rangle \sim \epsilon^{-1}$; the dashed-dotted curve, to results obtained from the Henry-Kazarinov [80] model.

2.5 Entraining Power Dropouts

The statistical analysis carried out in Sec. 2.4 manifested the existence of large time dispersion between power dropouts. However, this study only provides a partial characterization of the LFF process because it does not consider the influence of a generic external force on the time distributions. The possibility of controlling chaos began since the work by Ott-Grebogoy-Yorke (OGY) [98]. The idea behind chaos control is as brilliant as simple. If one thinks of a chaotic attractor as a collection of unstable periodic orbits, the question arises whether it is possible to keep the system locked to one of these unstable orbits by applying a small control signal. However, the major drawback in these feedback control schemes is the necessity of real-time detection of the commonly fast chaotic signal. Other strategies, founded in a stochastic basis, revealed that a proper choice of noise and modulation levels may enhance the periodicity of the signal. Among them, are worth mentioning experimental and numerical evidences of coherence [99, 100] and stochastic [101] resonance in a laser with optical feedback, which behaves as an excitable medium [89, 97].

In this work, we implement a sinusoidal modulation of the injection current in order to reduce the time dispersion between dropouts and obtain a more periodic output. This effect reflects itself in the appearance of preferred time intervals in the statistical distributions. For sufficiently large forcing and adequate frequencies the

phenomenon of entraining takes place, that is to say, power dropouts follow the period imposed by the external modulation. This phenomenon was first theoretically predicted [102] and experimentally demonstrated in Refs. [103, 104].

Next we describe the influence of both frequency and amplitude of the current modulation in the PDFs. We retake the parameters used in the previous section for the DFB laser which are given in Table 2.1. We consider operation within the LFF regime. The injection current is varied using a sinusoidal modulation

$$p(t) \equiv \frac{I(t)}{I_{th}^{sol}} = p_b + \Delta p \sin\left(2\pi \frac{t}{T_m}\right), \quad (2.41)$$

p_b being the bias current, Δp the normalized amplitude and T_m the modulation period.

Frequency dependence

For a weak modulation amplitude $\Delta p = 0.005$ ($\Delta I = 0.14$ mA) superimposed onto the bias current $p_b = 1.02$, we vary the modulation period by several decades, from the external cavity round-trip time up to the low frequency range (mean time between dropouts). We find an interesting behavior in the distribution functions and return plots as shown in Fig. 2.13: the influence of the modulation is limited to a finite bandwidth. When the modulation period is lower or equal to the external round-trip

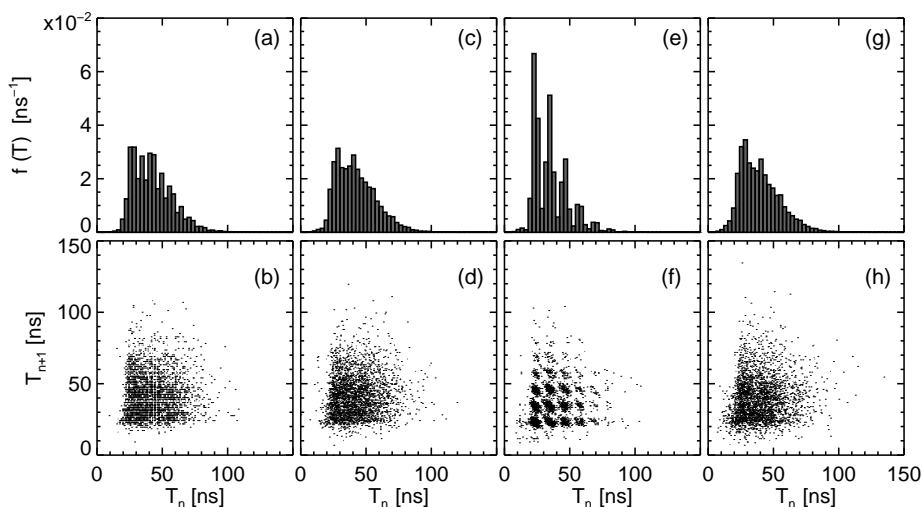


Figure 2.13. Probability density function $f(T)$ and return plots of the time interval T between subsequent LFF dropouts for a bias $p_b = 1.02$ and $\Delta p = 0.005$. (a,b) no modulation, (c,d) $T_m = \tau$, (e,f) $T_m = 5\tau$, (g,h) $T_m = 36.33\tau$.

time (c,d), the PDFs and return plots are almost unaffected when comparing with the simulation without modulation (a,b): a cloud of points indicating a lack of periodicity is obtained. When the modulation period is increased beyond τ , we observe the appearance of preferred times in the statistical distributions. The PDFs present peaks at the harmonic positions of the modulation period, but the 1:1 peak is absent. If the modulation is taken away from τ , but still below the typical mean time between power dropouts, the system is able to develop a peak at the modulation period. When the modulation period exceeds the typical mean time between dropouts, computed in the absence of modulation, the modulation-induced time-selectivity in the PDFs disappears. The magnitude of the peaks depend on the modulation amplitude as we will next discuss.

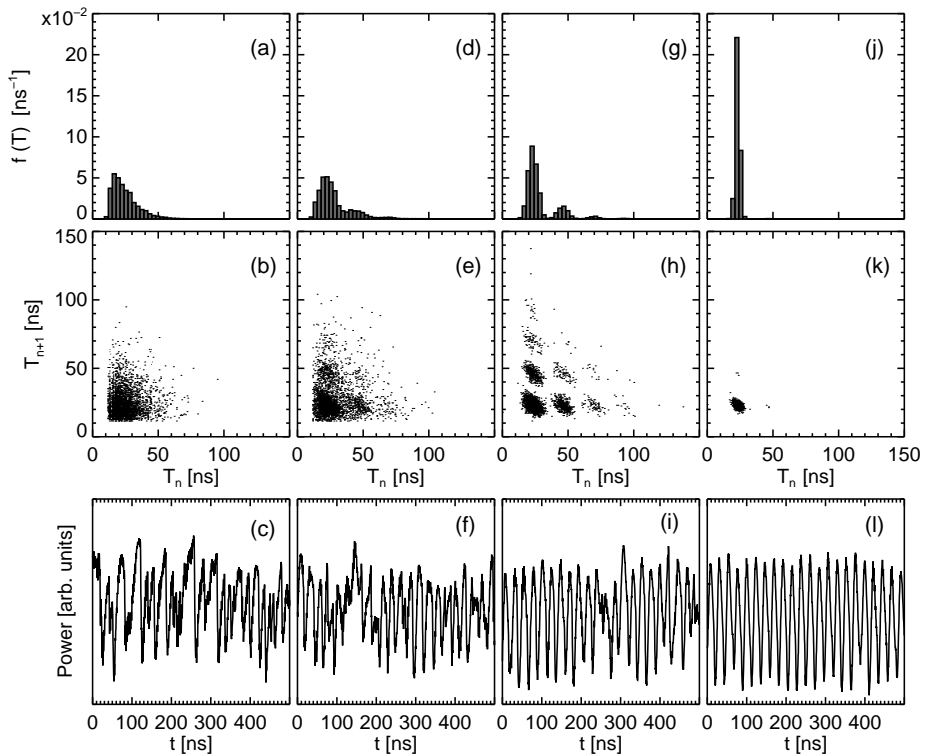


Figure 2.14. Probability density function $f(T)$ and return plots of the time interval T between subsequent LFF dropouts for a bias $p_b = 1.06$ and $T_m = 10\tau$. (a,b,c) no modulation, (d,e,f) $\Delta p = 0.01$, (g,h,i) $\Delta p = 0.02$, (j,k,l) $\Delta p = 0.04$. The typical power time traces are shown in panels (c,f,i,l).

Amplitude dependence

We consider a fix modulation period $T_m = 10\tau$ and a bias current $p_b = 1.06$ where time selectivity of power dropouts is achieved and a 1:1 peak is present in the PDFs. We take a larger bias current, still in the LFF regime, because the modulation amplitude is going to be enhanced. Fig. 2.14 shows the influence of the modulation amplitude on the PDFs (upper panels), return maps (middle panels) and time traces of the optical power (lower panels). We observe how the multi-peaked structure in the PDFs is enhanced when the amplitude is increased up to some critical level $\Delta p \sim 0.02$ or ~ 2 mA peak-to-peak modulation. Beyond this value the modulation amplitude is sufficiently large for allowing a perfect entrainment of power dropouts events with the modulation. The situation depicted in Fig. 2.14(j,k,l) shows a perfect entrainment of the power dropouts with the modulation period T_m .

We have demonstrated that by a proper choice of the modulation period, between τ and $\langle T \rangle$, and modulation amplitudes larger that ~ 2 mA (only $\sim 4\%$ of the bias current), the chaos control scheme allows for operation in a periodic orbit. Further investigation on current modulated LFFs, should provide a better understanding about this interesting dynamical chaotic regime.

2.6 Discussion

The onset of feedback-induced instabilities, namely low-frequency fluctuations in the regime IV, has been numerically and experimentally investigated. Numerical studies have focused on the Lang-Kobayashi model while experiments were done using distributed feedback lasers that exhibit single-longitudinal mode operation, thus approaching the model conditions to the experiment as much as possible.

First, we gave experimental evidences that multimode operation is not required for the occurrence of the above mentioned feedback-induced instabilities. This result reduces the number of degrees of freedom which have to be taken into account in stabilization, control, and synchronization problems when using this type of lasers. In particular, we have demonstrated quantitative identical parameter dependence in long-time LFF statistics including a characteristic scaling law for the mean time between dropouts. Second, the transition from stable operation to low-frequency fluctuation behavior has associated a scaling law from which stems the different possible interpretations of this phenomenon. The time between power dropouts scales with the current, normalized to the LFF onset, with an exponent very close to -1 . This effect suggests the existence of a type-II intermittent behavior [92] as was experimentally reported by Sacher [82]. However it is not obvious that this mechanism underlines the appearance of LFF in the LK model, because crisis-induced intermittency might also lead to the same scaling laws. We have obtained scaling properties

that are in agreement with experiments that use multi-longitudinal mode lasers, suggesting that these are general features of the laser dynamics and independent of the number of lasing modes.

Finally, we numerically implemented a chaos control scheme, i.e., the targeting of unstable periodic orbits, by applying a sinusoidal modulation of the current. A signal in which power dropouts are entrained to the modulation (1:1 response) appear for adequate modulation frequencies and sufficiently large amplitudes. In other situations, the PDFs display preferred time intervals corresponding to the harmonics of the modulation period. This scheme can be further analyzed using reduced versions of the LK model [105] or by the help of the paradigmatic dynamical model developed by Eguía et al [106].

Chapter 3

Bidirectionally Coupled Semiconductor Lasers

3.1 Introduction

Coupled¹ nonlinear oscillators have been extensively studied in the past due to their rich variety of possible behaviors and applications. The understanding of the dynamics of coupled nonlinear oscillators is essential for a wide range of scientific investigations. Periodic and chaotic oscillations have been reported in chemical reactions, population dynamics, physiological interactions, coupled neurons, mechanical oscillators, laser systems [107]-[110], etc.

Synchronization of these oscillators involves an adjustment of their rhythms due to a weak interaction [111]. Then, it is mandatory that each oscillator presents a self-sustained oscillation either in a periodic, quasi-periodic or chaotic form. Depending on the coupling conditions (*coupling strength*), this process may lead to a readjustment of oscillation frequencies towards a common frequency (*frequency locking*), and to a fixed relationship among the oscillation phases of two synchronized oscillators (*phase locking*).

The application of synchronization of chaotic systems in secure communication was suggested for the first time by Pecora and Carol in 1990 [112]. Since then, scientific interest has focused on chaotic systems exhibiting both, high-dimensional, and fast dynamics in order to hinder eventual message recovery by eavesdroppers attacks using spectral or advanced time series analysis tools. Communication systems using chaos can be considered as a generalization of the existing conventional

¹ This chapter is based on the papers:

J. Mulet, C. Masoller, and C. R. Mirasso, Phys. Rev. A **65**, 063815 (2002);

T. Heil, I. Fischer, W. Elsässer, J. Mulet, and C. R. Mirasso, Phys. Rev. Lett. **86**, 795 (2001);

J. Mulet, C. R. Mirasso, T. Heil, and I. Fischer, submitted for publication (2002).

communication systems. Here, the message is modulated within the chaotic signal of the transmitter. Thus, a broad spectrum of frequencies is used as a carrier for the information instead of a single frequency. The key for message recovery is the phenomenon of chaos synchronization. The receiver tuned, i.e. synchronized, to the chaotic signal of the transmitter allows message extraction². Finally, chaos synchronization is only possible if transmitter and receiver are (almost) identical chaotic systems [113].

Lasers turned out to be very attractive systems for this task, mainly because the maximum attainable transmission speed is considerably larger than the electronic encryption schemes using software. Already in 1994, synchronization was demonstrated in CO₂ lasers [114], and in Nd:YAG lasers [110]. A first breakthrough concerning the speed and the dimension of the synchronized chaotic dynamics was achieved by VanWiggeren and Roy using fiber lasers [115, 116]. Currently, semiconductor lasers (SCL) have the highest potential for a practical realization of communication systems using chaotic carriers. Synchronization in SCL has already been demonstrated numerically in laterally coupled lasers [117], and in distanced semiconductor lasers [75, 118]. Most of these studies have focused on lasers that exhibit chaos due to optical feedback (from an external mirror) [63], optical injection (from another laser) [119], and current modulation. Remarkably, only few studies have centered on instabilities arising from the mutual coupling among different lasers. Many of the real systems include a significant time delay between subsystems when they are coupled. However, and for the sake of simplicity, this delay is sometimes neglected or simply incorporated in the transmitter's local-time when the coupling is unidirectional. This last shortcut is not adequate when the coupling is bidirectional and time delay effects, some of them already discussed in Chap. 2, can yield absolutely unexpected behaviors, mainly due to the additional degrees of freedom introduced into the system.

The aim of this chapter is twofold: first, we perform a systematic derivation of the governing equations in the case of mutual optical coupling of two spatially separated Fabry-Perot SCL, and second, we investigate the synchronization properties by analyzing the dynamics of the system.

²In order to achieve confidentiality, the message has an amplitude much smaller than the one of the chaotic carrier. If the synchronization is robust against small perturbations, the receiver solely synchronizes to the chaos of the transmitter –chaos pass-filtering–. Then the message can be recovered by simply subtracting the injected signal to the output signal of the receiver.

Modeling

When the distance between the lasers is small, typically much less than the laser cavity, mutually coupled lasers can be considered as a single cleaved-compound-cavity (C^3) laser. These devices are formed by two individual sections, separated by a small air-gap, where the electrical injection can be applied independently. Under appropriate coupling conditions, there is an enhancement in mode selectivity that arises from the constructive and destructive interference of the fields in the two coupled cavities. Consequently, several achievements have been demonstrated: better single-mode operation [10], frequency tuning [120], frequency-chirp reduction under current modulation [121], and a lowering in intensity noise [122]. The evolution of the longitudinal modes in a C^3 laser can be described by means of a system of time-dependent coupled rate equations [123, 124].

A completely different operation regime appears when the distance between the lasers is enlarged [125]. Optical instabilities arise from the delayed optical injection from a laser to its counterpart and eventually due to optical feedback from the facet of the other laser. In Refs. [48, 126]-[129] the experimental observations were successfully interpreted in terms of a phenomenological singlemode rate equation model of weakly mutually coupled SCL. In the model each laser is described by rate equations, one for the complex optical field, E , and one for the carrier density, N . The mutual coupling is accounted for by adding the delayed field of laser 2 in the equation for the complex field of laser 1 and viceversa. A more detailed description of two multimode mutually-coupled semiconductor lasers has been recently reported in Ref. [130]. The latter, directly considers the spatiotemporal Maxwell-Bloch equations complemented with adequate boundary conditions. Such an approach can provide a very accurate description of the system, although the major drawback is the larger computational requirements.

To the best of our knowledge, the derivation of the phenomenological model, describing two coupled lasers, from basic principles has not been reported in the literature yet. In spite of the success of this model in describing the experimental findings, there is no systematic investigation of its range of validity as a function of the mutual coupling strength. In Sec. 3.2 we start from Maxwell's equations and derive equations for the field amplitudes in each laser cavity. We also derive rate equations for the total carrier number within each laser. For arbitrary coupling, we obtain a closed set of equations which we use in Sec. 3.3 to calculate the monochromatic solutions of the compound system. The influence of the coupling strength on the steady-state solutions gives insight into the range of validity of the phenomenological model.

Nonlinear dynamics

The dynamical properties of two mutually-coupled and spatially-separated SCL has been experimentally [128, 129] and theoretically [131]-[133] reported. This last scenario can be interpreted in terms of the behavior of mutually coupled nonlinear oscillators. When the lasers have dissimilar relaxation oscillation frequencies and intensities, their effective mutual coupling strength may be asymmetric. In this case, Hohl et al [48, 126] found that two coupled semiconductor lasers may exhibit a form of synchronization which is characterized by low amplitude oscillations in one laser, and large oscillations in the other one –*localized synchronization*–. On the other hand, Heil et al [128] found that two coupled lasers may exhibit subnanosecond synchronized chaotic dynamics. These studies complemented some previous investigations where the SCL were weakly coupled [48, 126]. Even in the case of identical lasers they found an asymmetric role among both: there exists a time lag, equal to the flight time from one laser to the other, between the dynamics of the two lasers.

The second part of the chapter is organized as follows. In Sec. 3.4 we derive a dynamical model valid for weak coupling. In this case we arrive to the phenomenological rate equation model previously used by several authors [48, 126]-[129]. The details of the experimental setup is briefly mentioned in Sec. 3.5. Next, we center the discussion on the dynamical instabilities, resulting from the mutual coupling, and the degree of synchronization among the intensity fluctuations. Results under perfect symmetric operation are in Sec. 3.6. In Sec. 3.7 we develop a more detailed rate equation model that accounts for higher-order terms in the coupling. We investigate the effect of these terms through several examples. Finally, Sec. 3.8 is devoted to concluding and summarizing the chapter.

3.2 The Model

We start from the Maxwell's equations (1.3a)–(1.3d) to obtain a wave equation describing the propagation of the electric field along the compound system. These equations are complemented with boundary conditions, at each laser facet, for the two counterpropagating waves. Next, we derive equations that describe the spatially averaged carrier densities within each laser cavity. Finally, we introduce the slowly-varying approximation.

Field equations

We begin from the wave equation (1.6) for the electric field wave equation

$$\vec{\nabla}^2 \vec{\mathcal{E}}_\omega + \left(\frac{\omega}{c}\right)^2 \epsilon_\omega \vec{\mathcal{E}}_\omega = \vec{0}, \quad (3.1)$$

where

$$\epsilon_\omega = 1 + \chi_\omega^l + \chi_\omega^{nl}(N) + i \frac{\sigma_\omega}{\epsilon_0 \omega}, \quad (3.2)$$

stands for the complex dielectric function. $c = 1/\sqrt{\mu_0 \epsilon_0}$ is the light speed in vacuum, ϵ_0 the vacuum permittivity, μ_0 the vacuum permeability, and σ_ω the electric conductivity of the medium. N represents the density of electron-hole pairs excited in the active region of the semiconductor laser.

As it is usually done in a Fabry-Perot cavity, we express the electric field as the superposition of two counterpropagating waves. For simplicity we neglect the transverse dependence of the field assuming a plane-wave-like solution

$$\mathcal{E}_j(\omega; z) = \tilde{\mathcal{E}}_j^+ e^{iq_j z} + \tilde{\mathcal{E}}_j^- e^{-iq_j z} + \text{c.c.} \quad (3.3)$$

The polarization direction of the electric field is taken transverse electric due to the geometry of the device. $\tilde{\mathcal{E}}_j^\pm$ are the amplitudes, at frequency ω , of the forward and backward propagating plane waves inside each laser section $j = 1, 2$ and in the inter-laser cavity $j = 0$, while q_j stand for their respective propagation constants. The inter-laser is defined by the physical separation between the two lasers. Upon substituting Eq. (3.3) into the wave equation (3.1), we find a dispersion relation for the propagation constant q_j that reads

$$q_j = \frac{\omega}{c} n_\omega(N_j) - \frac{i}{2} [g_\omega(N_j) - \alpha_\omega^{int}], \quad (3.4)$$

for $j = 1, 2$, where we have defined

$$n_\omega(N) = \sqrt{1 + \text{Re} \chi_\omega^l + \text{Re} \chi_\omega^{nl}(N)}, \quad (3.5a)$$

$$g_\omega(N) = - \left(\frac{\omega}{c} \right) \frac{1}{n_{e\omega}} \text{Im} \chi_\omega^{nl}(N), \quad (3.5b)$$

$$\alpha_\omega^{int} = \left(\frac{\omega}{c} \right) \frac{1}{n_{e\omega}} \left[\text{Im} \chi_\omega^l + \frac{\sigma_\omega}{\epsilon_0 \omega} \right], \quad (3.5c)$$

with $n_\omega(N)$ the modal refractive index, $g_\omega(N)$ the modal gain, α_ω^{int} the internal loss, and $n_{e\omega}^2 = 1 + \text{Re} \chi_\omega^l$ the background refractive index. The propagation in the inter-laser cavity is described through

$$q_0 = \frac{\omega}{c} + \frac{i}{2} \alpha_\omega^{ext}, \quad (3.6)$$

where α_ω^{ext} stands for the total coupling loss accrued due to, e.g., diffraction.

Boundary conditions

The situation of two device-identical SCL coupled in a face-to-face configuration, as the one depicted in the Fig. 3.1, consists in two Fabry-Perot cavities with length L and separated by a distance L_e determining the inter-laser cavity. We consider that all the laser facets are cleaved, acting as mirrors with an internal (external) reflectivity and transmittivity r' , t' (r , t). The Stokes relationships imply that $r = -r'$ and $tt' = 1 - r^2$. Imposing continuity of the electric field and its derivative at the laser facets, we arrive to the following boundary conditions for the amplitudes of the counterpropagating waves

$$z = -(L + l), \quad e^{-iq_1(L+l)} \tilde{\mathcal{E}}_1^+ = r' e^{iq_1(L+l)} \tilde{\mathcal{E}}_1^-. \quad (3.7a)$$

$$z = -l, \quad e^{iq_1 l} \tilde{\mathcal{E}}_1^- = r' e^{-iq_1 l} \tilde{\mathcal{E}}_1^+ + t e^{iq_0 l} \tilde{\mathcal{E}}_0^-, \quad (3.7b)$$

$$e^{-iq_0 l} \tilde{\mathcal{E}}_0^+ = r e^{iq_0 l} \tilde{\mathcal{E}}_0^- + t' e^{-iq_1 l} \tilde{\mathcal{E}}_1^+. \quad (3.7c)$$

$$z = l, \quad e^{iq_2 l} \tilde{\mathcal{E}}_2^+ = r' e^{-iq_2 l} \tilde{\mathcal{E}}_2^- + t e^{iq_0 l} \tilde{\mathcal{E}}_0^+, \quad (3.7d)$$

$$e^{-iq_0 l} \tilde{\mathcal{E}}_0^- = r e^{iq_0 l} \tilde{\mathcal{E}}_0^+ + t' e^{-iq_2 l} \tilde{\mathcal{E}}_2^-. \quad (3.7e)$$

$$z = L + l, \quad e^{-iq_2(L+l)} \tilde{\mathcal{E}}_2^- = r' e^{iq_2(L+l)} \tilde{\mathcal{E}}_2^+, \quad (3.7f)$$

with $l \equiv L_e/2$. Due to the high degree of symmetry, we have taken the origin of the z axis at the middle of the inter-laser cavity. We note, however, that the final equations governing the system are independent of this arbitrary choice. By using the Eqs. (3.7b)–(3.7e) we derive the coefficients of the scattering matrix \mathbf{S} , defined through

$$\begin{pmatrix} e^{iq_1 l} \tilde{\mathcal{E}}_1^- \\ e^{iq_2 l} \tilde{\mathcal{E}}_2^+ \end{pmatrix} = \begin{pmatrix} S_{11} & S_{12} \\ S_{21} & S_{22} \end{pmatrix} \begin{pmatrix} e^{-iq_1 l} \tilde{\mathcal{E}}_1^+ \\ e^{-iq_2 l} \tilde{\mathcal{E}}_2^- \end{pmatrix}. \quad (3.8)$$

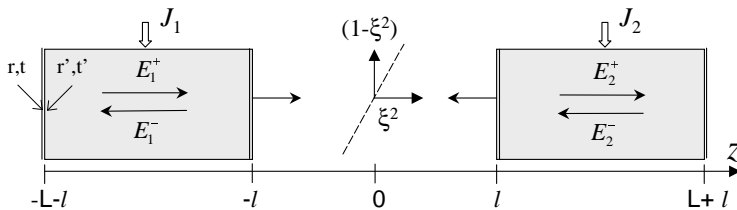


Figure 3.1. Sketch of two mutually coupled Fabry-Perot semiconductor lasers. The internal (external) laser facets have a reflectivity and transmittivity r' , t' (r , t). Only a fraction ξ^2 of optical power is transmitted by the effective coupler located within the inter-laser cavity.

The coefficients of the matrix are

$$S_{11} = S_{22} = r' \left[1 - \frac{(1-r^2)e^{i4q_0l}}{1-r^2e^{i4q_0l}} \right], \quad (3.9a)$$

$$S_{12} = S_{21} = \frac{(1-r^2)e^{i2q_0l}}{1-r^2e^{i4q_0l}}. \quad (3.9b)$$

These coefficients are similar to those given in Ref. [10] when describing C^3 lasers. On the other hand, the propagation constants within each medium are given by Eq. (3.4). In the inter-laser cavity we express the propagation constant as follows

$$e^{i2q_0l} = \xi e^{i\omega\tau}, \quad (3.10)$$

$\tau \equiv L_e/c$ being the one-way lag time. $\xi^2 \equiv \exp(-\alpha_\omega^{ext} L_e)$ can be regarded as the fraction of optical power transmitted by an equivalent coupler located in the inter-laser cavity [See Fig. 3.1].

Upon substituting Eqs. (3.7a) and (3.7f) into the scattering matrix we arrive at equations relating the outgoing field amplitudes in both lasers, $\tilde{\mathcal{E}}_1^-$ and $\tilde{\mathcal{E}}_2^+$, that read

$$[1 - r' S_{11} e^{i2q_1 L}] e^{iq_1 l} \tilde{\mathcal{E}}_1^- = r' S_{12} e^{i2q_2 L} e^{iq_2 l} \tilde{\mathcal{E}}_2^+, \quad (3.11a)$$

$$[1 - r' S_{22} e^{i2q_2 L}] e^{iq_2 l} \tilde{\mathcal{E}}_2^+ = r' S_{21} e^{i2q_1 L} e^{iq_1 l} \tilde{\mathcal{E}}_1^-. \quad (3.11b)$$

Finally, there is a subtle point that deserves some discussion. In this section we have described the interface semiconductor/air through a set of reflection and transmission coefficients. All through this chapter we will consider these coefficients as constants (independent of propagation constants)³. An alternative description of the interface is to include the different dielectric constants in the boundary conditions. Recently, Duarte and Solari [134] have studied the equivalence between these two approaches, in the case of a semiconductor laser with optical feedback. They showed that the two descriptions lead to similar results, for low and large coupling strengths. However, the approximation of constant coefficients fails for intermediate couplings where the metamorphosis (of the solitary laser solutions towards the compound cavity solutions) occurs. We assume that the mutual coupling strength is such that allows us to consider the reflection and transmission coefficients as constants. Even in the last section, where we will derive rate equations that take into account high-order terms in the coupling, the coupling is still weak (such that it is physically meaningful to consider the longitudinal modes of each laser).

³The continuity of $\tilde{\mathcal{E}}$ and $d_z \tilde{\mathcal{E}}$ at $z = -l$ directly yield $r' = (q_1 - q_0)/(q_1 + q_0)$ and $t' = 2q_1/(q_1 + q_0)$. By neglecting the frequency dispersion and carrier dependence on propagation constants, $q_{1,0} = (\omega/c)n_{e,1,0}$, r' and t' can be considered as constants. These are the well-known Fresnel relationships for a dielectric-dielectric interface under normal incidence.

Carrier equations

The above equations that describe the optical propagation of the electric field along the whole system have to be complemented with equations describing the interaction with the active material. The evolution of the carrier density within each laser is governed by equation (1.13)

$$\begin{aligned} \frac{\partial N_j(\vec{r}, t)}{\partial t} = & \frac{J_j(\vec{r})}{ed} - \gamma_e N_j + \mathcal{D} \frac{\partial^2 N_j}{\partial z^2} - \frac{i}{\hbar} [\mathcal{P}_j^{nl}(z, t) \mathcal{E}_j^*(z, t) \\ & - \mathcal{P}_j^{nl*}(z, t) \mathcal{E}_j(z, t)] , \end{aligned} \quad (3.12)$$

with $j = 1, 2$. $J_j(\vec{r})$ is the current-density distribution, d is the active layer thickness, e the absolute value of the electronic charge, γ_e is the spontaneous recombination rate, and \mathcal{D} is the diffusion coefficient. The induced material polarization $\vec{\mathcal{P}}_\omega$ can be expressed as in Eq. (1.5). In the mean-field approximation we neglect the carrier diffusion and we introduce the total carrier number \mathcal{N}_j ,

$$\mathcal{N}_j \equiv \int_{active} N_j(\vec{r}) d^3\vec{r}, \quad (3.13)$$

where the integration limits correspond to the active region of each laser. By assuming that the material polarization $\mathcal{P}_j^{nl}(z, t)$ adiabatically follows the evolution of the electric field, Eq. (3.12) can be approximated by

$$\dot{\mathcal{N}}_j(t) \approx \frac{I_j}{e} - \gamma_e \mathcal{N}_j + \frac{2\varepsilon_0 V}{\hbar} \text{Im} \chi^{nl}(\omega, \mathcal{N}_j) \frac{1}{L} \int_{z_0}^{z_0+L} |\mathcal{E}_j(z, t)|^2 dz, \quad (3.14)$$

where I_j stands for the total injection current in each laser, V is the active region volume, z_0 is the origin of the laser cavity, and L stands for its length. In the case of a monochromatic solution at frequency ω , the integral term in the right hand of the above equation can be determined by replacing Eq. (3.3) into Eq. (3.14) and taking into account that the amplitudes of the counterpropagating waves $\tilde{\mathcal{E}}_{j,\omega}^\pm$ in each laser are related through Eqs. (3.7a) and (3.7f),

$$\dot{\mathcal{N}}_j(t) \approx \frac{I_j}{e} - \gamma_e \mathcal{N}_j - \frac{2\varepsilon_0 V n_e c}{\hbar \omega} g_\omega(\mathcal{N}_j) \Gamma_j |e^{iq_j L} \mathcal{E}_j^\mp(t)|^2, \quad (3.15)$$

where the sign $-(+)$ corresponds to $j = 1$ ($j = 2$).

The integral terms Γ_j are defined through

$$\Gamma_j \equiv \frac{1}{L} \int_0^L \left| r' e^{iq_j(z+L)} + e^{-iq_j(z-L)} \right|^2 dz. \quad (3.16)$$

A subtle point in the determination of the carrier variables enters into the definition of the $\Gamma_{1,2}$ terms. These integrals represent the longitudinal average of the optical power resulting from the longitudinal standing wave inside the cavity, that in turn, is determined by the propagation constants. By evaluating the integral in Eq. (3.16) we can obtain explicit functional forms of these terms that read

$$\Gamma_j(\theta_j) = e^{-\text{Im}\theta_j} \left[2r' \text{sinc}(\text{Re}\theta_j) + \frac{e^{\text{Im}\theta_j} + r'^2(1 - e^{-\text{Im}\theta_j}) - 1}{\text{Im}\theta_j} \right], \quad (3.17)$$

$\theta_j \equiv 2Lq_j$ being the dimensionless propagation constant. Under free-running operation, the propagation constant is determined by the well-known round-trip condition [10]

$$e^{i\theta^{sol}} = \frac{1}{r'^2}, \quad (3.18)$$

and the integrals read

$$\Gamma^{sol} \equiv \Gamma_j(\theta^{sol}) = \frac{2(1 - r'^2)}{r'^2 \ln \frac{1}{r'^2}}. \quad (3.19)$$

In many situations this term can be scaled into the definition of the electric field, as we will see later.

Finally, the gain function g_ω calculated at a fixed frequency Ω is approximated by

$$g_\Omega(\mathcal{N}_j) \equiv \left(\frac{G_N}{v_g} \right) \frac{(\mathcal{N}_j - \mathcal{N}_t)}{1 + s|\mathcal{E}_j^\mp|^2}, \quad (3.20)$$

with $G_N \equiv \partial g_\omega(\mathcal{N})/\partial \mathcal{N}|_\Omega$ the differential gain (in rate), $v_g \equiv c/n_g$ the group velocity, \mathcal{N}_t the carrier number at transparency, and s the gain suppression parameter.

Dimensionless model

In this section, we summarize the equations governing the electric field and carrier dynamics which constitute our model. For the sake of clarity and numerical purposes, we rescale the dynamical variables through the following definitions

$$\begin{aligned} \tilde{A}_j &\equiv \sqrt{\frac{2\varepsilon_0 V n_e n_g}{\hbar \omega} \frac{\kappa \Gamma^{sol}}{\gamma_e \mathcal{N}_t}} e^{iq_j l} \tilde{\mathcal{E}}_j^\mp, \\ D_j &\equiv \frac{\mathcal{N}_j}{\mathcal{N}_t} - 1, \end{aligned}$$

where Γ^{sol} is defined in Eq. (3.19) and κ the total cavity decay rate [Eq. (2.20)]. In the case of free-running operation, the scaled $\tilde{\mathcal{A}}_j$ represent the outgoing fields calculated at the outer laser facets. By inserting the definition of the S_{ij} coefficients and expressing the electric fields in terms of the scaled ones, Eqs. (3.11a) and (3.11b) reduces to

$$[1 - r^2 e^{i4q_0 l} - r^2 (1 - e^{i4q_0 l}) e^{i2q_{1,2} L}] \tilde{\mathcal{A}}_{1,2} = r' (1 - r^2) e^{i2q_0 l} e^{i2q_{2,1} L} \tilde{\mathcal{A}}_{2,1}. \quad (3.21)$$

On the other hand, the equations for the normalized carrier densities read

$$\dot{D}_j(t) = \gamma_e \left[\mu_j - D_j - \mathcal{G}_j \frac{\Gamma_j}{\Gamma^{sol}} |\mathcal{A}_j(t)|^2 \right], \quad (3.22)$$

where the gain function can be expressed as

$$\mathcal{G}_j \equiv \frac{a D_j}{1 + \varepsilon |\mathcal{A}_j|^2}. \quad (3.23)$$

Finally, we have introduced the following dimensionless parameters

$$\mu_j \equiv \frac{I_j}{e \mathcal{N}_t \gamma_e} - 1, \quad \varepsilon \equiv \frac{\gamma_e \mathcal{N}_t}{\kappa \Gamma^{sol}} \frac{\hbar \omega}{2 \varepsilon_0 V n_e n_g} s, \quad a \equiv \frac{\mathcal{N}_t G_N}{\kappa}.$$

The injection current is also commonly measured with respect to the solitary laser threshold $p_j \equiv I_j / I_{th}^{sol}$, thus resulting $\mu_j = p_j (1 + 1/a) - 1$.

Equation (3.21) for the optical fields, together with Eq. (3.22) for the carrier densities constitute our model although still in the Fourier domain.

Slowly-varying approximation

In absence of coupling $\xi = 0$, the propagation constants of the free-running lasers obey the usual round-trip condition that leads to

$$\theta^{sol} \equiv 2Lq^{sol} = 2\pi M - i \ln \frac{1}{r^2}, \quad (3.24)$$

with $j = 1, 2$ and M being an integer number labeling the longitudinal modes. The second term in the right hand of the equation accounts for the losses through the mirrors as in Eq. (2.20). We consider that each solitary SCL emits close to a single-longitudinal mode M_0 of the cold Fabry-Perot cavity. The free-running emission frequencies are $\Omega_{1,2} = \pi M_0 c / (L_{1,2} n_{e,1,2}) + \kappa_{1,2} \alpha_{1,2}$ [See Eq. (2.27)] that nearly coincide because both lasers are device-identical. Small dissimilarities may be induced by the temperature dependence of the index of refraction $n_{e,1,2}$ and the cavity length $L_{1,2}$.

Thus, frequency tuning ($\Omega_1 = \Omega_2$) can be achieved by carefully controlling the temperature of these devices.

Since the fields are nearly monochromatic we expand the dispersion relations Eq. (3.4) around $\Omega_{1,2}$ keeping only dominant terms,

$$q_j(\omega, \mathcal{N}_j) - q_j(\Omega_j, \mathcal{N}^{sol}) = \frac{\partial q_j}{\partial \omega} \Big|_{\Omega_j, \mathcal{N}^{sol}} (\omega - \Omega_j) + \frac{\partial q_j}{\partial \mathcal{N}} \Big|_{\Omega_j, \mathcal{N}^{sol}} (\mathcal{N}_j - \mathcal{N}^{sol}) + \dots, \quad (3.25)$$

\mathcal{N}^{sol} being the carrier inversion at the solitary threshold. After some algebra, we obtain

$$\Delta\theta_{1,2} \approx i \tau_{in} \left[\pm i \Delta - iu - \frac{1}{2}(1 - i\alpha)\kappa (\mathcal{G}_{1,2} - 1) \right]. \quad (3.26)$$

We define the relative detuning as $\Delta \equiv (\Omega_1 - \Omega_2)/2$, the symmetric reference frame $\Omega \equiv (\Omega_1 + \Omega_2)/2$, the group velocity $v_g^{-1} = \partial_\omega (\omega n_\omega / c) |_\Omega$, the internal round-trip time $\tau_{in} = 2Lv_g^{-1}$, the linewidth enhancement factor $\alpha = \partial_N \text{Re } q |_\Omega / \partial_N \text{Im } q |_\Omega$, the material gain $\mathcal{G}_{1,2}$ [Eq. (3.23)], and the cavity decay rate κ [Eq. (2.20)]. We have also neglected gain differences between the two lasers due to their slightly different positions with respect to the gain curve when a detuning is present.

In the following section, we calculate the spectrum of monochromatic solutions by using the simplified dispersion relations $\Delta\theta(u)$ that stem from the slowly-varying amplitude (SVA) approximation. The SVA will be also useful in Sec. 3.6 when accessing to the dynamical properties of the system.

3.3 Monochromatic Steady-State Solutions

A basic step in any dynamical system consists in the calculation of its steady state solutions. A rapid way to understand that two distant mutually coupled lasers is a situation significantly different to the one of a C³ laser is by plotting the transmittivity function for the compound system. We consider that an electric field E_ω^{in} is injected at the $z = -(l + L)$ facet, and we compute the output field E_ω^{out} at the external $z = l + L$ facet [Fig. 3.1]. The total field transmittivity $\mathcal{T} = E_\omega^{out} / E_\omega^{in}$ gives insight into the resonances. In the case of a single cold Fabry-Perot cavity (filled by a linear medium with refractive index n_e), the transmittivity is an Airy function [135] with peaks at the position of the solitary longitudinal modes [Fig. 3.2(a)]. In a C³ laser, there is a noticeable rearrangement of the longitudinal modes, which depends not only on the ratio L_e/L , but also on the laser gains [Fig. 3.2(b)], which provides the tunability properties. Finally for two distant mutually coupled lasers, the solitary resonances are modulated by the extremely small free-spectral range of the inter-laser

cavity [Fig. 3.2(c)]. This simple analysis provides some intuition into the resonances of mutually coupled lasers, although it is incomplete because it considers each single laser as passive and linear. Then, under lasing conditions, it is necessary to include the dispersion relations of the active medium as well as the nonlinear interaction with the carrier variables.

In our case, a monochromatic steady-state solution is characterized by a common operating frequency ω of the electric field in the whole system, fixed carrier inversions $D_{1,2}$ and intensities $P_{1,2} \equiv |\tilde{\mathcal{A}}_{1,2}|^2$ in each laser, and a relative phase among the oscillation of the two electric fields. We look for solutions with a pinned relative phase, $\phi \equiv \arg(\tilde{\mathcal{A}}_2/\tilde{\mathcal{A}}_1)$, and proportional field amplitudes, $\rho \equiv |\tilde{\mathcal{A}}_2|/|\tilde{\mathcal{A}}_1|$. Hence, these results generalize the concept of injection locking in the case of unidirectional injection in SCL [20, 21]. In Sec. 3.2, we derived equations that govern the evolution of the optical variables. In the case of continuous-wave (cw) operation, we are interested in finding solutions where the field does not vanish in both lasers simultaneously. Thus, the system of Eqs. (3.11a) and (3.11b) should verify the condition of vanishing determinant, providing the following round-trip condition for the com-

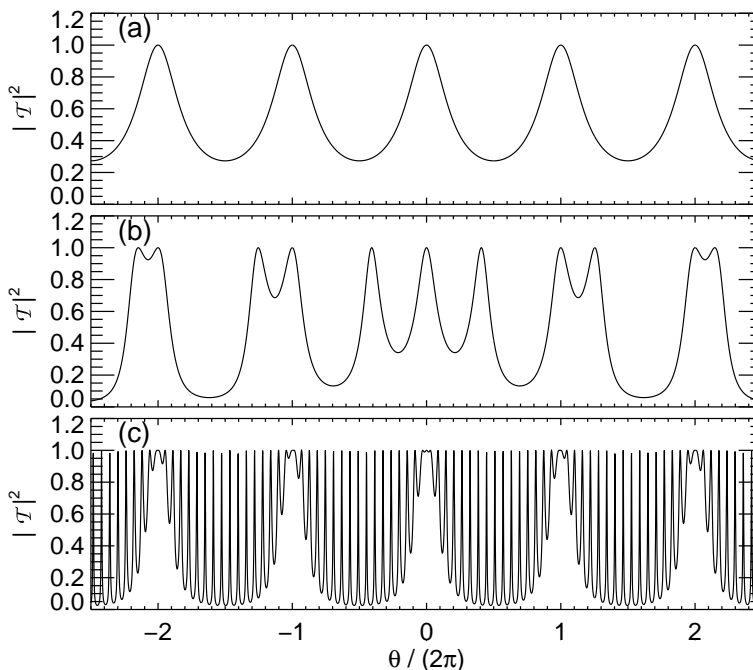


Figure 3.2. Frequency dependence of the transmittivity: a single Fabry-Perot cavity (a), a C^3 laser with $L_e = 0.42L$ (b), two distant coupled lasers with $L_e = 55L$ (c). In the three cases, the Fabry-Perot cavities are filled by a passive medium with index of refraction $n_e = 3.5$, mirror reflectivity $r = 0.56$, and lossless coupling cavity $\xi^2 = 1$.

pound system:

$$\left[1 - r' S_{11} e^{i2q_1 L}\right] \left[1 - r' S_{22} e^{i2q_2 L}\right] = r'^2 S_{12} S_{21} e^{i2q_1 L} e^{i2q_2 L}. \quad (3.27)$$

Using Eqs. (3.9a), (3.9b) and (3.24), the above equation can be expressed as

$$\left[\frac{e^{-i\theta_1}}{r' S_{11}} - 1\right] \left[\frac{e^{-i\theta_2}}{r' S_{11}} - 1\right] = \left(\frac{S_{12}}{S_{11}}\right)^2. \quad (3.28)$$

We focus on a typical situation where both SCL are pumped above the solitary threshold, then acting as active elements. In this case, the complex Eq. (3.28) can be regarded as two real equations involving three unknowns, i.e., the common operation frequency and the gain in both lasers. This relationship is a parametric equation for the gain and frequency in laser 2 as function of the gain in laser 1. However, the problem is not yet closed because the rates of stimulated emission in each laser are not independent, but they impose a ratio for their respective intensities ρ . From Eq. (3.22) and when the gain suppression is neglected, we arrive at

$$\rho^2 \approx \frac{(a\mu_2 - \mathcal{G}_2) \Gamma_1}{(a\mu_1 - \mathcal{G}_1) \Gamma_2}. \quad (3.29)$$

The ratio between intensities is in turn determined by either Eq. (3.11a) or (3.11b), which also provides the relative phase between the fields

$$\rho e^{i\phi} = \frac{S_{11}}{S_{12}} e^{i(\theta_1 - \theta_2)} \left[\frac{e^{-i\theta_1}}{r' S_{11}} - 1\right]. \quad (3.30)$$

In principle, Eqs. (3.28)–(3.30) represent a set of five real nonlinear equations that should provide the five unknowns defining a monochromatic solution, i.e., ω , \mathcal{G}_1 , \mathcal{G}_2 , ρ , and ϕ . Thereafter, the steady-state intensity in each laser can be simply determined from

$$P_j = \frac{(a\mu_j - \mathcal{G}_j)}{\mathcal{G}_j \left(\varepsilon + a \frac{\Gamma_j}{\Gamma_{sol}}\right)}. \quad (3.31)$$

3.3.1 Symmetric operation

As a starting point, we consider the case of symmetric operation, where the lasers share a common propagation constant $\theta^{sym} \equiv \theta_1 = \theta_2$. In this situation, θ^{sym} can be obtained from Eq. (3.28),

$$\theta_{\pm}^{sym} = 2\pi M - i \ln \frac{1}{r'^2} - i \ln \left[\frac{1 \pm r' e^{i2q_0 l}}{1 \pm \frac{e^{i2q_0 l}}{r'}} \right]. \quad (3.32)$$

The two first terms on the right hand of Eq. (3.32) are the contribution of the solitary laser, while the last term that behaves as $o(\xi)$ is the modification in propagation

constant due to the mutual coupling. We obtain two families of symmetric solutions, which depend on an integer number M labeling the longitudinal modes, and on a sign (\pm). Upon replacing the expression of θ^{sym} in Eq. (3.30) we find that these solutions are restricted to $\rho = 1$, $\mathcal{G}_1 = \mathcal{G}_2 = \mathcal{G}^{sym}$, and $\phi = 0, \pi$. Thus, a solution with sign $+$ ($-$) corresponds to a relative phase $\phi = 0$ ($\phi = \pi$), describing in-phase (anti-phase) dynamics among the two fields. The only solutions compatible with these peculiar characteristics are restricted to $\Delta = 0$ and $\mu_1 = \mu_2 \equiv \mu$.

The operating frequency and associated gain of the symmetric solutions can be easily calculated when taking the SVA around the solitary emission frequency Ω . Introducing Eq. (3.26) in Eq. (3.32), we arrive at

$$\eta^{sym} = \frac{\tau}{\tau_{in}} [\alpha \ln |z_{\pm}| + \arg z_{\pm}], \quad (3.33a)$$

$$\mathcal{G}^{sym} = 1 + \frac{2}{\kappa\tau_{in}} \ln |z_{\pm}|, \quad (3.33b)$$

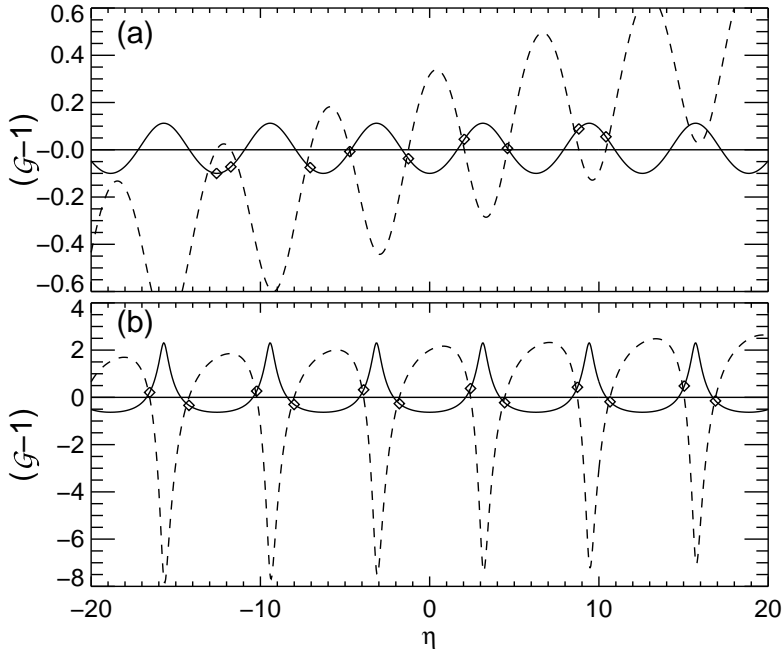


Figure 3.3. Frequency ($\eta = (\omega - \Omega)\tau$) dependence of the gain [Eq. (3.33b)] of symmetric solutions ($+$ sign, $\phi = 0$) in solid lines. Dashed lines represent the Eq. (3.33a) and the diamonds its zeros. Parameters: $r = 0.56$, $n_g = 4$, $L = 300\mu\text{m}$, $\alpha = 3.5$, $\tau = 0.5\text{ns}$, $\varphi_0 = 0$, $\xi = 0.05$ in panel (a), and $\xi = 0.45$ in panel (b).

with $\eta^{sym} \equiv (\omega^{sym} - \Omega)\tau$ and

$$z_{\pm} \equiv \frac{1 \pm r' \hat{\xi} e^{i\eta^{sym}}}{1 \pm \frac{\hat{\xi}}{r'} e^{i\eta^{sym}}}. \quad (3.34)$$

Once the eigenfrequency η is obtained by solving the nonlinear equation (3.33a) the associated gain can be calculated from Eq. (3.33b). It can be shown that by expanding the logarithmic and complex argument functions to first order in the parameter ξ , we obtain simpler equations for the eigenfrequency, which read

$$\eta^{sym} = \mp C \sin(\eta^{sym} + \arctan \alpha + \varphi_0), \quad (3.35a)$$

$$\mathcal{G}^{sym} = 1 \mp \frac{2\kappa_c}{\kappa} \cos(\eta^{sym} + \varphi_0), \quad (3.35b)$$

with $\varphi_0 = \Omega\tau \bmod 2\pi$, the coupling rate $\kappa_c \equiv (1 - r^2)\xi/(r\tau_{in})$, and the effective coupling parameter $C \equiv \kappa_c\tau\sqrt{1 + \alpha^2}$. In Sec. 3.4, we will show that the solutions of Eq. (3.35a) are nothing but the symmetric steady-state solutions of the phenomenological model [128]. These symmetric steady states resemble a laser with conventional optical feedback with round-trip time τ when $\phi = 0$, see Eq. (2.32).

Next, we proceed comparing the symmetric monochromatic solutions obtained from the complete model [Eq. (3.33a)] and those from the phenomenological model [Eq. (3.35a)], as function of the coupling parameter ξ . For the case of very weak coupling, $\xi = 0.05$, the frequency dependence of the gain function [Eq. (3.33b)] is sinusoidal as shown in Fig. 3.3(a). We note that this dependence agrees with that predicted by Eq. (3.35b). For larger couplings, however, $\xi = 0.45$, the gain function Eq. (3.33b) displays rapid variations with periodicity $1/\tau$ as can be clearly seen in Fig. 3.3(b).

The stationary solutions for several coupling conditions are shown in Fig. 3.4, ($\xi = 0.05$, $\kappa_c = 7.6 \text{ ns}^{-1}$) in panels (a,b), ($\xi = 0.3$, $\kappa_c = 45.9 \text{ ns}^{-1}$) in panels (c,d), and ($\xi = 0.5$, $\kappa_c = 76.6 \text{ ns}^{-1}$) in panels (e,f). Panels (a,c,e) correspond to the solutions of Eq. (3.33a), while panels (b,d,f) correspond to the solutions to first order in ξ , Eq. (3.35a). The symmetric steady-state solutions with $\phi = 0$ (π) are represented by diamonds (stars) in a $(\mathcal{G} - 1)$ vs η diagram. For the case of weak coupling, the monochromatic solutions are arranged in an ellipse, centered around $\eta = 0$ which corresponds to the free-running frequency. The solutions with large negative η have larger loss reduction and consequently larger associated optical power. For weak coupling we observe a very good agreement between both predictions. Typically, there is good agreement when the coupling coefficient is in the range of $\xi \sim 0 - 0.1$ (i.e., when less than 1% of the optical power is transmitted by the inter-laser cavity). When the coupling increases, we start to observe some differences at about $\xi = 0.3$ (9% power transmission) [Fig. 3.4(c,d)]. The solutions are still arranged in an ellipse

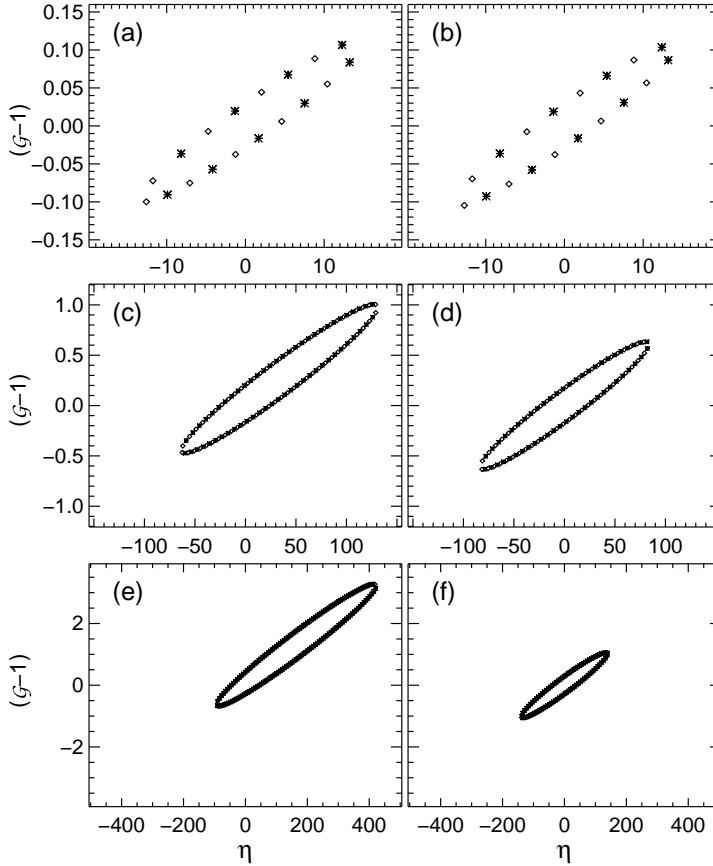


Figure 3.4. Symmetric steady state monochromatic solutions, (a,c,e) solutions of Eq. (3.33a) and (b,d,f) solutions of the $o(\xi)$ equation (3.35a), $\eta = (\omega - \Omega)\tau$. The meaning of the symbols are (\diamond) $\phi = 0$ and ($*$) $\phi = \pi$. The same parameters than Fig. 3.3 except $\xi = 0.05$ in (a,b), $\xi = 0.3$ in (c,d), and $\xi = 0.5$ in (e,f).

but many points prefer positive η and the loss reduction of the largest negative η is lower. This last effect is a result of a nonsinusoidal dependence of the gain as a function of η .

3.3.2 General case

The general analysis of the monochromatic solutions of two mutually coupled SCL is quite involved and, in this work, we restrict ourselves to give some guidelines for their calculation. As already commented, we have to solve a system of five real nonlinear equations, Eqs. (3.28)–(3.30). To overcome this problem, we take advantage of the symmetric solutions calculated in the preceding section. We look for solutions

around each of the symmetric steady state by defining $\theta_j = \theta^{sym} + \delta\theta_j$. The only assumption on $\delta\theta_j$ is that it admits a SVA form as in Eq. (3.26),

$$\delta\theta_j = -i \frac{\tau_{in}}{\tau} \left[i\delta\eta + \frac{1}{2}(1 - i\alpha)\kappa\tau \delta\mathcal{G}_j \right], \quad (3.36)$$

with $\delta\eta = \eta - \eta^{sym}$, and $\delta\mathcal{G}_j = \mathcal{G}_j - \mathcal{G}^{sym}$. With these new variables Eq. (3.28) reduces to

$$[(1 \pm T)e^{-i\delta\theta_1} - 1] [(1 \pm T)e^{-i\delta\theta_2} - 1] = T^2, \quad (3.37)$$

with $T = S_{12}/S_{11}$ and the signs \pm stand for $\phi = 0, \pi$ symmetric solutions.

In a general case, the gain in both lasers may differ, and Eq. (3.37) can be regarded as a parametric equation for $\delta\mathcal{G}_2$ and $\delta\eta$, once a value of $\delta\mathcal{G}_1$ is provided [11]. From Eq. (3.37), the gain variation in laser 2 reads

$$\delta\mathcal{G}_2 = \frac{-2}{\kappa\tau(1 - i\alpha)} \left[i\delta\eta + \frac{\tau}{\tau_{in}} \ln \left\{ \frac{1}{(1 \pm T)} \left(1 + \frac{T^2}{(1 \pm T)e^{-i\delta\theta_1} - 1} \right) \right\} \right]. \quad (3.38)$$

The frequency shift $\delta\eta$ can be obtained imposing $\text{Im} \delta\mathcal{G}_2 = 0$ in the above equation. The final result is that, under cw operation, the laser gains must follow a curve in

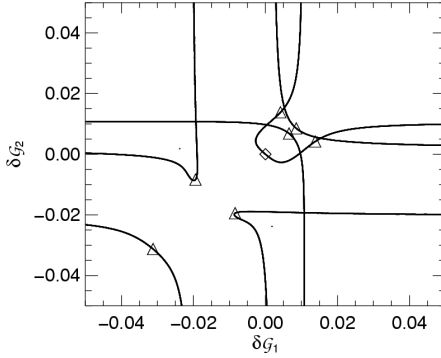


Figure 3.5. $\delta\mathcal{G}_1 - \delta\mathcal{G}_2$ diagram around an in-phase symmetric solution (\diamond). The curves are solutions of the Eq. (3.37). The asymmetric solutions are represented with the symbol (\triangle). Parameters: $r = 0.56$, $\alpha = 3.5$, $n_g = 4$, $\tau = 0.5\text{ns}$, $L = 300\mu\text{m}$, $\varphi_0 = 0$, $\xi = 0.01$, $p = 1.50$, $\mathcal{N}_t = 1.5 \cdot 10^8$, $G_N = 3 \cdot 10^{-6}\text{ns}^{-1}$.

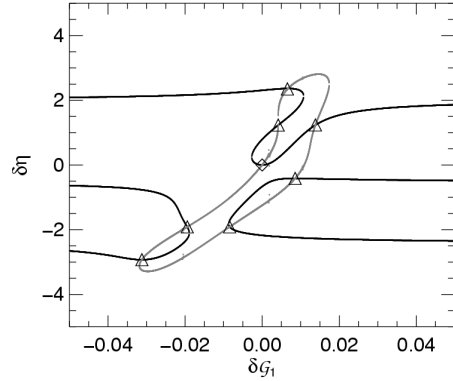
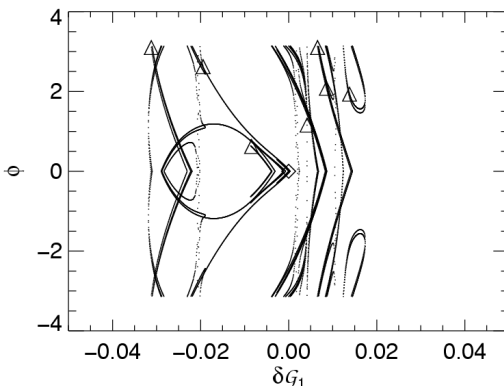


Figure 3.6. Frequency shift $\delta\eta$ with respect to an in-phase symmetric solution (\diamond). The black curves are obtained from Eq. (3.37), while gray ones from Eq. (3.39). Crossings between these two curves are steady-state monochromatic solutions. The asymmetric solutions are represented with the symbol (\triangle). The same parameters as in Fig. 3.5.

Figure 3.7. Relative phase among the oscillation of the two electric fields obtained from Eq. (3.30). Only asymmetric solutions (\triangle) with $\phi > 0$ are represented. The same parameters as in Fig. 3.5.



the $(\delta\mathcal{G}_1 - \delta\mathcal{G}_2)$ plane, as the one shown in Fig. 3.5. The point $(0, 0)$ in this diagram represents a symmetric steady-state solution studied in the preceding section. The existence of asymmetric solutions still depends on a condition associated to the roots of an additional equation. Upon combining Eqs. (3.29) and (3.30), we arrive at

$$\frac{(a\mu_2 - \mathcal{G}^{sym} - \delta\mathcal{G}_2) \Gamma_1}{(a\mu_1 - \mathcal{G}^{sym} - \delta\mathcal{G}_1) \Gamma_2} - e^{-2\text{Im}(\delta\theta_1 - \delta\theta_2)} \left| \frac{(1 \pm T)e^{-i\delta\theta_1} - 1}{T} \right|^2 = 0. \quad (3.39)$$

For each point of the parametric curves $\delta\mathcal{G}_1 - \delta\mathcal{G}_2$ in Fig. 3.5, the above equation is solved for $\delta\eta$. In Fig. 3.6, we represent these solutions in a $\delta\eta$ vs $\delta\mathcal{G}_1$ plot. The black lines represent the solutions obtained from Eq. (3.38), while gray lines are those from Eq. (3.39). A generic monochromatic solution appears when both lines cross. Around the in-phase symmetric solution (\diamond) there are seven crossings marked with the symbol (\triangle) and therefore seven asymmetric solutions appear. In contrast to the symmetric solutions, the number of asymmetric solutions depends on the injection current. Hence, we have demonstrated that, even though the high degree of symmetry in the system, solutions in which both lasers evolve asymmetrically are indeed possible. An approach similar to the one presented in this section should be applied in the case that the lasers operate under asymmetric conditions (detuning or different current injection). Finally, the relative phase ϕ associated to each of these solutions can be recovered from Eq. (3.30), and it is plotted in Fig. 3.7. As a final remark, we have to comment that in the case of a perfectly symmetric system, pairs of asymmetric solutions appear restoring the initial symmetry of the system; i.e., both $(\eta, \mathcal{G}_1, \mathcal{G}_2, \rho, \phi)$ and $(\eta, \mathcal{G}_2, \mathcal{G}_1, \rho^{-1}, -\phi)$ must be solutions. Due to the symmetry $\rho \rightarrow \rho^{-1}$ and $\phi \rightarrow -\phi$; each crossing in Fig. 3.6 represents two asymmetric solutions.

3.4 Phenomenological Rate Equation Model

The Fourier domain representation has been useful for the description of the monochromatic solutions, however, time-domain equations are required in order to access to the dynamical properties of the system.

We define the slowly-varying envelope (SVE) of the electric fields A_j , around the symmetric reference frame $\Omega \equiv (\Omega_1 + \Omega_2)/2$, by means

$$\mathcal{A}_j(t) \equiv A_j(t)e^{-i\Omega t}. \quad (3.40)$$

Since the fields are nearly monochromatic around Ω , $\tilde{\mathcal{A}}_j(\omega) = \tilde{A}_j(\omega - \Omega)$ is non-vanishing for $u \equiv \omega - \Omega \approx 0$.

Upon introducing the following relationships

$$\omega = \Omega + u, \quad e^{i2q_j L} = \frac{1}{r^2} e^{i\Delta\theta_j},$$

into Eq. (3.21), we arrive at

$$\left[1 - r^2 \hat{\xi}^2 e^{i2u\tau} - \left(1 - \hat{\xi}^2 e^{i2u\tau} \right) e^{i\Delta\theta_{1,2}} \right] \tilde{A}_{1,2} = \frac{(1-r^2)}{r} \hat{\xi} e^{iu\tau} e^{i\Delta\theta_{2,1}} \tilde{A}_{2,1}, \quad (3.41)$$

$\hat{\xi} \equiv \xi e^{i\Omega\tau}$ being the effective coupling parameter. Eq. (3.41) represents our optical model for the Fourier components of the electric fields in both lasers. In order to obtain a dynamical model, we have to take the inverse Fourier transform of the above equations. For the sake of clarity, we leave this point until Sec. 3.7. We instead express all the terms in Eq. (3.41) to lower order in the coupling parameter ξ . The left-hand side of these equations simply reduces to $[1 - e^{i\Delta\theta_j}] \approx i\Delta\theta_j$, while for the right-hand term it is necessary to assume that the change in propagation constants behaves as $o(\xi)$ in order to approximate $\hat{\xi} e^{i\Delta\theta_j} \approx \hat{\xi}$. Upon introducing Eq. (3.26), the lower order equations read

$$-iu\tilde{A}_{1,2} = \mp i\Delta\tilde{A}_{1,2} + \frac{1}{2}(1-i\alpha)\kappa[\mathcal{G}_{1,2} - 1]\tilde{A}_{1,2} + \frac{(1-r^2)}{r}\hat{\xi}e^{iu\tau}\tilde{A}_{2,1}. \quad (3.42)$$

By Fourier transforming Eq. (3.42) to time domain, $-iu \rightarrow d_t$, we arrive to the dynamical system

$$d_t A_{1,2}(t) = \mp i\Delta A_{1,2} + \frac{1}{2}(1-i\alpha)\kappa[\mathcal{G}_{1,2} - 1]A_{1,2} + \hat{\kappa}_c A_{2,1}(t - \tau), \quad (3.43a)$$

$$d_t D_{1,2}(t) = \gamma_e [\mu_{1,2} - D_{1,2} - \mathcal{G}_{1,2}|A_{1,2}|^2], \quad (3.43b)$$

$$\mathcal{G}_{1,2} = \frac{aD_{1,2}}{1 + \varepsilon|A_{1,2}|^2}, \quad (3.43c)$$

with $\hat{\kappa}_c \equiv (1 - r^2)\xi \exp(i\Omega\tau)/(r\tau_{in})$. In this procedure we have assumed nearly stationary carrier densities, being a justified approximation in SCL since they evolve at slower time scales than the optical fields.

Analyzing Eq. (3.43a), we find that the terms $\hat{\kappa}_c A_{2,1}(t - \tau)$ describe the mutual delayed injection from one laser to its counterpart. We remark that neither feedback reflections involving terms like $A(t - 2\tau)$ nor higher-order corrections of the propagation constants due to the mutual injection are accounted at this level of approximation. Eq. (3.43a) for the SVA of the complex electric fields together with Eq. (3.43b) for the normalized carrier numbers within each laser constitute the *phenomenological* rate-equation model previously studied [127, 128].

A final point deserves some discussion. In Eq. (3.43b), the correction prefactors Γ_j/Γ^{sol} acting onto the stimulated recombination terms have been neglected since, in the case of very weak coupling, the modification in propagation constants is small enough to allow the substitution of the longitudinal standing wave by the solitary one. We will return to the discussion of these terms in Sec. 3.7.

Threshold analysis

We define the threshold of the compound system as the circumstance where the “off” state, $A_1 = A_2 = 0$ and $D_{1,2} = \mu_{1,2}$, loses the stability. Upon linearizing the field perturbations $\delta A_{1,2}(t)$ and neglecting fluctuations in the stimulated recombination terms of the carrier equations, we obtain

$$\dot{\delta A}_{1,2}(t) = \frac{1}{2}(1 - i\alpha_{1,2})\kappa[a\mu_{1,2} - 1]\delta A_{1,2}(t) + \hat{\kappa}_c\delta A_{2,1}(t - \tau), \quad (3.44)$$

where $\Delta = 0$ has been taken for simplicity. For this linear system we propose an exponential-like solution,

$$\begin{bmatrix} \delta A_1(t) \\ \delta A_2(t) \end{bmatrix} = \begin{bmatrix} \delta A_{1\lambda} \\ \delta A_{2\lambda} \end{bmatrix} e^{\lambda\kappa t/2}, \quad (3.45)$$

that leads to

$$\begin{bmatrix} (1 - i\alpha_1)x_1 - \lambda & Ke^{-\lambda\theta} \\ Ke^{-\lambda\theta} & (1 - i\alpha_2)x_2 - \lambda \end{bmatrix} \begin{bmatrix} \delta A_{1\lambda} \\ \delta A_{2\lambda} \end{bmatrix} = \begin{bmatrix} 0 \\ 0 \end{bmatrix}, \quad (3.46)$$

with $\theta \equiv \kappa\tau/2$, $K \equiv 2\hat{\kappa}_c/\kappa$, and $x_{1,2} \equiv (a\mu_{1,2} - 1)$. The complex eigenvalue $\lambda = \sigma - i\Omega$ describes the growth rate (σ) and oscillation frequency (Ω) of the perturbation. Imposing the secular condition of vanishing determinant as well as the threshold condition $\sigma = 0$,

$$\{x_1 + i(\Omega - \alpha_1 x_1)\} \{x_2 + i(\Omega - \alpha_2 x_2)\} = K^2 e^{i2\theta\Omega}. \quad (3.47)$$

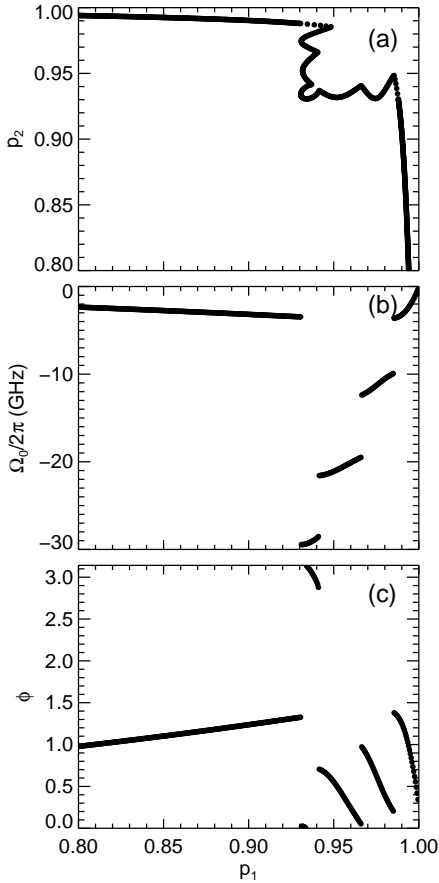


Figure 3.8. Threshold analysis: (a) threshold curve, (b) emission frequency at threshold, and (c) relative phase. Parameters: $\alpha = 4$, $\kappa_c = 22.5 \text{ ns}^{-1}$, $\varphi_0 = 0$, $N_t = 1.5 \cdot 10^8$, $\kappa = 197.7 \text{ ns}^{-1}$, $G_N = 3 \cdot 10^{-6} \text{ ns}^{-1}$. The coupling time is $\tau = 0.1 \text{ ns}$.

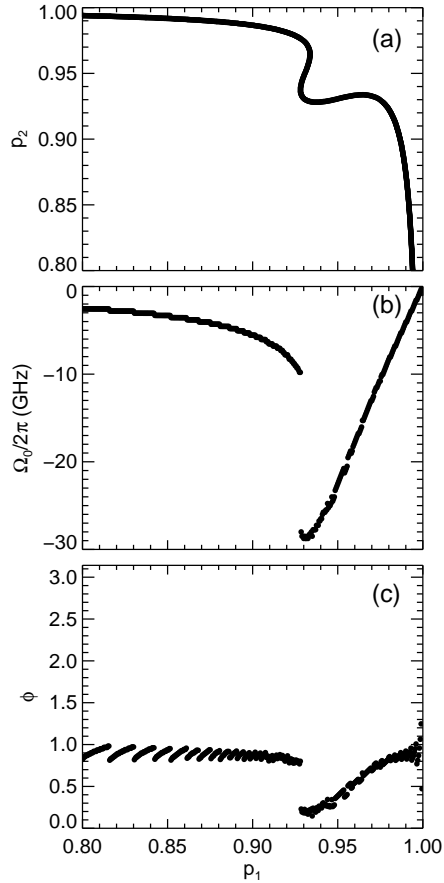


Figure 3.9. Threshold analysis: (a) threshold curve, (b) emission frequency at threshold, and (c) relative phase. The same than in 3.8 but for long cavity regime. The coupling time is $\tau = 4 \text{ ns}$. $p_{1,2}$ is the current normalized to the solitary threshold.

The above equation can be understood as follows: for a given current in laser 1 (fixed x_1), the threshold condition takes place for a particular current in laser 2, x_2 , and oscillation frequency Ω that have to be determined from (3.47). We numerically solve this transcendent complex equation for short and long external cavities, assuming that carrier inversions in both lasers are not so different to consider that $\alpha_1 \approx \alpha_2 \equiv \alpha$.

In Figs. 3.8(a) and 3.9(a), we represent in a p_1 versus p_2 diagram the locus of the

threshold condition. We recall that p_j is the injection current normalized to the solitary threshold for the laser j . Below this threshold line the perturbations decay. Due to symmetry considerations, the curve is symmetric around the diagonal $p_1 = p_2$. When the injection is preferentially applied to one of the lasers, we observe that the threshold reaches an approximately constant value. This value is slightly below the solitary threshold current due to the passive optical feedback from the other laser, as commented in the next section. The total current required to achieve threshold conditions is minimum in a neighborhood of the symmetric $p_1 = p_2$ point, where the curve displays a bite. In the short cavity regime, this bite contains a substructure, sensible to the coupling phase $\Omega\tau$, owing to hopping among different compound-cavity modes. The frequency splitting corresponds to $\sim 1/\tau$ as can be appreciated in Fig. 3.8(b). For larger coupling times, the modes appear very close one to the other in frequency and consequently the threshold curve is smooth.

In order to better understand these threshold properties, specially the appearance of a bite in the threshold curve, we define a relative phase among the fluctuation of the two fields (at threshold) by means $\phi \equiv \arg(\delta A_{2\lambda}/\delta A_{1\lambda})$ in Eq. (3.46). In Figs. 3.8(c) and 3.9(c) we represent the dependence of the relative phase upon variation of the current in laser 1. Near the bite region, the relative phase experience large variations, and thus suggesting that it is originated from the constructive interference among the two optical fields. When the fluctuations in both lasers interference constructively, there exists a cooperative effect that produces the largest threshold reduction.

It is worth mentioning that the above analysis has been corroborated by close-to-threshold numerical simulation of the phenomenological model. Both the threshold locus, emission frequency, and relative phase obtained from numerical simulations are in excellent agreement with our analytical theory.

Reduction to the active-passive case

From the above analysis, we have seen that the threshold condition takes place by a proper combination of the injection currents $\mu_{1,2}$ in both lasers. The case in which the laser 2 is pumped below transparency, thus acting as a passive element, deserves of a more detailed discussion. Owing to the low injection in laser 2, the carrier variations induced by stimulated recombination are rather small, and thus we consider approximately constant absorption and index of refraction. Although it is not essential for our purposes, we take lower linewidth enhancement factor in laser 2 because the lower carrier density ($\alpha_2 \ll \alpha_1$). In this situation, the dynamical system

(3.43a)–(3.43c) can be effectively replaced by

$$d_t A_1(t) = \frac{1}{2}(1 - i\alpha_1)\kappa[\mathcal{G}_1 - 1]A_1(t) + \hat{\kappa}_c F(t), \quad (3.48a)$$

$$d_t F(t) = -\Gamma(1 - i\alpha_2)F(t) + \hat{\kappa}_c A_1(t - 2\tau), \quad (3.48b)$$

with $F(t) \equiv E_2(t - \tau)$, and $\Gamma \equiv (1 - a\mu_2)\kappa/2 > 0$ the absorption parameter. Note that Eq. (3.48b) is linear and can be formally solved using integration in the complex plane. Introducing the expression obtained for $F(t)$ into (3.48a), we arrive at

$$d_t A_1(t) = \frac{1}{2}(1 - i\alpha_1)\kappa[\mathcal{G}_1 - 1]A_1(t) - \hat{\kappa}_c^2 \int_{-\infty}^{t-2\tau} dt' A_1(t') e^{-\Gamma(1-i\alpha_2)(t-t'-2\tau)}. \quad (3.49)$$

From Eq. (3.49) turns out that the active-passive configuration is equivalent to a laser with frequency-filtered optical feedback [136]. The filter is Lorentzian with a FWHM Γ around a central frequency $-\alpha_2\Gamma$. More important, the feedback received from the second laser is a linear process of that emitted by laser 1, although partially filtered due to the interferometric effect in the second Fabry-Perot cavity.

We notice that this approximation is doubtful when laser 2 is pumped above transparency, and inconsistent when both lasers act as active elements –similar pumping–. In contrast to the active-passive case, the active-active configuration can be regarded as a system with *nonlinear feedback*: the effective reflectivity (amplitude and phase) of each laser cavity is a function of the frequency, and more important, the carrier inversion which is nonlinearly coupled to the field dynamics. This last situation is analyzed in the following sections by the help of numerical simulations.

3.5 Experimental Setup

Figure 3.10 depicts a schematic of the experimental setup. Two device-identical SCL are mutually coupled with a delay via their coherent optical fields. The distance between the lasers is 1.20 m determining the coupling delay by the propagation of the light between the lasers. Hence, the coupling delay amounts to $\tau=4$ ns. The lasers are two uncoated Hitachi HLP1400 Fabry-Perot SCL produced from the same wafer in order to achieve the highest possible degree of symmetry in the system. The temperature of each laser is stabilized to better than 0.01 K, and selected such that the free-running frequencies of the two lasers match with an accuracy better than 1 GHz. The polarizer guarantees a coherent coupling between the lasers via the dominant transverse electric (TE) mode of the optical field. A neutral density filter placed between the two SCL is used to control the coupling strength. In the present experiment, a

symbol	meaning	value	dimension
α	linewidth enhancement factor	4.0	—
κ	cavity loss rate	243	ns ⁻¹
G_N	differential gain	3.2×10^{-6}	ns ⁻¹
κ_c	coupling rate	~ 20	ns ⁻¹
τ	one-way delay time	~ 5	ns
γ_e	carrier decay rate	1.66	ns ⁻¹
\mathcal{N}_t	carrier number at transparency	1.5×10^8	—
ε	(scaled) gain saturation	10^{-1}	—
β_{sp}	spontaneous emission factor	10^{-5}	—

Table 3.1. Symbols, their meaning and numerical values. The dimensionless gain constant $a \approx 2$ and the threshold current is $I_{th}^{sol} \approx 60$ mA.

maximum amount of 5% of the output power of each laser is injected into its counterpart. In the detection branch of the setup, two photoreceivers with a bandwidth of 6 GHz are used to detect the intensity dynamics of both lasers simultaneously via their rear facet emission. The signal of the photoreceivers is analyzed by a fast digital oscilloscope of 3 GHz analog bandwidth recording the temporal waveforms, and an electrical spectrum analyzer recording the corresponding rf-spectra. In addition, the optical spectra of the lasers are monitored with a grating spectrometer with a resolution of 0.1 nm. Finally, the time averaged output power of both lasers is detected by two p-i-n photodiodes.

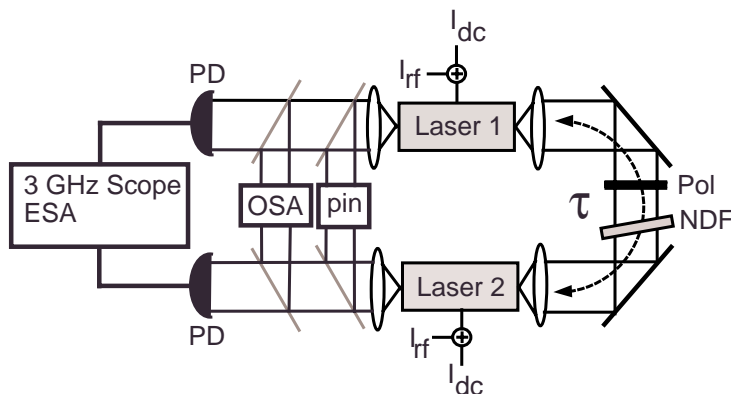


Figure 3.10. Scheme of the experimental setup of two mutually coupled SCL. Polarizer (Pol), neutral density filter (NDF), optical spectrum analyzer (OSA), electrical spectrum analyzer (ESA).

3.6 Results Under Symmetric Operation

We concentrate the analysis to the case of two identical SCL emitting at the same free-running frequency and under equal current injection. In this case, the equations are perfectly symmetric under the interchange of the two lasers, except for noise terms. We center our discussion on the instabilities that arise under weak to moderate coupling conditions (maximum 5% of the light emitted is injected) and long external cavities ($\tau \sim 4$ ns). We find that under these operating conditions the external delay time, being much larger than any other typical time scale of the laser, plays an important role in the determination of the dynamics of the global system.

In order to gain insight into the dynamical properties of the system we perform numerical simulations of Eqs. (3.43a)–(3.43c). We explore the behavior of the system under variations of two easily accessible and controllable parameters, namely, the amount of mutual coupling κ_c and the symmetric injection current $\mu \equiv \mu_1 = \mu_2$.

3.6.1 Coupling-induced instabilities

Operating close to the solitary threshold current and in the absence of coupling, the two lasers emit fully uncorrelated light due to the presence of spontaneous fluctuations. When the coupling is activated, the two laser intensities display a behavior that consists in irregular pulsations with small correlation among them. Hence, we find numerically and experimentally a first threshold, associated to a coupling rate κ_c^I , for the onset of the coupling-induced instabilities. Increasing further the coupling strength, the instabilities reshape into similar pulsations but now accompanied with sudden power dropouts followed by a gradual recovering of the optical power. The interesting fact is that pulsations in both lasers start to display a good correlation beyond a second threshold for the coupling strength κ_c^{II} .

In order to better characterize this twofold threshold behavior, we introduce the crosscorrelation function [137, 138] $S(\Delta t)$ between two variables $x_1(t)$ and $x_2(t)$ (with mean values being subtracted)

$$S(\Delta t) = \frac{\langle x_1(t) x_2(t + \Delta t) \rangle}{\sqrt{\langle x_1^2(t) \rangle \langle x_2^2(t) \rangle}}, \quad (3.50)$$

where $\langle \cdot \rangle$ means time average. We look for the time shift Δt where the maximum correlation of the laser intensities is achieved, $\max\{S(\Delta t)\}$, referred as correlation degree. In Fig. 3.11, we observe that the correlation degree increases very rapidly from zero when the coupling strength is increased until it reaches a saturation value. Above this critical value, the correlation degree does not significantly increase displaying a plateau with a relatively high maximum around $\sim 90\%$. The value κ_{max} corresponds to the maximum coupling accessible to the experiment that roughly

corresponds to $\kappa_{max} = 25 \text{ ns}^{-1}$. It is worth remarking the excellent agreement between theoretical and experimental dependencies, demonstrating that large degree of synchronization is possible for a wide range of coupling strengths. High correlation degree (80–90%) persists for injection currents up to twice the solitary threshold current. The correlation degrades when the injection is increased beyond this value. In the latter, the lasers spectra display a broad band of frequencies $\sim 100 \text{ GHz}$, indicating that they operate within a fully-developed coherence-collapse regime [25].

This large correlation between the intensities motivate us to further investigate the transition towards synchronization of the coupling-induced instabilities. A typical example of the dynamics beyond the second coupling threshold ($\kappa_c > \kappa_c^{II}$) is depicted in Fig. 3.12. In numerical simulations we took a coupling strength of $\kappa = 20 \text{ ns}^{-1}$ in correspondence with experimental conditions. We represent the time traces of the two lasers LD_1 (a), and LD_2 (b) when the lasers operate at the solitary threshold current. In a first place, we analyze the low-frequency component of these signals, by applying a low-pass filter with 250 MHz bandwidth. The resulting signals are plotted using grey lines in the figure 3.12, whereas the unfiltered signals are in black lines. We find that the low frequency dynamics, being much slower than any other time scale of the system, consist in power dropouts that display a good correlation between the two lasers. Power dropouts appear for a wide range of coupling rates and injection currents close to the solitary laser threshold. For higher injection currents, power dropouts disappear and the system enters in a coherence collapsed (CC) regime [See Fig. 3.12(c)-(d)]. These numerical results are corroborated by experimental observations shown in Fig. 3.13. The mean time between dropouts, the dependence with the injection current as well as the transition to the CC regime are well reproduced by the delayed rate equation model.

3.6.2 Synchronization properties

Looking at nanosecond time scales, we observe that the optical power is organized in a sequence of fast irregular pulses [Fig. 3.14]. This fast pulsing behavior appears to be well correlated only if one series is shifted by a time τ with respect to the other, that precisely corresponds to the coupling time. The solution where the dynamics of the lasers occurs with a time shift is referred as leader-laggard operation [128] or achronal synchronization [133]. These interesting findings motivate us to investigate the mechanisms that originates this asymmetric role of the two subsystems. In particular it has been already commented that the governing equations are symmetric under the interchange of the lasers owing to the symmetric operating conditions. Thus, one might immediately ask why the solution where both lasers evolve at the same time (isochronal solution) does not appear?

In order to clarify this point, we have performed deterministic numerical sim-

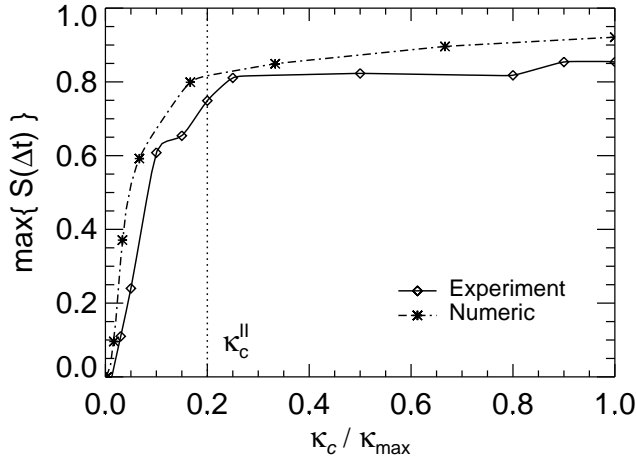


Figure 3.11. Numerical and experimental comparison of the maximum degree of correlation achieved as function of the coupling strength, $\kappa_{max} \approx 25 \text{ ns}^{-1}$, when $p_1 = p_2 = 1$.

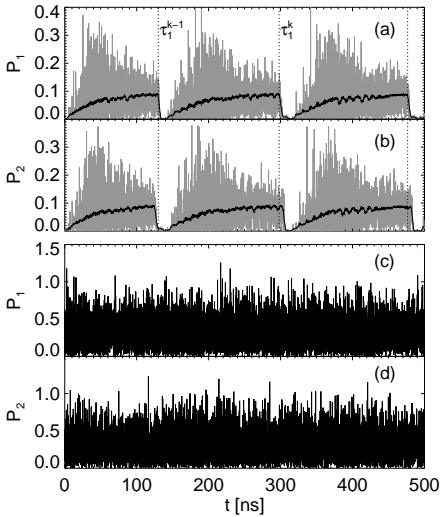


Figure 3.12. Numerical time traces of the laser intensities for injection current (a,b) $p = 1.0$ and (c,d) $p = 1.17$. The coupling rate is $\kappa = 20 \text{ ns}^{-1}$ and $\tau = 5 \text{ ns}$ while the rest of parameters are given in Table 3.1.

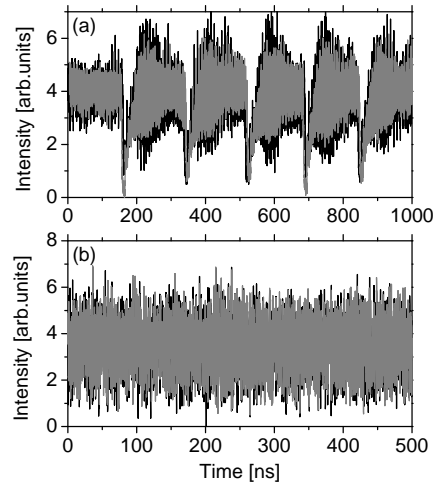


Figure 3.13. Experimental time traces of the intensity emitted by the two lasers when running under resonant conditions. The injection current is (a) $p = 0.98$ and (b) $p = 1.17$.

ulations to decide whether the achronal state appears as a general property of the system or is just a consequence of the noise sources included in the equations. In Fig. 3.15, we artificially switch-off the noise and we prepare both lasers to start from identical initial conditions. We can appreciate that the system evolves in an isochronal state ($P_1(t) = P_2(t)$, $D_1(t) = D_2(t)$) until a small perturbation is externally introduced at $t = 200$ ns (the intensity of the laser 1 is modified by 1%). In spite of the absence of noise for $t > 200$ ns, this small perturbation is able to destabilize the isochronal state and the system evolves towards the achronal solution. The achronal solution is characterized by highly correlated time series of the two lasers. However, the high correlation is only achieved when shifting one time series with respect to the other in time by $+\tau$ or $-\tau$. Since the system remains in the achronal solution for any arbitrarily long integration times, we conjecture that the isochronal solution is intrinsically unstable in our system, and that the spontaneous emission prevents such state to appear. The dynamical properties of the achronal state are particularly interesting because they are originated from the bidirectional coupling of perfectly symmetry subsystems. Next, we make use of two standard techniques, namely, crosscorrelation functions and generalized return plots, in order to better characterize this solution.

A standard tool for detecting the dependencies between the two laser intensities is the crosscorrelation function $S(\Delta t)$ defined in Eq. (3.50). The crosscorrelation function, obtained from numerical simulations depicted in Fig. 3.16(a), displays dominant peaks at odd resonances of the coupling time, that is to say, $\Delta t = \pm n\tau$ with $n = 1, 3, 5, \dots$. Consequently, successive peaks are separated by a distance 2τ that corresponds to a roundtrip in the interlaser cavity. The correlation at the successive peaks decay when the index n increases, while it is almost vanishing near the zero shift $\Delta t = 0$, indicating that fluctuations occurring at the same time are in-

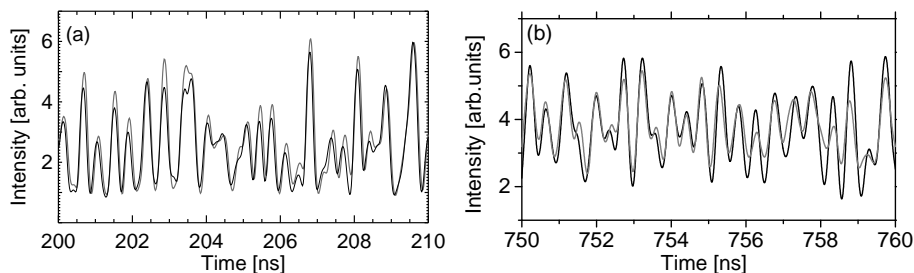


Figure 3.14. Subnanosecond synchronized dynamics between two consecutive power dropouts using time shifted series: (a) numerical and (b) experimental results. The same conditions as in Fig. 3.12, and $p_1 = p_2 = 1.0$. The numerical traces have been filtered at 3 GHz bandwidth corresponding to the analog bandwidth of the experimental detection setup.

dependent. The experimental correlation function, obtained from the time traces in Fig. 3.13, is shown in Fig. 3.16(b). The function display the same features as described above: the peaks are located at the correct positions with similar values of the correlation degree as those obtained numerically. The crosscorrelation function obtained for larger injection currents, display similar features. However, two last points are worth mentioning. First, the background in the correlation function, that is a direct consequence of the low frequency dynamics, is more pronounced in the experiments owing to the partial filtering during the detection. Second, the crosscorrelation function may present small asymmetries around the zero shift.

The quality of the synchronization can be also studied by plotting the intensity of the Laser 2 versus the intensity of the Laser 1. We remark that we need to time-shift one signal, otherwise one only gets a cloud of points without any tendency. Then a squeezed cloud of points arranged around a 45 degree straight line is obtained. As it can be seen in Fig. 3.17, experimental and numerical tendencies are in agreement. The dispersion of the points with respect to the linear tendency is linked to the maximum degree of correlation achieved. We note that the maximum degree of correlation increases from zero very rapidly when the coupling strength is increased until it reaches a saturation value as discussed in Fig. 3.11.

A final point enters in the discussion of the achronal solution that occurs for currents within LFF regime. After a careful analysis of Fig. 3.12(a)-(b) and Fig 3.13, we observe that power dropout events do not occur simultaneously in both lasers but with a small time lag τ_0 . The instant in which the laser 1 drops, indicated by vertical dashed lines in Fig. 3.12(a)-(b). In order to better quantify this phenomenon, we define a time lag by means $\tau_0 \equiv \tau_1^k - \tau_2^k$, where τ_j^k stands for the k -th drop of the laser j . The means to decide whether a power dropout occurs is by looking at those events

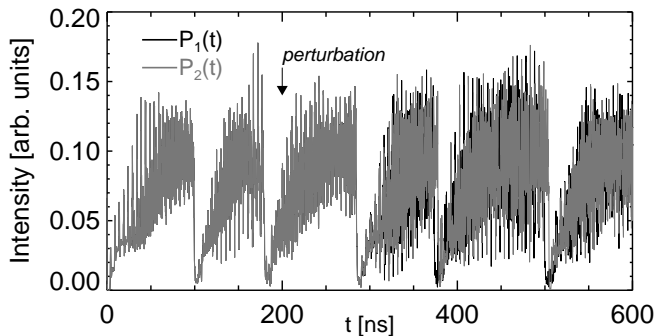


Figure 3.15. Deterministic numerical simulation describing the destabilization of the isochronal solution due to an external perturbation applied at $t = 200$ ns. The intensity time traces are filtered at 2 GHz. Traces of laser 2 are plotted in grey color.

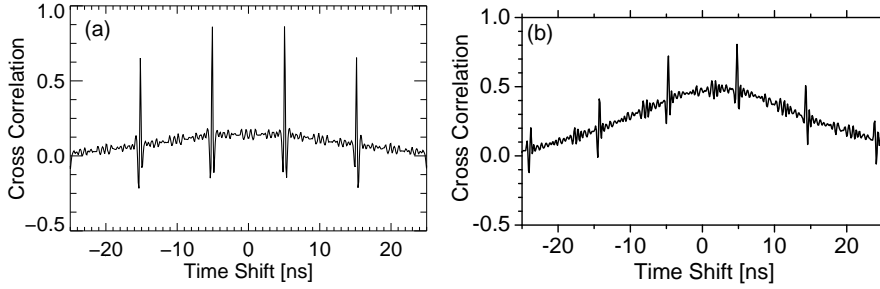


Figure 3.16. Crosscorrelation function (a) numerical (b) experimental. Same conditions than in Fig. 3.14 and $p_1 = p_2 = 1$.

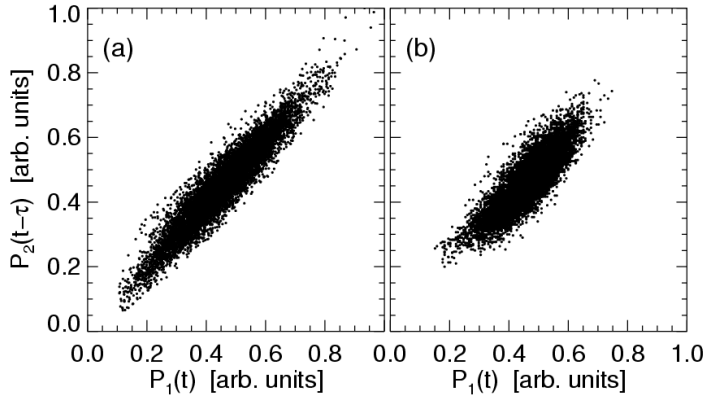
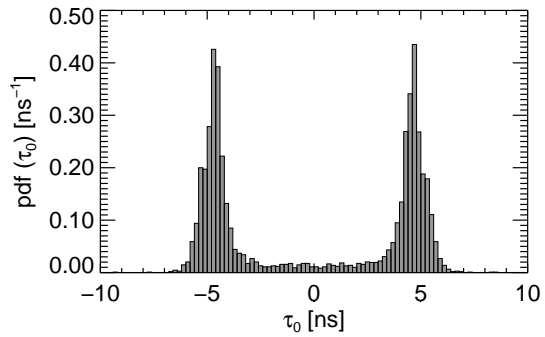


Figure 3.17. Numerical (a) and experimental (b) generalized return plots for the same conditions than in Fig. 3.16. The maximum correlation degree is about 85% in both cases.

Figure 3.18. Probability distribution function of the time shift between power dropouts of the two lasers τ_0 , for $\tau = 5$ ns, $\kappa = 20$ ns⁻¹, and $p = 1.01$.



where the laser intensity crosses a predefined threshold. Hence, positive (negative) τ_0 means that the laser 2 drops first (later) than laser 1. By analyzing a large number of power dropouts ($\sim 10^4$ events), for different cavity length regimes, we find that the time lag is randomly distributed presenting marked peaks at times $\tau_0 \approx \pm\tau$ and strong decay for larger times. The probability of synchronized dropouts, i.e., $\tau_0 = 0$ is rare although non-vanishing. The probability distribution function of τ_0 , shown in Fig. 3.18, is symmetric around $\tau_0 = 0$ indicating that the number of dropout events where the laser 1 and laser 2 drops first is in average equal. This fact suggests that the statistical quantities, computed over long time intervals of an achronal state, are invariant under the interchange of the lasers.

3.6.3 Phase dynamics

Numerical simulations allow us to easily track the optical phases of the electric fields. The coherent nature of the coupling [139, 140] becomes evident when expressing Eq. (3.43a) into equations for the power and optical phase through, $A_{1,2}(t) = \sqrt{P_{1,2}(t)} e^{i\varphi_{1,2}(t)}$, that finally leads to

$$d_t P_{1,2}(t) = \kappa [\mathcal{G}_{1,2}(t) - 1] P_{1,2}(t) + \kappa_c \sqrt{P_{1,2}(t) P_{2,1}(t - \tau)} \cos(\eta_{1,2}(t) + \varphi_0) + 4\beta_{sp}\kappa(D_{1,2} + 1) + F_{P_{1,2}}(t), \quad (3.51a)$$

$$d_t \varphi_{1,2}(t) = -\frac{\alpha}{2} \kappa [\mathcal{G}_{1,2}(t) - 1] + \kappa_c \sqrt{\frac{P_{2,1}(t - \tau)}{P_{1,2}(t)}} \times \sin(\eta_{1,2}(t) + \varphi_0) + F_{\varphi_{1,2}}(t), \quad (3.51b)$$

where $\eta_{1,2}(t) = \varphi_{2,1}(t - \tau) - \varphi_{1,2}(t)$ are the injection phases from laser 1 to laser 2 and vice versa, whereas $\varphi_0 \equiv \Omega_0\tau \pmod{2\pi}$ stands for the global phase accrued

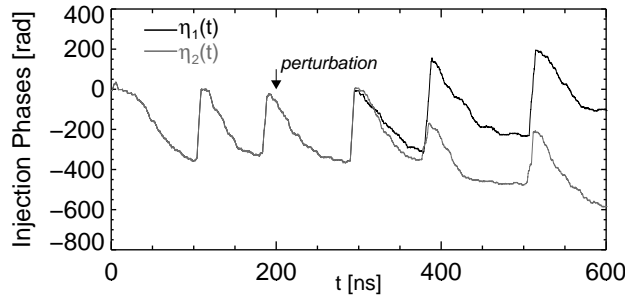


Figure 3.19. Dynamics of the injection phases. Deterministic numerical simulation describing the destabilization of the isochronal solution due to an external perturbation applied at $t = 200$ ns.

within the inter-laser cavity. Finally $F_{P_{1,2}}(t)$ and $F_{\varphi_{1,2}}(t)$ represent two independent real Langevin noise sources.

In the limit of very small coupling conditions, where the intensity can be assumed constant, Eqs. (3.51a)-(3.51b) can be reduced to a Kuramoto model [141] for the injection optical phases $\eta_{1,2}(t) = \varphi_{2,1}(t - \tau) - \varphi_{1,2}(t)$. The injection phases represent, in the case of bidirectional coupling, the phase difference between the oscillator and the force (which actually corresponds to the other oscillator a time τ before). An analysis beyond the constant intensity approximation has been performed using a two-time scale analysis [126, 142]. From these analysis, it turns out that phase dynamics is, at last stage, the underlying mechanism in many coupling induced instabilities.

In a first place, we analyze the transition from isochronal to achronal behavior discussed in the numerical simulations of Fig. 3.15. For such a transition, we follow the evolution of the injection phases $\eta_{1,2}(t)$. During the initial transient and before the perturbation is applied, the two injection phases evolve in an identical fashion, $\eta_1(t) = \eta_2(t)$, as can be appreciated in Fig. 3.19. The injection phases move close to the modes of the compound system [131], displaying a chaotic itinerancy towards smaller frequencies very similar to the one in SCL with optical feedback [63]. Power dropout events produce a rapid increase of the injection phases and, consequently shifting the emission to higher frequencies. When the perturbation is applied, this

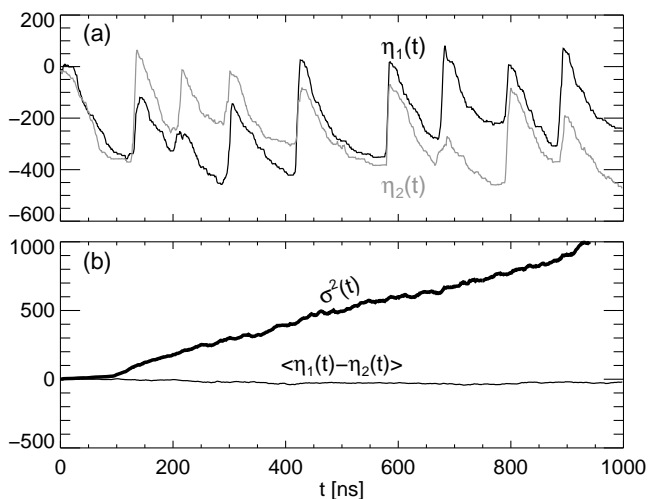


Figure 3.20. Statistical properties of the injection phases under symmetric operation of the lasers, $I_1 = I_2 = I_{th}^{sol}$.

operating mode turns out to be unstable because the two injection phases start to separate. The existence of a phase instability associated to the isochronal solution was claimed in [133] when analyzing its stability. Fig. 3.20(a) shows the phase dynamics at later times, both injection phases continue displaying the chaotic itinerancy behavior, however the separation between the injection phases has an intrinsic dynamics.

A synchronous state requires that the phase difference (between the oscillator and the force) remains bounded. It is worth recalling that when a SCL (laser 1) is unidirectionally injected by a monochromatic field at a given frequency (from a laser 2), a necessary condition for locking requires operation of the laser 1 at the frequency imposed by laser 2. In the case of bidirectional injection the opposite situation must also occur, thus requiring of a monochromatic solution (at frequency Ω) along the compound system. However, we do not observe locking to fixed values of $\eta_{1,2}$ for this dynamical operation conditions. Instead, we appreciate from the figure 3.20(a) that $\eta_{1,2}$ are bounded because their difference $\Delta\eta(t) \equiv \eta_1(t) - \eta_2(t)$ visits positive and negative values.

Looking to the time interval during two power dropouts, $\Delta\eta(t)$ is approximately constant whereas large excursions occur at the power dropout events. In order to better characterize the striking dynamics of $\Delta\eta(t)$, we have investigated its statistical properties. The monochromatic solutions verify that the relative injection phase is $\Delta\eta(t) = 2\pi n$ with $n = 0, \pm 1, \dots$. Under dynamical conditions the system moves along these solutions. Fig 3.20(b) shows in solid lines the average $\langle \Delta\eta(t) \rangle$, and the variance $\sigma^2(t) \equiv \langle \Delta\eta^2(t) \rangle - \langle \Delta\eta(t) \rangle^2$ in bold lines of the relative injection phase. Note that $\langle \cdot \rangle$ now means average over different noise realizations and initial conditions. We observe how $\Delta\eta(t)$ diffuses with the same probability in both directions. This fact is corroborated by a zero mean $\langle \Delta\eta(t) \rangle$ and variance that increases linearly with time $\sigma^2(t) \sim t$. It is worth noting that the same statistical properties are fulfilled by a Wiener process (random walk) [143].

Although the experimental operating conditions corresponds to injection-locking, also demonstrated analytically by the existence of phase-locked monochromatic solutions, our results indicate that phase-locked operation is unstable.

3.7 Dynamical Model Including Higher-Order Terms

From the steady state analysis, we have found that the applicability of the phenomenological model is restricted to weak coupling strength, typically less than 5% of coupler transmission. In this section, our aim is to explore the dynamical consequences when the coupling exceeds, although by a small amount, the limit of validity of the phenomenological model.

It is worth recalling that our problem now consists in Fourier transforming to time domain Eq. (3.41). Following the guidelines given in [58], we proceed introducing the auxiliary variables

$$\tilde{R}_{1,2}(u) \equiv \frac{[1 - e^{i\Delta\theta_{1,2}}]}{\tau_{in}} \tilde{A}_{1,2}(u), \quad (3.52)$$

which represent the variation in propagation constants with respect to the free-running laser. Upon introducing these expressions into Eq. (3.41), we obtain

$$\begin{aligned} \tilde{R}_{1,2}(u) &= \hat{\kappa}_c e^{iu\tau} \tilde{A}_{2,1}(u) - \hat{\kappa}_f e^{i2u\tau} \tilde{A}_{1,2}(u) + \\ &\quad \hat{\xi}^2 e^{i2u\tau} \tilde{R}_{1,2}(u) - \hat{\sigma} e^{iu\tau} \tilde{R}_{2,1}(u), \end{aligned} \quad (3.53)$$

where we have defined the effective injection rate $\hat{\kappa}_c = (1 - r^2)\hat{\xi}/(r\tau_{in})$, the effective feedback rate $\hat{\kappa}_f = (1 - r^2)\hat{\xi}^2/\tau_{in}$ and $\hat{\sigma} = (1 - r^2)\hat{\xi}/r$. Equation (3.53) can be straightforwardly transformed from Fourier to time domain obtaining

$$\begin{aligned} R_{1,2}(t) &= \hat{\kappa}_c A_{2,1}(t - \tau) - \hat{\kappa}_f A_{1,2}(t - 2\tau) + \\ &\quad \hat{\xi}^2 R_{1,2}(t - 2\tau) - \hat{\sigma} R_{2,1}(t - \tau). \end{aligned} \quad (3.54)$$

The above equation provides the value of the variables $R_{1,2}(t)$ as function of the past history of the system. The first term in the right-hand of Eq. (3.54) describes the delayed injection from one laser to its counterpart, while the second term accounts for passive reflections at the external facet of the other laser. The last two terms, involving electric fields with arbitrary large delays, describe the modification in propagation constants due to multiple reflections within the inter-laser cavity.

On the other hand, we need to specify which is the temporal evolution of the electric fields in terms of the $R_{1,2}$ variables. The Eq. (3.52) can be transformed to time domain resulting

$$R_{1,2}(t) = \frac{1}{\tau_{in}} \left[A_{1,2}(t) - e^{\tau_{in}[\mp i\Delta + \frac{1}{2}(1-i\alpha)\kappa(\mathcal{G}_{1,2} - 1)]} A_{1,2}(t - \tau_{in}) \right]. \quad (3.55)$$

The above equation, in finite differences, can be approximated by a differential equation in the limit of $\tau_{in} \rightarrow 0$.

$$R_{1,2}(t) \approx d_t A_{1,2}(t) \pm i\Delta A_{1,2}(t) - \frac{1}{2}(1 - i\alpha)\kappa[\mathcal{G}_{1,2}(t) - 1]A_{1,2}(t). \quad (3.56)$$

As a final step, we need to reconsider the longitudinal confinement integrals Γ_j [Eq. (3.16)] in order to fully determine the evolution of the carrier variables. We express Eq. (3.17) in terms of the variation in propagation constants $\Delta\theta_j$

$$\Gamma_j = \frac{1}{r^2} e^{-\text{Im} \Delta\theta_j} \left[2r' \text{sinc}(\text{Re} \Delta\theta_j) + \frac{r^2(1 + e^{\text{Im} \Delta\theta_j}) - (1 + e^{-\text{Im} \Delta\theta_j})}{\ln(r^2) + \text{Im} \Delta\theta_j} \right]. \quad (3.57)$$

We expand Eq. (3.57) to first order in variations

$$\Gamma_j = \Gamma^{\text{sol}} [1 - \lambda \text{Im} \Delta\theta_j + \dots] \approx \Gamma^{\text{sol}} e^{-\lambda \text{Im} \Delta\theta_j}, \quad (3.58)$$

with Γ^{sol} given in Eq. (3.19) and

$$\lambda = 1 + \frac{1 + r^2}{2(1 - r^2)} + \frac{1}{\ln r^2}. \quad (3.59)$$

These integral terms depend, to lower order, on the imaginary part of the propagation constants or the gain. Since the gain in both lasers may differ, there is no way to rescale these terms into the definition of the field amplitudes. However, it is possible to replace these approximate expressions in the stimulated recombination of the carrier equations.

In summary, our model for two bidirectionally coupled lasers taking into account higher order corrective terms reads

$$d_t A_{1,2}(t) = \mp i \Delta A_{1,2}(t) + \frac{1}{2} (1 - i\alpha) \kappa [\mathcal{G}_j(t) - 1] A_{1,2}(t) + R_{1,2}(t), \quad (3.60a)$$

$$R_{1,2}(t) = \hat{\kappa}_c A_{2,1}(t - \tau) - \hat{\kappa}_f A_{1,2}(t - 2\tau) + \hat{\xi}^2 R_{1,2}(t - 2\tau) - \hat{\sigma} R_{2,1}(t - \tau), \quad (3.60b)$$

$$\dot{D}_j(t) = \gamma_e \left[\mu_j - D_j - \mathcal{G}_j e^{-\lambda \frac{\text{Im} \Delta\theta_j}{2} \kappa [\mathcal{G}_j(t) - 1]} |A_j|^2 \right], \quad (3.60c)$$

$$\mathcal{G}_j = \frac{a D_j}{1 + \varepsilon |A_j|^2}. \quad (3.60d)$$

We use Eqs. (3.60a) and (3.60c) to update the electric fields and carrier variables, while Eq. (3.60b) describes the interaction among the lasers. We finally remark that the phenomenological model can be recovered by approximating $R_{1,2}(t) \approx \hat{\kappa}_c A_{2,1}(t - \tau)$ in Eq. (3.60a).

Comparison

We perform numerical simulations of the complete model, Eqs. (3.60a)–(3.60d), and the phenomenological model, Eqs. (3.43a)–(3.43b), for different values of the coupling strength, ξ . We focus the discussion on the instabilities that arise under weak to moderate coupling conditions and long external cavities. We assume that both lasers are equally pumped, their currents slightly above the solitary threshold, and no detuning is present.

In Fig. 3.21, the coupling is very weak, only 0.25% of the light is transmitted ($\kappa_c = 7.6 \text{ ns}^{-1}$). We can observe how the laser intensities undergo irregular fast pulses (partially washed-out by the filtering), in sub-ns time scales, accompanied with sudden power dropouts followed by a gradual recovering of the optical power when looking to μs time scales. This low frequency dynamics displays a good correlation between the two time series. Zooming into Fig. 3.21, we can observe that actually power dropouts do not occur simultaneously but with a small lag time. Thus, the asymmetric role between the two lasers, obtained from the phenomenological model, is also captured by the more sophisticated description. It is worth noting, that for these very weak coupling conditions, the results obtained from the phenomenological model [Fig. 3.21(b)] are in good agreement with the complete model. Hence, this fact suggests that the existence of LFFs in bidirectionally coupled lasers is a consequence of the delayed mutual injection, although they could be eventually modi-

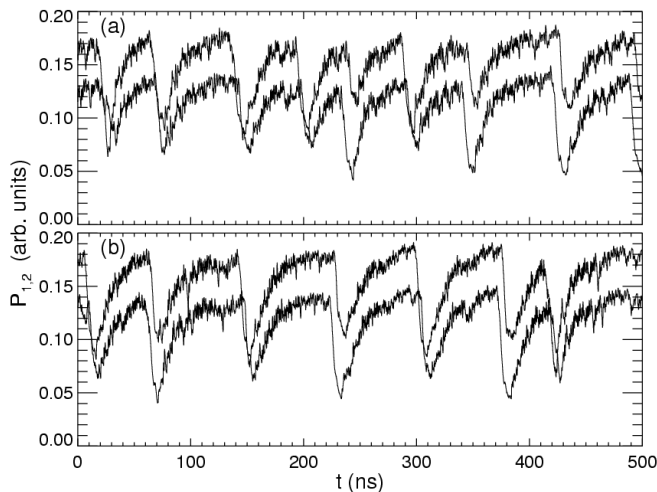


Figure 3.21. Numerical simulation of the complete dynamical model [Sec. 3.7] (a), and the phenomenological model (b), $P_{1,2} \equiv |A_{1,2}|^2$. The parameters are: $r = 0.56$, $L = 300 \mu\text{m}$, $\tau = 4 \text{ ns}$, $\varphi_0 = 0$, $n_g = 4$, $\gamma_e = 1 \text{ ns}^{-1}$, $\mathcal{N}_t = 1.5 \times 10^8$, $G_N = 3 \times 10^{-6} \text{ ns}^{-1}$, $\alpha = 3.5$, $\alpha^{int} = 20 \text{ cm}^{-1}$, $\varepsilon = 0.03$, $\xi = 0.05$, and $p = 1.01$. The time traces of the laser 2 have been vertically shifted for clarity.

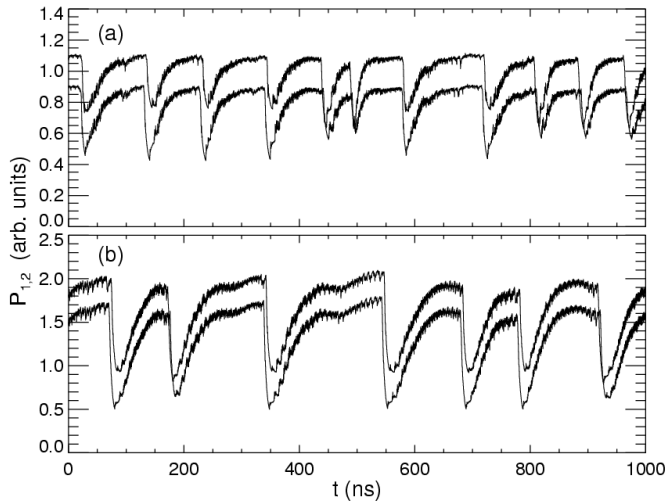


Figure 3.22. Numerical simulation of the complete dynamical model [Sec. 3.7] (a), and the phenomenological model (b), $P_{1,2} \equiv |A_{1,2}|^2$. The same parameters than Fig. 3.21 except for $\xi = 0.25$ and $p = 1.04$.

fied due to passive feedback reflections. In Fig. 3.22, the coupling has been enhanced to 6% of light transmission ($\kappa_c = 38.3\text{ns}^{-1}$). The larger the coupling, the larger the discrepancies between the two models due to the existence of higher-order corrective terms. For instance, power dropouts appear more frequently in the complete model, and we can also appreciate lower mean power levels. In conclusion, this last coupling value $\xi \approx 5\%$ sets the limit of validity of the phenomenological model.

3.8 Summary

In this chapter we have theoretically, numerically and experimentally investigated the dynamical properties of two mutually coupled semiconductor lasers. The setup under study is conceptually equivalent to the one of coupled-cavity lasers, except for the air-gap that is assumed to be much longer than the laser cavities. In addition, we have restricted ourselves to the case of device-identical lasers, being equally pumped and tuned to achieve equal free-running emission frequencies. Our description have focused on the propagation of the electric field through the compound system, complemented by adequate boundary conditions. We have demonstrated that, in the limit of weak coupling and single longitudinal mode operation, the model can be reduced to rate equations describing the evolution of the slowly-varying envelope of the electric field and the carrier number within each semiconductor laser. Taking the limit of small transmittivity of the coupler, the rate equation model can be reduced to

the so-called phenomenological model, that only accounts for mutual injection from one laser into its counterpart and viceversa.

From the steady-state analysis, we have found three different types of phase-locked solutions: in-phase and anti-phase symmetric solutions, and asymmetric solutions. In the symmetric solutions, the two lasers oscillate with a relative phase that is restricted to be either 0 (in-phase) or π (anti-phase). In spite of the high degree of symmetry in the system, asymmetric solutions, in which the gain in both lasers is different, have also been found. We have seen, from numerical simulations, that many of these solutions become unstable when the coupling is increased. The spectrum of symmetric monochromatic solutions was calculated for different values of the mutual coupling strength. From this steady-state analysis, we have inferred the limit of validity of the phenomenological model, that is restricted to typically less than 5% of coupler transmission.

We have presented a detailed numerical and experimental investigation of the dynamical instabilities that arise from the mutual optical coupling of two semiconductor lasers. We have found a twofold threshold scenario that appears upon variation of the coupling strength. We obtained a first threshold associated with the onset of coupling-induced instabilities and a second threshold indicating the transition to synchronization. These instabilities are quite generic features that appear in a wide range of coupling strengths and injection currents covering the LFF and CC regimes. In spite of the high degree of symmetry in the system, the solution selected corresponds to an achronal state, i.e., a time shift between the dynamics of the two laser intensities is present. Deterministic numerical simulations have been undertaken, demonstrating that the isochronal solution is unstable. We have demonstrated that the achronal solution persists even in the absence of the spontaneous emission, thus being an intrinsic feature of the dynamical system. Although the achronal solutions distinguish between the lasers, statistical quantities (probability distribution, cross-correlation, etc.) computed over long time intervals are invariant under the interchange of the lasers. From a crosscorrelation analysis, we have found synchronization with a time shift of the subnanosecond pulsation of the laser intensities. The generalized return plots present a linear tendency only when a signal is time shift as well. The maximum degree of synchronization is about 80-90%. As a final step, we have investigated the dynamical properties of the complete model, being able to incorporate the effects of higher-order corrective terms. For weak coupling, the phenomenological model yields correct results, but for higher couplings, passive feedback and multiple reflections produce a decrease in mean optical power and that power dropouts appear more frequently.

The study of mutually-coupled semiconductor lasers is important from the point of view of fundamental physics, dynamical systems theory, and also for their tech-

nological aspects. A thorough understanding of the synchronization properties is crucial for their potential implementation in, e.g., encoded communication systems.

Chapter 4

Conclusions to Part One

We have analyzed the dynamical properties of edge-emitting semiconductor lasers (SCL) with added degrees of freedom. We have considered the effect of delayed optical feedback and the mutual coupling of two twin semiconductor lasers. We tackled both problems looking for models that, including the minimal ingredients, describe the experimentally observed features. Experiments using distributed feedback lasers (DFB) allowed us to obtain an optimum match between experimental and theoretical conditions. Hence, the evolution of the longitudinal mode amplitude of the electric field has been described through delayed differential equations. It is worth recalling that the validity of these models is limited to single longitudinal mode operation of the lasers and weak coupling conditions. Multiple reflections are neglected, flat material gain spectrum and the same α -factor for all the compound-cavity solutions is considered, and the slowly varying approximation is used. A more detailed description of this class of systems, although out of the scope of the thesis, should consider the Maxwell Bloch semiconductor equations complemented with (delayed) boundary conditions. Proceeding in this way, semiconductor specific effects and multilongitudinal emission would be naturally accounted for. We note however the greater numerical complexity as well as the lack of intuition upon variations of parameters when comparing with the rate-equation descriptions.

In Chapter 2 we discussed the properties of SCL subject to delayed optical feedback. The generation of chaotic optical signals containing a broad frequency band is currently of large interest in optical chaos communication using laser-diode transmitters (OCCULT). We performed a statistical characterization of the power dropouts occurring in the low-frequency fluctuation (LFF) regime. Extensive numerical simulation of the Lang-Kobayashi (LK) model was carried out. In particular, we analyzed the statistical distribution of the time between subsequent power dropouts when varying the injection current. In spite of the apparent irregularity in the dynamics, the transition from stable operation to LFF has associated scaling laws that

seem to be independent of the number of longitudinal modes. For our theoretical description, based on the LK model, we bet for the existence of a deterministic crisis-induced intermittent process. The most outstanding results obtained from the LK model and experiments with DFB lasers include

1. Numerical and experimental evidence of the alternation between stable operation (in a high-gain external-cavity mode) and low frequency-frequency fluctuations (LFF). Importance of spontaneous emission noise for ejecting the system from the stable point.
2. Probability distribution functions of the time between power dropouts for distributed feedback lasers (DFB): Dead time interval for short times and exponential decay for longer times.
3. Scaling law $\langle T \rangle \sim (p/p_c - 1)^{-1}$ associated to the transition from stable operation to LFF.
4. Possibility of entraining power dropouts with a weak periodic modulation of current with adequate frequencies. This effect was theoretically predicted first [102] and experimentally corroborated later [103].

Chapter 3 generalized the previous studies of compound-cavity semiconductor lasers to two spatially-separated bidirectionally-coupled SCL. A detailed electromagnetic analysis revealed that, under weak coupling conditions, the system can be described as a mutual injection problem with delay. A detailed analysis of the monochromatic solutions showed the existence of phase-locked solutions, thus generalizing the concepts of unidirectional injection-locking. We numerically and experimentally observed the appearance of coupling-induced instabilities when increasing the coupling strength. Further increase of the coupling yields synchronization with high correlation degree of these instabilities. Experimental results are in agreement with the predictions of the simple bidirectional injection model (phenomenological model). The dynamics within the regime of synchronization was investigated in the case of symmetric operating conditions: no detuning between the lasers and identical injection current. We addressed the importance of the role of the time delay in mutual coupling. In spite of the large degree of symmetry in the system, the solution where the two twin SCL operate simultaneously (isochronal solution) appeared to be unstable and an achronal state is selected instead. Nevertheless, we found that statistical quantities, computed over long time intervals, are invariant under the interchange of the lasers. Finally, we inferred about the validity of the phenomenological model, by developing a model that include high-order terms in the coupling. From this simple analysis, we found that the coupling has to be weak ($< 5\%$ of transmission) in order to guaranty the validity of the phenomenological model. The summary of results in Chap. 3 is

1. Existence of phase-locked monochromatic solutions: in-phase, anti-phase and asymmetric solutions.
2. Twofold threshold behavior: i) Appearance of instabilities in the mutual coupling with delay of two twin semiconductor lasers, and ii) transition towards synchronization.
3. Large degree of synchronization between the laser intensities only when a signal is time shifted by the coupling time τ (achronal synchronization).
4. Validity of the phenomenological model restricted to sufficiently weak coupling.

Part II

Polarization and Transverse Mode Dynamics in Vertical-Cavity Surface-Emitting Lasers

Preface to the Second Part

In this second part we deal with vertical-cavity surface-emitting lasers (VCSELs). VCSELs have received great deal of attention during the last decades, specially for their potential implementation in optical communication systems. VCSELs present clear advantages over the conventional edge-emitting lasers (EELs), such as easy testing, single-longitudinal mode emission, integration in 2D arrays, narrow circular output beams, low threshold currents, etc. However, VCSEL's cavity lacks an effective mechanism to pin the polarization of the optical field. Consequently, light-polarization instabilities are often observed when the current is increased [30]. In addition, relatively large apertures are required in order to obtain substantial optical power, which lead to multitransverse mode behavior of the VCSEL [12, 35]. The understanding of the polarization and transverse modes is essential if one wants to manipulate and exploit these degrees of freedom in view of novel applications. This fact motivates the study, characterization and control of polarization and transverse dynamics.

This second part is structured in three chapters that are ordered according to the modeling complexity. In Chap. 5, we investigate the small-signal properties of VCSELs that operate in the fundamental transverse mode. We center the study on the anticorrelated fluctuations among the polarization components. We use a standard description of the polarization dynamics, the so-called Spin-Flip Model (SFM), whereas the spontaneous emission noise is treated within a semiclassical framework. In Chap. 6, we develop a spatiotemporal model for the large-signal dynamics of VCSELs which describes polarization and spatial effects by including a frequency-dependent susceptibility. This provides a natural generalization of the SFM to the realistic band structure of a quantum-well laser. In this case, we study the mechanisms that define the selection of transverse modes and the dynamics occurring under large-signal modulation of the current. We briefly discuss about the polarization mode selection mechanisms. In Chap. 7, we give evidence for the need of a spatiotemporal description of the large-signal dynamics in gain-guided VCSELs instead of modal expansion methods.

Chapter 5

Intensity and Polarization Noise in VCSELs

5.1 Introduction

Since¹ the development of a modern semiconductor technology, it has been possible to construct semiconductor structures in the nanometer scales (nanostructures) and reducing the laser size up to a single wavelength limit. Due to this constant reduction of scales, quantum effects in the confinement of electrons and light field have increased considerably. As a consequence, the laser light is not pure but contains random fluctuations that arise from spontaneous emission processes. A correct treatment requires the quantization of the electromagnetic fields and dipole amplitudes [60]. We instead consider that, under a sufficiently intense field, the deterministic field dynamics is well described by the classical Maxwell's equations [60, 144]. In any case, the semiconductor material has to be treated by using quantum mechanics. Within this semiclassical approach, the quantum fluctuations are modeled by means classical Langevin noise sources. The semiclassical approach has been extensively used in the literature [10]. Obviously, the strength of these fluctuations can only be determined from quantum mechanical requirements as commented in Appendix C.

One widely extended means of characterizing noisy signals is the relative intensity noise (RIN) or power spectra of the amplitude fluctuations. In multimode devices, the total noise is distributed among the different modes according to a quantity referred as mode partition noise (MPN) [145]. MPN gives fundamental information

¹This chapter is mainly based on the papers:
J. Mulet, C. R. Mirasso and M. San Miguel, *Phys. Rev. A* **64**, 023817 (2001).
M. San Miguel, S. Balle, J. Mulet, C. R. Mirasso, E. Tolkachova, and J. R. Tredicce, *Proc. SPIE* **3944**, 242-251 (2000).

on the dynamical properties in semiconductor lasers. From the point of view of applications in optical communications, the degradation of the signal to noise ratio associated with MPN fixes limits on the receiver sensitivity and bit error rates. Vertical-cavity surface-emitting lasers (VCSELs) operate in a single longitudinal mode, although multitransverse mode operation is common. MPN among these transverse modes and anticorrelated fluctuations of the modes have been described in different experiments and RIN measurements [146]-[155] and theoretically characterized [156]-[158]. The basic physical mechanism for this phenomenon is the same as for MPN among longitudinal modes of edge-emitting lasers, that is, spatial hole burning with modes competing for the same spatial carrier reservoir. Transverse modes can have different polarization, but still MPN among different transverse modes is mostly caused by spatial effects.

A more subtle form of MPN occurs in VCSELs operating close to threshold. In this situation VCSELs lase in the fundamental transverse mode, but MPN arises from the competition of the two independent polarization components with essentially the same spatial profile. The effect of polarization fluctuations in the total intensity noise can significantly degrade the RIN characteristics [12] in a system with polarization sensitive elements. The importance of the fluctuations in the polarization component perpendicular to the dominant one has been characterized in detail [159]-[162]. Evidence of anticorrelated fluctuations of the two polarization components of the fundamental transverse mode has also been reported [162, 163] and it can be appreciated in Fig. 5.1. Anticorrelated dynamics of the polarization components may also manifest in chaotic regimes caused by optical feedback [164].

Due to their high quantum efficiency, low threshold, and single mode operation, VCSELs have been proposed as good candidates for the production of quantum squeezed light. In fact, production of squeezed light from VCSELs has been re-

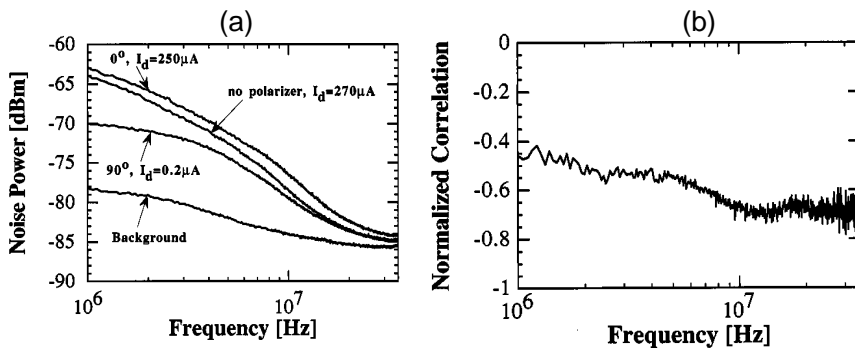


Figure 5.1. (a) Intensity noise of the 5 μm device measured through a Glan-Thompson polarizer. (b) Normalized crosscorrelation between the two degenerate polarization modes in the 5 μm device. Extracted from Ref. [163].

ported by several groups [149, 155, 165]. In this context an important question that has been addressed is the relevance of polarization partition noise (PPN) in degrading or achieving quantum squeezing [166].

A standard model for the study of polarization dynamics of VCSELs is the so-called Spin-Flip Model (SFM), and reduced versions [167]. Two important parameters of the model that enter into the description of the dynamical coupling of the two polarization components are the cavity birefringence and the spin-flip rate. The latter measures the direct coupling between the two groups of carriers with opposite spin that recombine into photons of opposite circular polarization. Previous studies of polarization fluctuations [159, 162, 166] take the SFM as a starting point. But, invoking the limit of fast spin-flip rate and large birefringence, the SFM is reduced to a simple model with one degree of freedom or to the rate equations for a two-mode laser [145]. However, for VCSELs with small birefringence there is experimental evidence of the role of the nonlinear anisotropies associated with a finite spin-flip rate. These effects are seen at least in three different characterizations of polarization fluctuations: A polarization type of four-wave mixing detected in the optical spectrum, polarization resolved intensity noise, and difference in the frequency splitting of the two polarizations components at both sides of a polarization switching (PS) [159, 161]. In addition, and also for VCSELs with small birefringence, there is evidence of polarization switching [168] caused by phase-amplitude mechanisms of nonthermal origin described by the SFM [30, 32, 33, 169]. These results motivate the detailed analysis of the complete SFM presented here. Such analysis allows us to gain a full understanding of the dependence of polarization fluctuations on birefringence and spin-flip rate in different ranges of values of these parameters.

In this chapter, we study the polarization resolved intensity noise of VCSELs operating in the fundamental transverse mode. We investigate the dynamical origin of the anticorrelated fluctuations of the polarization components. Such correlations emerge from mechanisms of polarization coupling and competition that are in principle independent of spatial mode profiles. We consider here the polarization dynamics within a semiclassical approach. This should give the necessary understanding for detailed studies of the quantum properties [170]. Our analysis focuses on the two circularly polarized components of the electric field. These are the natural variables for describing the lasing transitions in an active semiconductor material. They are directly phase coupled by the cavity birefringence and also coupled through the carrier populations mixed by the spin-flip. Focusing on the circularly polarized components, we are able to obtain explicit analytical expressions for their power spectra (in the approximation of linearized fluctuations). The competing roles of birefringence and spin-flip rate become clear from these expressions. Our results for the circularly polarized components are discussed and compared with the polarization

resolved spectra of the linearly polarized (LP) components obtained by a numerical analysis.

This chapter is organized as follows. We begin discussing in Sec. 5.2 the relationship between spin dynamics and light polarization state in VCSELs. The equations for the spin-flip model together with the Langevin noise sources are put forward in Sec. 5.3. We recall the possible linearly-polarized solutions of the model and their stability. In Sec. 5.4 we discuss the regimes with qualitative different dynamical operation in the SFM, associated with different values of anisotropies and spin-flip. In Sec. 5.5 we present our results for the polarization resolved intensity noise for the circular and linear components on both sides of a polarization switch. In Sec. 5.6 we present the power spectra of the polarization angles in the different regimes of operation. In Sec. 5.7 we discuss the role of birefringence and spin-flip rate by visualizing the polarization fluctuations on the Poincaré sphere. In Sec. 5.8 we give a quantitative description of the anticorrelation of polarization fluctuations for circular and linear polarization components. We analyze the whole range of frequencies, from small frequency to frequencies beyond the relaxation oscillation frequency.

5.2 Spin Dynamics and Light Polarization State

The light emitted by an edge-emitter is linearly-polarized along the heterojunction plane of a rectangular-shaped resonator, thus determining a transverse electric (TE) mode. In VCSELs the polarization direction is not a priori fixed due to their inherent circular geometry. So, an important question that we address is what does determine the light polarization state in VCSELs?

In weakly-index guided or purely gain-guided devices, the optical field inside the VCSEL cavity can be considered as almost totally polarized in the transverse plane to the cavity axis². In a system with perfect cylindrical symmetry, any linearly polarized state of the optical field is allowed. In crystals with cubic symmetry, this rotational invariance is not perfectly preserved. Moreover the VCSEL cavity has weak optical anisotropies (due to either residual strain incorporated during device processing or to other sources as the elasto-optic [171] or electro-optic effects [172]) that select two preferred orthogonal orientations for the optical field, \hat{x} and \hat{y} , which usually correspond to the underlying crystallographic axes. For simplicity, we assume that the preferred orientations are the same in all epitaxial layers defining the VCSEL cavity, hence the optical properties of the passive cavity are diagonal in the basis of linearly polarized states. However, the polarization state of the optical field emitted by the VCSEL also depends on its interaction with the active region's material, governed by the selection rules of quantum mechanics. In crystals with cubic symmetry,

²This is the so-called weak guidance approximation discussed in Appendix E.

and when the optical field propagates along the quantization axes of the crystal (\hat{z}), the selection rules for the transitions impose, among others, the conservation of the third component of the angular momentum. Hence, changes in the total angular momentum of $\Delta J_z = +1$ (-1) corresponds to the emission of a left (right) circularly polarized photon. The optical properties of the active region are therefore diagonal in the basis of circularly polarized states of the optical field, hence we switch to it due to the resulting simplified description of the dynamical interaction with the active material. It is worth recalling the relationship among linear and circular basis. The field components A_i and unitary vectors \hat{e}_i transform according to

$$A_{\pm} = \frac{A_x \pm iA_y}{\sqrt{2}}, \quad \hat{e}_{\pm} = \frac{\hat{e}_x \mp i\hat{e}_y}{\sqrt{2}}. \quad (5.1)$$

It is then also natural to distinguish between spin-up and spin-down electrons and holes, since they couple to optical transitions with opposite circular polarization. In addition, spin-up and spin-down carriers are coupled among them through spin-flip mechanisms that may reverse the particle's spin [173], and which we shall describe through an effective spin-relaxation rate.

The original SFM considers optical transitions in a four-level system as sketched in Fig. 5.2. It can be regarded as a generalization of the gas laser theory to the magnetic sublevels of the conduction and heavy-hole bands of a QW. The conduction band is replaced by two levels populated by electrons with opposite spin orientations and angular momentum $J_z = \pm 1/2$. In the same way, the heavy hole band (HH) is replaced by two levels populated by holes with opposite spin orientations and $J_z = \pm 3/2$. The total carrier density into spin-up and spin-down carrier reservoirs. The population inversion in the two spin channels is given by $N_{\pm} \equiv N_{\pm}^c - N_{\pm}^v$, where N_{\pm}^c (N_{\pm}^v) stands for the population in the conduction (valence) spin subbands. In absence of magnetic fields, the two spin channels are energetically degenerated.

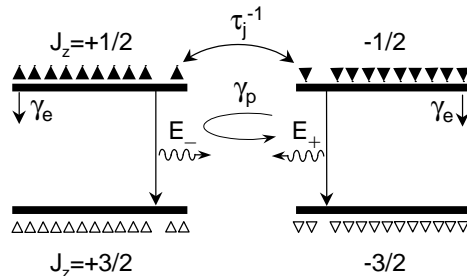


Figure 5.2. Sketch of a four level system in the SFM. Allowed optical transitions, recombination and mixing mechanisms are indicated in the figure. $\gamma_s = 2\tau_j^{-1} + \gamma_e$.

Spin-relaxation rate

An important parameter that enters in the determination of the polarization properties is the spin-relaxation time τ_j . This quantity determines the mean lifetime for electrons in a given spin state. Various spin-relaxation mechanisms in semiconductor QWs have been proposed, see e.g., [173]-[175]: D'yakonov-Perel' (DP), Elliot-Yafet (EY), and Bir-Aronov-Pikus (BAP). In the DP process, the spin-orbit effect causes the splitting in energy of the magnetic conduction bands that in conjunction with the lack of inversion symmetry causes the re-orientation of the spins. In DP, $\tau_j \sim E_{1e}^{-2}$, with E_{1e} the first electron confinement energy in the QW. The EY process leads to spin-relaxation due to the mixing of the valence-band states into the conduction-band. Finally in BAP, the spin-flip appears as a consequence of an interchange of scattering interaction between electrons and holes. In both EY and BAP processes, $\tau_j \sim E_{1e}^{-1}$, although the relative importance of BAP is significant only below 100 K. The predictions of these models are contrasted with experimental determination of the spin-relaxation time. One possible way for doing this consists in optically pump the active medium with circularly polarized pulses $p_{\pm}(t)$ and to analyze the circularly polarized emission. In the case of optical pumping below the lasing threshold, the stimulated recombination terms can be neglected in the evolution of the carrier densities

$$\frac{dN_{\pm}}{dt} = p_{\pm}(t) - \gamma_e N_{\pm} \mp \frac{1}{\tau_s} (N_+ - N_-), \quad (5.2)$$

determine the photoluminescence in both circular components. The inversion difference $n = (N_+ - N_-)/2$ evolves according

$$\frac{dn}{dt} = \frac{1}{2} [p_+(t) - p_-(t)] - \gamma_s n,$$

$\gamma_s \equiv \gamma_e + 2\tau_j^{-1}$ being the spin-flip rate. Thus, spin-flip processes tend to balance the population in both spin channels. From experiments, the main contribution to τ_j in GaAs QWs ($\bar{\lambda} \approx 0.85 \mu\text{m}$) at room temperature is the DP process yielding a typical value of $\tau_j \approx 40$ ps ($\gamma_s \approx 50 \text{ ns}^{-1}$) for electron confinement energies around $E_{1e} = 100$ meV [175]. However, the most plausible candidate for the spin relaxation in InGaAs/InP QWs ($\bar{\lambda} \approx 1.5 \mu\text{m}$) at room temperature is the EY process due to the smaller band-gap. In this case, a typical value at room temperature of the spin-relaxation time is $\tau_j \approx 5$ ps ($\gamma_s \approx 400 \text{ ns}^{-1}$) for confinement electron energies $E_{1e} = 50$ meV [174].

It is worth remarking that γ_s corresponds to the spin relaxation rate for electrons in the conduction band. Spin-flip for holes is usually neglected because sub-picosecond spin relaxation time is found at room temperature. The implications of a finite spin-flip rate for electrons in the polarization properties of QW VCSELs will be discussed along this work.

5.3 Spin-Flip Model

The evolution of the electric field within the VCSEL cavity is governed by the Maxwell's equations whereas the the carrier populations can be determined using the density-matrix formalism [60] applied to a four level system. In the absence of transverse effects, the polarization dynamics of a single longitudinal and transverse mode VCSEL is described by the spin-flip model. The original equations read [37]

$$\dot{A}_{\pm}(t) = -\kappa A_{\pm} + ig_{QW} P_{\pm} - (\gamma_a + i\gamma_p) A_{\mp} + G_{A_{\pm}}(t), \quad (5.3a)$$

$$\dot{P}_{\pm}(t) = -\gamma_{\perp}(1 - i\Delta)P_{\pm} - ig_{QW}(N \pm n - N_0)A_{\pm} + G_{P_{\pm}}(t), \quad (5.3b)$$

$$\dot{N}(t) = -\gamma_e(N - \sigma) - ig_{QW} [A_+^* P_+ + A_-^* P_- - \text{c.c.}] + G_N(t), \quad (5.3c)$$

$$\dot{n}(t) = -\gamma_s n - ig_{QW} [A_+^* P_+ - A_-^* P_- - \text{c.c.}] + G_n(t). \quad (5.3d)$$

A_{\pm} are the complex slowly-varying amplitudes of the electrical field, written in terms of the circular polarization components. The slowly-varying circular-components of the material polarization P_{\pm} appear in a diagonal form only in the circular basis. $N \equiv (N_+ + N_-)/2$ is associated to the total population inversion between the conduction and valence bands and $n \equiv (N_+ - N_-)/2$ is the difference in population inversions of the two spin channels separately. N_0 stands for the total population inversion at transparency. The total population inversion decays with rate γ_e , while the differences in population inversions n relaxes with spin-flip rate γ_s , introduced at this level as a phenomenological parameter. $\Delta = (\Omega - \omega_g)/\gamma_{\perp}$ represents the normalized detuning between the longitudinal mode resonance Ω and the transition frequency ω_g . The material polarization decay rate is γ_{\perp} whereas the cavity decay rate is κ . g_{QW} stands for the effective coupling constant between the material dipoles and the electric field. The pumping parameter σ is related to the injection current level.

In a real situation the VCSEL structure is not perfectly symmetric under the interchange of the \hat{x} and \hat{y} directions due to, for instance, imperfections during the fabrication. This effect is accounted through the linear cavity anisotropies. The amplitude anisotropy γ_a is referred as dichroism while γ_p is the phase anisotropy or birefringence. The effect of the dichroism is to introduce different losses depending on the polarization orientation while birefringence introduces different refractive indexes and modal frequencies. Several mechanisms contribute to birefringence: mechanical strain [176], linear electro-optic effect [177], and elasto-optic effect [178]. The repercussion of these two important parameters, γ_a, γ_p , will be discussed in detail in the next section.

The physical meaning of the different (deterministic) terms in Eqs. (5.3a)-(5.3d) follows from the general interpretation of rate equations. Eq. (5.3a) represents a balance between the material gain, provided by $\sim -\text{Im } P_{\pm}$, and cavity losses; while the

imaginary terms $\sim \text{Re } P_{\pm}$ induce a nonlinear frequency shift. The balance between the decay of material polarization and the excitation of dipoles (electron-hole pairs) due to the presence of an electric field is described through Eq. (5.3b). In Eq. (5.3c), the total carrier population increases due to current injection, and decreases due to recombination of carriers, being either spontaneous or stimulated recombination. Finally, Eq. (5.3d) gives a detailed balance between the difference in number of stimulated recombination events that take place in each spin channel separately; in addition, spin-flip processes introduce a damping in this difference.

The terms $G_{A_{\pm}}, G_{P_{\pm}}, G_N, G_n$ represent semiclassical Langevin noise sources. $G_{P_{\pm}}$ models the quantum fluctuations of the photon-dipole interaction. From Eq. (C.8) in the appendix, we have that $\langle G_{P_{\pm}}(t)G_{P_{\pm}}^*(t') \rangle = \gamma_{\pm}(N \pm n)\delta(t-t')$, $(N \pm n)$ representing the dipole number per spin channel. Equivalently, $G_{P_{\pm}}$ can be expressed in terms of complex random numbers $\xi'_{\pm}(t)$, with zero mean $\langle \xi'_{\pm}(t) \rangle = 0$ and correlation $\langle \xi'_{\pm}(t)\xi'^*_{\pm}(t') \rangle = 2\delta(t-t')$ by means

$$G_{P_{\pm}}(t) = \sqrt{\frac{\gamma_{\pm}}{2}}(N \pm n)\xi'_{\pm}(t). \quad (5.4)$$

$\langle G_{A_{\pm}}(t)G_{A_{\pm}}^*(t') \rangle$ is proportional to the mean number of thermal photons that we consider negligible around $\lambda = 0.85 \mu\text{m}$. G_N and G_n include among others, the pump fluctuations statistics and the shot noise from the time uncertainty in the recombination processes. For the sake of simplicity, pump fluctuations $\delta\sigma(t)$ are also neglected.

Adiabatic elimination

From experimental measurements of the spin relaxation rate in QWs, the different rate constants in Eqs. (5.3a)–(5.3d) verify that

$$1 \text{ ns}^{-1} \sim \gamma_e \ll \gamma_s \lesssim \kappa \ll \gamma_{\pm} \sim 10^4 \text{ ns}^{-1}.$$

From this time scale analysis, we conclude that the material polarization is the dynamical variable that relaxes faster. Hence, it is justified to adiabatically eliminate the material polarization assuming that it reaches nearly instantaneously its steady state, i.e., $\dot{P}_{\pm} \approx 0$ in Eq. (5.3b). In this limit, we obtain an expression for P_{\pm} that reads

$$P_{\pm}(t) \approx -ig_{QW} \frac{(N \pm n - N_0)}{\gamma_{\pm}(1 + \Delta^2)} (1 + i\Delta)A_{\pm} + \frac{G_{P_{\pm}}(t)}{\gamma_{\pm}(1 - i\Delta)}. \quad (5.5)$$

Upon replacing Eq. (5.5) into the remaining equations, scaling the dynamical variables by

$$D \equiv \frac{g}{\kappa}(N - N_0), \quad d \equiv \frac{g}{\kappa}n, \quad g \equiv \frac{g_{QW}^2}{\gamma_{\pm}(1 + \Delta^2)},$$

and performing a change of reference frame for the electric field from Ω to $\Omega - \kappa\Delta$

$$E_{\pm} \equiv \sqrt{\frac{2g}{\gamma_e}} e^{-i\kappa\Delta t} A_{\pm},$$

we arrive to the following rate equations describing the polarization dynamics of single longitudinal and transverse mode VCSELs in presence of spontaneous emission

$$\dot{E}_{\pm}(t) = \kappa(1 - i\alpha)[D \pm d - 1]E_{\pm} - (\gamma_a + i\gamma_p)E_{\mp} + F_{\pm}(t), \quad (5.6a)$$

$$\dot{D}(t) = -\gamma_e [D - \mu + (D + d)|E_+|^2 + (D - d)|E_-|^2] - F_D(t), \quad (5.6b)$$

$$\dot{d}(t) = -\gamma_s d - \gamma_e [(D + d)|E_+|^2 - (D - d)|E_-|^2] - F_d(t). \quad (5.6c)$$

A correct description of the semiconductor dynamics requires to identify the normalized detuning Δ with the linewidth enhancement factor of semiconductor lasers; for the two-level system $\alpha \approx -\Delta$. The linewidth enhancement factor is the responsible of the phase-amplitude coupling and it plays an important role in enhancing the emission linewidth, causing frequency-chirped pulses, and in many other phase-induced instabilities [179]. The scaled injection current $\mu \equiv g(\sigma - N_0)/\kappa$ is such that at threshold $\mu_{th} \approx 1$. This reduced version of the SFM constitutes a nonlinear system of six real ordinary differential equations. In contrast to the traditional formulation of rate equations in EELs [9], in the SFM phase and amplitude variables can not be described separately, but they are directly coupled through the linear anisotropies and the α -factor. The Langevin noise sources resulting from the adiabatic elimination of P_{\pm} read

$$F_{\pm}(t) = \sqrt{\beta_{sp}\gamma_e(D \pm d)} \xi_{\pm}(t), \quad (5.7a)$$

$$F_{(D/d)}(t) = \frac{\gamma_e}{2\kappa} \left[\sqrt{\beta_{sp}\gamma_e(D + d)} E_+ \xi_+^*(t) \pm \sqrt{\beta_{sp}\gamma_e(D - d)} E_- \xi_-^*(t) + c.c. \right]. \quad (5.7b)$$

$\xi_{\pm}(t)$ are two independent complex white noise terms with the same properties than $\xi'_{\pm}(t)$ in Eq. (5.4). In terms of the new variables, the scaled spontaneous emission factor reads³

$$\beta_{sp} = \beta_0 \frac{1}{(1 + \alpha^2)} \frac{\kappa}{\gamma_e}. \quad (5.8)$$

³ β_0 stands for the fraction of spontaneously emitted photons that goes into the lasing mode [180].

Accordingly, the scaled spontaneous emission rate is $R_{sp} = 4\gamma_e\beta_{sp}D_0$, $D_0 \sim 1$ being the degree of inversion. To get an impression of the magnitude of the rescaling, a noise level in the original equations of $\langle AA^* \rangle_{SQL} = 1/2$ corresponds to $\langle EE^* \rangle_{SQL} = \beta_0/(1 + \alpha^2) \approx 10^{-7}$ in the new variables.

Linearly-polarized solutions

We start our discussion, by analyzing the steady-state solutions of Eqs. (5.6a)-(5.6c). A generic monochromatic solution can be expressed by

$$E_{\pm}(t) = Q_{\pm}e^{-i(\nu_0 t \pm \phi + \varphi_0)}, \quad (5.9)$$

where Q_{\pm} are the real circular amplitudes, ν_0 the frequency shift, ϕ a relative phase among the circular components, and φ_0 an arbitrary global phase for the electric field. The linearly-polarized (LP) solutions are restricted to $Q_+ = Q_- \equiv Q$ and $\phi = 0$ ($\phi = \pi/2$) providing a solution LP along the \hat{x} (\hat{y}) axis. Therefore, LP states can be regarded as phase locking of the two circular components to a relative angle 2ϕ . In addition, $D(t) = D_0$ and $d(t) = d_0$ in the steady state. Upon inserting these conditions in Eqs. (5.6a)–(5.6c) and neglecting the noise terms, we find

$$\begin{aligned} \nu_0 &= \varepsilon(\gamma_p + \alpha\gamma_a), \\ D_0 &= 1 + \varepsilon\gamma_a/\kappa, \end{aligned} \quad (5.10)$$

$\varepsilon = 1$ (-1) when a \hat{x} (\hat{y})-LP solution is considered. The birefringence splits in frequency the two LP solutions by a distance $2\gamma_p$. When $\gamma_p > 0$, \hat{x} (\hat{y}) is referred as the high (low) frequency mode. It is worth remarking that for a perfectly symmetric VCSEL, i.e., $\gamma_p = 0$ and $\gamma_a = 0$, any polarization orientation ϕ provides a possible LP state. Finally

$$\begin{aligned} Q^2 &= \frac{1}{2} \frac{(\mu - D_0)}{D_0}, \\ d_0 &= 0. \end{aligned} \quad (5.11)$$

Linearized spin-flip model

In this section, we present the equations governing the linearized dynamics close to an arbitrary LP solution. A fundamental question is to understand the role of the spin-flip in determining the stability of the LP solutions. In addition, the resulting linear systems are the basis for the study of fluctuations. The stability and fluctua-

tions of a LP solution are studied by writing it as

$$\begin{aligned} E_{\pm}(t) &= [Q + a_{\pm}(t)] e^{-i(\nu_0 t \pm \phi)}, \\ D(t) &= D_0 + \Delta(t), \\ d(t) &= d_0 + \delta(t), \end{aligned} \quad (5.12)$$

with ν_0, Q, ϕ, D_0, d_0 given above. $a_{\pm}(t)$ are complex perturbations of the electric field, while $\Delta(t)$ and $\delta(t)$ stand for real perturbations of the carrier variables. The stability analysis of the LP solutions provides a system of equations that decouple (in the linear approximation) for the new variables, $S = a_+ + a_-$ and $R = a_+ - a_-$. The first subset, $\{S, S^*, \Delta\}$, describes the fluctuations of the total intensity

$$\begin{pmatrix} \dot{S} \\ \dot{S}^* \\ \dot{\Delta} \end{pmatrix} = \begin{pmatrix} 0 & 0 & \kappa(1 - i\alpha)Q \\ 0 & 0 & \kappa(1 + i\alpha)Q \\ -\gamma_e D_0 Q & -\gamma_e D_0 Q & -\gamma_e \mu / D_0 \end{pmatrix} \begin{pmatrix} S \\ S^* \\ \Delta \end{pmatrix}. \quad (5.13)$$

From this subset, a complex pair of eigenvalues determines the frequency and damping of the relaxation oscillations (ROs) that undergo the total intensity, i.e., $\lambda_{\pm} = -\Gamma_R \pm i\Omega_R$. Their expressions are

$$\Gamma_R = \frac{\gamma_e \mu}{2D_0}, \quad \Omega_R = \sqrt{2\kappa\gamma_e(\mu - D_0) - \Gamma_R^2}. \quad (5.14)$$

The remaining⁴ eigenvalue is zero and it is associated with the arbitrariness in a global phase φ_0 , or equivalently, with the invariance in temporal translations.

The second subset, $\{R, R^*, \delta\}$

$$\begin{pmatrix} \dot{R} \\ \dot{R}^* \\ \dot{\delta} \end{pmatrix} = \begin{pmatrix} \pm 2(\gamma_a + i\gamma_p) & 0 & 2\kappa(1 - i\alpha)Q \\ 0 & \pm 2(\gamma_a - i\gamma_p) & 2\kappa(1 + i\alpha)Q \\ -\gamma_e D_0 Q & -\gamma_e D_0 Q & -(\gamma_s + 2\gamma_e Q^2) \end{pmatrix} \begin{pmatrix} R \\ R^* \\ \delta \end{pmatrix} \quad (5.15)$$

characterizes the polarization stability. An alternative way to study the polarization stability is to introduce the polarization orientation angle ϕ and the ellipticity angle χ through the real and imaginary parts of the complex amplitude difference $R(t)$

$$\delta\chi = \frac{R + R^*}{4Q}, \quad \delta\phi = i \frac{(R - R^*)}{4Q}.$$

⁴Note that under multitransverse mode operation additional RO frequencies of the total intensity associated with different transverse modes might appear [181].

This description will be useful when describing fluctuations of the polarization angles in Sec. 5.6. The second subset provides a third order characteristic polynomial that reads

$$\begin{aligned} \mathcal{D}(\lambda) = & \lambda^3 + (\gamma_s + 2\gamma_e Q^2 \mp 4\gamma_a) \lambda^2 + \\ & 4 [\gamma_p^2 + \gamma_a^2 + \kappa\gamma_e Q^2 D_0 \mp \gamma_a (\gamma_s + 2\gamma_e Q^2)] \lambda + \\ & 4 [\gamma_p^2 + \gamma_a^2] (\gamma_s + 2\gamma_e Q^2) \mp 8\kappa\gamma_e Q^2 D_0 (\gamma_a - \alpha\gamma_p) . \end{aligned} \quad (5.16)$$

The signs $-$, $+$ are associated to the stability of \hat{x} , \hat{y} - LP states, respectively. $\mathcal{D}(\lambda) = 0$ determines the polarization stability, i.e., the state is unstable when there exists at least one eigenvalue with $\text{Re } \lambda > 0$, while the state is stable when $\text{Re } \lambda < 0$ for the three eigenvalues.

Polarization switching

Polarization switching (PS) takes place as consequence of a change in the stability of the polarization states, for instance, when increasing the injection current. Let us consider that $\gamma_a \gtrsim 0$, therefore the \hat{y} -LP state has lower losses and it is consequently selected when the current crosses the threshold. Both \hat{x} -LP and \hat{y} -LP states are stable below PS (coexistence region) except for currents close to threshold, due to the presence of γ_a [See Fig. 5.3]. Increasing further the injection current, the \hat{y} -LP solution becomes unstable and a PS from the low frequency to the high frequency solution takes place [See Fig. 5.4]. This type of switching, is successfully explained within the SFM [30, 32], and it is commonly referred as nonthermally induced PS since it occurs at constant active region temperature [169]. We remark that this type of switching is restricted to finite value of the spin-flip rate γ_s , and non-vanishing α and γ_p . Another type of PS, commonly present in experiments [31, 176, 182], is the thermally induced PS. It arises from the temperature dependence of the gain difference between the two polarization states. A unified description of thermal and nonthermal induced PS has recently been introduced in terms of a dressed SFM in [33, 183] that will be presented in the following chapter.

5.4 Regimes of Operation

The dynamical behavior, in the approximation of linear perturbations, is determined from the eigenvalues and eigenvectors associated to a stable fixed point. Hence, we focus in regions where at least one linearly-polarized solution is stable. A (negative) real eigenvalue determines the damping while a pair of complex conjugated eigenvalues determine the damping and oscillation frequency. In presence of fluctuations

Figure 5.3. Linear stability of the linearly-polarized solutions in the plane current-birefringence. The regions are: \hat{x} -LP stable (x), \hat{y} -LP stable (y), both stable (bistable). The parameters are: $\alpha = 3$, $\gamma_e = 1 \text{ ns}^{-1}$, $\kappa = 300 \text{ ns}^{-1}$, $\gamma_a = 0.1 \text{ ns}^{-1}$, and $\gamma_s = 100 \text{ ns}^{-1}$. The arrow indicates a nonthermal polarization switch from LF to HF states.

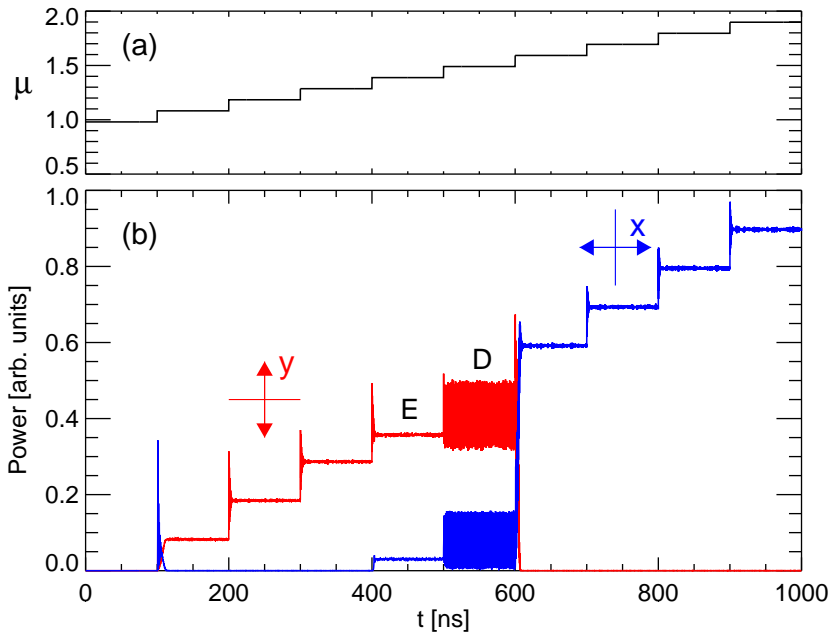
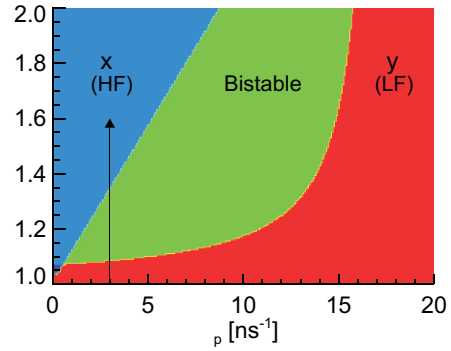


Figure 5.4. (a) Injection current increased by steps from below to above threshold. (b) Typical polarization switching from the low to the high frequency solution, taking place across elliptical (E) and dynamical states (D). The same parameters than Fig., except for $\gamma_p = 3 \text{ ns}^{-1}$.

(noise), the understanding of the deterministic behavior is useful to interpret the noise spectra in each of these regions, as will be shown later.

A detailed analysis of the possible regimes of operation in the SFM has been described in [30, 184], discussing the effect of the spin-flip relaxation rate, birefringence, and current injection. The behavior of the total intensity is already understood. From Eq. (5.14), we have oscillations at frequency Ω_R and damping rate Γ_R . Hence, the main issue is to understand the polarization behavior described by the linear system of Eq. (5.15). In spite of narrow regions where the polarization is unstable, and other ones without oscillations⁵, two qualitative different situations arise [30].

- *Polarization relaxation oscillations* (PROs): This regime is characterized by oscillations of the ellipticity angle $\chi(t)$ and the carrier difference $d(t)$. The polarization angle $\phi(t)$ displays an exponential decay. This regime tends to appear for small linear anisotropies and currents far from threshold.
- *Coupled oscillations* (COs): This regime is characterized by coupled oscillations of the ellipticity angle $\chi(t)$ and the polarization angle at a frequency Ω_P given by Eq. (B.3). The carrier difference $d(t)$ exhibits an exponential decay. This regime is favored for large spin-flip values and currents close-to-threshold.

Further characterization of these regions can be found in Appendix B.

5.5 Fluctuation of the Intensity Components

In order to better understand the intensity fluctuations of the polarization components, Eqs. (5.6a)–(5.6c) can be translated from the field description $E_{\pm}(t)$ to equations for the circular intensities $P_{\pm}(t)$ and the phase difference $\phi(t) \equiv \phi_+(t) - \phi_-(t)$ through $E_{\pm}(t) = \sqrt{P_{\pm}(t)}e^{i\phi_{\pm}(t)}$. The stochastic transformation in the Itô sense [Ap-

⁵The limits $\kappa \gg \gamma_e, \gamma_p, \gamma_s$ and $\gamma_e \sim \gamma_s \gg \kappa, \gamma_p$ also correspond to qualitative different regimes; however being unusual in SCL. In both cases the typical time scales for the decay of the electric field κ and those for the carrier variables γ_e, γ_s decouple. The exchange of energy is unfavored avoiding the appearance of oscillations.

pendix C] of Eqs. (5.6a)–(5.6c) reads

$$\begin{aligned}\dot{P}_{\pm}(t) &= 2\kappa[D \pm d - 1]P_{\pm} - 2\sqrt{P_+P_-}[\gamma_a \cos \phi \pm \gamma_p \sin \phi] \\ &\quad + 2\beta_{sp}\gamma_e[D \pm d] + F_{P_{\pm}}(t),\end{aligned}\quad (5.17a)$$

$$\begin{aligned}\dot{\phi}(t) &= 2\kappa\alpha d - \sqrt{\frac{P_-}{P_+}}[\gamma_p \cos \phi - \gamma_a \sin \phi] + \sqrt{\frac{P_+}{P_-}}[\gamma_p \cos \phi \\ &\quad + \gamma_a \sin \phi] + F_{\phi},\end{aligned}\quad (5.17b)$$

$$\dot{D}(t) = -\gamma_e[D - \mu + (D + d)P_+ + (D - d)P_-] - F_D(t), \quad (5.17c)$$

$$\dot{d}(t) = -\gamma_s d - \gamma_e[(D + d)P_+ - (D - d)P_-] - F_d(t), \quad (5.17d)$$

with the Langevin terms

$$F_{P_{\pm}} = \sqrt{4\beta_{sp}\gamma_e(D \pm d)P_{\pm}} \xi_{P_{\pm}}, \quad (5.18a)$$

$$F_{\phi} = \sqrt{\frac{\beta_{sp}\gamma_e(D + d)}{P_+}} \xi_{\phi_+} - \sqrt{\frac{\beta_{sp}\gamma_e(D - d)}{P_-}} \xi_{\phi_-}, \quad (5.18b)$$

$$F_{(D)} = \frac{\gamma_e}{\kappa} \left[\sqrt{\beta_{sp}\gamma_e(D + d)P_+} \xi_{P_+} \pm \sqrt{\beta_{sp}\gamma_e(D - d)P_-} \xi_{P_-} \right], \quad (5.18c)$$

$\xi_{P_{\pm}}, \xi_{\phi_{\pm}}$ being real white Gaussian random numbers with zero mean and correlation $\langle \xi_a(t)\xi_b(t') \rangle = \delta_{a,b}\delta(t - t')$, resulting from an orthogonal transformation of ξ_{\pm} [Eqs. (C.16)–(C.17)].

In order to calculate the power fluctuations of the total intensity and circular components, we linearize Eqs. (5.17a)–(5.17d) around their steady states. We have $P_{\pm 0} = Q^2$, $d_0 = 0$, and $D_0 = 1 + \varepsilon\gamma_a/\kappa$ when $\phi_0 = 0, \pi$. For convenience, we calculate the fluctuations of the total intensity $\delta P(t) = \delta P_+(t) + \delta P_-(t)$ and the intensity difference $\delta q(t) = \delta P_+(t) - \delta P_-(t)$. The linearized equations can be straightforwardly solved via Fourier transform, yielding the expressions

$$\delta\tilde{P}(\omega) = \sqrt{2Q^2R_{sp}} \frac{[\gamma_e - i\omega] \tilde{\xi}_P}{[\omega - \Omega_R - i\Gamma_R][\omega + \Omega_R - i\Gamma_R]}, \quad (5.19a)$$

$$\begin{aligned}\delta\tilde{q}(\omega) &= -\sqrt{2Q^2R_{sp}} \times \\ &\quad \frac{[\varepsilon 4\alpha Q^2 \gamma_e \gamma_p + (i\omega + \varepsilon 2\gamma_a)(\gamma_s - i\omega)] \tilde{\xi}_q + \varepsilon 2\gamma_p (\gamma_s + 2\gamma_e Q^2 - i\omega) \tilde{\xi}_{\Phi}}{\mathcal{D}(-i\omega)},\end{aligned}\quad (5.19b)$$

where Γ_R and Ω_R are given by Eq. (5.14) and $\mathcal{D}(\lambda)$ is given by Eq. (5.16); $\varepsilon = 1(-1)$ stands for a \hat{x} (\hat{y}) LP solution. The Fourier transformed noise sources $\tilde{\xi}_P(\omega)$, $\tilde{\xi}_q(\omega)$ and $\tilde{\xi}_{\Phi}(\omega)$ verify that $\langle \tilde{\xi}_i(\omega)\tilde{\xi}_j(\omega') \rangle = \delta_{i,j} \delta(\omega - \omega')$ for $i, j = P, q, \phi$.

The power spectra of the total and difference intensities can be derived from its definition in Eq. (C.11)

$$S_P(\omega) = \int_{-\infty}^{\infty} \langle \delta\tilde{P}(\omega) \delta\tilde{P}^*(\omega') \rangle d\omega',$$

and from Eqs. (5.19a)–(5.19b) yielding

$$S_P(\omega) = 2Q^2 R_{sp} \frac{(\omega^2 + \gamma^2)}{\left[(\omega - \Omega_R)^2 + \Gamma_R^2 \right] \left[(\omega + \Omega_R)^2 + \Gamma_R^2 \right]}, \quad (5.20a)$$

$$S_q(\omega) = 2Q^2 R_{sp} \frac{(\mathcal{A}_\chi(\omega) + \mathcal{B}_\chi(\omega))}{\mathcal{C}(\omega)}. \quad (5.20b)$$

The functions $\mathcal{A}_\chi, \mathcal{B}_\chi, \mathcal{C}$ are given in Appendix D, and $R_{sp} = 4\gamma\beta_{sp}D_0$. We note that the relative intensity noise is defined as the power spectrum divided by the square of the mean value of the total power, $\bar{P}^2 = (2Q^2)^2$.

The power spectrum of the circular components $S_\pm(\omega)$ can be obtained from Eqs. (5.20a) and (5.20b) by taking into account that the noise terms appearing in the fluctuations $\delta\tilde{P}(\omega)$ and $\delta\tilde{q}(\omega)$ are independent,

$$\delta P_\pm \equiv \frac{\delta P \pm \delta q}{2}, \quad S_+(\omega) = S_-(\omega) = \frac{S_P(\omega) + S_q(\omega)}{4}. \quad (5.21)$$

It is worth remarking that the contribution to the noise of the circular components arises from the linear superposition of the total intensity noise S_P and the polarization fluctuations S_q . This separation is possible in LP states because the total intensity fluctuations and the intensity difference fluctuations decouple (at first order). However, for other states (elliptical [185] and dynamical states [32]) the decoupled description is not valid requiring, in principle, the study of a five-dimensional system.

Let P_u and P_v be the power of each orthogonal component ($u = +, v = -$ for the circular components, or alternatively $u = x, v = y$ for the linear components). Since the fluctuation of the total intensity is a scalar we can express it in any of the two basis

$$\delta P = \delta P_+ + \delta P_- = \delta P_x + \delta P_y.$$

However, this result does not hold for the power spectra. Instead one finds

$$S_P(\omega) = S_u(\omega) + S_v(\omega) + \int_{-\infty}^{\infty} 2\text{Re} \langle \delta\tilde{P}_u(\omega) \delta\tilde{P}_v^*(\omega') \rangle d\omega'. \quad (5.22)$$

In the particular case of the circular components and making use of Eq. (5.21) we obtain

$$\operatorname{Re} \int_{-\infty}^{\infty} \langle \delta \tilde{P}_+(\omega) \delta \tilde{P}_-(\omega') \rangle d\omega' = \frac{S_P(\omega) - S_q(\omega)}{4}, \quad (5.23)$$

which implies that the fluctuations of the circular components δP_+ , δP_- are correlated when $S_P(\omega) > S_q(\omega)$, anticorrelated when $S_P(\omega) < S_q(\omega)$ and uncorrelated where $S_P(\omega) = S_q(\omega)$. In the Sec. 5.8 we will come back to the correlation between polarization components.

5.5.1 Fluctuations of the circular components

We present analytical and numerical results of the polarization resolved intensity noise. Since the circular basis is the most natural representation of the optical transitions, we begin investigating the power fluctuations of the circular components.

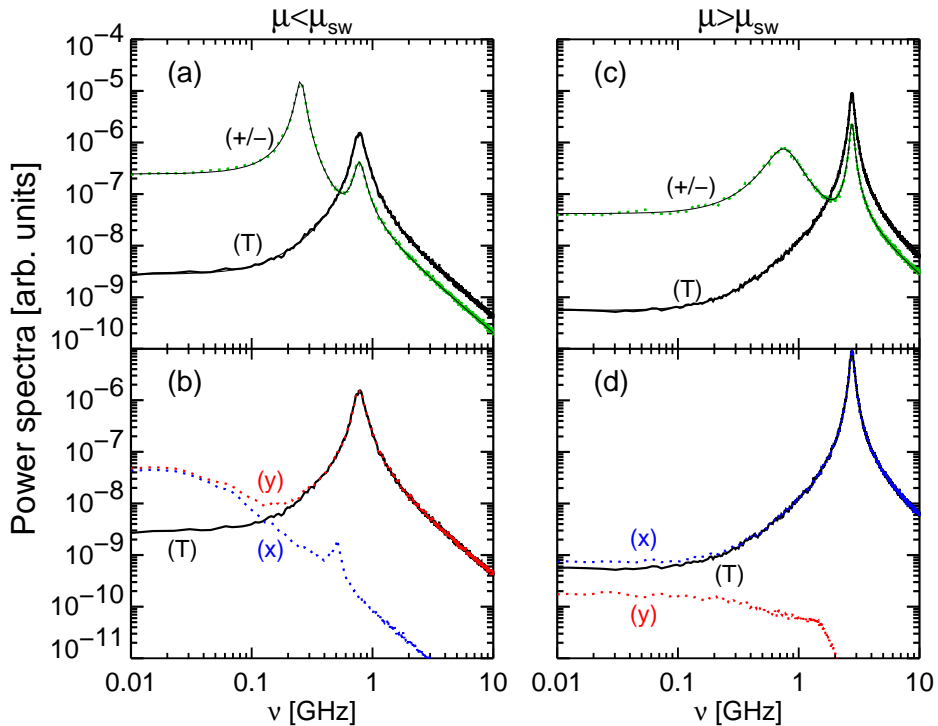


Figure 5.5. Power spectra in arbitrary units for currents below PS (a,b), and above PS (c,d). Solid thin lines in (a) and (c) represent the theoretical predictions given by Eqs. (5.20a) and (5.21). Parameters: $\gamma_e = 1 \text{ ns}^{-1}$, $\kappa/\gamma_e = 300$, $\alpha = 3$, $\gamma_p/\gamma_e = 1$, $\gamma_s/\gamma_e = 100$ and $\beta_{sp} = 10^{-5}$.

Their experimental determination can be performed by using $\lambda/4$ plate techniques [160].

We compute the power spectra for different values of the spin-flip rate and birefringence while maintaining the rest of the laser parameters fixed. We concentrate our study on moderate values of the spin-flip rate and relatively small birefringence which corresponds to COs regime. The dichroism is set to $\gamma_a \gtrsim 0$ in order to select the low frequency mode (\hat{y}) at threshold. A nonthermal PS takes place from the low frequency mode (\hat{y} -LP) to the high frequency one (\hat{x} -LP) when the injection current is increased.

In Fig. 5.5 we plot the power spectra obtained for $\gamma_s = 100 \text{ ns}^{-1}$, $\gamma_p = 1 \text{ ns}^{-1}$; $\mu = 1.04 < \mu_{sw}$ in panels 5.5(a,b), while $\mu = 1.5 > \mu_{sw}$ in panels 5.5(c,d). Analytical results obtained from Eqs. (5.20a) and (5.21) are plotted in Fig. 5.5(a,c) with solid thin lines. As can be seen, they are in very good agreement with the numerical results. The spectrum of the total intensity has a single peak located at the relaxation oscillation frequency $\nu_R = \Omega_R/(2\pi)$. This peak is due to fluctuations in the total photon number. In contrast, the power spectra of the circular components coincide and display an additional peak at the CO frequency $\Omega_P/(2\pi)$, which moves toward γ_p/π when $\gamma_s \rightarrow \infty$, in agreement with Eq. (B.3). We note that the height of the CO peak is larger and it appears at lower frequency before the PS, in qualitative agreement with Ref. [160]. It can be clearly seen that the noise in the two circular components is much larger than the total intensity noise at low frequencies, a sign of anticorrelation between δP_+ and δP_- . This anticorrelation is interrupted at higher frequencies due to the peak associated with the fluctuations in the total intensity. In fact, we find maximum correlation at Ω_R , as will be discussed later.

5.5.2 Fluctuation of the linear components

When a LP state is considered, there is a linear component that captures nearly the total intensity (lasing component), with mean power level \bar{P}_l , and one with very small intensity (nonlasing component) with \bar{P}_{nl} . Although a LP state is considered, we find that fluctuations in the nonlasing component are relevant.

It is illustrative to analyze the way in which the fluctuations are distributed among different polarization components. The probability density function (PDF) of an intensity component P is computed through

$$p.d.f(P_0) \approx \frac{\mathcal{P}[P_0 < P < P_0 + \Delta P_0]}{\Delta P_0},$$

where $\mathcal{P}[P_0 < P < P_0 + \Delta P_0]$ is the probability that the intensity takes the values within the interval $[P_0, P_0 + \Delta P_0]$. We approximate this quantity by the fraction of data points within $[P_0, P_0 + \Delta P_0]$, i.e. $\mathcal{N}[P_0 < P < P_0 + \Delta P_0]/N$. The PDF of circular components $p.d.f(P_{\pm})$, in Fig. 5.6(b), coincide and display a Gaussian shape with

a maximum around its mean value. In the same panel, we plot the PDF associated with the total intensity that is also Gaussian but with narrower width as a result of anticorrelated fluctuations between circular components [see Fig. 5.6(a)]. The PDF of the lasing component, in panel (d), and the total intensity are similar. Hence, the fluctuations of the total intensity, circular components, and the lasing component can be described by Ornstein-Uhlenbeck stochastic processes, which their associated Fokker-Planck equations have Gaussian distributions as stationary solutions. However, we observe in Fig. 5.6(c) that the fluctuations of the nonlasing component prefer intensity levels lower than the mean value. In addition, the associated PDF displays a single-sided exponential decay like that of “thermal” fluctuations.

The power spectrum of the total intensity and the linear lasing component has a peak located at the RO frequency, as can be seen in Fig. 5.5(b, d). However, the CO peak is not present in this case. While the lasing component captures nearly all the noise at high frequency, the power spectrum of the nonlasing component has a small contribution to the total noise at high frequencies, displaying a clear Lorentzian de-

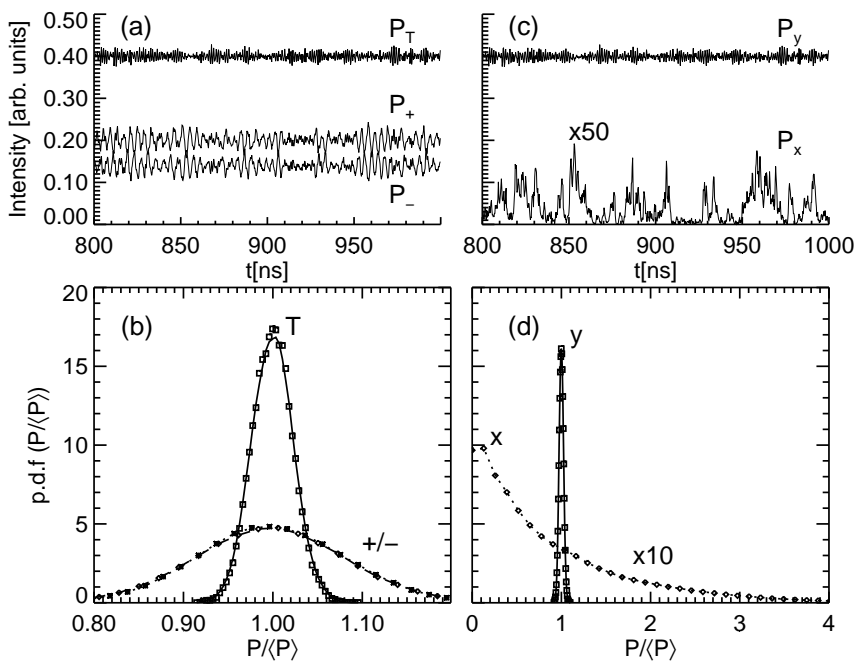


Figure 5.6. (a) Temporal trace of the total intensity P_T and the circular components P_{\pm} . Note that the P_- has been vertically shifted to aid the eye. (b) Probability density function (PDF) for P_T, P_{\pm} . (c) Temporal trace of the lasing P_x and nonlasing fluctuations P_y . (d) Probability density function (PDF) for P_x, P_y . The same parameters as in Fig. 5.5(a,b).

cay [162]. For weak birefringence, the nonlasing component also display a small peak close to the frequency beating between Ω_R and Ω_P . The power spectrum of the total intensity results from the superposition of the fluctuations of the lasing and non-lasing components. The behavior at the MHz frequencies requires a more subtle study. The noise in the two polarization components can exceed the total noise by several orders of magnitude at low frequencies. This particular behavior occurs in LP states with important fluctuations in the polarization orientation, yielding relative high values of the partition noise $M \equiv \overline{P}_{nl}/\overline{P}_l$. Below the PS, in the coexistence regime, strong anticorrelated fluctuations appear at low frequencies [Fig. 5.5(b)]. On the contrary, above the PS, M decreases and anticorrelation nearly vanishes as can be seen in Fig. 5.5(d). PPN has been claimed to be sensitive to the parameter M [145].

We showed that the circular components phase-lock to a relative phase $\phi = \phi_+ - \phi_-$. However, phase-locking among linear components is not possible because they operate at different frequency due to the birefringence. By expressing the linear components of the electric field through $E_{x,y} = \sqrt{P_{x,y}} e^{i\phi_{x,y}}$, the relative phase $\phi_x - \phi_y$ evolves at a typical time scales of $\sim 2\gamma_p$. It is then possible, by invoking the limit of large γ_p , to eliminate the information carried by the phase dynamics and reduce the SFM to equations describing a two-mode laser [159, 166]. An approximate expression for M can be determined from a simplified version of the SFM based on a high-friction or low mass limit Kramers' problem. In this limit, the expression for M reads [160]

$$M \sim \frac{\gamma_s \beta_{sp}}{\kappa(\mu - D_0)},$$

which tells that the noise in the nonlasing component increases when the noise strength is increased, when operating close-to-threshold, and when large values of the spin-flip rate are considered.

5.6 Fluctuation of the Polarization Angles

In order to study polarization fluctuations, it is convenient to express the electric field in terms of the polarization orientation ϕ and ellipticity χ angles

$$\begin{aligned} \vec{\mathcal{E}}(t) = & \sqrt{P} [(\cos \chi \cos \phi - i \sin \chi \sin \phi) \hat{\mathbf{x}} \\ & + (\cos \chi \sin \phi + i \sin \chi \cos \phi) \hat{\mathbf{y}}] e^{-i(\Omega t + \varphi_0)}, \end{aligned} \quad (5.24)$$

or alternatively in the circular representation⁶

$$\vec{\mathcal{E}}(t) = \sqrt{\frac{P}{2}} [(\cos \chi + \sin \chi) e^{-i\phi} \hat{\mathbf{e}}_+ + (\cos \chi - \sin \chi) e^{i\phi} \hat{\mathbf{e}}_-] e^{-i(\Omega t + \varphi_0)}, \quad (5.25)$$

⁶The unitary circular vectors read $\hat{\mathbf{e}}_{\pm} = \frac{1}{\sqrt{2}}(\hat{\mathbf{x}} \mp i\hat{\mathbf{y}})$.

P being the total power and φ_0 an arbitrary phase. The meaning of these two angles become more clear by introducing the Stokes parameters S_j defined by the following relationships

$$S_0 = |E_+|^2 + |E_-|^2 = |E_x|^2 + |E_y|^2 = P, \quad (5.26a)$$

$$S_1 = 2\text{Re}(E_+E_-^*) = |E_x|^2 - |E_y|^2 = P \cos(2\phi) \cos(2\chi), \quad (5.26b)$$

$$S_2 = -2\text{Im}(E_+E_-^*) = -2\text{Re}(E_x^*E_y) = P \sin(2\phi) \cos(2\chi), \quad (5.26c)$$

$$S_3 = |E_+|^2 - |E_-|^2 = -2\text{Im}(E_x^*E_y) = P \sin(2\chi). \quad (5.26d)$$

Hence S_j/S_0 for $j = 1, 2, 3$ describes the Cartesian components of a unit sphere. The spherical coordinates are the polarization angle $2\phi \in [0, 2\pi]$ and the ellipticity angle $2\chi \in [-\pi/2, \pi/2]$. The polarized light is such that the relation $S_0^2 = S_1^2 + S_2^2 + S_3^2$ is fulfilled at any time.

In the steady state, $\phi = 0(\phi = \pi/2)$ for a \hat{x} -LP (\hat{y} -LP) and $\chi = 0$. Fluctuations of the polarization angles around LP states are obtained by linearizing Eq. (5.25). We find that

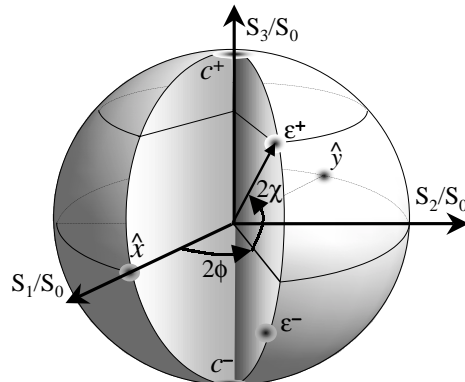
$$\delta\chi = \frac{R + R^*}{4Q}, \quad \delta\phi = i \frac{(R - R^*)}{4Q}, \quad (5.27)$$

where R and R^* were defined in Pag. 111. Equation (5.27) reveals the connection between the ellipticity fluctuations and the power fluctuations of the circular components.

The fluctuations in $\delta\phi$ and $\delta\chi$ are governed by

$$\begin{pmatrix} \dot{\delta\phi} \\ \dot{\delta\chi} \\ \dot{\delta} \end{pmatrix} = \begin{pmatrix} \pm 2\gamma_a & \mp 2\gamma_p & \alpha\kappa \\ \pm 2\gamma_p & \pm 2\gamma_a & \kappa \\ 0 & -4\gamma_e D_0 Q^2 & -(\gamma_s + 2\gamma_e Q^2) \end{pmatrix} \begin{pmatrix} \delta\phi \\ \delta\chi \\ \delta \end{pmatrix} + \begin{pmatrix} F_\phi \\ F_\chi \\ F_\delta \end{pmatrix} \quad (5.28)$$

Figure 5.7. Poincaré sphere: $x(y)$ -LP state along the $\hat{x}(\hat{y})$ direction; c^\pm are right and left circularly polarized states, ε^\pm are right and left elliptically polarized states. Shaded circles represent fluctuations around these states.



which is directly obtained from Eqs. (5.15) and (5.27). The real Langevin terms obey

$$\begin{aligned}
\langle F_\phi(t)F_\phi(t') \rangle &= \langle F_\chi(t)F_\chi(t') \rangle = \frac{\gamma_e\beta_{sp}D_0}{2Q^2}\delta(t-t'), \\
\langle F_\delta(t)F_\delta(t') \rangle &= \left(\frac{\gamma_e}{\kappa}\right)^2 2\beta_{sp}D_0Q^2\delta(t-t'), \\
\langle F_\chi(t)F_\delta(t') \rangle &= \frac{\gamma_e^2\beta_{sp}D_0}{\kappa}\delta(t-t'), \\
\langle F_\phi(t)F_\chi(t') \rangle &= \langle F_\phi(t)F_\delta(t') \rangle = \langle F_\phi(t)F_\chi(t') \rangle = 0.
\end{aligned} \tag{5.29}$$

Equation (5.28) is the starting point of other works that, by invoking the limit of large γ_s , i.e. $\dot{\delta} \approx 0$, reduce the dimensionality to two. In this limit, the fluctuations of δ are slaved to the fluctuations of $\delta\chi$

$$\delta(t) \approx \frac{-4\gamma_e D_0 Q^2}{\gamma_s + 2\gamma_e Q^2} \delta\chi(t) + \frac{F_\delta(t)}{\gamma_s + 2\gamma_e Q^2}.$$

It is worth noting that such an approximation is only justified well within the COs region. In spite of generality, we maintain the dynamics of $\delta(t)$, which allows us to analyze fluctuations for any value of γ_s .

The spectral density of the polarization fluctuations is obtained by solving the linear system of Eq. (5.28) in the Fourier domain. The result is

$$S_\Xi(\omega) = \frac{\gamma_e\beta_{sp}D_0}{2Q^2} \left[\frac{\mathcal{A}_\Xi(\omega) + \mathcal{B}_\Xi(\omega)}{\mathcal{C}(\omega)} \right] \tag{5.30}$$

where $\Xi = \phi, \chi, \delta$ and $\mathcal{A}, \mathcal{B}, \mathcal{C}$ are polynomial functions of ω defined in the Appendix D.

Some other interesting relationships, connecting the fluctuations of the polarization components and polarization angles, can be obtained upon linearization of Eqs. (5.26a)–(5.26d)

$$S_q(\omega) = 4Q^2 S_\chi(\omega), \tag{5.31a}$$

$$S_+(\omega) = S_-(\omega) = \frac{1}{4} S_P(\omega) + Q^2 S_\chi(\omega), \tag{5.31b}$$

$$\begin{aligned}
M &\equiv \left\langle \frac{P_{nl}}{P_l} \right\rangle \approx \langle |\delta\phi(t)|^2 \rangle + \langle |\delta\chi(t)|^2 \rangle = \\
&= \frac{1}{2\pi} \int_{-\infty}^{\infty} [S_\phi(\omega) + S_\chi(\omega)] d\omega.
\end{aligned} \tag{5.31c}$$

First, we consider a situation where a PS takes place within a region of COs. The power spectra of the polarization fluctuations, $S_\phi(\omega)$, $S_\chi(\omega)$, $S_\delta(\omega)$ in Fig. 5.8, display a single peak at the COs frequency Ω_P . Note that the peak at Ω_R is absent in all

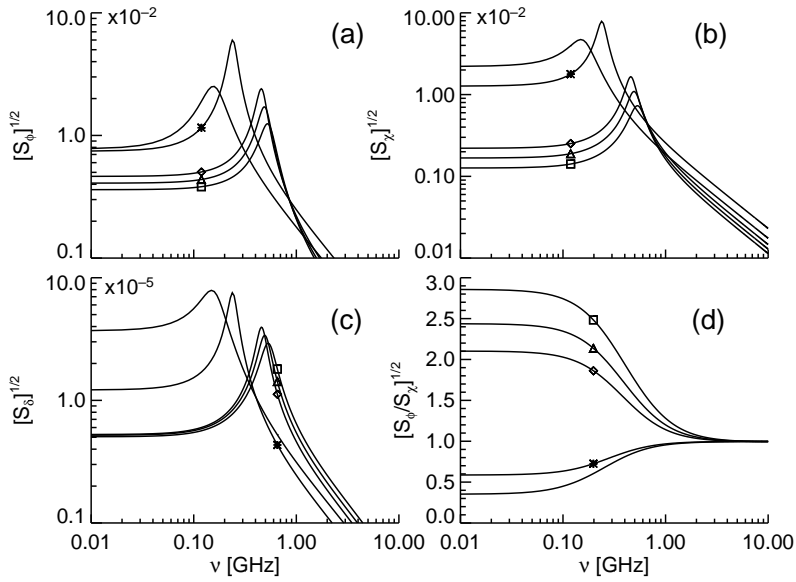


Figure 5.8. Power spectra (in arbitrary units) of the polarization fluctuations, (a) $S_\phi(\omega)$, (b) $S_\chi(\omega)$, (c) $S_\delta(\omega)$ and (d) the ratio $S_\phi(\omega)/S_\chi(\omega)$. The same parameters as in Fig. 5.5(a,b), corresponding to a COs region and when crossing a PS. Meaning of the symbols: (*) $\mu = 1.030$, (no symbol) $\mu = 1.048$, (\diamond) $\mu = 1.075$, (\triangle) $\mu = 1.120$, (\square) $\mu = 1.20$. The switching occurs for $\mu_{sw} \approx 1.066$. The LF solution is considered below PS while the HF solution is the only stable above the PS.

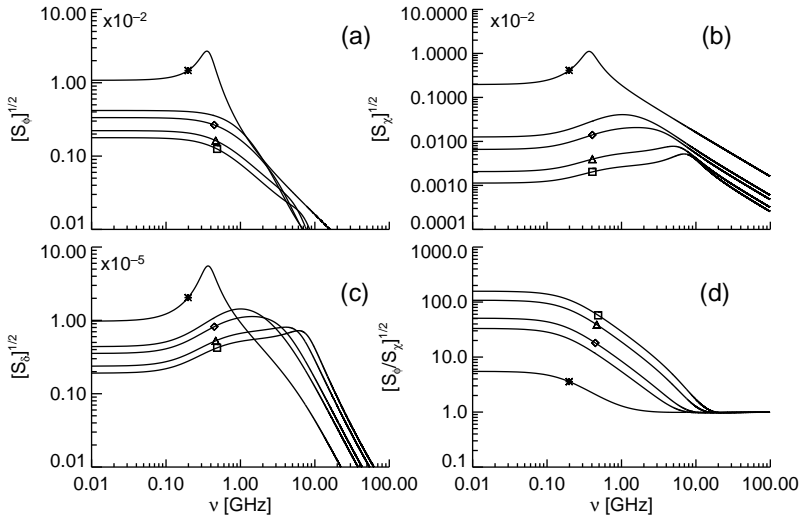


Figure 5.9. Power spectra (in arbitrary units) of the polarization fluctuations, (a) $S_\phi(\omega)$, (b) $S_\chi(\omega)$, (c) $S_\delta(\omega)$ and (d) the ratio $S_\phi(\omega)/S_\chi(\omega)$. The parameters correspond to the situation described in Fig. B.1(b), taking $\gamma_s/\gamma = 40$. The HF solution is considered for different currents: (*) $\mu = 1.04$, (no symbol) $\mu = 1.45$, (\diamond) $\mu = 2.08$, (\triangle) $\mu = 3.12$, (\square) $\mu = 5.00$.

the cases. When increasing the injection current from threshold up to PS, the LF solution lases and the frequency Ω_P decreases while the effective dichroism increases reflecting itself in broad peaks in the power spectra. Below the PS, the fluctuations in the ellipticity angle are considerably larger than in the polarization orientation, being reflected in the ratio $S_\phi(\omega)/S_\chi(\omega)$ shown in Fig. 5.8(d). Once the PS takes place, the HF solution starts to lase and the frequency Ω_P increases linearly when increasing the current level. We also note that in this situation, the peaks are much narrower and the polarization fluctuations prefer the polarization orientation angle. Fig. 5.9 illustrates the behavior of the polarization fluctuations in the limit of small linear anisotropies. PS does not occur in this case and the VCSEL always operates in the HF solution. Close-to-threshold there exists a narrow region of COs that leads to a behavior similar to that already mentioned in Fig. 5.8. For higher injection levels a region of PROs appears, where the fluctuations in the polarization angle ϕ decouple and experience a damped relaxation without oscillation. Consequently, the power spectra of $S_\phi(\omega)$ does not display any peak, while $S_\chi(\omega)$, $S_\delta(\omega)$ have a peak at the PROs frequency, rather broad due to the relatively large damping.

5.7 Role of the Spin-Flip and Birefringence

Since our theoretical description is valid for arbitrary values of the birefringence and spin-flip rate, in this section we give a complete description of the role of these parameters. We look at the power spectra while the polarization state is followed on the Poincaré sphere.

Power spectra for small and large values of γ_s , in the absence of birefringence, are shown in Fig. 5.10. As expected, the CO peak is absent in the power spectra of the circular components [See Fig. 5.10(a,d)]. The main difference between the two cases appears at low frequency: while P_\pm have large anticorrelation for large γ_s , this anticorrelation is reduced for small γ_s . This effect can be understood as follows: for slow spin-flip rates each one of the two circular components burns carriers from its own reservoir N_\pm separately. In this case there is no competition and therefore small anticorrelated fluctuations are observed in Fig. 5.10(a). On the other hand, for fast spin-flip rates, the two circular components have to share almost the same carrier reservoir since $N_+ \approx N_-$. The latter causes strong anticorrelation because of polarization partition noise [Fig. 5.10(d)]. The power spectra of the two linear components coincide displaying a similar trend for any γ_s [Fig. 5.10(b,e)]. They show pronounced anticorrelations at low frequencies linked to important fluctuations of the polarization orientation. Both spectra display a peak at the relaxation oscillation frequency.

The role of the birefringence is shown in Fig. 5.11 for a fixed value of the spin-flip rate. For small birefringence, $\gamma_p = 0.1 \text{ ns}^{-1}$, we observe large anticorrelation of

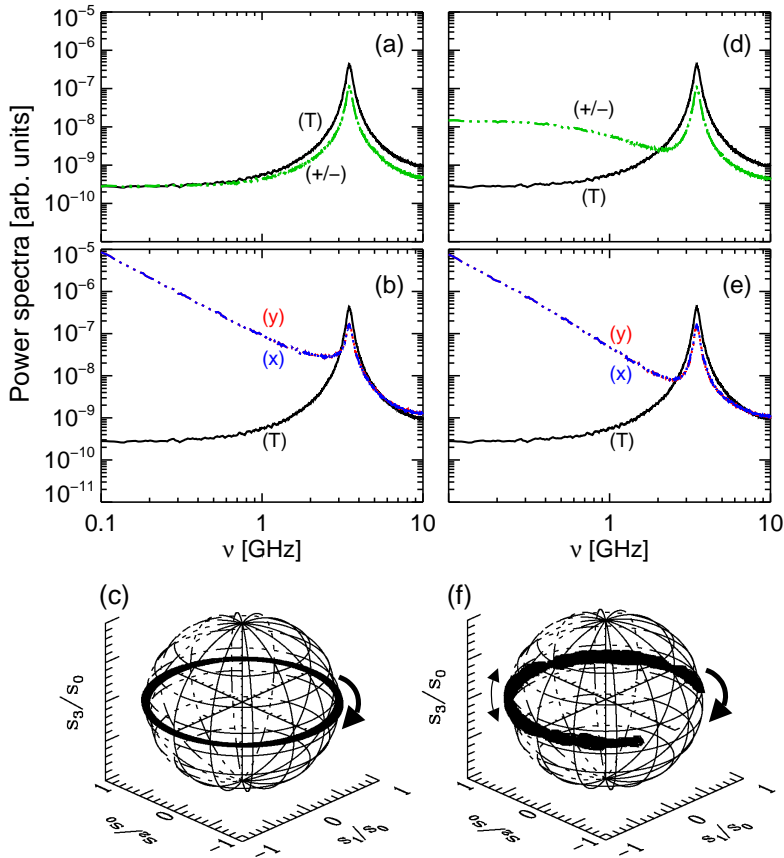


Figure 5.10. Study of the effect of γ_s in the absence of birefringence, in the power spectra of the circular (a,d) and linear components (b,e). Evolution of the polarization state on the Poincaré sphere (c,f) for small values of the spin-flip rate $\gamma_s = 10 \text{ ns}^{-1}$ in (a,c), $\gamma_s = 100 \text{ ns}^{-1}$ in (d,f). The normalized current is $\mu = 1.8$. The meaning of the symbols is: (T) = S_P , (+/-) = S_{\pm} , (x) = S_x and (y) = S_y . The average is performed over different initial conditions and noise realizations.

the circular and linear components at low frequencies [Fig. 5.11(a,b)]. This fact indicates important polarization fluctuations. The main role of the birefringence is to fix a polarization orientation, thus reducing the polarization fluctuations. For a larger birefringence, $\gamma_p = 10 \text{ ns}^{-1}$, we observe that the anticorrelation of the circular components has been considerably reduced [Fig. 5.11(d)] being negligible for the linear components [Fig. 5.11(e)]. We note that a PS occurs when the birefringence is increased and the fluctuations on the Poincaré sphere move to the opposite direction on the equator of the sphere. In addition, the CO peak appears at larger frequency than the RO one.

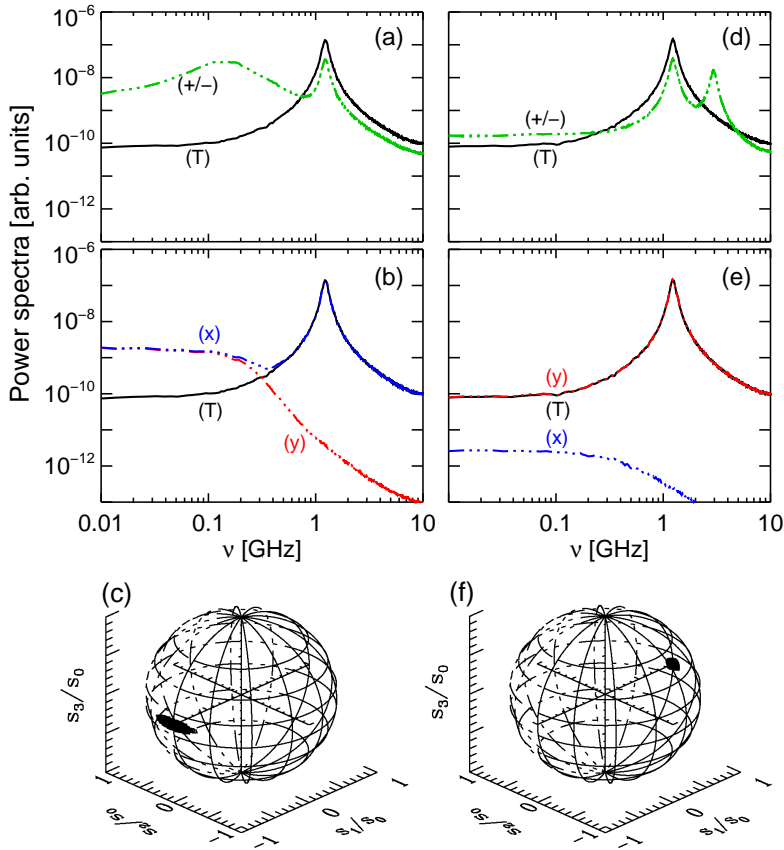


Figure 5.11. Study of the effect of γ_p on power spectra of the circular (a,d) and linear (b,e) components when $\gamma_s = 50 \text{ ns}^{-1}$. Evolution on the Poincaré sphere for small birefringence $\gamma_p = 0.1 \text{ ns}^{-1}$ (a,c) and $\gamma_p = 10 \text{ ns}^{-1}$ (d,f). The normalized current is $\mu = 1.1$. The meaning of the symbols is the same as in Fig. 5.10.

It is also illustrative to analyze the evolution of the polarization state on the Poincaré sphere [Fig. 5.7]. We observe that for small γ_p the fluctuations prefer the equatorial direction [Fig. 5.11(c)]. In the limiting case of $\gamma_p=0$, there is a zero eigenvalue of Eq. (5.16) associated with the arbitrariness of the polarization orientation, and the polarization diffuses along LP states with different orientation angles due to the presence of noise. The polarization evolves along the equator of the sphere with small ellipticity fluctuations controlled by γ_s [Fig. 5.10(c,f)]. When γ_s is large, the two remaining eigenvalues become real. One of them approaches to zero when $\gamma_s \rightarrow \infty$, describing diffusion of the ellipticity angle. In the latter, there is no preference for any polarization state and the fluctuations cover the whole surface of the Poincaré sphere [186]. When $\gamma_p \neq 0$, the eigenvalue that describes the diffusion of the po-

larization orientation angle becomes nonzero, providing the stability of the steady state. For moderate to large values of γ_p , we observe that the polarization orientation is fixed and the fluctuations on the Poincaré sphere have a rather circular shape [Fig. 5.11(f)].

5.8 Polarization Anticorrelations

To better characterize the correlations among two orthogonal components we compute the normalized cross-power spectral density [163] which reads

$$C_{AB}(\omega) = \frac{S_{A+B}(\omega) - S_A(\omega) - S_B(\omega)}{2\sqrt{S_A(\omega)S_B(\omega)}}, \quad (5.32)$$

where $A(t)$ and $B(t)$ are two given signals, while S_A and S_B represent their respective power spectra. $C_{AB}(\omega) = 1$ (-1) corresponds to perfect correlation (anticorrelation) in the fluctuations of the two signals. The normalized cross-power spectral density between the power fluctuations of the two circular components δP_+ and δP_-

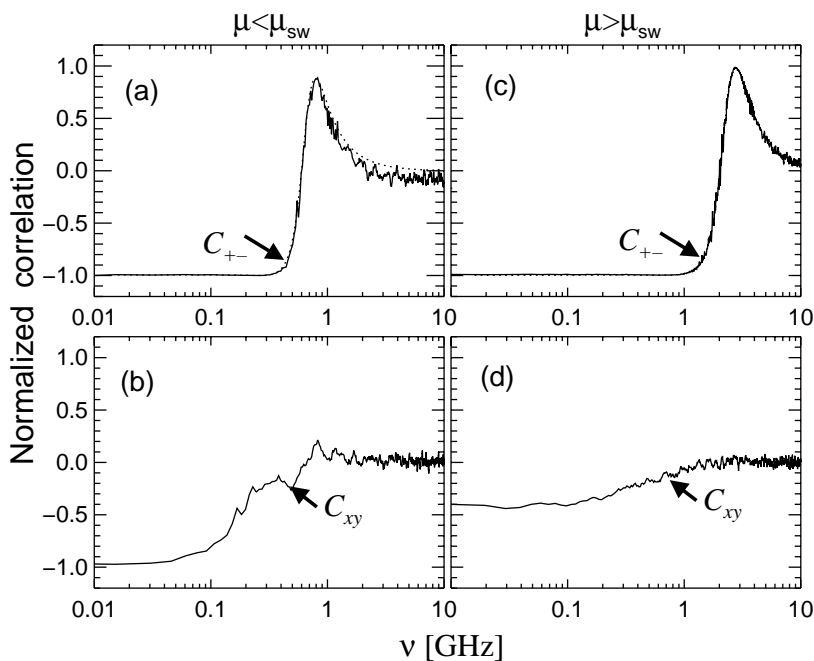


Figure 5.12. Normalized crosscorrelation of the circular components C_{+-} (a,c) and of the linear components C_{xy} (b,d) corresponding to the same situation as in Fig. 5.5. Dotted lines in (a,c) represent theoretical prediction given by Eq. (5.33).

can be obtained from

$$\begin{aligned}
 C_{+-}(\omega) &= \frac{S_P(\omega) - S_q(\omega)}{S_P(\omega) + S_q(\omega)} \\
 &= \frac{\operatorname{Re} \int_{-\infty}^{\infty} \langle \delta \tilde{P}_+(\omega) \delta \tilde{P}_-^*(\omega') \rangle d\omega'}{\int_{-\infty}^{\infty} \langle \delta \tilde{P}_{\pm}(\omega) \delta \tilde{P}_{\pm}^*(\omega') \rangle d\omega'}.
 \end{aligned} \tag{5.33}$$

By replacing the expressions for $S_P(\omega)$ and $S_q(\omega)$ from Eqs. (5.20a) and (5.20b) into Eq. (5.33) we obtain the exact expression for C_{+-} . This expression can be simplified at low frequencies in the case of close to perfect anticorrelation, i.e., $C_{+-}(\omega \approx 0) \approx -1$, to

$$C_{+-}(\omega = 0) \approx -1 + \frac{1}{2Q^4} \frac{\left[\frac{\gamma_P}{\kappa} \Gamma - \varepsilon \alpha \right]^2}{[\alpha^2 + \Gamma^2]}, \tag{5.34}$$

with $\Gamma \equiv \gamma_s / (2\gamma_e Q^2)$. It is easy to see from Eq. (5.33) that the fluctuations are correlated at the frequency where $S_P(\omega) \gg S_q(\omega)$, close to Ω_R , whereas the fluctuations are anticorrelated when $S_P(\omega) \ll S_q(\omega)$, near the CO peak Ω_P . We can interpret these two limits with the help of the Poincaré sphere. The fluctuations of the total number of photons are linked to movements perpendicular to the Poincaré sphere surface [Fig. 5.7]. These movements are equivalent for all the points on the sphere, and therefore provide correlation between circular components. Anticorrelations between components are associated with movements on the Poincaré sphere, i.e., polarization orientation and ellipticity fluctuations.

In Fig. 5.12 we show the results for the normalized crosscorrelation function, Eq. (5.33), under the same conditions as in Fig. 5.5. In the circular basis C_{+-} , we find close to perfect anticorrelations for low frequencies, and strongly correlated fluctuations ($C_{+-} \approx 1$) for frequencies close to the RO peak. In the linear basis, C_{xy} displays partially anticorrelated fluctuations at low frequency ($\nu \leq 1$ GHz) due to polarization partition noise [145, 187] above the PS, and large anticorrelation below the PS which corresponds to the two LP states being stable. The lack of anticorrelation above PS might be attributed to the modification of the effective birefringence due to the nonlinearities when the injection current is increased. Below the PS, the effective birefringence Ω_P/π , reaches a minimum. This fact leads to preferential fluctuations of the polarization orientation, and consequently anticorrelated fluctuations of the linear components. On the contrary, above the PS, the effective birefringence gradually increases with increasing distance from the PS leading to a reduction of the anticorrelation.

5.9 Summary, Discussion and Perspectives

The polarization field vector of vertical-cavity surface-emitting lasers (VCSELs) has been investigated within a model that considers optical transitions among the magnetic sub-levels of the conduction and valence bands of QW-semiconductors, namely, the spin-flip Model (SFM) introduced by San Miguel-Feng-Moloney in 1995. We put forward the governing equations that apply for single longitudinal VCSELs operating in the fundamental transverse mode. We justified, from the fluctuation-dissipation theorem, the semiclassical Langevin noise sources that arise from spontaneous emission processes. The linearization of the SFM, when considering fluctuations around stationary linearly polarized solutions, was introduced as the starting point for a later investigation of intensity and polarization fluctuations. We concentrated our discussion in those physical parameters that can be relevant in the polarization mode selection and in the determination of the polarization fluctuations.

We have presented analytical and numerical investigations of the polarization resolved power spectra of the linearly-polarized states based on a semiclassical framework, valid for arbitrary values of the spin-flip rate and birefringence. It constitutes a generalization of previous studies where the adiabatic elimination of the spin dynamics was taken. A proper classification of the regimes of operation in terms of the eigenvalues and eigenvectors of the linearized systems has been useful for the subsequent formulation and interpretation of the polarization fluctuations. Two qualitative different regimes of operation were observed, namely *polarization relaxation oscillations* of the ellipticity angle and carrier difference (PROs), and *coupled oscillations* of the polarization angles (COs). Most of the reported results apply to VCSELs operating in the COs regime but the access to the PROs is just a matter of parameters: the current level and the spin-flip rate. We have presented specific results for the power spectra of linearly polarized states when the VCSEL is driven across a non-thermal polarization switching. The power spectrum of the total intensity fluctuations displays a peak at the relaxation oscillation frequency. In the regime of coupled oscillations, the power spectra of the two circular components coincide and show an additional peak associated with the effective birefringence splitting. When analyzing the evolution of the polarization state on the Poincaré sphere, we were able to separate the effects of the birefringence and the spin-flip rate. In the absence of birefringence, the spin-flip rate controls the ellipticity fluctuations that are related to the fluctuations of the circular components. On the other hand, for a fixed spin-flip rate the birefringence controls the polarization orientation fluctuations. The frequency dependence of the normalized cross-correlation function for both linear and circular components was also presented. In particular, we found that the two circular components are strongly anticorrelated at low frequencies while they display a nearly

perfect correlation close to the relaxation oscillation peak. The linear components (lasing and nonlasing) present a nonvanishing crosscorrelation function at low frequencies. Linear components display partially anticorrelated fluctuations below the polarization switching which correspond to the two linearly polarized states being stable. Above the polarization switching, the anticorrelation nearly vanishes being attributed to an abrupt increase of the effective birefringence that reduces the magnitude of the polarization fluctuations. Further investigations of the polarization resolved power spectra of elliptical and dynamical states, where the total intensity and polarization fluctuations do not decouple, should provide a complete understanding of the noise properties of vertical-cavity surface-emitting lasers.

Although our semiclassical analysis of fluctuations is consistent with quantum noise sources, there are several aspects that become important to achieve quantum noise levels, such as the standard quantum limit and quantum squeezing. They include shot noise in the carrier recombination, statistics of the pump fluctuation and interference of the vacuum field entering in to the VCSEL cavity (input-output formalism [188]). Notwithstanding, the semiclassical approach have led to valuable theoretical predictions that successfully compares with the experiments, namely: polarization switching from the low frequency to the high frequency mode of nonthermal origin, existence of anticorrelated fluctuations between the polarization components, interpretation of the characteristic frequencies in the power spectra, nonlinear anisotropies, etc. Hence, our study should establish the elementary concepts for further investigation based on sophisticated fully quantum-mechanical models.

There exist however several hypothesis when deriving the SFM rate equations, some of them have been already commented, that fix the limits of applicability. Some of the more restrictive are

- *Flat gain spectrum:* When replacing the band structure of the semiconductor material by a four-level system, we lose the contribution of the possible optical transitions at electron wavevectors $k_{\perp} \neq 0$. The resulting gain spectrum that results has a Lorentzian shape –typical of an atomic system–. This spectrum becomes flat when invoking the limit of large γ_{\perp} , i.e., when the material polarization is adiabatically eliminated.
- *α -factor:* The α -factor in a two-level system has to be artificially introduced as the normalized frequency detuning with respect to the gain peak. Operation on the blue side of the gain spectrum ($\Omega > \omega_g$) leads to negative values for the α -factor and to carrier-guiding, being in contradiction with the basic properties of semiconductor lasers. Moreover, the α -factor in a quantum well semiconductor laser is not a constant, but in general, a function of the frequency and the carrier inversion.

- *Transverse effects:* The standard SFM assumes fundamental transverse mode operation. However, it is commonly observed that high-order transverse modes start to appear when the VCSEL is driven far from the threshold current. Transverse effects inherently occur in a quite broad frequency-band and involve inhomogeneous carrier distributions; thus a correct description of the gain and α -factor spectra is essential.
- *Thermal effects:* The SFM assumes constant active region operation. However, two thermal effects appear when the injection current increases. First, when the current flows through the VCSEL structure, predominantly heats the spatial zone close to the cavity axis, which leads to an inhomogeneous temperature distribution across the lateral direction. And second, the cavity modes and gain curve redshifts due to the temperature dependence of the materials composing the VCSEL.

In the following chapter we account for some of these effects by developing a dressed SFM. This model will include: realistic gain and refractive index spectra of QWs, realistic α -factor for the quantum well, carrier-antiguinding, thermal effects, transverse and polarization dynamics. The resulting model will be suitable for investigating large-signal dynamics.

Chapter 6

Spatiotemporal Modeling of the Optical Properties of VCSELs

6.1 Introduction

Most¹ studies of polarization dynamics have been concerned with devices where the spatial degrees of freedom can be disregarded, e.g., small active-region diameter devices subject to moderate injection currents. A first explanation for the observed polarization dynamics and instabilities was put forward by Choquette and coworkers [189, 190]. Their main argument was that, due to residual cavity anisotropies, linearly-polarized modes experience different net modal gains, and consequently at threshold the mode with larger gain (usually that closest to the gain peak) is selected. However, as the current is increased the temperature of device also increases, leading to a redshift of the gain curve relative to the linearly polarized modes that may cause a polarization switching from the high-frequency mode to the low-frequency mode. This model has been further extended to account for the effects of thermal lensing, gain-dispersion and temperature-dependent free-carrier absorption [176, 191]. A different kind of explanation for polarization switching in singlemode devices is given by the so-called Spin-Flip Model (SFM) [37] that has been used in the preceding chapter to analyze polarization fluctuations across a nonthermal polarization switching. The SFM explains the polarization switching in vertical-cavity surface-emitting lasers (VCSELs) as the result of an instability of the phase-locking among the circularly-polarized components of the optical field that arises

¹ This chapter is based on the papers:

J. Mulet and S. Balle, *IEEE J. Quantum Electron* **38**, 291 (2002);

J. Mulet, C. R. Mirasso, S. Balle, and M. San Miguel, *Proc. SPIE* **4283**, 139 (2001).

from the coupling between amplitude and phase through the linewidth enhancement factor. The SFM has been extensively applied to analyze the polarization selection and instabilities: the interplay of linear and nonlinear cavity anisotropies in polarization switching, the influence of magnetic fields [30], polarization mode hopping, and the polarization resolved intensity noise [192]. Recently, the SFM has been justified from a microscopic point of view [193] and it has also been extended for including the frequency-dependence of the carrier-induced gain and refractive index, showing [183, 194] that the thermal mechanism discussed before and that coming from phase instabilities can coexist in some VCSELs.

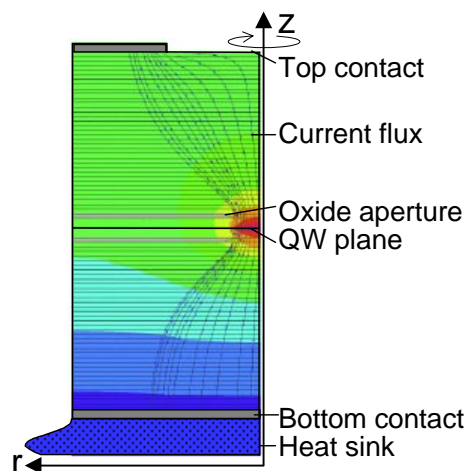
On the other hand, several methods have been recently devised to analyze the cavity modes of VCSELs in a scalar, semi-vectorial or fully-vectorial description [195]-[199]. These methods are able to determine the modal frequencies, profiles and threshold gains from the distribution of index of refraction associated with a given device structure. However, they cannot be directly applied to the study of spatiotemporal dynamics of the system because these methods are passive and static, so that they disregard the coupling of the optical field with the carrier density and the associated index change through spatial hole burning, which has been found to be relevant in VCSELs despite the presence of other guiding mechanisms [200]. Moreover, the index of refraction of the materials defining the cavity is temperature dependent, hence the refractive index distribution changes as the current increases due to device self-heating (Joule heat dissipation). Heat is generated mainly close to the cavity axis, so a radial profile of temperature develops with higher temperatures close to the cavity axis [Fig. 6.1]. As a consequence, besides a global increase of the average index that is responsible for the observed redshift of the cavity modes, the refractive index is higher at the center of the device than in the outer regions, a phenomenon known as thermal lensing (TL). TL effects are usually weak, since the thermal rate of change in index of refraction is $|\partial n/\partial T|_{\lambda} \sim 5 \times 10^{-4} K^{-1}$. Nevertheless, TL can strongly influence the transverse mode properties in weakly-index guided lasers —such as oxidized VCSELs with the oxide layer placed close to a field node— or purely gain-guided diode lasers which do not possess any built-in index waveguide and where lateral confinement of the optical field occurs only via a combination of gain-guiding and index anti-guiding mechanisms [38, 200].

In order to model the dynamics of VCSELs with spatial degrees of freedom, a modal expansion of the electric field is often used [156, 201], thereby including spatial holeburning effects. However, a drawback of such an approach is that the number and type of modes considered in the description has to be fixed and determined *a priori*, and usually only a few low order modes are included. In the following chapter we will identify the limitations of an optical modal expansion when describing the transverse mode structure in gain-guided devices. In relatively large VCSELs that

support several transverse modes, some of which may have quite similar frequencies, it is preferable to directly investigate the spatiotemporal dynamics of the optical field, either considering [202, 203] or not [204, 205] the polarization of the optical field. The inclusion of transverse effects in the dynamics of multimode VCSELs requires the consideration of the frequency dependence of both gain and refractive index of the material that constitutes the active region. In addition, they should also correctly incorporate the nonlinear dependence on the carrier density because of the inhomogeneous carrier distribution arising from the localized injected current. The most natural way to incorporate both the gain and refractive index is through the optical susceptibility of the active region, which could be obtained in either a microscopic [206]-[210] or mesoscopic framework [211]-[213]. The former gives a very accurate description but requires a huge computational effort; the latter, despite approximations, can provide an accurate description of the active medium and allows to be included directly into the laser dynamics [183, 210, 214].

In this chapter, we develop an optical dynamical model for VCSELs which describes, in an unified way, polarization and spatial effects. In section 6.2 we present a detailed description of the optical model, which generalizes the SFM in order to include i) the spatial dependence of both the field and carrier densities and ii) a susceptibility tensor that describes the frequency-dependence of the gain and refractive index distributions induced by the carriers. The model is based on equations for the lateral dependence of the slowly-varying amplitudes of the optical field in both circular polarization components, and equations for the carrier density in both spin orientations. In its present form, the model assumes a given functional dependence of the guiding mechanisms (built-in refractive index and thermal lensing) as well as the spatial dependence of the current density. Section 6.5 discusses the selection of po-

Figure 6.1. Temperature distribution in a top-emitting VCSEL using a color scheme from blue (coldest) to red (hottest). Arrows indicate the current flux from the top to the bottom electric contacts.



larization modes when spatial effects are disregarded. In section 6.6 we analytically and numerically investigate the selection of transverse modes for close-to-threshold operation. In section 6.7 we present the results for the subnanosecond electrical excitation. Finally, section 6.8 is devoted to summarizing and concluding the chapter.

6.2 Optical model

In order to obtain our dynamical model for the VCSEL taking into account both the polarization and transverse degrees of freedom, we recall the concepts outlined in Sec. 5.2. We start from Maxwell's equations in the frequency domain assuming that, in gain-guided devices, the optical field inside the VCSEL cavity can be considered as almost totally polarized in the plane perpendicular to the cavity axis [Fig. 6.2]. The optical susceptibility of the active region is diagonal in the basis of circularly-polarized states of the optical field, resulting in a simplified description of the dynamical interaction with the active material. It is then also natural to distinguish between spin-up and spin-down electrons and holes densities, since they couple to optical transitions with opposite circular polarization. After determining the optical carrier frequency of the VCSEL emission, we return to the time domain in order to find the dynamical equations for the slowly-varying amplitudes (SVA) of the circularly-polarized optical field components.

From Maxwell's equations in the frequency domain, the distribution of each linearly-polarized component of the optical field, $\tilde{\mathcal{E}}_k(\vec{r}; \omega)$ (with $k = \hat{x}, \hat{y}$) is given

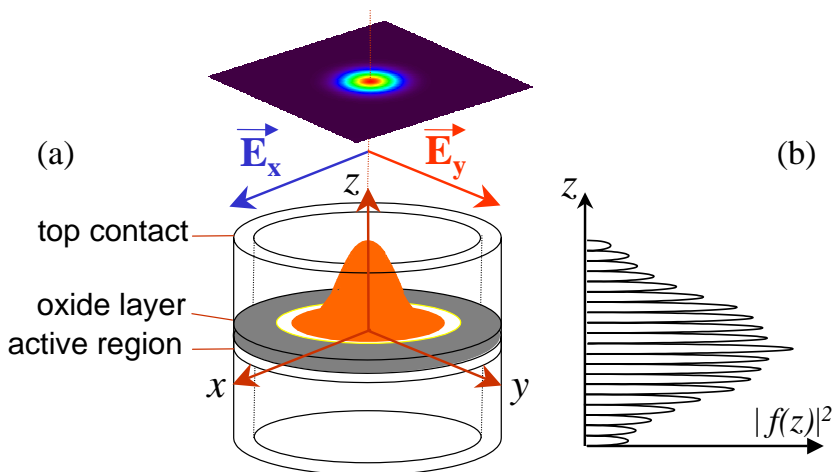


Figure 6.2. (a) Polarization of the field vector in the VCSEL cavity. The oxide layer determines the active region and the shape of the optical mode which is displayed Gaussian. (b) Standing longitudinal wave.

by

$$\left\{ \nabla_{\perp}^2 + \partial_z^2 + \frac{\omega^2}{c^2} [1 + \chi_b^k(\vec{r}; \omega)] \right\} \tilde{\mathcal{E}}_k(\vec{r}; \omega) = -\frac{\omega^2}{c^2} \left\{ \frac{\tilde{\mathcal{P}}_k(\vec{r}; \omega)}{\varepsilon_0} - \chi_b^k(\vec{r}; \omega) \tilde{\mathcal{E}}_k(\vec{r}; \omega) \right\} R_W(z, z_0), \quad (6.1)$$

where $\nabla_{\perp}^2 = \partial_x^2 + \partial_y^2$ and $\chi_b^k(\vec{r}; \omega)$ is the frequency dependent susceptibility distribution of the passive material filling the cavity for a field polarized along the k -direction. $\tilde{\mathcal{P}}_k(\vec{r}; \omega)$ stands for the k -component of the material dipole density due to the active material, thus providing both gain and refraction-index change. $R_W(z, z_0)$ is a rectangle function, which is 1 if $z_0 < z < z_0 + W$ and zero otherwise, that specifies the position of the active region, which we consider made of a single QW whose thickness is W . In the case of multiple QWs, we assume that they are all in the same electrical state, so that the total thickness of the active region is scaled with the number of wells.

By considering that due to the short cavity length L , the VCSEL supports a single longitudinal mode in the vicinity of the gain maximum, the optical field components can be split into their longitudinal and transverse parts,

$$\tilde{\mathcal{E}}_k(\vec{r}; \omega) = \left(e^{iq_k z} + \frac{e^{-iq_k z}}{r_1^k} \right) \tilde{\mathcal{A}}_k(\vec{r}_{\perp}; \omega) \equiv f_k(z) \tilde{\mathcal{A}}_k(\vec{r}_{\perp}; \omega), \quad (6.2)$$

where $\vec{r}_{\perp} = (x, y)$. The longitudinal modes of the VCSEL cavity are determined by the round-trip condition in the plane-wave approximation. For a linearly-polarized wave, it reads

$$r_1^k r_2^k e^{2iq_k L} = 1, \quad (6.3)$$

where q_k stands for the complex propagation constant of the longitudinal mode linearly polarized along the k -direction, with its real and imaginary parts determining the wavelength and threshold gain for this mode, and L is the physical cavity length corresponding to the separation between the two Bragg mirrors. r_1^k and r_2^k denote the frequency-dependent amplitude reflectivities of the top and bottom Bragg reflectors. Moreover, Bragg mirrors contain some residual birefringence, displaying polarization dependent reflectivities $r_{1,2}^x \neq r_{1,2}^y$. This effect provides different propagation constants and, in general, different longitudinal profiles for the two linearly polarized modes.

Upon substitution of Eq. (6.2) into Eq. (6.1) and by projecting onto the longitudinal mode $f_k(z)$, the transverse field distributions in the cavity section, $\tilde{\mathcal{A}}_k(\vec{r}_{\perp}; \omega)$, are given by

$$\left\{ \nabla_{\perp}^2 + \frac{\omega^2}{c^2} [1 + \chi_e^k(\vec{r}_{\perp}; \omega)] - q_k^2 \right\} \tilde{\mathcal{A}}_k(\vec{r}_{\perp}; \omega) = -\frac{\omega^2}{\varepsilon_0 c^2} \tilde{\mathcal{B}}_k(\vec{r}_{\perp}; \omega), \quad (6.4)$$

where we have defined

$$F_k(z) = \frac{e^{iq_k z} + \frac{1}{r_1^k} e^{-iq_k z}}{\sqrt{\int_0^L dz \left| e^{iq_k z} + \frac{1}{r_1^k} e^{-iq_k z} \right|^2}}, \quad (6.5a)$$

$$\chi_e^k(\vec{r}_\perp; \omega) = \int_0^L dz \chi_b^k(\vec{r}; \omega) |F_k(z)|^2 - \int_{z_0}^{z_0+W} dz \chi_b^k(\vec{r}; \omega) |F_k(z)|^2, \quad (6.5b)$$

$$\tilde{\mathcal{B}}_k(\vec{r}_\perp; \omega) = \int_{z_0}^{z_0+W} dz \tilde{\mathcal{P}}_k(\vec{r}; \omega) F_k^*(z). \quad (6.5c)$$

Therefore, $F_k(z)$ represents the normalized longitudinal field profile, χ_e^k the longitudinal average of the passive material's susceptibility, and $\tilde{\mathcal{B}}_k$ the projection of the active material's dipole density onto the corresponding k -component of the longitudinal mode.

As already mentioned, the selection rules for the optical transitions impose the conservation of the axial component of the angular momentum, hence the interaction with the active material is diagonal in the basis of circularly polarized optical states. Therefore we express the optical fields in the basis of left- and right-circularly polarized components

$$\mathcal{A}_\pm = \frac{\mathcal{A}_x \pm i\mathcal{A}_y}{\sqrt{2}}. \quad (6.6)$$

Then, Eq. (6.4) reads

$$\left\{ \nabla_\perp^2 + \frac{\omega^2}{c^2} [1 + \chi_e(\vec{r}_\perp; \omega)] - q^2 \right\} \tilde{\mathcal{A}}_\pm(\vec{r}_\perp; \omega) + \left[\frac{\omega^2}{c^2} \delta\chi_e(\vec{r}_\perp; \omega) - \delta q^2 \right] \tilde{\mathcal{A}}_\mp(\vec{r}_\perp; \omega) = -\frac{\omega^2}{\varepsilon_0 c^2} \tilde{\mathcal{B}}_\pm(\vec{r}_\perp; \omega), \quad (6.7)$$

where we have defined

$$\chi_e(\vec{r}_\perp; \omega) = \frac{\chi_e^x(\vec{r}_\perp; \omega) + \chi_e^y(\vec{r}_\perp; \omega)}{2}, \quad (6.8a)$$

$$\delta\chi_e(\vec{r}_\perp; \omega) = \frac{\chi_e^x(\vec{r}_\perp; \omega) - \chi_e^y(\vec{r}_\perp; \omega)}{2}, \quad (6.8b)$$

$$q^2 = \frac{q_x^2 + q_y^2}{2}, \quad (6.8c)$$

$$\delta q^2 = \frac{q_x^2 - q_y^2}{2}, \quad (6.8d)$$

$$\tilde{\mathcal{B}}_\pm(\vec{r}_\perp; \omega) = \frac{\tilde{\mathcal{B}}_x(\vec{r}_\perp; \omega) \pm i\tilde{\mathcal{B}}_y(\vec{r}_\perp; \omega)}{\sqrt{2}}. \quad (6.8e)$$

Given the QW's susceptibility components in the circular basis, $\tilde{\mathcal{P}}_{\pm} = \varepsilon_0 \chi_{\pm}(\vec{r}; \omega) \tilde{\mathcal{E}}_{\pm}$, the linear components of the material dipole density can be expressed as

$$\tilde{\mathcal{P}}_x(\vec{r}_{\perp}, z; \omega) = \varepsilon_0 \left[\frac{(\chi_+ + \chi_-)}{2} f_x(z) \tilde{\mathcal{A}}_x(\vec{r}_{\perp}; \omega) - \frac{(\chi_+ - \chi_-)}{2i} f_y(z) \tilde{\mathcal{A}}_y(\vec{r}_{\perp}; \omega) \right], \quad (6.9a)$$

$$\tilde{\mathcal{P}}_y(\vec{r}_{\perp}, z; \omega) = \varepsilon_0 \left[\frac{(\chi_+ - \chi_-)}{2i} f_x(z) \tilde{\mathcal{A}}_x(\vec{r}_{\perp}; \omega) + \frac{(\chi_+ + \chi_-)}{2} f_y(z) \tilde{\mathcal{A}}_y(\vec{r}_{\perp}; \omega) \right], \quad (6.9b)$$

and upon substituting the above expressions into Eqs. (6.5c) and (6.8e), we obtain

$$\tilde{\mathcal{B}}_{\pm} = \varepsilon_0 \left(\tilde{\mathcal{A}}_+ S_{\pm} + \tilde{\mathcal{A}}_- T_{\pm} \right), \quad (6.10)$$

where

$$S_{\pm} = \int_{z_0}^{z_0+W} dz \left[\frac{\chi_+ + \chi_-}{4} (|F_x(z)|^2 \pm |F_y(z)|^2) + \frac{\chi_+ - \chi_-}{4} \left(\frac{f_x^*(z) f_y(z)}{\int_0^L dz |f_x(z)|^2} \pm \frac{f_x(z) f_y^*(z)}{\int_0^L dz |f_y(z)|^2} \right) \right], \quad (6.11a)$$

$$T_{\pm} = \int_{z_0}^{z_0+W} dz \left[\frac{\chi_+ + \chi_-}{4} (|F_x(z)|^2 \mp |F_y(z)|^2) - \frac{\chi_+ - \chi_-}{4} \left(\frac{f_x^*(z) f_y(z)}{\int_0^L dz |f_x(z)|^2} \mp \frac{f_x(z) f_y^*(z)}{\int_0^L dz |f_y(z)|^2} \right) \right]. \quad (6.11b)$$

By splitting the total carrier density inside the QW as $N = N_+ + N_-$ —where N_{\pm} stand for the electron density with spin up and down, respectively—the susceptibility components in the circularly polarized basis are $\chi_{\pm} \equiv \chi_{\pm}(\omega, N_+, N_-)$. Since the QW thickness W is much smaller than the diffusion length, it can be assumed that, inside the QW, the carrier density is almost constant along z , i.e., $N_{\pm}(\vec{r}) \simeq \bar{N}_{\pm}(\vec{r}_{\perp}) \equiv (1/W) \int_{z_0}^{z_0+W} dz N_{\pm}(\vec{r})$. Moreover, for weak cavity anisotropies the longitudinal propagation constants q_x and q_y are quite similar, so that we can consider that the longitudinal mode profiles are almost the same, $f_x(z) \approx f_y(z) \equiv f(z)$. In this case, Eq. (6.10) simply reduces to

$$\tilde{\mathcal{B}}_{\pm}(\vec{r}_{\perp}; \omega) = \varepsilon_0 \Gamma \chi_{\pm}(\omega, \bar{N}_+(\vec{r}_{\perp}), \bar{N}_-(\vec{r}_{\perp})) \tilde{\mathcal{A}}_{\pm}(\vec{r}_{\perp}; \omega), \quad (6.12)$$

where

$$\Gamma = \frac{\int_{z_0}^{z_0+W} dz |f(z)|^2}{\int_0^L dz |f(z)|^2} \quad (6.13)$$

is the longitudinal optical confinement factor that represents the fraction of the intracavity power that is confined in the QW active region. As already mentioned, in the case of a multiple QW active region, we consider that all the QWs are identical and in the same state, hence we simply scale the single-QW confinement factor by the number of wells. Therefore, Eq. (6.7) becomes

$$\left\{ \nabla_{\perp}^2 + \frac{\omega^2}{c^2} [1 + \chi_e(\vec{r}_{\perp}; \omega)] - q^2 \right\} \tilde{\mathcal{A}}_{\pm}(\vec{r}_{\perp}; \omega) + \left[\frac{\omega^2}{c^2} \delta \chi_e(\vec{r}_{\perp}; \omega) - \delta q^2 \right] \tilde{\mathcal{A}}_{\mp}(\vec{r}_{\perp}; \omega) = -\Gamma \frac{\omega^2}{c^2} \chi_{\pm}(\omega, \bar{N}_+, \bar{N}_-) \tilde{\mathcal{A}}_{\pm}(\vec{r}_{\perp}; \omega) . \quad (6.14)$$

We then define

$$1 + \chi_e(\vec{r}_{\perp}; \omega) = [n_e(\omega) + i\bar{\alpha}_i(\omega) + \Delta n(\vec{r}_{\perp}; \omega)]^2 , \quad (6.15)$$

where $n_e(\omega)$ corresponds to the effective background refractive index experienced by the field in the isotropic and homogeneous cavity. $\bar{\alpha}_i(\omega) \ll n_e(\omega)$ determines the effective absorption in the passive material, and $\Delta n(\vec{r}_{\perp}; \omega)$ represents the (small) excess index distribution responsible for the lateral confinement of the optical field. $\Delta n(\vec{r}_{\perp}; \omega)$, contains all the waveguiding mechanisms present in the device except the carrier induced refractive index, which is included through the real part of χ_{\pm} . Hence, in a cavity without anisotropies we have that the longitudinal mode considered has an optical frequency Ω , determined, from Eqs. (6.3), (6.14) and (6.15), by the condition

$$\frac{\Omega}{c} n_e(\Omega) = \text{Re } q(\Omega) , \quad (6.16)$$

where $\text{Re } q(\Omega)$ stands for the real part of the propagation constant of the longitudinal mode. The frequency dependence of q stems from the frequency-dependent reflectivity of the Bragg mirrors, which mainly arises from the reflection phases within the stop-band of the reflectors. Since the indexes of the materials forming the passive cavity and the Bragg reflectors are temperature dependent, Eq. (6.16) incorporates the thermal shift of the cavity mode.

Time-domain equations

Once the longitudinal mode frequency, Ω , has been determined, we can tackle the dynamical evolution of the transverse field profile in the SVA approximation. For

the active VCSEL, the optical field is quasimonochromatic around the carrier optical frequency Ω , so that $\tilde{\mathcal{A}}_{\pm}(\vec{r}_{\perp}; \omega) \equiv \tilde{E}_{\pm}(\vec{r}_{\perp}; \nu)$, with $\nu = \omega - \Omega$, is different from zero only in the close vicinity of Ω . Thus, in time domain the circularly-polarized components of the optical field can be written as

$$\mathcal{A}_{\pm}(\vec{r}_{\perp}; t) = E_{\pm}(\vec{r}_{\perp}; t)e^{-i\Omega t} + c.c. , \quad (6.17)$$

where $E_{\pm}(\vec{r}_{\perp}; t)$ are the SVAs of the circularly polarized components of the optical field, which verify that $|\partial_t E_{\pm}| \ll \Omega |E_{\pm}|$.

For frequencies $\omega \simeq \Omega$, we approximate

$$\begin{aligned} \frac{\omega^2}{c^2} [1 + \chi_e(\vec{r}_{\perp}; \omega)] - q^2 \approx & 2 \frac{\Omega}{c} n_e \frac{n_g}{c} \nu \\ & + \left(\frac{\Omega}{c} \right)^2 2n_e [\Delta n(\vec{r}_{\perp}; \Omega) + i\alpha_i(\Omega)] - 2i \frac{\Omega}{c} n_e \text{Im } q(\Omega) , \end{aligned} \quad (6.18)$$

where $n_e \equiv n_e(\Omega)$ is the effective index at the cavity frequency, and $n_g \equiv \left| \frac{d}{d\omega} (\omega n_e - c \text{Re } q) \right|_{\omega=\Omega}$ is the corresponding group refractive index. By neglecting the frequency dependence of $\delta\chi_e$ and δq in Eq. (6.14) and transforming it to time domain ($-i\nu \rightarrow \partial_t$), we have that

$$\begin{aligned} & 2i \frac{\Omega}{c} n_e \frac{n_g}{c} \partial_t E_{\pm}(\vec{r}_{\perp}; t) + \left\{ \left(\frac{\Omega}{c} \right)^2 2n_e [\Delta n(\vec{r}_{\perp}; \Omega) + i\alpha_i(\Omega)] \right. \\ & \left. - 2i \frac{\Omega}{c} n_e \text{Im } q(\Omega) \right\} E_{\pm}(\vec{r}_{\perp}; t) + \left[\frac{\Omega^2}{c^2} \delta\chi_e(\vec{r}_{\perp}; \Omega) - \delta q^2(\Omega) \right] E_{\mp}(\vec{r}_{\perp}; t) \\ & = -\Gamma \frac{\Omega^2}{c^2} P(\vec{r}_{\perp}; t) , \end{aligned} \quad (6.19)$$

where

$$P(\vec{r}_{\perp}; t) \equiv \int_{-\infty}^{\infty} \frac{d\nu}{2\pi} e^{-i\nu t} \chi_{\pm}(\Omega + \nu, \bar{N}_+, \bar{N}_-) \tilde{E}_{\pm}(\vec{r}_{\perp}; \nu) . \quad (6.20)$$

The above expression does not allow for an exact integration, except for very particular forms of χ_{\pm} , e.g., Lorentzian shapes. We take this expression as a formal solution, but keeping in mind that some approximation is required as will be discussed in Sec. 6.4. After some straightforward algebra we get

$$\partial_t E_{\pm} = -\kappa E_{\pm} + i\hat{\mathcal{L}} E_{\pm} + i \frac{\Gamma}{2} \frac{c}{n_g} \frac{\Omega}{c n_e} P_{\pm} - [\tilde{\gamma}_{a,\Omega}(\vec{r}_{\perp}) + i\tilde{\gamma}_{p,\Omega}(\vec{r}_{\perp})] E_{\mp} . \quad (6.21)$$

In the above equation, we have defined

$$\kappa = \frac{c}{n_g} \left[\frac{\Omega}{c} \bar{\alpha}_i(\Omega) - \text{Im } q(\Omega) \right] , \quad (6.22)$$

as the total cavity loss rate, and

$$\gamma_{a,\Omega}(\vec{r}_\perp) = \frac{\Omega}{2n_e n_g} \text{Im} \left[\frac{\Omega^2}{c^2} \delta\chi_e(\vec{r}_\perp; \Omega) - \delta q^2(\Omega) \right], \quad (6.23a)$$

$$\gamma_{p,\Omega}(\vec{r}_\perp) = -\frac{\Omega}{2n_e n_g} \text{Re} \left[\frac{\Omega^2}{c^2} \delta\chi_e(\vec{r}_\perp; \Omega) - \delta q^2(\Omega) \right], \quad (6.23b)$$

which represent the effective dichroism and birefringence in the cavity. Anisotropies have two different contributions: $\delta\chi_e$, which represents the anisotropies that arise from the passive material filling the cavity, and δq^2 , which arises from the Bragg mirrors. For simplicity, we consider that γ_a and γ_p are constant, independent of both position and frequency.

The waveguide operator in Eq. (6.21) reads

$$\hat{\mathcal{L}}E_\pm = \frac{c^2}{2\Omega n_e n_g} \left[\nabla_\perp^2 + \left(\frac{\Omega}{c} \right)^2 2n_e \Delta n(\vec{r}_\perp; \Omega) \right] E_\pm, \quad (6.24)$$

since we have assumed weak guidance², i.e., $\Delta n(\vec{r}_\perp; \Omega) \ll n_e$. It is worth remarking that $\hat{\mathcal{L}}$ does not incorporate the carrier-induced refractive index, which is included separately through the real part of the susceptibility. However, all other guiding mechanisms, and in particular thermal effects due to carrier injection, are indeed included in $\hat{\mathcal{L}}$ because both the cavity frequency Ω and the excess refractive index distribution $\Delta n(\vec{r}_\perp; \Omega)$ are sensitive to the injected current due to device self-heating. The eigenfunctions of $\hat{\mathcal{L}}$ are thus the cavity modes corresponding to the effective waveguide and if this guide is strong enough, the interaction with the carriers will not distort them too strongly. It is worth remarking that with our definition of $\hat{\mathcal{L}}$, the cavity modes and modal frequencies are polarization independent. This effect is accounted for through the linear cavity anisotropies γ_a and γ_p .

6.3 Material model

As already mentioned, due to the quantum-mechanical selection rules that apply to optical transitions in the QW, the interaction with the active material is diagonal in the basis of circularly polarized states. It is then natural to split the total carrier density into spin-up and spin-down carrier reservoirs. Each of them interacts only with one of the two circularly polarized components of the optical field, but scattering processes that reverse the spins of the carriers couple the two densities. We model this coupling by means of an effective spin-flip rate, γ_j , that phenomenologically describes the equalization of the densities of spin-up and spin-down carriers [30, 173].

²More details are given in the Appendix E.

The evolution of each of the spin-resolved electronic densities can be found from the density matrix formalism [60] applied to semiconductor systems, which leads to [193, 205]

$$\begin{aligned} \partial_t \bar{N}_\pm &= \frac{J(\vec{r}_\perp; t)}{2eW} - R_{sp}(\bar{N}_\pm) + \mathcal{D}\nabla_\perp^2 \bar{N}_\pm \mp \gamma_j(\bar{N}_+ - \bar{N}_-) \\ &+ \frac{\Gamma}{W} \frac{2\varepsilon_0}{\hbar} \int_0^L dz |f(z)|^2 \frac{1}{2i} (P_\pm E_\pm^* - P_\pm^* E_\pm) , \end{aligned} \quad (6.25)$$

where e is the absolute value of the electron charge, \mathcal{D} is the in-plane ambipolar diffusion coefficient, $R_{sp}(\bar{N}_\pm) = A\bar{N}_\pm + B\bar{N}_\pm^2$ is the total spontaneous recombination of carriers (we neglect Auger recombination), and $\gamma_j(\bar{N}_+ - \bar{N}_-)$ represents all spin-flip processes that tend to equalize the two carrier densities with opposite spin. Finally, $J(\vec{r}_\perp; t)$ denotes the distribution of the current flowing through the active region, which is assumed to be equally distributed among the two spin orientations. Thus, the total injected current is $I = \int d^2\vec{r}_\perp J(\vec{r}_\perp; t)$.

Our optical model is given by Eqs. (6.21) and (6.25) which determines the distribution of the SVA fields and carrier densities. However, it still has to be completed by providing a specification for the optical susceptibility components, χ_\pm , that describe the interaction of the optical field and the QW material: the imaginary parts describe the energy exchange (absorption or stimulated emission) between the circular components of the field and the medium, while the real parts describe the dispersive effect (refractive index change) accompanying such a process [215]. Therefore, once the susceptibility components and evolution of the carrier densities have been specified, our model naturally includes the effects of spatial-hole burning that enters in the determination of both the modal frequencies and the modal profiles. For index-guided devices, this last effect can be usually neglected and it is enough to determine the imaginary parts of χ_\pm as a function of the frequency and the carrier densities.

Models for calculating gain and refraction index spectra from the electronic structure of the semiconductor material have been developed, some of them neglecting many-body effects [216]-[223] while others taking into account [42, 206]-[210, 224]. These microscopic theories describe individual transitions by the occupation of the initial and final electronic states, and the material polarization by superposing the contributions from each transition. A dynamical description of the lasing process then requires dealing with plenty of Two-Level-like systems, coupled among them by carrier scattering processes and by the optical field. In this way, all physical mechanisms in the material are accounted for, but the complexity of such a description is so high that it requires intensive numerical computation even without considering spatiotemporal dynamics.

In order to reduce the computational cost and to gain physical insight, it is useful

to develop simpler descriptions for the optical susceptibility of semiconductor media. One possibility is to use a semi-analytical approximation for the optical gain (see for instance [225] and references therein) and then determine the refractive index by Kramers-Krönig relations. Another possibility is to use an analytical approximation to the full optical susceptibility [211]-[213], which although less accurate, it still captures the essential features of the gain and index spectra. For this reason, we consider an analytical approximation to the optical susceptibility of the QW, equivalent to that given in Ref. [211], but for the circular components of the optical field. The circular components (\pm) of the optical susceptibility in the rotating wave approximation and perfect k conservation reads [60]

$$\chi_{\pm}(\omega) = -\frac{i}{\varepsilon_0} \frac{1}{V} \sum_{lm} \sum_k |M_{lm_s}(k)|^2 \frac{f_{l_s}(k) - f_{m_s}(k)}{i[E_{lm_s}(k) - \hbar\omega] + \hbar\gamma_{\pm}(k)}, \quad (6.26)$$

where $s = \downarrow (\uparrow)$ stands for the spin band orientation, V the crystal volume, $|M_{lm_s}|^2$ the dipole matrix element, f_{m_s} and f_{l_s} electronic occupation probabilities, E_{lm_s} the energy difference between electronic states, and $\gamma_{\pm}(k)$ the transition linewidth. The summation runs over the all the bands (lm) and electron wavenumbers k within the first Brillouin zone³.

We proceed along the lines given in [211], and we consider only one valence and one (heavy-hole) conduction bands, both parabolic and degenerated for the two spin orientations [See Fig. 6.3]. This situation is appropriate for describing thin, strained QW where the light-hole band has substantially higher energy than the heavy-hole

³The summations are replaced by integrals according to the density of states.

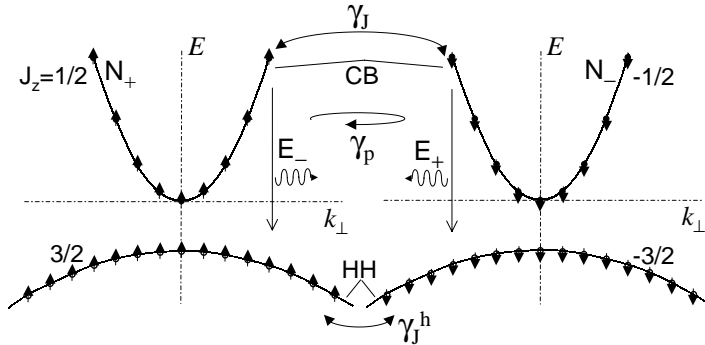


Figure 6.3. Scheme of the allowed transitions in the spin subbands of a strained QW, (HH) heavy hole with $J_z = \pm 3/2$ and (CB) conduction bands with $J_z = \pm 1/2$. Electrons with opposite spin are mixed at rate γ_j . Emitted photons with opposite circular polarization (E_{\pm}) are coupled through the linear birefringence γ_p .

band, so it is not optically active until quite high carrier densities. By assuming $M_{lms}(k)$ and $\gamma_{\perp}(k)$ independent of k and spin, the optical susceptibility reduces to

$$\chi_s(\omega) = \frac{|M_{eh}|^2}{V\varepsilon_0} \sum_k \frac{f_s^e(k) + f_s^h(k) - 1}{[\hbar\omega - E_c(k) + E_v(k)] + i\hbar\gamma_{\perp}}, \quad (6.27)$$

where the quasi-equilibrium Fermi-Dirac distributions read

$$f_{\uparrow(\downarrow)}^{e(h)} = \frac{1}{1 + e^{\beta(E - F_{\uparrow(\downarrow)}^{e(h)})}}, \quad (6.28)$$

with $\beta^{-1} = k_B T$ the plasma temperature, and $F_{\uparrow(\downarrow)}^{e(h)}$ the quasi-Fermi levels for electrons and holes with spin orientation up (down)⁴. The density of carriers in each of these spin bands is obtained from the corresponding quasi-Fermi level through

$$N_{+(-)}^{e(h)} = \frac{1}{V} \sum_k f_{\uparrow(\downarrow)}^{e(h)}. \quad (6.29)$$

It is impossible to analytically treat the full optical susceptibility at finite temperatures due to the long tails of the Lorentzian contributions. A further approximation consists in assuming low temperature ($T=0$ K), where the quasi-equilibrium Fermi-Dirac distributions can be replaced by step functions. In this limit the analytical expression for the optical susceptibility reads

$$\begin{aligned} \chi_{\pm}(\Omega + \nu, N_{\pm}^e, N_{\pm}^h) = \\ - \chi_0 \left[\ln \left(1 - \frac{2D_{\pm}^e}{u + i} \right) + \ln \left(1 - \frac{2D_{\pm}^h}{u + i} \right) - \ln \left(1 - \frac{b}{u + i} \right) \right]. \end{aligned} \quad (6.30)$$

where the first term on the right-hand side represents the contribution of the electrons, the second one that of the holes, and the third one the susceptibility of the system when no carriers are excited. In the above equation, we have defined

$$\begin{aligned} \chi_0 &= \frac{m|M_{eh}|^2}{2W\pi\varepsilon_0\hbar^2}, \quad b = \frac{\hbar k_m^2}{2m\gamma_{\perp}}, \quad D_{\pm}^{eh} = \frac{\pi W \hbar}{m\gamma_{\perp}} \bar{N}_{\pm}^{eh} \equiv \frac{\bar{N}_{\pm}^{eh}}{N_t}, \\ u &= \Delta + \frac{\nu}{\gamma_{\perp}} + \sigma(D_-^e + D_+^e)^{1/3}, \end{aligned}$$

where m is the reduced mass of the electron-hole pair, k_m the maximum wavenumber contained in the first Brillouin zone, N_t is the (total) transparency carrier density, and $|M_{eh}|^2$ and γ_{\perp} are the oscillator strength and width of the transition, both

⁴ The difference between quasi-Fermi levels with opposite spin orientation introduces unbalance spin densities, that in turn, is responsible for the magnetization. In a semiconductor this difference is usually small due to the spin flip processes. Currently, the development of magnetic semiconductors, including localized magnetic ions, Mn^+ , etc., is of great interest for *spintronic* applications [226].

assumed constant over the whole band. The frequency dependence is incorporated through u ; $\Delta = (\Omega - \omega_g)/\gamma_\perp$ measures the normalized detuning of the longitudinal mode resonance with respect to the nominal bandgap, and $\sigma(D_-^e + D_+^e)^{1/3}$ phenomenologically describes bandgap renormalization due to Coulomb interaction between electrons and holes, σ being the bandgap renormalization parameter.

A last approximation allow us to elude the hole densities in the susceptibility and carrier dynamics. The spin relaxation rate for the holes is commonly large [173] and thus $D_+^h \approx D_-^h$. If we also assume charge neutrality, $D_+^e + D_-^e = D_+^h + D_-^h$, we find that the second term in Eq. (6.30) can be expressed as $2D_\pm^h \approx (D_+^e + D_-^e)$. In order to simplify the notation, we skip in what follows the superindex e when denoting electronic carrier densities.

As discussed in detail in Ref. [211], the optical susceptibility given by Eq. (6.30) provides a good qualitative description of the characteristics of both gain and refractive index spectra [Fig. 6.4(a),(b)], including bandfilling effects (i.e., the blue shift of the gain peak relative to the bandedge as the carrier density is increased) and the nonlinear dependence of the gain and index spectra on the carrier density. Now, the linewidth enhancement factor

$$\alpha(\omega, D) \equiv \frac{\text{Re}(\partial\chi_\pm/\partial D)}{\text{Im}(\partial\chi_\pm/\partial D)} \quad (6.31)$$

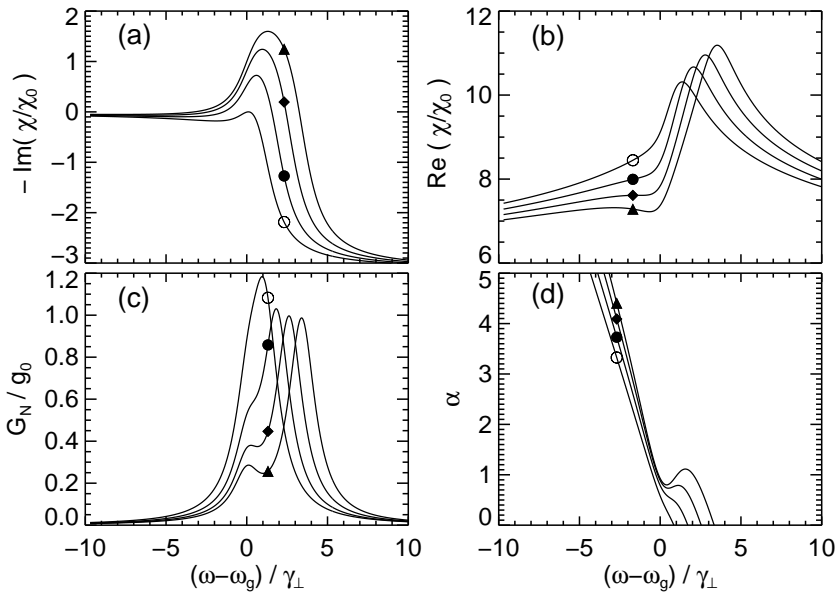


Figure 6.4. Optical gain (a), refractive-index (b), differential gain spectrum (c), and alpha factor (d). Eq. (6.30) for the parameters given in Table 6.1. Symbols correspond to a total carrier density $1.0 N_t$ (\circ), $1.8 N_t$ (\bullet), $2.6 N_t$ (\blacklozenge), and $3.4 N_t$ (\blacktriangle).

and the differential gain

$$G_N(\omega, D) \equiv -g_0 \frac{\partial \text{Im} \chi_{\pm}}{\partial D} \quad (6.32)$$

with $g_0 = \omega/(cn_e N_t)$ become functions of the frequency and carrier density [Fig. 6.4(c),(d)]. By using this approximation for χ_{\pm} in Eqs. (6.21) and (6.25), the spatiotemporal description of the system incorporates the frequency dependence of both the gain and refractive index in a simple, although efficient and qualitatively accurate way. Anyway, it should be stressed once again that other approximations for the susceptibility components could be used. In particular, when one wishes to analyze in detail the behavior of a particular device, computational complexity arises because of the need for a realistic and accurate modeling of the the gain and index spectra.

6.4 Dimensionless model

For the sake of clarity and numerical purposes it is convenient to use a dimensionless version of the VCSEL model. To this end, we work with the carrier densities normalized to the transparency carrier density, $D_{\pm} = \bar{N}_{\pm}/N_t$, and we scale the fields as

$$A_{\pm}(\vec{r}_{\perp}; t) = \left[\frac{2\varepsilon_0 n_g n_e}{\hbar \Omega} \frac{\Gamma}{W N_t} \int_0^L dz |f(z)|^2 \right]^{1/2} E_{\pm}(\vec{r}_{\perp}; t) . \quad (6.33)$$

We also consider that the shape of the transverse current density distribution is fixed by the structure of the device, so that $J(\vec{r}_{\perp}; t) = eW N_t C(\vec{r}_{\perp}) \mu(t)$, where $C(\vec{r}_{\perp})$ is the current shape and $\mu(t)$ its time dependence, hence the total injected current reads

$$I(t) = \mu(t) e N_t W \iint_{-\infty}^{\infty} C(\vec{r}_{\perp}) d^2 \vec{r}_{\perp} . \quad (6.34)$$

Then, the final form for the model is

$$\begin{aligned} \partial_t A_{\pm}(\vec{r}_{\perp}; t) &= -\kappa A_{\pm} + i \hat{\mathcal{L}} A_{\pm} + i \frac{a \Gamma}{2} P_{\pm}(\vec{r}_{\perp}; t) \\ &\quad - (\gamma_a + i \gamma_p) A_{\mp} + \sqrt{A \beta_{sp} D_{\pm}} \xi_{\pm}(\vec{r}_{\perp}; t) , \end{aligned} \quad (6.35a)$$

$$\begin{aligned} \partial_t D_{\pm}(\vec{r}_{\perp}; t) &= \frac{\mu(t)}{2} C(\vec{r}_{\perp}) - A D_{\pm} - (B N_t) D_{\pm}^2 \mp \gamma_j (D_+ - D_-) \\ &\quad + \mathcal{D} \nabla_{\perp}^2 D_{\pm} + \frac{a}{2i} (P_{\pm} A_{\pm}^* - P_{\pm}^* A_{\pm}) , \end{aligned} \quad (6.35b)$$

$$P(\vec{r}_{\perp}; t) \equiv \int_{-\infty}^{\infty} \frac{d\nu}{2\pi} e^{-i\nu t} \chi_{\pm}(\Omega + \nu, \bar{N}_+, \bar{N}_-) \tilde{A}_{\pm}(\vec{r}_{\perp}; \nu) , \quad (6.35c)$$

where $a \equiv \Omega/(n_e n_g)$, and the susceptibility is that given in Eq. (6.30). Since $\nu \ll \Omega$ we expand $\chi_{\pm}(\Omega + \nu)$ to first order in ν , integrate term by term, and formally summing the series, the evolution of the material polarization is determined by

$$\begin{aligned}
 P_{\pm}(\vec{r}_{\perp}; t) &= \int_{-\infty}^{\infty} \frac{d\nu}{2\pi} [\chi_{\pm}(\Omega) + \nu\chi'_{\pm}(\Omega) + \dots] \tilde{A}_{\pm}(\nu)e^{-i\nu t} = \\
 &= \chi_{\pm}(\Omega)A_{\pm}(t) + \chi'_{\pm}(\Omega)i\partial_t A_{\pm}(t) + \dots \approx \\
 &\approx \chi_{\pm} \left(\Omega + i \frac{\partial_t A_{\pm}(\vec{r}_{\perp}; t)}{A_{\pm}(\vec{r}_{\perp}; t)} \right) A_{\pm}(t), \tag{6.36}
 \end{aligned}$$

The carrier densities are assumed to be constant in the material polarization time scales (γ_{\pm}^{-1}). Also note that the final result in Eq. (6.36) is exact for a monochromatic solution. In the first place, the optical frequency Ω is selected by the cavity through Eq. (6.16). In the second place, a correction to the optical frequency Ω appears through the “instantaneous frequency” $i\partial_t A_{\pm}/A_{\pm}$ in χ_{\pm} ; such a contribution takes into account the changes in the susceptibility due to the frequency pulling or pushing due to nonlinearities. It also describes the variations in susceptibility experienced through frequency chirping during the transients but, more important, it also determines that the carrier-induced gain and refractive index experienced by different transverse modes are different due to their different modal frequencies.

For the sake of simplicity, we assume that the lateral current distribution at the active layer, is given in terms of explicit functional forms of $C(r)$. We approximate this function by a supergaussian distribution in the case of bottom-emitting devices, while a ring-shaped current distribution is taken for top-emitting devices. In the same way, the radial dependence of the excess refractive index $\Delta n(r)$, that arises from the TL effect, is assumed to be parabolic. Although the electrical and thermal models have not been implemented yet, they may be included in our optical model in order to self-consistently determine the distribution in current density, temperature and optical field. A summary of the meaning and numerical values of the device and material parameters can be found in Table 6.1.

Finally, the last term in Eq. (6.35a) models spontaneous emission processes in the semiclassical approximation [192]. $\xi_{\pm}(\vec{r}_{\perp}; t)$ are random numbers with zero mean ($\langle \xi_{\pm}(\vec{r}_{\perp}; t) \rangle = 0$) and delta-correlated in both space, time and polarization ($\langle \xi_i^*(x, y; t) \xi_j(x', y'; t') \rangle = 2\delta_{i,j} \delta(x - x') \delta(y - y') \delta(t - t')$, with $i, j = +, -$). Although noise effects are not essential for the scope of this work, they may affect the performance of the system through switch-on time jitter, reduction of the eye diagram aperture, and mode hopping in the case of multimode operation.

Symbol	Meaning	Value	Dimensions
$a\chi_0$	effective gain constant	$1.3 \cdot 10^4$	ns^{-1}
Γ	longitudinal confinement factor	0.045	—
γ_{\perp}	polarization decay rate	20	ps^{-1}
n_e	background refractive index	3.3	—
n_g	group refractive index	3.5	—
λ	free-space wavelength	0.85	μm
σ	bandgap shrinkage	0.2	—
b	empty band contribution to χ	10^4	—
κ	cavity losses	300	ns^{-1}
γ_a	linear dichroism	0.5	ns^{-1}
γ_p	linear birefringence	30	ns^{-1}
A	non-radiative recombination rate	1.0	ns^{-1}
B	bimolecular recombination rate	10^{-10}	$\text{cm}^3 \text{s}^{-1}$
N_t	transparent carrier density	10^{18}	cm^{-3}
γ_j	spin flip rate	50	ns^{-1}
\mathcal{D}	bimolecular diffusion	0.4	$\mu\text{m}^2 \text{ns}^{-1}$
β_{sp}	spontaneous emission factor	10^{-5}	—

Table 6.1: Device and material parameters.

6.5 Polarization Mode Selection in the Fundamental Transverse Mode

In this section we show how a joint interplay of semiconductor nonlinear dynamics, spin dynamics, and thermal shift, enters in the selection of polarization modes in VCSELs [33, 183]. The complexity of the spatiotemporal model (6.35a)–(6.35c) can be largely simplified by neglecting spatial effects, namely, field diffraction and carrier diffusion. In this case the VCSEL equations simply read

$$\begin{aligned}
 d_t A_{\pm}(t) &= -\kappa A_{\pm} + i \frac{a\Gamma}{2} \chi_{\pm} \left(\Omega + i \frac{d_t A_{\pm}}{A_{\pm}}, D_+, D_- \right) A_{\pm} \\
 &\quad - (\gamma_a + i\gamma_p) A_{\mp} + \sqrt{A\beta_{sp}D_{\pm}} \xi_{\pm}(t), \tag{6.37a}
 \end{aligned}$$

$$\begin{aligned}
 d_t D_{\pm}(t) &= \frac{J}{2} - AD_{\pm} - BD_{\pm}^2 \mp \gamma_j (D_+ - D_-) \\
 &\quad + a \text{Im} \chi_{\pm} \left(\Omega + i \frac{d_t A_{\pm}}{A_{\pm}}, D_+, D_- \right) |A_{\pm}|^2. \tag{6.37b}
 \end{aligned}$$

$J = I/(eVN_t)$ is the total injection current I divided by the carrier density at transparency N_t .

Monochromatic solutions

The two orthogonal linearly-polarized solutions can be expressed as

$$A_{\pm}(t) = Qe^{-i(\nu_0 t \pm \phi)}, \quad D_{\pm}(t) = D_0, \quad (6.38)$$

with $\phi = 0$ in \hat{x} -polarized states and $\phi = \pi/2$ in \hat{y} -polarized states. Inserting Eqs. (6.38) into Eq. (6.37a) we obtain a set of two nonlinear algebraic equations for (ν_0, D_0)

$$\begin{cases} -\frac{a\Gamma}{2} \text{Im} \chi(\Omega + \nu_0, D_0) = \kappa \pm \gamma_a, \\ -\frac{a\Gamma}{2} \text{Re} \chi(\Omega + \nu_0, D_0) = \nu_0 \mp \gamma_p, \end{cases} \quad (6.39)$$

that is solved by Newton-Raphson iteration [227]. From Eq. (6.37b) we obtain the total optical intensity

$$2Q^2 = \frac{\Gamma}{2} \left[\frac{J - J_{th}}{\kappa \pm \gamma_a} \right], \quad (6.40)$$

where the sign $+(-)$ corresponds to \hat{x} -polarized (\hat{y} -polarized) solution. The threshold current is given by $J_{th} = 2(AD_0 + BD_0^2)$ which is temperature-dependent through the relative detuning Δ .

Nonthermal and thermal polarization switching

The linear stability analysis of the linearly-polarized solutions allows to determine the domain in parameter space where each LP state is stable and thus the possible

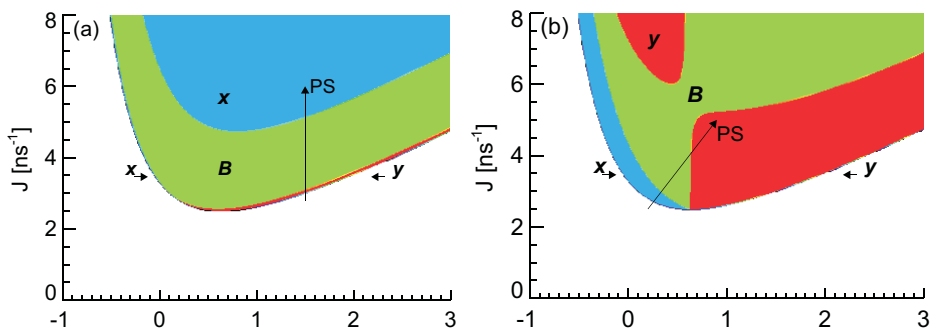


Figure 6.5. Current-detuning linear stability diagram for the linearly polarized solutions. The lower curves give the dependence of threshold current on the detuning Δ . Parameters used are those of Table 6.1 with (a) $\gamma_p = 3 \text{ ns}^{-1}$, $\gamma_a = 0$ and (b) $\gamma_p = 35 \text{ ns}^{-1}$, $\gamma_a = 0$. The stability regions are identified as follows: (x) only \hat{x} -LP is stable, (B) both \hat{x} and \hat{y} -LP are stable, (y) only \hat{y} -LP is stable.

occurrence of polarization switching. PS can occur as the system is brought from one parameter region to another region of different stability properties. We follow the procedure outlined in Pag. 111, although we skip here the details of the calculations.

A typical stability diagram for a relatively small value of the birefringence ($\gamma_p = 3 \text{ ns}^{-1}$) are shown in Fig. 6.5(a) in the current versus detuning plane. There is a minimum threshold around $\Delta_m \approx 0.5$ corresponding to the alignment of the cavity resonance with the gain peak. Generally, for a given Δ , the LP state selected at threshold is the closest to the gain peak, i.e., \hat{x} for $\Delta < \Delta_m$ and \hat{y} for $\Delta > \Delta_m$ (in the absence of dichroism). Well above the threshold line we find that only the high-frequency solution \hat{x} -LP is stable despite the sign of the detuning. A rather wide bistability region also appears due to nonlinear gain saturation induced by the lasing mode. A PS occurs as the system is brought from \hat{y} to \hat{x} by increasing the current at constant detuning (temperature).

Fig. 6.5(b) displays a typical stability diagram for a higher birefringence ($\gamma_p = 35 \text{ ns}^{-1}$). An important difference with Fig. 6.5(a) is that now \hat{y} is stable on almost the whole frequency range and currents far from threshold. Therefore, no PS at constant temperature appears for detunings $\Delta > \Delta_m$. Instead, a PS occurs for constant J as Δ is varied across Δ_m . Within our framework, we call this as thermally-induced PS since it appears by scanning Δ , either by changing substrate temperature or by device self-heating as the current is increased [See path in Fig. 6.5(b)].

Hence two possible independent ways to produce a PS have been identified [33]. One that typically occurs for relatively large birefringence is thermally-induced and corresponds to the mechanism discussed by Choquette et al. [31]. A second mechanism may occur for small birefringence while increasing the current at constant Δ [169]. We call this second mechanism nonthermal since it occurs at constant detuning while staying on one of the sides of the gain peak. These two mechanisms can coexist depending on the device characteristics [Fig. 6.5(b)].

6.6 Transverse Mode Selection at Threshold

A basic step in the characterization and modeling of VCSELs is to determine their threshold properties. In particular, the difference in threshold currents for the different transverse modes provides a rough estimate of the modes that can be excited for a given current, although above threshold the excitation of higher order transverse modes is favored because of spatial hole burning. In addition, the modal profiles and frequencies can be modified, especially for very weak guiding. One of the primary effects of TL is to modify the threshold characteristics of the VCSEL by changing both the threshold current and the mode selected at threshold.

The threshold current and the transverse mode selection for a given VCSEL can

be determined in a simple way by analyzing the linear stability of the “off” state, i.e., $A_{\pm} = 0$. We apply to the “off” state a small perturbation $\delta A_{\pm}(\vec{r}_{\perp}, t)$, in such a way that stimulated emission can be neglected when determining the carrier densities. Hence, from Eq. (6.35c) we have that the carrier densities in each spin orientation are equal, $D_+ = D_- = D_s(\vec{r}_{\perp})$ since electrons with opposite spin orientations are in average equally injected, and given by

$$0 = \frac{\mu}{2} C(\vec{r}_{\perp}) - AD_s - (BN_t)D_s^2 + \mathcal{D}\nabla_{\perp}^2 D_s. \quad (6.41)$$

The solutions of Eq. (6.41) in turn determine the inhomogeneous distribution of the optical susceptibility, that in this case is the same for the two polarization components. The dynamics of $\delta A_{\pm}(\vec{r}_{\perp}; t)$ is given by

$$\partial_t \delta A_{\pm} = -\kappa \delta A_{\pm} + i\hat{\mathcal{L}}\delta A_{\pm} + i\frac{a\Gamma}{2}\chi\left(\Omega + i\frac{\partial_t \delta A_{\pm}}{\delta A_{\pm}}, D_s\right)\delta A_{\pm} - (\gamma_a + i\gamma_p)\delta A_{\mp}. \quad (6.42)$$

It is natural to expand the perturbation in modes of the waveguide operator $\hat{\mathcal{L}}$,

$$\delta A_{\pm}(\vec{r}_{\perp}; t) = \sum_{ml} \delta A_{ml} e^{\mp i\phi + \lambda_{ml} t} \Phi_{ml}(\vec{r}_{\perp}) e^{-i\omega_{ml} t}. \quad (6.43)$$

δA_{ml} stands for the perturbation's amplitude and λ_{ml} the perturbation's eigenvalue in each of these modes. Phase-locking among the two circularly polarized components at $\phi = 0, \pi/2$ provides linearly polarized light along the \hat{x} and \hat{y} axis respectively. The cavity modes Φ_{ml} and the modal frequencies ω_{ml} are determined by the eigenvalue problem

$$\left[\nabla_{\perp}^2 + \left(\frac{\Omega}{c}\right)^2 2n_e \Delta n_{tl}(r) \right] \Phi_{ml} = \left(\frac{W_{ml}}{r_g}\right)^2 \Phi_{ml}. \quad (6.44)$$

As we have already mentioned, the refractive index distribution is approximated by a truncated parabolic profile

$$\Delta n_{tl}(R) = \begin{cases} \Delta n_{tl} [1 - R^2] & \text{if } R < 1 \\ 0 & \text{if } R \geq 1 \end{cases}, \quad (6.45)$$

with $R \equiv r/r_g$, r_g being the TL radius. The eigenmodes and eigenfrequencies are given in Appendix E.

From Eqs. (6.24) and (6.35a) the modal frequencies, referred to Ω , read

$$\omega_{ml} = -\frac{c^2}{2\Omega n_e n_g} \left(\frac{W_{ml}}{r_g}\right)^2. \quad (6.46)$$

Inasmuch as $\omega_{ml} < 0$, it describes the redshift of the modes due to the thermal lensing with respect to the flat index distribution. The stronger the TL strength the larger the redshift, which also increases as the mode order $\mathcal{O} \equiv (2m + l - 1)$ decreases.

Upon substituting Eq. (6.43) into Eq. (6.42) and projecting onto a mode LP_{ml} , the perturbation's eigenvalue λ_{ml} is given by the solution of the implicit equation

$$\lambda_{ml} = -\kappa \mp (\gamma_a + i\gamma_p) + i \frac{a\Gamma}{2} \frac{\iint \chi(\Omega + \omega_{ml} + i\lambda_{ml}, D_s(r; \mu)) |\Phi_{ml}|^2 d^2\vec{r}}{\iint |\Phi_{ml}|^2 d^2\vec{r}}, \quad (6.47)$$

where the sign $-(+)$ corresponds to $\hat{x}(\hat{y})$ linearly-polarized light. The perturbation's growth rate is $\text{Re } \lambda_{ml}$, while it oscillates at a frequency shifted by $\text{Im } \lambda_{ml}$ respect to $\Omega + \omega_{ml}$. The integral term on the right-hand side of Eq. (6.47) describes the modal gain (real part) and the nonlinear frequency shift (imaginary part) of the transverse mode under consideration, taking into account any possible frequency pulling or pushing of the modal frequencies due to the carrier induced refractive index change.

Therefore, the threshold current for every linearly polarized transverse mode LP_{ml} , $\mu_{th}(m, l, \pm; \Delta)$, is found from the condition $\text{Re } \lambda_{ml} = 0$. Threshold currents for the two linearly polarized solutions (\pm) are slightly different in the presence of linear anisotropies, hence we define the threshold for a given transverse mode as

$$\mu_{th}(m, l; \Delta) \equiv \min_{\pm} \{\mu_{th}(m, l, \pm; \Delta)\}. \quad (6.48)$$

and the absolute laser threshold is thus determined by

$$\mu_{th}(\Delta) \equiv \min_{m,l} \{\mu_{th}(m, l; \Delta)\}.$$

It is worth remarking that, given the carrier density distribution associated with the current injection in Eq. (6.41), the threshold current of transverse modes is determined jointly by the modal frequencies, that establish the material gain, and the overlap of the modal profile with the carrier distribution. These effects are in turn dependent on both the relative detuning and the thermal lensing strength. In the next two subsections, we discuss the threshold behavior of bottom and top emitter VCSELs corresponding to different shapes of the injected current.

Bottom-Emitting VCSEL

The current distribution across the active region of bottom-emitting VCSELs is quite homogeneous due to their circular p^+ contact and the typical high doping levels of the n-substrate [38], although current crowding at the aperture edges is observed when the VCSEL diameter is large. As we have already commented, we consider that

for this device structure the current distribution at the active layer is supergaussian, $C(r) = \exp[-(r/r_c)^6]$, with r_c being the radius of the active region. The total injected current is then $I(t) = \mu(t) \frac{\pi}{3} \Gamma(\frac{1}{3}) e N_t W r_c^2$, and the exponential tails of the supergaussian function take into account the current spreading effect [228]. We consider a device with an active region diameter, $r_c = 7.5 \mu\text{m}$, and a larger diameter of the thermal lens, $r_g = 9 \mu\text{m}$, in order to mimic heat diffusion across the cavity axis.

In Fig. 6.6, we represent the threshold curves obtained from Eq. (6.48) for the fundamental (solid lines) and first-order (dash-dot lines) transverse modes as function of the normalized detuning, Δ . We consider different values of the TL refractive index strength $\Delta n_{tl} = 10^{-2}$ (a), $\Delta n_{tl} = 10^{-3}$ (b) and $\Delta n_{tl} = 5 \cdot 10^{-4}$ (c). For a fixed Δn_{tl} , the threshold curves for the different modes as function of the detuning display a minimum when the modal frequency aligns with the gain peak. The position of such a minimum notably depends on the thermal waveguide, but also on the coupling with the carrier density through bandfilling and bandgap shrinkage included in χ . The curves are asymmetric around the minimum threshold with a smoother increase toward the blue side of the gain spectrum as a result of a higher differential gain. For small Δn_{tl} , which corresponds to an on-axis temperature excess of about $1 K$, we observe that besides the global increase of the threshold current, the threshold for the first-order transverse mode is very large (out of scale in Fig. 6.6). For moderate Δn_{tl} , the threshold of the fundamental mode is sensibly smaller than the first-order transverse mode, so the laser displays fundamental transverse mode operation at moderate currents above threshold. We observe that the threshold discrimination of the first-order transverse mode is more noticeable when the cavity resonance is located on the blue side of the gain curve, although in this case the threshold current increases. For large Δn_{tl} , we observe that the threshold differences between the two modes are very small over the whole range of detunings, thus indicating a strong tendency toward multimode emission. An interesting aspect is that, when the VCSEL operates in the red side of the gain spectrum, the first-order transverse mode has lower threshold than the fundamental one.

This general scenario can be interpreted from Eq. (6.47) as the interplay of two separate aspects. On one hand, the TL waveguide establishes the modal profiles Φ_{ml} , and frequencies ω_{ml} . The latter alone would define the modal gain if the active region were of infinite extent and homogeneously injected. Then the threshold curves for the different modes would follow the material gain spectrum, and one would therefore expect that the threshold would correspond to the mode whose frequency is the closest to the gain peak. However, due to the finite extent of the carrier density distribution, a geometrical correction that accounts for the overlap of the carrier density and the mode profile sets in. This effect is usually described by means of a lateral confinement factor that corresponds to the fraction of the modal power contained in

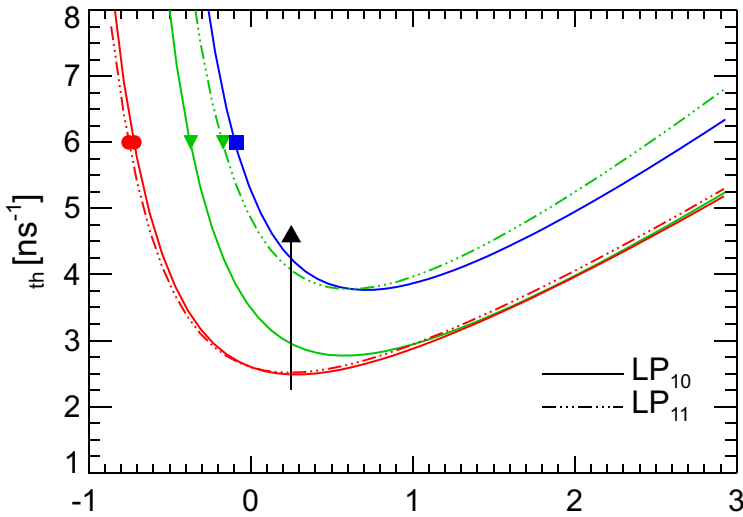


Figure 6.6. Threshold curves for the fundamental (solid lines) and first-order transverse modes (dashed lines) as function of the normalized detuning. The thermal lensing strength is $\Delta n_{tl} = 10^{-2}$ (\bullet), $\Delta n_{tl} = 10^{-3}$ (\blacktriangledown), $\Delta n_{tl} = 5 \cdot 10^{-4}$ (\blacksquare).

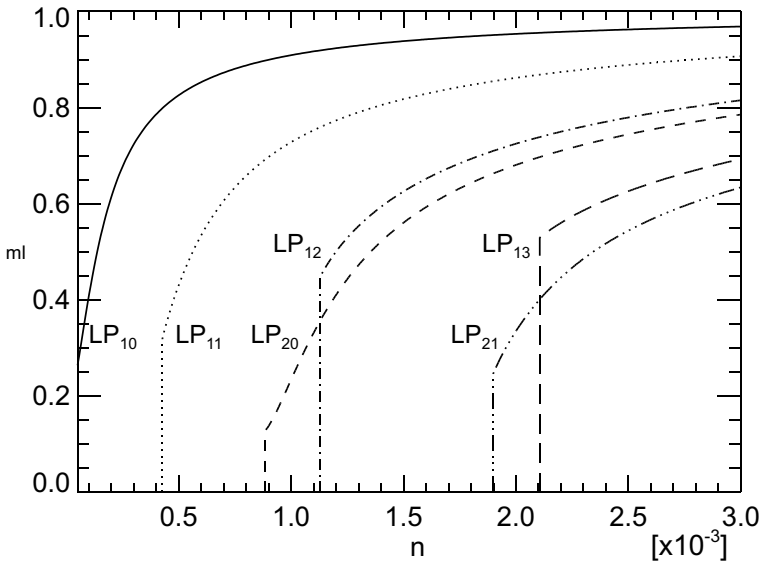


Figure 6.7. Lateral confinement factor of the modes supported by the TL waveguide as function of the TL strength. The carrier distribution corresponds to the bottom-emitter VCSEL.

the nucleus of the waveguide. In our case, however, the carrier distribution is inhomogeneous, thus we define a lateral confinement factor through

$$\Gamma_{ml} \equiv \frac{\iint |\Phi_{ml}|^2 \mathcal{S}(\vec{r}_\perp) d^2\vec{r}}{\iint |\Phi_{ml}|^2 d^2\vec{r}}, \quad (6.49)$$

where $\mathcal{S}(\vec{r}_\perp)$ is a normalized weight function, ranging from zero to one, that describes the shape of the active region. For simplicity, we take $\mathcal{S}(r) \equiv D_s(r)/\max\{D_s(r)\}$ with $D_s(r)$ the steady state carrier distribution given by Eq. (6.41). When the carrier density in the active region is approximated by a disc, $\mathcal{S}(r) = \Theta(r_c - r)$, our definition of the lateral confinement coincides with the fraction of modal power within the active region. With our choice for \mathcal{S} , the lateral confinement factor describes the degree of overlap of the modal profiles with the carrier distribution. Note that Γ_{ml} does not depend either on the modal frequencies or on the cavity detuning. Hence, we are able to separate the geometrical contributions to the laser threshold from those arising from the frequency dependence of the gain curve.

The lateral confinement, obtained from Eq. (6.49) for the guided modes considered above, is depicted in Fig. 6.7. As expected, we observe a fast decrease of the confinement factors as the TL strength decreases, suddenly dropping to zero when the mode is no longer confined by the TL waveguide. It is clear from Fig. 6.7 that for strong TL the confinement factors for the fundamental and the first-order transverse modes become very similar and close to one. In such a case, the material gain differences arising from different modal frequencies may be large enough to overcompensate the difference in confinement factors. Hence, the device can start to lase in the first-order transverse mode in spite of being homogeneously pumped. In order to improve the range of single-mode operation, it is desirable to work below the cut-off for the first-order transverse mode, which—for a fixed geometry—can be achieved by reducing the amount of TL through an increase of the device's lateral heat conductivity. For our particular configuration, the TL strength has to be moderate, and our analysis suggests that the on-axis excess temperature should be kept below $\sim 5 K$, since in this case the confinement factor for the first-order transverse mode is only 7% below that of the fundamental mode. However, it must be noted that the first-order transverse mode could start lasing well above threshold due to spatial-hole burning in the carrier density.

Top-Emitting VCSEL

Top-emitting VCSELs have a top contact of annular shape that leads to preferential injection in the outer edges of the active region both due to the ring contact and to current crowding at the aperture edges in the case of oxidized VCSELs. This strongly affects the overlap of the modal profiles with the carrier density, and thus the mode

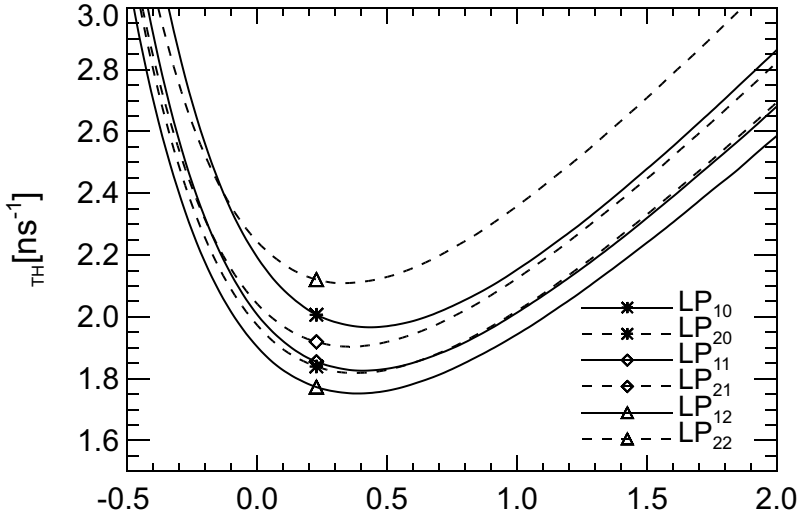


Figure 6.8. Threshold curves for the successive transverse modes of the top-emitter VCSEL. The position of the symbols denote the detuning of operation and its corresponding threshold current. The thermal lensing strength is $\Delta n_{tl} = 5 \cdot 10^{-3}$.

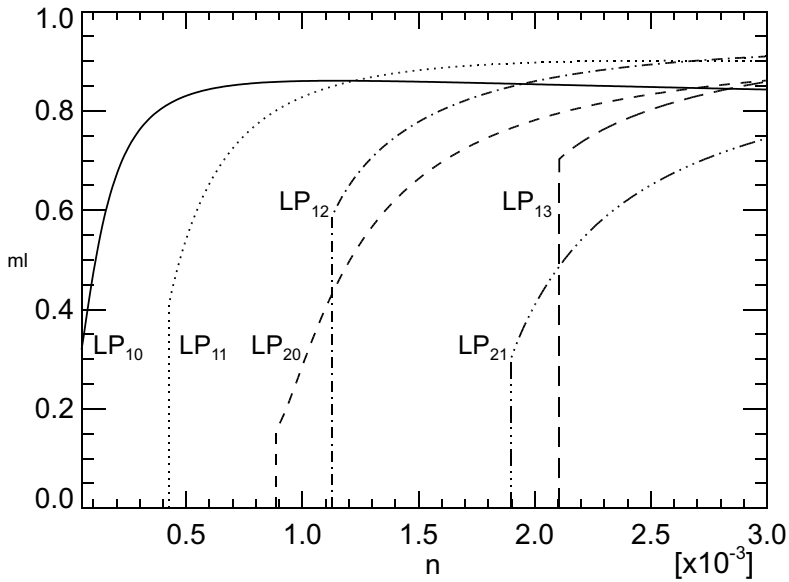


Figure 6.9. Lateral confinement factor of the modes supported by the TL waveguide as function of the TL strength. The carrier distribution corresponds to the top-emitter VCSEL.

selection at threshold. In order to illustrate this effect, we take the radial dependence of the injected current as: $C(\rho) = e^{-\rho^6} e^{\rho^2}$, with $\rho = r/r_c$ in such a way that the total injected current in the device is $I(t) \approx 1.24\mu(t)eWN_t\phi_c^2$. The variation in carrier density from the center to the carrier crowding radius is of the order of 25% for the actual diffusion coefficient. For simplicity and an easier comparison with the bottom-emitting VCSEL, we assume that the thermal lensing profile is unaffected by the ring in the current distribution, although such an approximation is unrealistic in the case of small radial thermal conductivity and when a marked ring-shaped current distribution is considered.

The threshold curves of the transverse modes, for a moderate value of TL ($\Delta n_{tl} = 5 \cdot 10^{-3}$), are shown in Fig. 6.8. The fundamental transverse mode is unfavored, with respect the other modes, due to its poor overlap with the carrier density resulting from the ring-shaped current injection. For these specific operating conditions, the lowest threshold corresponds, over the whole range of detunings, to the four lobed LP_{12} mode. Again, it can be observed that the range of single-mode operation of the device can be improved by detuning the cavity resonance to the blue side of the gain peak. It must be noted, however, that in this case the LP_{12} mode is further away from the gain peak than modes of lower order, hence clearly showing the dominance of the geometrical effects over the material gain.

The lateral confinement factor defined in Eq. (6.49) is plotted in Fig. 6.9 versus the TL strength. As the TL strength is increased, we observe that different transverse modes are favored depending on the TL conditions. From this purely geometrical point of view, the fundamental mode LP_{10} tends to dominate due to a better overlap with respect to the other modes for $\Delta n_{tl} < 1.2 \cdot 10^{-3}$. For $1.2 \cdot 10^{-3} < \Delta n_{tl} < 2.7 \cdot 10^{-3}$ the first-order transverse mode LP_{11} is favored while for $\Delta n_{tl} > 2.7 \cdot 10^{-3}$ the four-lobed LP_{12} displays the maximum confinement factor.

6.6.1 Numerical simulations

In order to give more specific evidences of the interplay of TL and the shape of the gain distribution, we perform numerical simulations of Eqs. (6.30), (6.35a) and (6.35c). We discuss the switch-on dynamics of bottom- and top-emitting VCSELs when they operate close to threshold. Some guidelines about the numerical integration scheme can be found in the Appendix F.

In this section, we assume that the nominal detuning is $\Delta = 0.25$, chosen to achieve operation near the gain peak, and a moderate value for the TL strength $\Delta n_{tl} = 5 \cdot 10^{-3}$. In these conditions, the threshold analysis presented in the previous section shows that the mode with the lowest threshold is the fundamental one, with \hat{y} -polarization. In Fig. 6.10 we show the dynamics of the bottom-emitting VCSEL when is biased close to threshold. The evolution of the total intensity near fields

is shown in panels (a)-(c) for three different currents ranging from $\mu = 1.05\mu_{th}$ up to $\mu = 1.25\mu_{th}$. Near field images are plotted with an inverted scale scheme using maximum contrast, therefore comparison of the relative intensity between images is not possible. For the lower injection current we obtain stable fundamental mode operation in a well established polarization. When the current is slightly increased the near field is still Gaussian but its position changes from image to image. Increasing further the injection current, we find that this last stage ignites the appearance of the first-order transverse mode as can be clearly seen in panel (c). As it is commonly observed, the first-order transverse mode switches-on in the orthogonal polarization of the lasing one. We note that this result is not a direct consequence of the threshold analysis presented in Sec. 6.6, but a nonlinear competition between transverse and polarization degrees of freedom. The total intensity evolves according to Fig. 6.10(d) when the current is $\mu = 1.10\mu_{th}$. The VCSEL emits preferentially in the lower frequency polarization component (\hat{y} -LP), being selected by the actual value of the dichroism. The orthogonal component is considerably suppressed in CW, although it appears during the transient following the switch-on. The optical spectra of the linear components of the electric field, defined through

$$\mathcal{OS}_k(\omega) = \iint dx' dy' \left| \int_{-\infty}^{\infty} dt A_k(x', y'; t) e^{i\omega t} \right|^2, \quad (6.50)$$

with $k = (x, y)$, is an efficient way to separate the spectral content of the signal. The optical spectrum of the dominant polarization, under CW operation, displays a dominant peak at the position of the fundamental transverse mode frequency. The orthogonal polarization component clearly exhibits the dominance of the first-order transverse mode. It is worth remarking that the current at which such a mode appears is smaller than that predicted by the threshold analysis due to the role of the spatial hole burning. This is, the steady state carrier distribution for this current is no longer supergaussian but displays a hole at the center due to the increased stimulated recombination in this region.

In view of the above results, one might think to preferentially excite one of the transverse modes by proper selection of the current profile. To explore this possibility, we perform numerical simulations of the top-emitting VCSEL biased close to the threshold current. The current is switched-on from slightly below threshold to above threshold, $\mu = 1.1\mu_{th}$. In Fig. 6.11(a) we represent the evolution of the total intensity accompanied by the near field images at different stages. In the 'off' state, the spontaneous emission near field displays a hole at the center as a result of the ring-shaped carrier distribution. As soon as the laser switches-on we observe that a transverse mode with four lobes is selected. Nevertheless, the orientation of the mode is not fixed and starts to rotate, alternating between odd and even LP_{12}

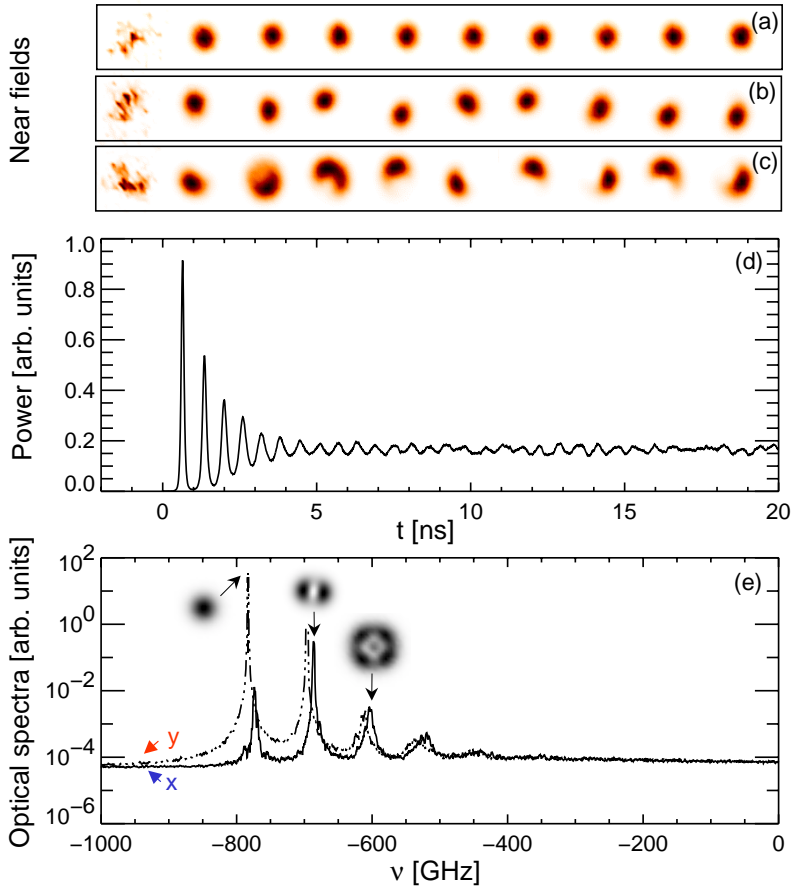


Figure 6.10. Switch-on dynamics of the bottom emitter VCSEL. Evolution of the total intensity near-fields: (a) $\mu = 1.05\mu_{th}$, (b) $\mu = 1.10\mu_{th}$, and (c) $\mu = 1.25\mu_{th}$. (d) Temporal evolution of the total intensity at $\mu = 1.10\mu_{th}$. (e) Optical spectra of both linear polarizations under CW operation at $\mu = 1.10\mu_{th}$.

modes. The polarization-resolved optical spectra, computed under CW operation [See Fig. 6.11(b)], reveals that the device exhibits nearly single-mode operation with a predominant peak that corresponds to the four-lobed LP_{12} mode. However, a daisy mode with six lobes is weakly excited ($\sim 40dB$ of side mode suppression ratio). The four-lobed structure of the LP_{12} mode burns a hole in the carrier distribution along the angular direction that induces the rotation of the mode, and this yields the weak excitation of the daisy mode. We also note reminiscent peaks, with much lower power, at the frequency positions of the fundamental and first-order transverse modes.

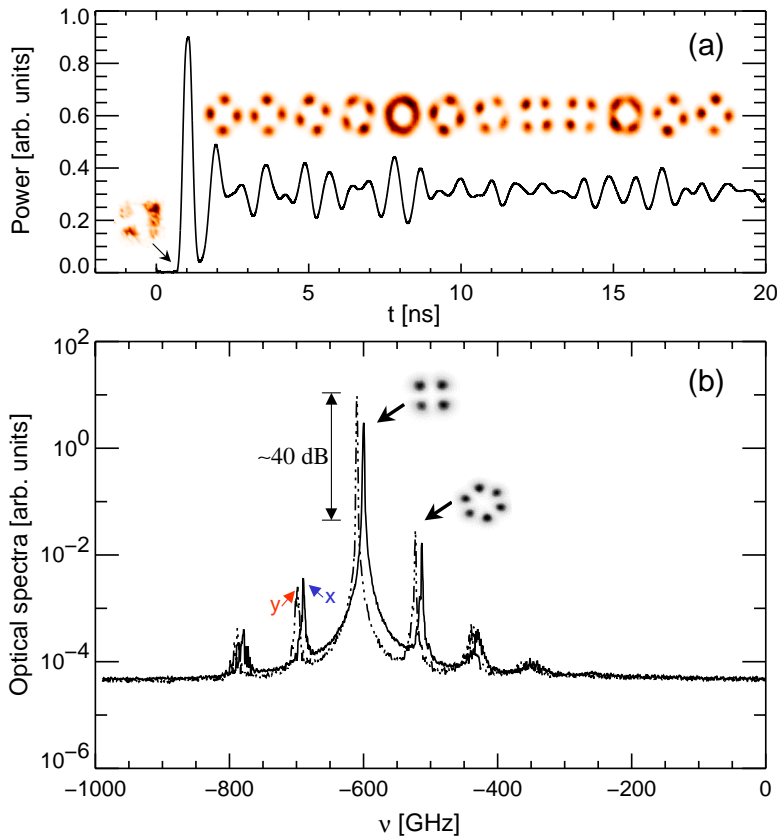


Figure 6.11. Higher-order transverse mode selection for the top-emitter VCSEL. (a) Close-to-threshold temporal evolution of the total intensity at $\mu = 1.10\mu_{th}$. (b) Corresponding optical spectra in both polarizations under CW operation. Near field images are obtained using the maximum contrast of an inverted scale.

6.7 Subnanosecond Electrical Excitation

The mechanisms governing the selection of transverse modes close to the lasing threshold have been identified from the previous analysis. An important question that we now address is the transient multimode dynamics during subnanosecond electric excitation (large-signal). In particular, we analyze the influence of thermal lensing on the spectral properties of these devices. The understanding of these effects is essential in applications that include high-speed current modulation. Moreover, the numerical results can be contrasted with reported experimental investigations [229, 230] using gain-guided VCSELs: the onset of transverse modes is characterized by a turn-on delay which strongly depends on the device geometry as well as the thermal lensing strength.

We numerically integrate the partial differential Eqs. (6.35a)–(6.35c) for VCSELs of two different aperture diameters. The lateral dimensions of the VCSEL A are $r_c = r_g = 6.25 \mu\text{m}$ whereas VCSEL B $r_c = 11 \mu\text{m}$ and $r_g = 15 \mu\text{m}$. The electrical excitation consists in a current pulse that is switched-on at $t = 0$ from $\mu_b = 0.85\mu_{th}$ to μ_{on} varying from μ_{th} up to $9\mu_{th}$. μ_{th} represents the laser threshold current at the detuning of operation, $\Delta = 0.5$. Pulses have 1 ns of duration and 50 ps of rise and fall times. Since the duration of the pulse is much shorter than the thermal time ($\tau_t \sim 1\mu\text{s}$), it is justified to use a fixed TL which effective value is determined from the operating bias current. From the near field images, we find fast changes on the spatial distribution of power suggesting that many transverse modes are involved. In order to better characterize this dynamics we perform a spectral analysis of the spatiotemporal data.

Optical spectra

Optical spectra of both polarization components, \hat{x} -LP (solid lines) and \hat{y} -LP (dotted lines), under pulsed excitation are shown in Figs. 6.12–6.13. Both linear polarizations are excited by the current pulse and remain active during all the transient. We observe a birefringence splitting of ~ 10 GHz between the two polarizations that results from the birefringence splitting γ_p/π . The position of the fundamental mode (α) is redshifted with respect to the longitudinal mode resonance Ω as result of the TL and nonlinear frequency shift effects described through Eq. (6.47). The full-width at half-maximum (FWHM) of the fundamental mode, that almost corresponds to the first optical peak in Fig. 6.14, is broaden during the transient due to the α -factor that for our case is $\alpha \sim 1 - 2$. The effective detuning of the fundamental mode with respect the bandgap is $\Delta_{eff} \approx 0.47$. Therefore the fundamental mode position is located close to the maximum of the gain spectrum, where the material gain for the successive higher-order transverse modes decreases. The peculiar excitation scheme favors the excitation of higher order transverse modes (β, ξ, \dots) that can be also identified in the optical spectra. The frequency separation between transverse modes decreases with the waveguide radius according to Eq. (6.46), thus reducing the differences in material gain. For the VCSEL A , the typical mode separation in frequency is of the order of 100 GHz [Fig. 6.12] while for the VCSEL B is only 44 GHz [Fig. 6.13]. Moreover, the relative confinement of the modes improves with the waveguide radius that induces the excitation of more high-order modes in Fig. 6.13 than in Fig. 6.12. The amplitude of the current pulse is also decisive for determining the transient variations of carrier densities, and thus the number of excited transverse modes.

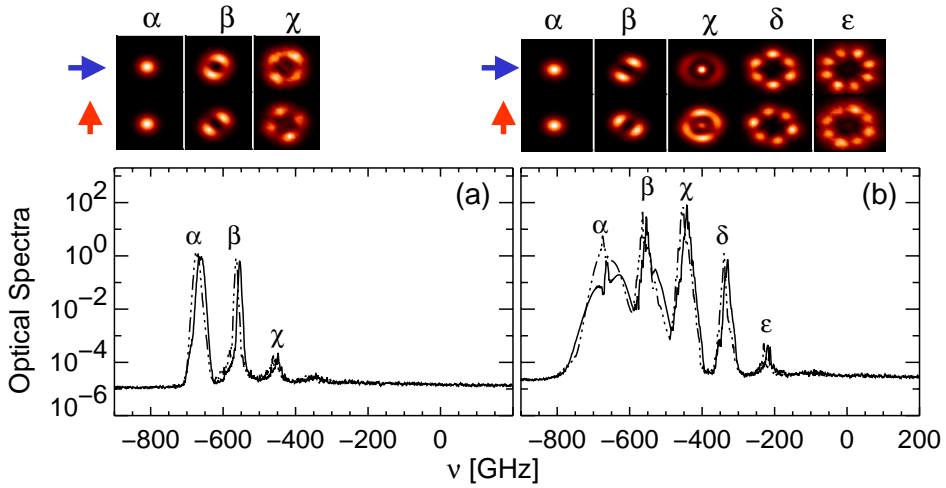


Figure 6.12. Optical spectra for the VCSEL *A* in both polarizations: $\mu_{on} = 1.5\mu_{th}$ (a), and $\mu_{on} = 9\mu_{th}$ (c). Filtered near field images in both orthogonal polarizations $\rightarrow (\hat{x}$ -LP) and $\uparrow (\hat{y}$ -LP).

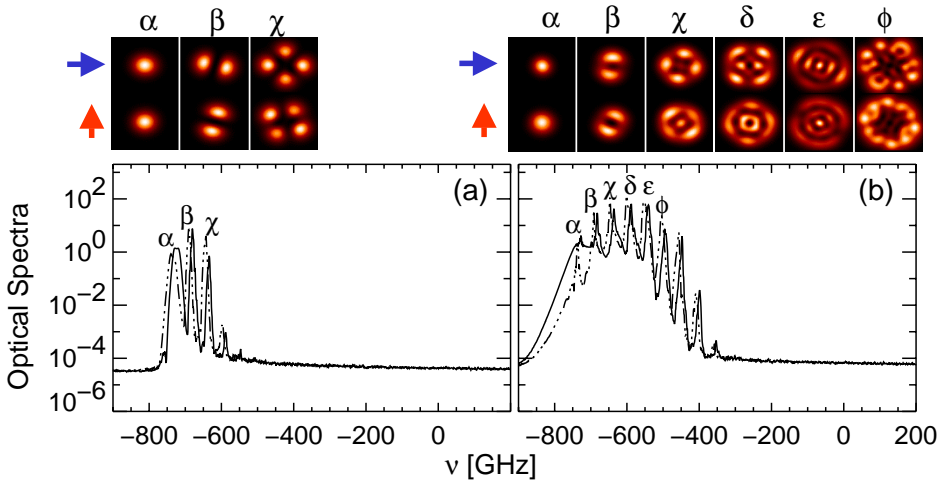


Figure 6.13. Optical spectra for the VCSEL *B* in both polarizations under the same conditions than in Fig. 6.12.

Modal evolution

In order to investigate the separate evolutions of the transverse modes, we filter the optical field components $A_k(x, y; t)$, $k = x, y$ around each modal frequency, as done when using a monochromator. Numerically, we use a Lorentzian filter of width $\Delta\nu$

$$[A_k * L^i](x, y; t) \equiv \frac{1}{2\pi} \int_{-\infty}^{\infty} \frac{\tilde{A}_k(x, y; \nu)}{1 + \left(\frac{\nu - \nu_i}{\Delta\nu}\right)^2} e^{-i\nu t} d\nu. \quad (6.51)$$

We can reconstruct i) the time-averaged power distribution of the modes in each orthogonal polarization (modal profiles)

$$\overline{NF}_k^i(x, y) = \frac{1}{T} \int_0^T [A_k * L^i](x, y; t) dt, \quad (6.52)$$

and ii) the temporal evolution of the modal optical power

$$P_k^i(t) = \iint dx dy [A_k * L^i](x, y; t). \quad (6.53)$$

We note however that high-order peaks may contain several nearly degenerated LP_{ml} modes that the filtering process is not able to separate. Proceeding in this way, the polarization-resolved near field images in Figs. 6.12 and 6.13 correspond to the time-averaged power distribution of each transverse mode. Near fields become more complex as the 'on' current and the active region diameter are increased.

In Fig. 6.14 we plot the temporal evolution of the total optical power of the different transverse modes by using the filtering technique. In both VCSEL A and B, we observe that the laser switches-on in the fundamental transverse mode (α) followed by the successive excitation of several higher-order transverse modes. We also observe that the laser switch-off occurs in a higher-order transverse mode. We note that the same qualitative behavior is observed for different turn-on events. For the larger VCSEL the modes tend to operate simultaneously, exhibiting a strong competition for the available gain in the active region [Fig. 6.14(b)]. In addition, stronger multi-transverse mode behavior was expected owing to a better overlap of the higher-order transverse modes with the spatial gain distribution. We observe that the excitation of the mode (β) rapidly ignites the state (χ). Hence, the onset for the excitation of higher order transverse modes appears much faster in VCSEL B.

These results are in good agreement with the reported experimental observations [229, 230] where a roughly estimation of the turn-on delay for large-aperture VCSELs was carried out in terms of a simple model. The latter treats each mode as independent; neglecting the current profile, spatial hole burning and frequency

dependence of the gain curve. From our description, and going beyond this simple analysis, we find that two independent mechanisms are crucial to determine the switch-on sequence of transverse modes: spatial hole burning and transient blue shift of the gain curve. In the former, once a low order mode has switched-on, spatial hole burning favors higher order modes because of their better overlap with the resulting carrier distribution. In the latter, the transient increase in carrier density after the application of the current pulse leads, due to bandfilling, to a blue shift of the gain spectrum that progressively enhances the material gain corresponding to higher-order modes. Consequently, our model contains the ingredients that allow us to describe the sequence of excited modes without any restriction, neither on aperture diameter nor on the current profile.

Turn-on delay

The modal evolution can be better characterized by computing the switch-on times of the transverse modes: the time required for a mode to reach a predefined inten-

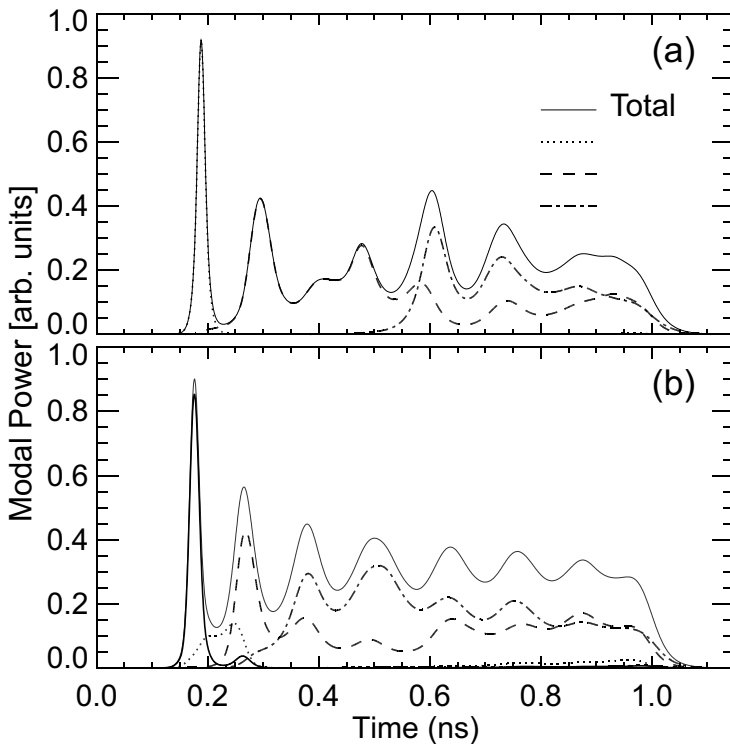


Figure 6.14. Evolution of the modal power of each transverse mode and the total intensity for the VCSEL *A* (a), and *B* (b).

sity threshold. Let T_ξ be the switch-on time of a higher-order mode LP_ξ , the turn-on delay of a higher order transverse mode is the switch-on time referred to the fundamental one, i.e. $\Delta T_\xi = T_\xi - T_\alpha$. In Fig. 6.15 we show the dependence of the turn-on delay of the transverse modes on the pulse current (normalized to threshold). As was expected the turn-on delay for all the modes rapidly increases when approaching to threshold, displaying an asymptotic behavior for $\mu_{on}/\mu_{th} \gtrsim 1$. Another striking property is that after the application of the current pulse, the transverse modes appear in a quite definite sequence. For this reason, we always find that the turn-on delay increases when increasing the order of the transverse mode for any value of the ‘on’ current. The turn-on delay for the VCSEL B [Fig. 6.15(b)] is considerably reduced for the same modes that are present in VCSEL A [Fig. 6.15(a)]. As already mentioned, a larger number of transverse modes become excited in the VCSEL B. In general we find that these results are in good agreement with those experimentally reported [229]-[231].

Dependence with thermal-lensing

We consider the transient response of a bottom-emitter VCSEL with $r_c = 7.5 \mu\text{m}$ and $r_g = 9 \mu\text{m}$ for three different TL strengths: $\Delta n_{tl} = 10^{-2}$ (a), $\Delta n_{tl} = 5 \cdot 10^{-3}$ (b), and $\Delta n_{tl} = 5 \cdot 10^{-4}$ (c). The bias current determines the heat dissipated by Joule effect, and provides a means of experimentally vary the TL strength. In Fig. 6.16, we represent snapshots of the intensity distribution in the two linear components. When analyzing the spatiotemporal response to the current pulse, we observe that laser initially switches-on in the fundamental transverse mode followed by the successive

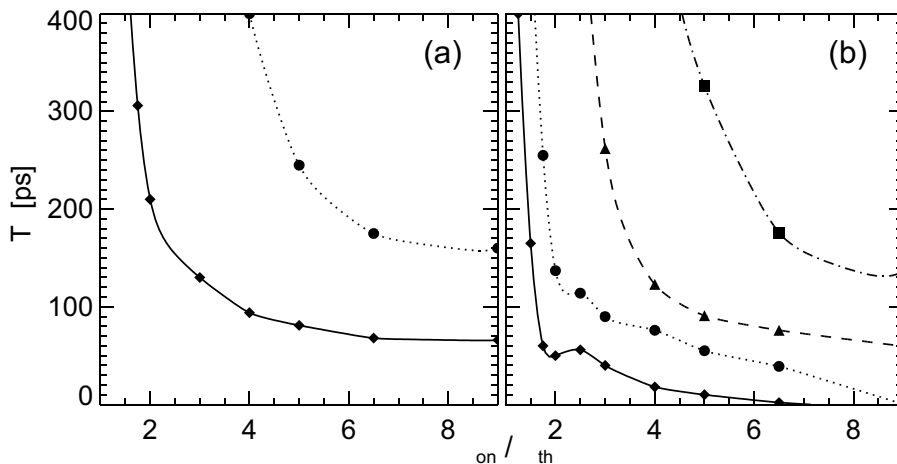


Figure 6.15. Turn-on delay as function of the ‘on’ current. Results for the VCSEL A (a) and VCSEL B (b).

excitation of higher-order transverse modes. Modal behavior depends dramatically on TL: the weaker the TL, the smaller the number of excited modes with much longer turn-on times .

In Fig. 6.17, we show the polarization resolved optical spectra corresponding to the previous dynamics. Both linear polarizations \hat{x} -LP (\hat{y} -LP) are depicted in solid (dashed) lines. We find that the frequency separation between successive transverse modes, that is approximately constant for a parabolic waveguide, depends drastically on the TL properties. We obtain a frequency separation between the fundamental and first-order transverse mode of 120 GHz (a), 80 GHz (b) and 54 GHz (c). For the first two cases, these frequency differences agree quite well with those predicted by Eq. (6.46), $(\omega_{11} - \omega_{10})/(2\pi) = 118\text{GHz}$ and 83GHz , respectively. However, this is not so in Fig. 6.17(c), where Eq. (6.46) predicts a frequency difference of 23 GHz. The reason is that the waveguide distortion caused by the carrier-induced refractive in-

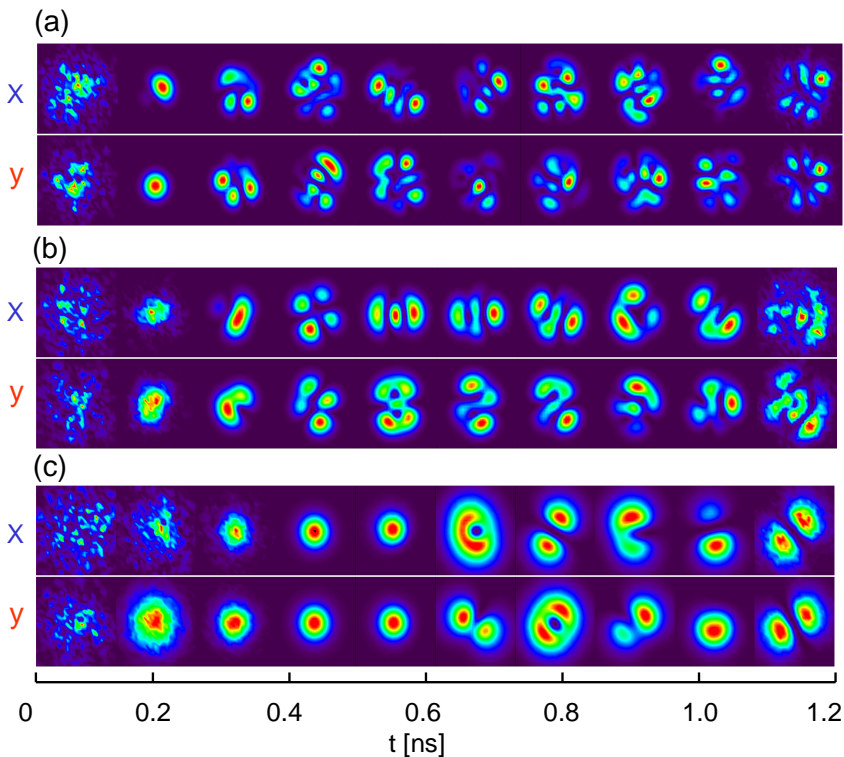


Figure 6.16. Response to a current pulse of the bottom-emitter VCSEL of $15\mu\text{m}$, $\mu_b = 0.85\mu_{th}$ and $\mu_{on} = 4\mu_{th}$. Snapshots of the near field power distribution in \hat{x} and \hat{y} polarization components. The thermal lensing strength is $\Delta n_{tl} = 10^{-2}$ (a), $\Delta n_{tl} = 5 \cdot 10^{-3}$ (b) and $\Delta n_{tl} = 5 \cdot 10^{-4}$ (c).

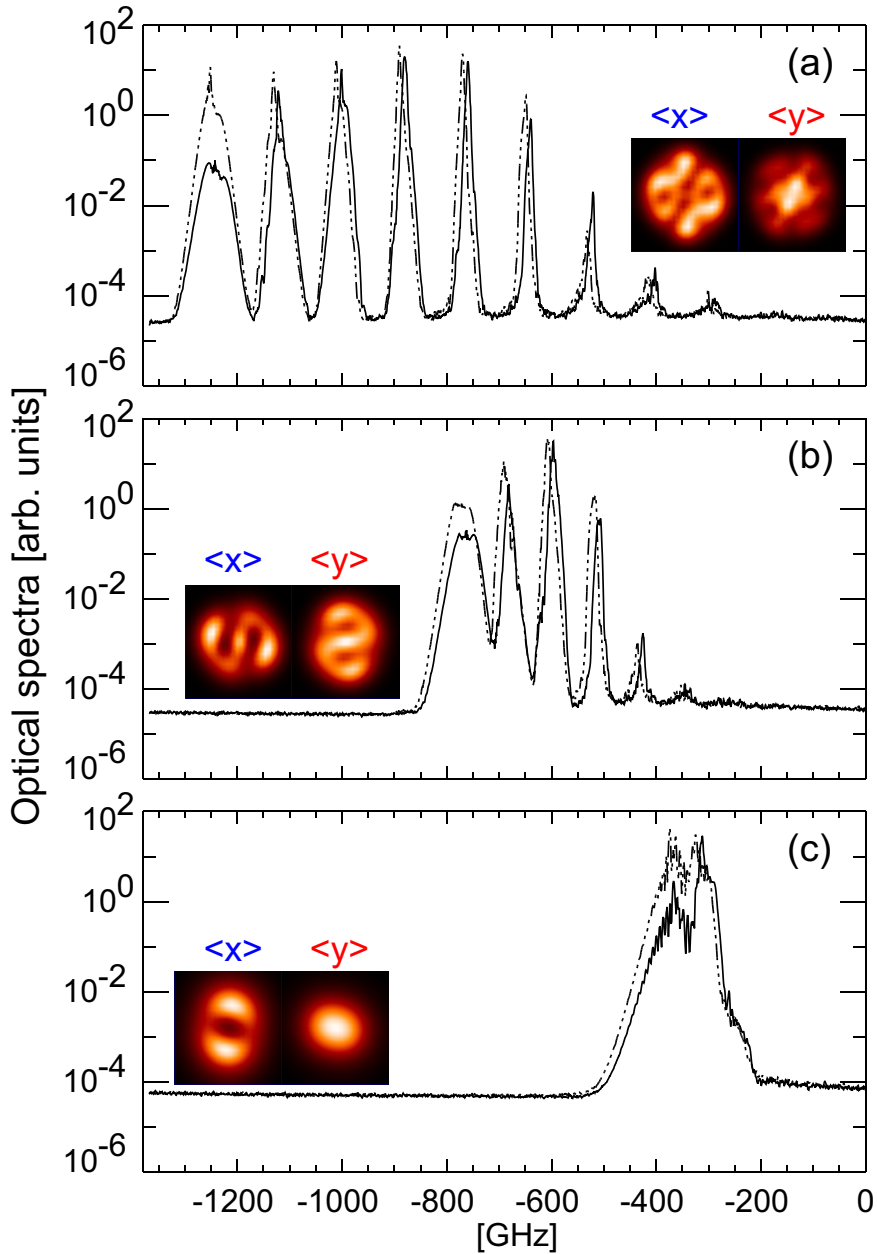


Figure 6.17. Polarization resolved optical spectra of the bottom-emitter VCSEL, \hat{x} -LP (solid lines) and the \hat{y} -LP (dash lines). The thermal lensing strengths correspond to those used in Fig. 6.16. Near field images depict the time averaged power distribution in both linear polarization components.

dex strongly modifies the modal profiles and frequencies. In this case, the analysis performed in Sec. 6.6 is no longer valid and alternative methods, that take into account these effects, are required in the calculation [232]. In addition, we can see that both polarizations are active during the transient regime displaying similar dynamics. Their spectra show a birefringence splitting of 10 GHz that corresponds to γ_p/π . The near-field images, in this figure, depict the time-averaged power distribution in each linear polarization. As consequence of the number of modes excited by the current pulse, we go from complex near fields resulting from the superposition of several transverse modes (a) to simpler ones (c).

6.8 Summary and Discussion

We have developed an optical model for the large-signal dynamics of multimode VCSELs that incorporates both spatial and polarization degrees of freedom simultaneously. We have assumed that the lateral current distribution at the active layer is known, an explicit functional form that only depends on the structure of the device. We have approximated these functions by a supergaussian in the case of bottom-emitting devices, while a ring-shaped current distribution has been taken for top-emitting devices. Similarly, the radial dependence of the excess refractive index $\Delta n(r)$ has been assumed to be parabolic, thus allowing to analyze the effects of thermal lensing in the device. Although the electrical and thermal models have not been yet implemented, they might be included in our optical model in order to self-consistently determine the distribution in current density, temperature and optical field.

In the absence of spatial effects, the selection of polarization modes reveals that two different ways for polarization switching are possible: one that typically occurs for relatively large birefringence is thermally-induced, and a second mechanism that may occur for small birefringence has a nonthermal origin. The selection of transverse modes has been systematically discussed in top- and bottom-emitting VCSELs in two different operating conditions: close-to-threshold and under large-signal excitation of the current.

The close-to-threshold behavior of top- and bottom-emitting VCSELs have been analyzed by means semi-analytical methods and corroborated by the results of numerical simulations. We have found that transverse mode selection (close to threshold) depends on a joint interplay between the lateral confinement factor and the material gain spectrum. VCSELs with disk-shaped current injection select the fundamental transverse mode at threshold unless the cavity resonance is strongly detuned to the red side of the gain peak. The evolution of the near fields has been followed, demonstrating that the laser onset of a top emitting VCSEL, with ring-shaped cur-

rent profiles, may be initiated from a higher-order transverse mode depending on the strength of the thermal lens. In this case, the overlap of the mode profile with the ring-shaped carrier density dominates for the mode selection at threshold. Low to moderate values of the thermal lensing are required in order to maintain single-mode operation since for strong thermal lensing the confinement of all the modes increases while their frequency spacing is not strongly affected, hence leading to poor mode discrimination at threshold.

The selection of transverse modes in gain-guided VCSELs subject to an electrical excitation of short duration have been investigated for different active-region diameters, excitation amplitudes and thermal lensing conditions. This setup has simplified considerably the analysis because the temperature distribution is approximately constant during the pulse. We have obtained a well defined sequence for the excitation of the different transverse modes that were characterized by a turn-on delay. The dependence of the turn-on delay with the amplitude of the current pulse and with the thermal lensing strength is in good agreement with experimental observations. In view of the results, we infer that when these devices are used in optical communication systems, and when they are being modulated across threshold by a sequence of bits, the ratio of a single bit duration with respect to the modal turn-on delay provides an estimation of the number of modes that can be excited. In this case, however, one has to include all possible memory effects that arise from variations in the initial conditions for the emission of each optical pulse [233]. We have found a clear tendency toward multimode emission even in the case of weak TL, which may affect the performance of the device in data-transmission applications because of an enhanced pulse dispersion that lowers the degree of spatial coherence of the beam profile and therefore the modal noise in multimode-fiber optical links. In order to enhance single-mode operation, cavity detunings on the blue side of the gain peak would be recommended, although in this case there would be an increase in threshold current. Moreover, the thermal shift of the cavity mode as the current is increased would reduce the operation range through thermal roll-off.

Chapter 7

Transverse Mode Dynamics: Spatiotemporal versus modal expansion descriptions

7.1 Introduction

Vertical-cavity¹ surface-emitting lasers (VCSELs) display instabilities associated with the polarization state of the light and/or the excitation of transverse modes of higher order that have been described in the previous chapters. As already commented, the large complexity of the problem arises from the fact that several physical mechanisms are involved [38]; namely, diffraction, thermal effects, gain and refractive-index spectra, current distribution, etc. The initial studies of polarization instabilities in VCSELs [32, 37] considered the polarization dynamics in the absence of spatial effects, but the increasing evidence of the interplay of polarization and spatial effects has stimulated research incorporating this dependence [193, 234]. The numerical complexity of a spatiotemporal description of the VCSEL can be largely alleviated by expanding the optical field in cavity modes [156], specially for devices with a low number of confined modes. This approach has been extensively used in index-guided devices (air-post [196, 235], etched mesa [236], or oxidized layer [237]) where methods for obtaining both scalar [238] and vectorial [198, 239] modes are well-known. However, lateral confinement of the optical field in gain-guided devices solely relies on the spatial distribution of the gain, with the help of a generally weak, thermally-induced lens [38]. Different approximate analytical methods have been

¹ This chapter is based on the papers:

J. Mulet and S. Balle, *Phys. Rev. A* **66**, 053802 (2002);
A. Valle, J. Mulet, L. Pesquera, and S. Balle, *Proc. SPIE* **4649**, 50 (2002);
J. Mulet and S. Balle, *IEEE J. Quantum Electron* **38**, 291 (2002).

proposed for determining the modal structure of these devices, e.g., the complex square-law medium [232] or variational methods [240]. However, their applicability to study large signal dynamics in these systems is dubious because the modes can be quite sensitive to the spatial distribution of the carrier density, which in turn depends on the optical pattern through spatial hole burning. The dynamical description of the interplay between optical field and carrier density requires consideration of the full² optical susceptibility of the active medium, obtained either from microscopic theories [210] or from some semiclassical approximation [211]. In any case, the gain and refractive-index spectra induced by the carriers, as well as their nonlinear dependence on carrier density, are required.

In this chapter, we investigate the limits of validity and usefulness of a modal description of gain-guided VCSELs by analyzing the impact of the carrier-induced gain and refractive-index spectra on the stability of the transverse modes. We compare the results obtained from the spatiotemporal description and the modal expansion, under dynamical conditions. The study focuses on the off-state bounce phenomenon that, induced by carrier diffusion, appears under large-signal modulation of the current: secondary pulsations of the optical power follow the current turn-off transient [241]. We demonstrate that there exists a critical value for the lateral guiding above which the predictions of the modal expansion coincide with those of the full spatiotemporal model. In the opposite case the modal description yields results that deviate from those in the spatiotemporal model. The differences arise from the dynamical redistribution in carrier-induced refractive index that produce a shrinkage of the mode profile. This last effect is not included in the modal expansion, and it determines the limits of validity of such an approach for gain-guided devices. The chapter is organized as follows: In Sec. 7.2 we perform the modal expansion of the spatiotemporal model presented in chapter 6. In Sec. 7.3 we perform the comparison between both models, and finally Sec. 7.4 is devoted to summarizing and concluding the chapter.

7.2 Optical Modal Expansion

We consider the spatiotemporal model for the dynamics of the optical field in VCSELs given in the preceding chapter. This model describes the lateral dependence of the slowly-varying amplitudes (SVA) of the electric field around the optical carrier frequency Ω , expressed in the basis of circular polarization components, A_{\pm} . The circular components interact only with spin-up or spin-down carriers, and the two carrier densities are coupled among them by spin-flip processes.

²Both gain and refraction-index spectra are required.

Obtaining the solutions of this model requires intensive computation due to the explicit spatial dependence of the optical field components. Such an explicit dependence can be eluded, in the same way as in Refs. [156, 241]-[244], by expanding the SVAs of the optical field in “cold-cavity” modes, Φ_{ml} , of the transverse waveguide operator $\hat{\mathcal{L}}$ [Eq. (6.24)]. Then the electric field evolves according with a set of ordinary differential equations for the mode amplitudes. The major inconvenience in such an approach is that the interaction with the active material has to be weak so that possible distortions of the cold-cavity modes can be neglected. In this chapter, we demonstrate that the last hypothesis is not always fulfilled in gain-guided VCSELs and that there exists a minimum required lateral guiding.

The modes Φ_{ml} and the modal frequencies ω_{ml} are determined by the eigenvalue problem [238]

$$\left[\nabla_{\perp}^2 + \left(\frac{\Omega}{c} \right)^2 2n_e \Delta n(r) \right] \Phi_{ml}(r, \theta) = \left(\frac{W_{ml}}{r_g} \right)^2 \Phi_{ml}(r, \theta), \quad (7.1)$$

r_g being the waveguide radius. The modal frequencies ω_{ml} , given in Eq. (6.46), describe the frequency redshift between the mode considered and the longitudinal carrier frequency Ω . The eigenmodes verify the orthogonality relation

$$\iint \Phi_{ml}(\vec{r}_{\perp}) \Phi_{m'l'}^*(\vec{r}_{\perp}) d^2 \vec{r}_{\perp} = \delta_{mm'} \delta_{ll'}. \quad (7.2)$$

We express the SVA of each circular component of the field as

$$A_{\pm}(\vec{r}_{\perp}; t) = \sum_{ml} \Phi_{ml}(\vec{r}_{\perp}) a_{\pm ml}(t) e^{-i\omega_{ml}t}, \quad (7.3)$$

where $a_{\pm ml}(t)$ stands for the complex circular components of the modal amplitude associated with the transverse mode Φ_{ml} . In the frequency domain, Eq. (7.3) reads

$$\tilde{A}_{\pm}(\vec{r}_{\perp}; \nu) = \sum_{\alpha} \Phi_{\alpha}(\vec{r}_{\perp}) \tilde{a}_{\pm \alpha}(\nu - \omega_{\alpha}), \quad (7.4)$$

where $\alpha = \{m, l\}$ is a shorthand index for the transverse modes, with $m = 0, 1, \dots$ and $l = 0, \pm 1, \dots$. By substituting it into the constitutive relationship for the material polarization (in frequency domain), we have

$$\begin{aligned} \tilde{P}_{\pm}(\vec{r}_{\perp}, \nu) &= \chi_{\pm}(\Omega + \nu, D_+, D_-) \tilde{A}(\vec{r}_{\perp}; \nu) \\ &= \sum_{\alpha} \chi_{\pm}(\Omega + \nu, D_+, D_-) \tilde{a}_{\pm \alpha}(\nu - \omega_{\alpha}) \Phi_{\alpha}(\vec{r}_{\perp}). \end{aligned} \quad (7.5)$$

Since the modal amplitudes are nearly monochromatic around each modal frequency ($\tilde{a}_{\pm \alpha}(\nu - \omega_{\alpha}) \neq 0$ only when $\nu \approx \omega_{\alpha}$) we use the modal reference frames

$u_\alpha \equiv \nu - \omega_\alpha$ for transforming to time domain. Using the same technique as in Eq. (6.36) for performing such a step, we obtain

$$P_\pm(\vec{r}_\perp, t) \approx \sum_\alpha \left[\chi_\pm(\Omega + \omega_\alpha + i\frac{\dot{a}_{\pm\alpha}(t)}{a_{\pm\alpha}(t)}, D_+, D_-) a_{\pm\alpha}(t) \Phi_\alpha(\vec{r}_\perp) e^{-i\omega_\alpha t} \right]. \quad (7.6)$$

Upon substitution of Eqs. (7.3) and (7.6) into the field equation (6.35a) and by projecting onto a mode $\Phi_\beta^*(\vec{r}_\perp)$, we arrive at the rate equation for the amplitude of the mode considered

$$\dot{a}_{\pm\beta}(t) = -\kappa a_{\pm\beta} + \frac{ia\Gamma}{2} p_{\pm\beta}(t) - (\gamma_a + i\gamma_p) a_{\mp\beta} + F_\beta(t), \quad (7.7)$$

while by substituting Eqs. (7.3) and (7.6) into Eq. (6.35c) we obtain

$$\begin{aligned} \partial_t D_\pm(\vec{r}_\perp; t) = & \frac{\mu(t)}{2} C(\vec{r}_\perp) - AD_\pm - (BN_t) D_\pm^2 \mp \gamma_j (D_+ - D_-) \\ & + \mathcal{D}\nabla_\perp^2 D_\pm + \frac{a}{2i} \sum_{\alpha, \beta} \left[e^{i(\omega_\beta - \omega_\alpha)t} \Phi_\alpha \Phi_\beta^* \times \right. \\ & \left. \chi_\pm \left(\Omega + \omega_\alpha + i\frac{\dot{a}_{\pm\alpha}(t)}{a_{\pm\alpha}(t)}, D_+, D_- \right) a_{\pm\alpha}(t) a_{\pm\beta}^*(t) - \text{c.c.} \right]. \quad (7.8) \end{aligned}$$

Note that the stimulated recombination terms in the above equation retain the local spatial dependence of the carrier variables. On the contrary, in the modal material polarization defined through

$$\begin{aligned} p_{\pm\beta}(t) = & \sum_\alpha \left[e^{i(\omega_\beta - \omega_\alpha)t} a_{\pm\alpha}(t) \times \right. \\ & \left. \int_{-\infty}^{\infty} \Phi_\beta^* \chi_\pm \left(\Omega + \omega_\alpha + i\frac{\dot{a}_{\pm\alpha}(t)}{a_{\pm\alpha}(t)}, D_+, D_- \right) \Phi_\alpha d^2\vec{r}_\perp \right], \quad (7.9) \end{aligned}$$

the carriers appear under an integral sign. Hence, the dependence of $p_{\pm\beta}$ on the carrier variables has a nonlocal character. $p_{\pm\beta}$ represents the projection of the active material polarization onto the modal profile $\Phi_\beta^*(\vec{r}_\perp)$, i.e., the carrier-induced gain and refractive-index change experienced by the mode. The model is thus similar to that developed in Refs. [156, 244], where the spatial dependence on the carrier density is explicitly maintained for the computation of the modal gains, thus including the effects of spatial-hole burning. Our description, though, includes not only self-saturation effects of the modal gains, but also cross-saturation effects among the modes, because the β -component of the material polarization is not diagonal in the field amplitudes a_β , rather it contains a superposition of different contributions arising from all the modes. By taking the usual definition of the modal gain X_α^\pm of a

transverse mode α , as the imaginary part of the coefficient of the diagonal element of $p_{\pm\beta}$

$$X_{\alpha}^{\pm} \equiv -\frac{a\Gamma}{2} \iint \text{Im} \chi_{\pm}(\Omega + \omega_{\alpha}, D_{+}, D_{-}) |\Phi_{\alpha}|^2 d^2 \vec{r}_{\perp}, \quad (7.10)$$

it is clear that the other, nondiagonal terms in $p_{\pm\beta}$ lead to crosssaturation. Moreover, it is worth noting that the modal beat notes $(\omega_{\beta} - \omega_{\alpha})$ appear in the evolution of the carrier densities, Eq. (7.8). These beat terms will be negligible when the frequency splitting between transverse modes is large enough, since in this case nonstimulated carrier recombination induces a low-pass filtering effect that strongly damps them, but not otherwise. We shall thus include in our description only the terms arising from frequency-degenerate modes and neglect the other ones.

Finally, the statistical properties of the projected Langevin noise sources $F_{\pm\beta}(t)$ are

$$\langle F_{\pm\beta}(t) \rangle = 0, \quad (7.11a)$$

$$\langle F_{\pm\beta}(t) F_{\pm\alpha}^{*}(t') \rangle = \delta_{\pm} \delta(t - t') 2A\beta_{sp} \iint_{-\infty}^{\infty} \Phi_{\beta}^{*}(\vec{r}_{\perp}) D_{\pm} \Phi_{\alpha}(\vec{r}_{\perp}) d^2 \vec{r}_{\perp}, \quad (7.11b)$$

indicating that, in general, correlation may exist between the spontaneous emission terms into different transverse modes due to the limited extent of the pump region.

Injection and response of the active medium

For the sake of simplicity, we assume that the radial distribution of injection current in the quantum well (QW) plane is approximated by

$$C(\rho) = e^{-\rho^6} e^{n\rho^2}, \quad (7.12)$$

with $\rho = r/r_c$, r_c being the radius of the contact. When $n = 0$, the current distribution is super-Gaussian and describes a disk-shaped electrical contact, while a ring-shaped contact is described by $n > 0$, with larger current crowding the larger n . In addition, a truncated parabolic waveguide mimics the effect of a thermal lens [Eq. (6.45)]. Finally, we consider an analytical approximation to the optical susceptibility of the QW, equivalent to that given in Eq. (6.30). This description captures the essential features of the gain and index spectra in QWs.

7.3 Results

In this section we perform a comparison between both methods in order to discuss the usefulness and limits of validity of a modal description. We focus our discussion on the VCSEL dynamics during turn-on and turn-off transients accompanying a large-signal modulation of the current.

7.3.1 Single-mode operation

As a starting point, we consider the case of a single-mode VCSEL ($r_c = r_g = 3 \mu\text{m}$) with a disc-shaped contact ($n = 0$) being modulated by a square-wave signal from threshold to four times threshold with a modulation period $T = 10 \text{ ns}$.

In Fig. 7.1 we plot the results obtained from direct integration of the two dimensional (2D) model (solid lines) together with those obtained after performing the modal expansion (dashed lines) for a relatively strong thermal lens, $\Delta n_{tl} = 10^{-2}$. The two models yield very similar results for the dynamics of both the power and carrier density, although it can be seen that for very low power levels, there are some small differences among them due to the different way of including spontaneous emission noise in each model. During the current switch-on, the intensity and modal gain undergo typical relaxation oscillations. Following the turn-off transient, we observe the appearance of an optical pulse, generally, with low intensity levels. We explicitly define a secondary pulsation [241] as the first optical peak that follows the current turn-off. This effect is also referred as *off-state bounce* in optical transmission systems using digital encoding [243, 245]-[248]. Since this is a detrimental effect that can influence the performance of the bit recovering process, it is imperative to have a thorough understanding and control of such a phenomenon, thus requiring fast and accurate simulation tools. Secondary pulsations can be characterized by two figures of merit, namely: the OFF/ON ratio that measures the power relation between the maximum of the first optical secondary peak with respect to the CW mean power, and the time T_{off} elapsed between the current turn-off and the first secondary pulsation. The presence of spontaneous emission noise induces small fluctuations in these magnitudes from one bit to the other [249]. As has been already commented, these pulsations can not be explained in terms of the typical relaxation oscillations that appears in gain-switched semiconductor lasers, since the bias current is usually set at the threshold or slightly below it. In contrast to relaxation oscillations, secondary pulsations are explained in terms of a diffusive spatial effect. When the laser switches-on, the spatial-hole burning effect causes a hole in the center of the carrier distributions [See Fig. 7.1(c)]. When the current is turned-off, the hole in the carrier distribution is filled by diffusion processes and, under appropriate conditions, provides extra gain during a short period that finally produces the optical pulses.

Both models exhibit, for the parameters considered, anomalous turn-off transients with multiple secondary pulsations, whose peak power reaches about 40% of the CW power in both models. Also, the time at which the secondary pulses occur are almost the same in both models ($T_{\text{off}} \approx 0.22$ ns), and the degree of spatial hole burning in the carrier density is also very similar. We also find that the strength of the secondary pulsations, OFF/ON ratio, decreases both when the bias current is reduced and when the ‘on’ current approaches threshold in correspondence with previous studies [241, 242].

Performing the same analysis for a weaker thermal lens, $\Delta n_{tl} = 3 \times 10^{-3}$, the agreement between the two models becomes worse. Solid lines in Fig. 7.2 represent the results obtained by direct integration of the 2D-model, whereas dashed lines are those obtained after performing the modal expansion. In this case, although the two models yield the same qualitative turn-off dynamics and they lead to the same CW

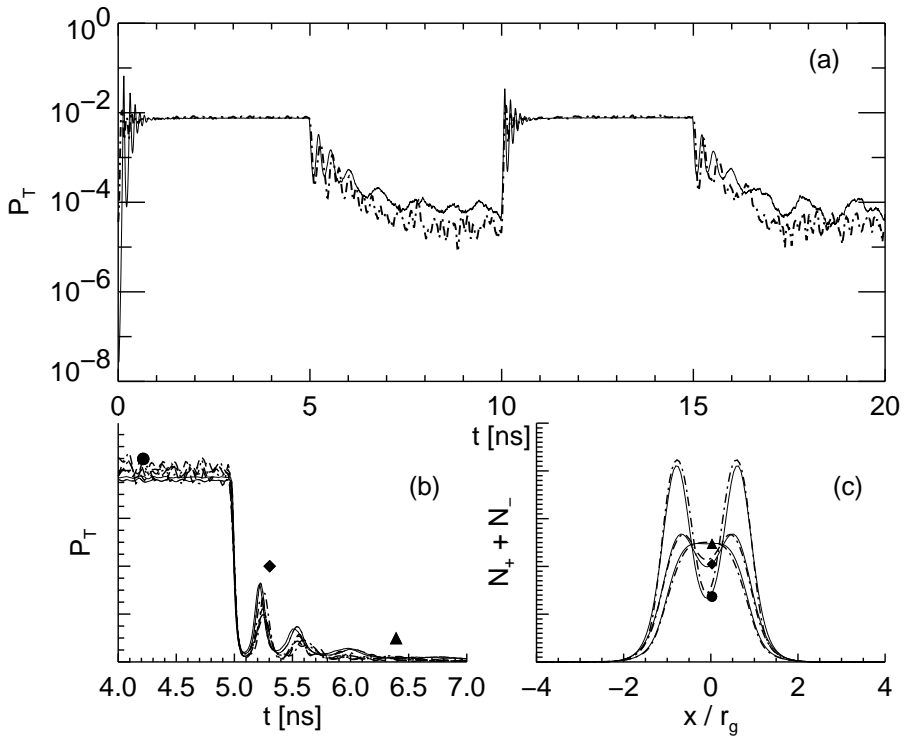


Figure 7.1. Turn-on and turn-off transients for strong lateral guiding conditions. Numerical simulation of the spatiotemporal dynamics (solid lines) in comparison with modal expanded method (dashed lines). The same parameters that in Table 6.1 except for $\gamma_{\perp} = 20 \text{ ps}^{-1}$, and $b = 10^4$. Parameters: disk electric contact with $n = 0$, $\mu_b = \mu_{th}$, $\mu_{on} = 4\mu_{th}$, $r_c = r_g = 3 \text{ }\mu\text{m}$, $\mathcal{D} = 0.5 \text{ }\mu\text{m}^2/\text{ns}$, $\Delta n_{tl} = 10^{-2}$, $\Delta = 1.0$.

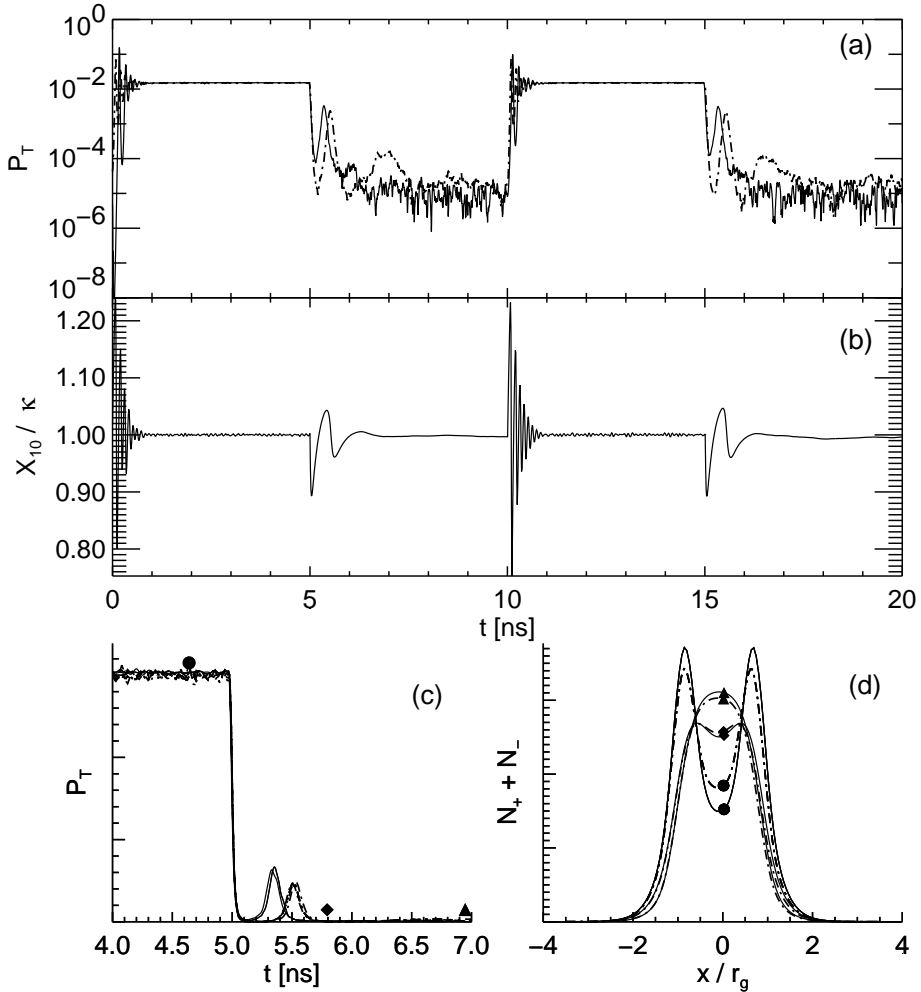


Figure 7.2. Evolution of the optical intensity in log-scale (a), modal gain scaled to losses (b), detail of the turn-off transients in linear scale (c), and cross-section of the carrier densities at different time stages (d). The results from the 2D model are plotted in solid lines and the corresponding optical profiles are shown in Fig. 7.4(c). We use dashed lines for the modal expansion, except in panel (b). The secondary pulsations obtained from the 2D model have OFF/ON $\sim 22\%$ and $T_{\text{off}} \sim 0.34$ ns while OFF/ON $\sim 16\%$ and $T_{\text{off}} \sim 0.52$ ns from the modal expansion. Disk electric contact with $n = 0$, $\mu_b = \mu_{th}$, $\mu_{on} = 4\mu_{th}$, $r_c = r_g = 3 \mu\text{m}$, $\mathcal{D} = 0.5 \mu\text{m}^2/\text{ns}$, $\Delta n_{tl} = 3 \times 10^{-3}$, $\Delta = 1.0$.

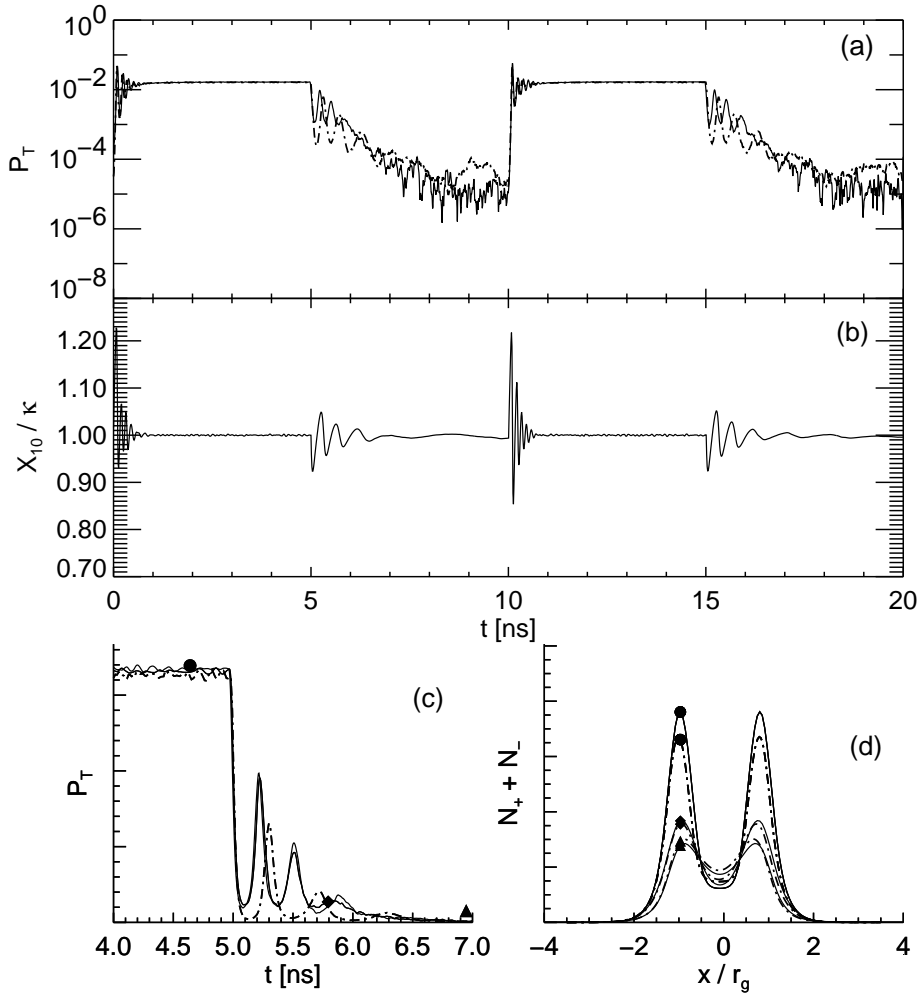


Figure 7.3. Typical secondary pulsations during the turn-off transient of a VCSEL with a ring-shaped electrical contact with ($n = 2$). Secondary pulsations from the 2D model OFF/ON $\sim 59\%$ and $T_{\text{off}} = 0.22$ ns, and from the modal expansion OFF/ON $\approx 40\%$ and $T_{\text{off}} \approx 0.30$ ns. The remaining parameters are the same as in Fig. 7.2.

powers, significant quantitative differences can be observed among them during the dynamics. In particular, the ratio of the secondary pulse height to the CW power (OFF/ON) is significantly higher for the 2D-model ($\approx 22\%$) than for the modal expansion ($\approx 16\%$ only). Moreover, the time at which the secondary pulses appear is also significantly different for the two models: in the first, the secondary pulse appears with a delay $T_{\text{off}} \approx 0.34$ ns after the current is switched-off, while in the second, the delay is $T_{\text{off}} \approx 0.52$ ns. Finally, the spatial hole burnt in the carrier density is larger in the 2D-model. Further reduction of Δn_{tl} leads to larger differences between the two models.

In Fig. 7.3 we compare the results obtained with the two models for the same parameters as before, but in the case of a ring contact with depth $n = 2$. In this case, the carrier distribution develops a marked peak at the carrier crowding radius in order to provide sufficient gain to reach lasing in the fundamental mode, and the threshold is larger than in the former case due to the smaller overlap among the Gaussian mode and the ring-shaped carrier distribution. This effect finally leads to carrier distributions with strong radial gradients. When the current is turned-off, this large gradient produces a rapid filling of the hole, providing small T_{off} times and rather large OFF/ON ratios. However, the shape of the current injection does not affect the conclusions regarding the influence of Δn_{tl} on the agreement between the two models: the quantitative discrepancies between the two models are even larger than for the disk-contact VCSEL and they also increase as the thermal lens weakens, although their results match for relatively large Δn_{tl} . In panels 7.2(b) and 7.3(b), we represent the evolution of the modal gain of the fundamental mode (obtained from the modal expansion). The modal gain equals losses at the threshold, $X_{10} \approx \kappa$, which coincides with our bias current. Following the turn-on transients, we observe modal gain variations resulting from the relaxation oscillations. On the other hand, during the turn-off transients, the hole filling produces oscillations in the modal gain that finally lead to the appearance of secondary pulsations. However, as already mentioned, the spatial hole is deeper in the 2D model, which leads to an underestimation of the height and time of the secondary pulsations.

In order to clarify the origin of these discrepancies, we have analyzed how robust the modal profiles are during the switch-on and turn-off dynamics due to the changes in refractive index associated with the carrier density. Any changes in the modal profiles are naturally accounted for within the spatiotemporal description, but not in the modal expansion. In Fig. 7.4, we represent a cross-section of the optical profiles at different time stages. For large thermal lensing strength, the modal profiles and modal frequencies are quite robust against perturbations produced by the carrier-induced refractive index. In this limit, the modal expansion provides an accurate description of the turn-off dynamics since the modal profiles do not change.

However, this is not the case when the thermal lens is weak [See Fig. 7.4(d)]. In this case, following the laser switch-on, we observe a considerable mode shrinkage. When the laser switches-on, it produces spatial-hole burning in the carrier distribution. Thus, the resulting distribution of refraction index is disturbed, being larger in the center than in the carrier crowding radius. This leads to a waveguide that provides an extra lateral confinement of the electric field that, in turn, is responsible for the mode shrinkage. The above observations allow to simply explain the discrepancies between the two models observed in the dynamics: for weak thermal lensing, the passive waveguide is noticeably distorted due to the carrier-induced index change, as can be seen in Fig. 7.5. The extra lateral confinement of the field in the 2D-model due to the spatial hole burnt in the carrier density favors the activation of secondary pulsations, which are stronger and occur sooner than in the modal expansion method because in this case the field is less confined to the injection region. From this analysis we conclude that in the single-mode case the modal expansion method requires $\Delta n_{tl} \geq 5 \times 10^{-3}$ for having good quantitative agreement with the 2D-model. Qualitatively correct results can be obtained with the modal expansion

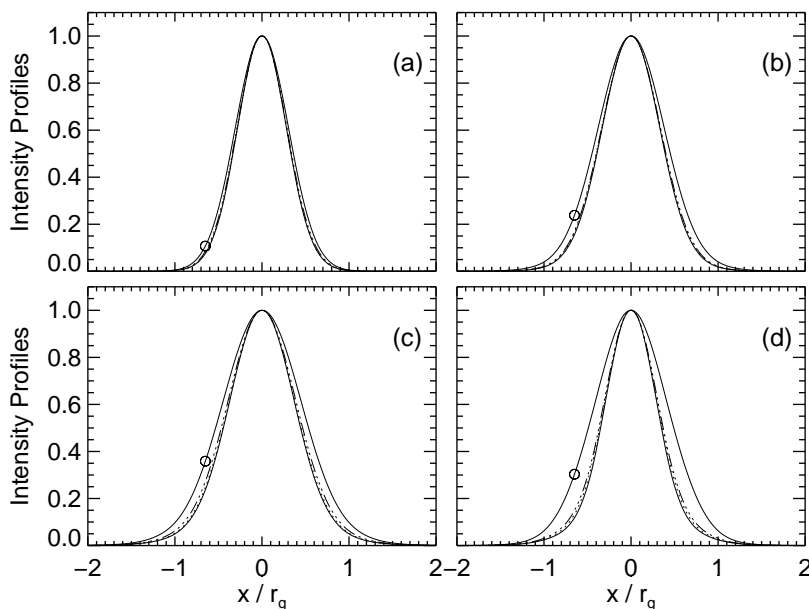


Figure 7.4. Optical profiles computed from the numerical integration of the spatiotemporal dynamics at different time stages: beginning of the laser onset (solid lines and circle), under continuous wave operation (solid lines), first peak of secondary pulsations (dotted lines), and first optical valley (dashed-dotted lines). The mode shrinkage is (a) $\sim 7\%$ for $\Delta n = 10^{-2}$, (b) $\sim 12\%$ for $\Delta n = 5 \times 10^{-3}$, (c) $\sim 17\%$ for $\Delta n = 3 \times 10^{-3}$, and (d) $\sim 30\%$ for $\Delta n = 9 \times 10^{-4}$.

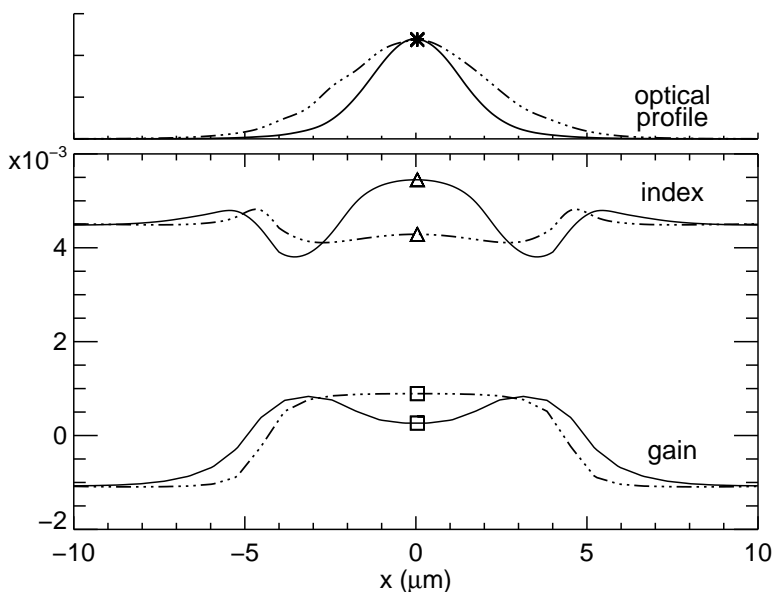


Figure 7.5. Evolution of the active-material susceptibility obtained from integration of the 2D model. Cross section of (*) the optical profile in arbitrary units, (\square) gain $-\Gamma \text{Im} \chi_{\pm}/(2n_e)$ and (\triangle) total index of refraction $\Delta n(r) + \Gamma \text{Re} \chi_{\pm}/(2n_e)$ both in dimensionless units. Two time stages are plotted: the beginning of the laser onset (dashed lines) and cw operation (solid lines). The same parameters as in Fig. 7.2 except for $\Delta n_{tl} = 9 \times 10^{-4}$.

method for $\Delta n_{tl} \geq 3 \times 10^{-3}$. Below this value, the modal expansion approximation can no longer be used, since it leads to qualitative discrepancies with the 2D-model.

7.3.2 Multimode operation

As a final example, we consider a multimode VCSEL with larger radius $r_c = r_g = 4 \mu\text{m}$, and moderate thermal lensing strength $\Delta n_{tl} = 4 \times 10^{-3}$. So, the transverse modes involved in the dynamics are the fundamental LP_{10} and the first-order transverse LP_{11} modes in any of the two possible polarizations. In this situation, we analyze square-wave modulation of the injection current.

The total intensity and the intensity of the secondary polarization component, obtained from the spatiotemporal model, are separately depicted in Fig. 7.6. We considered that the fundamental mode resonance is blue shifted with respect to the gain peak by $\Delta = 1$. The general trend observed is that both polarizations initially switch-on carrying significant amount of power. The secondary polarization remains active during a transient time, ~ 1 ns in the figure. When the secondary polarization

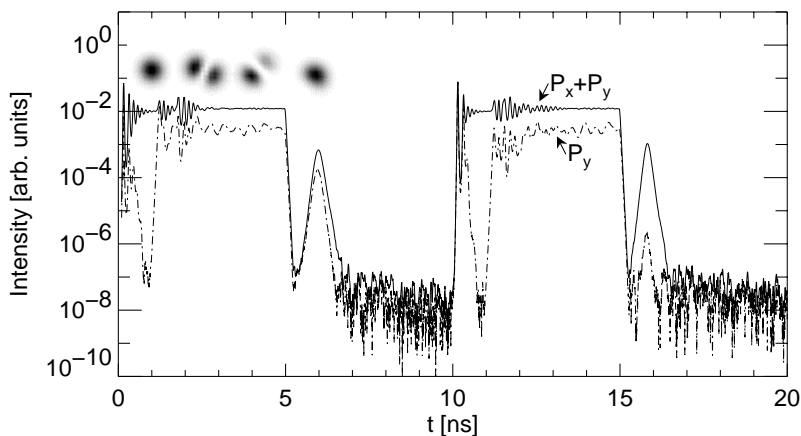


Figure 7.6. Secondary pulsations in a multimode VCSEL from the full spatiotemporal model, OFF/ON $\approx 6\%$. Total intensity (solid line) and secondary polarization (dashed line). Parameters: super-Gaussian current profile, $r_c = r_g = 4 \mu\text{m}$, $\mu_{bias} = \mu_{th}$, $\mu_{on} = 4\mu_{th}$, $\Delta n_{tl} = 4 \times 10^{-3}$, and $\Delta = 1.0$.

reaches the noise level, the total intensity undergoes additional relaxation oscillations leading to a reactivation of the secondary polarization. In order to better understand this phenomenon we have analyzed the computed near field images, shown in Fig. 7.6 for certain time stages. The result is that ~ 1 ns after the laser switch-on, the first-order transverse mode starts lasing in the secondary polarization (dashed lines), and coexisting with the Gaussian mode until the current is turned-off. By analyzing the evolution of the near-field images in the dominant polarization, we observe that the orientation of the LP_{11} is not fixed, but it rotates between the \cos and \sin modes. Following the current turn-off, we find that secondary pulsations take place in the fundamental transverse mode and that both linear polarizations carry significant amount of power. Even though the role of higher-order transverse modes is to suppress the magnitude of secondary pulsations [242], we can still observe an OFF/ON $\approx 6\%$.

The modal expansion allow us to easily follow the separate evolution of the transverse mode amplitudes LP_{10} and LP_{11} [Fig. 7.7(a)]. The fundamental transverse-mode is initially selected. Then, as a consequence of the global increase in carrier density and due to the spatial hole burning in the carrier distribution, the first-order transverse mode LP_{11} can profit from the available material gain. The first-order transverse mode switches-on at $t \sim 1$ ns causing additional relaxation oscillations. This mode coexists with the fundamental mode until the current is turned-off. Secondary pulsations appear in the fundamental mode and they have similar OFF/ON as those obtained with the spatiotemporal model. In Fig. 7.7(b), we represent the evo-

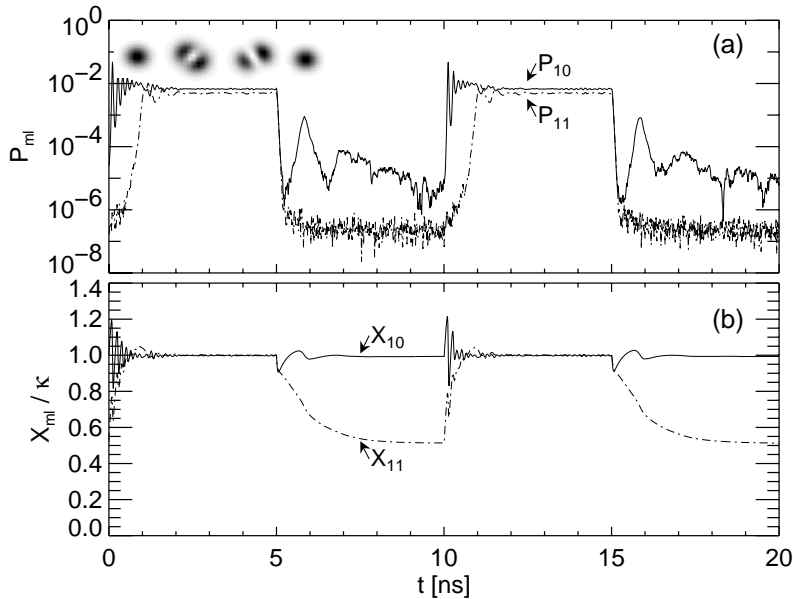


Figure 7.7. Secondary pulsations in a multimode VCSEL from the modal expansion. The same parameters as in Fig. 7.6. Power of the LP₁₀ mode (solid line) and power of the LP₁₁ mode (dashed line).

lution of the modal gain for both transverse modes. During the current turn-off the X_{10} modal gain exceeds the losses during a short period, which in turn originates the appearance of the secondary pulsation. However, the monotonic decrease in modal gain of X_{11} is worth noting: when the current is turned-off, there is a sudden interruption in carrier injection at the edges of the distribution that produces a worse overlap with the mode LP₁₁ and thus a decrease in modal gain. The rotation of the LP₁₁ mode is also found in the modal expansion, resulting from the cross-saturation terms between the two degenerated first-order transverse modes. The reconstructed near-field images in Fig. 7.7(a) are in good agreement with those computed from the full spatiotemporal model.

7.4 Conclusions

The usefulness and limits of validity of a modal expansion for analyzing large-signal dynamics in gain-guided VCSELs have been investigated by comparing the predictions of the modal expansion method with those from the full spatiotemporal description. The modal expansion presented in this work generalizes previous models by incorporating polarization effects and gain cross-saturation terms among degenerate transverse modes. The comparison has mainly focused on the secondary pul-

sations that appear under square-wave modulation of the injection current. We have found that the modal expansion yields qualitatively correct results for thermal lensing strengths above $\Delta n_{tl} \sim 3 \times 10^{-3}$. However, quantitative agreement between the two models requires $\Delta n_{tl} > 5 \times 10^{-3}$ independently of the shape of the current injection. This value of Δn_{tl} is about one order of magnitude larger than the contribution arising from the carrier-induced refractive index, thus confirming that the discrepancies originate from the fact that the modal expansion neglects the effects of the carrier-induced index of refraction on the modal profiles and frequencies: for weak lateral guiding the mode profiles significantly change during the evolution. Furthermore, we conclude that the practical applicability of the modal expansion is limited to small VCSELs where a reduced number of transverse modes is involved. Otherwise, the computational times required for accounting for such a large number of modes is nearly equivalent to that when directly dealing with the full spatiotemporal model.

Chapter 8

Conclusion to Part Two

In the second part of the thesis, we have explored the optical instabilities displayed by vertical-cavity surface-emitting lasers (VCSELs). In chapter 5, we focused on the light-polarization state of VCSELs operating in the fundamental transverse mode. Our starting point was the Spin-Flip model that generalized the atomic laser theory to the magnetic sub-levels of the quantum well. This model describes the interaction of circularly-polarized light with spin up/down carrier reservoirs. Using a semiclassical description of the spontaneous emission processes, we discussed the small fluctuations in the polarization components of the laser light. We found that the magnitude of the anticorrelated fluctuations between the circular components depends on the spin-flip rate. On the contrary, the anticorrelation between the linear components is sensible to the polarization mode partition noise. The birefringence tends to fix a polarization orientation, thus reducing the anticorrelation between linear components. In conclusion, evidences of the spin dynamics in the determination of the light polarization state and fluctuations have been found, specially in devices that present weak linear anisotropies.

In chapter 6 we described transverse effects in VCSELs simultaneously with the polarization of the light. We investigated the transverse mode selection mechanisms in gain-guided devices. The modeling of multimode gain-guided VCSELs can be more easily tackled by directly considering the spatiotemporal dynamics through a frequency-dependent susceptibility because the important variations in index of refraction induced by the active material. Therefore, we developed a spatiotemporal optical description for the large-signal dynamics of multimode VCSELs. The main results are

1. Polarization mode selection in the absence of transverse effects depends on a joint interplay of spin dynamics, semiconductor dynamics and thermal effects. Two possible ways, thermal and nonthermal, of producing a polarization

switching have been identified.

2. Transverse mode selection at threshold depends on the relative position on the gain curve but also on the geometry of the electric contact. The laser onset can be initiated from a high-order transverse mode for devices that develop a sufficiently marked ring-shaped current distribution.
3. Transverse mode selection under large-signal excitation presented a peculiar behavior characterized by a defined sequence for the onset of modes, that appear after a certain turn-on delay. The dependence of the turn-on delay with the current pulse, contact diameter, and thermal lensing strength have been investigated using the spatiotemporal model. The numerical results are in good agreement with reported experiments using gain-guided VCSELs [229, 230].
4. Thermal effects are important in 2. and 3. We have found a clear tendency toward multimode emission even in the case of weak thermal lensing. Moreover, the thermal shift of the cavity mode as the current is increased reduce the operation range through thermal roll-off.

Finally in chapter 7, we discussed the feasibility of an optical modal expansion, derived from the spatiotemporal model, for the transverse dynamics of small gain-guided VCSELs. We analyzed the secondary pulsations that appear during the turn-off transients occurring under large-signal modulation of the current. We demonstrated that there exists a critical value of the lateral guiding to ensure that the description in terms of a cold-cavity modes (modal expansion) to be valid. Below this value, the modal expansion provides results with quantitative discrepancies with respect the original spatiotemporal model. The evolution of the active material susceptibility showed that spatial-hole burning cause a redistribution of carrier-induced refractive index in such a way that tends to enhance the effective thermal lens and then to focalize the modes.

Concluding Remarks

This thesis contributes to the study of the semiconductor laser dynamics. We have paid special attention to the optical processes occurring in these devices. The modeling work mainly considered two configurations depending on the geometry of the laser resonator: i) compound-cavity edge-emitting lasers, and ii) vertical-cavity surface-emitting lasers. The advantages of each configuration was outline in Chap. 1. We recall here some of the interesting instabilities displayed by these devices. The identification of the relevant physical mechanisms underlying each instability has been one the major challenges of the thesis. A thorough understanding of the physical mechanisms behind the laser instabilities is essential for they manipulation and avoidance. In i) the compound-cavity modes define the standing-wave solutions in the longitudinal direction. Since the frequency separation between modes is commonly small the competition for the available gain is strong. Consequently the dynamics involves many of these modes being very irregular (chaotic form). In ii) the peculiar cavity is able to select only one longitudinal mode, however instabilities associated with the polarization of the light as well as the excitation of transverse modes are favored. The need of controlling these instabilities in communication applications has been pointed out. The selection and dynamics of polarization and transverse modes stem from a very complex interplay of many physical mechanisms: optical, thermal and electrical.

In many examples treated in the thesis, the importance of the coherence of the laser field is evident: the system cannot be simply described by photon-number and carrier-number rate equation, but the optical phase of the electric field have to be considered. The phase of the optical field plays a crucial role because it introduces interferometric effects (constructive and destructive). Furthermore, phase variations induce amplitude variations through the linewidth enhancement factor of SCL. We recall some examples where these effects occur: the existence of external-cavity modes in a laser with optical feedback, compound-cavity modes and achronal synchronization in two bidirectionally coupled lasers, linearly-polarized light as phase-locking of circular waves, and polarization switching of nonthermal origin.

There are several methodological aspects used in the different problems ad-

dressed in the thesis. The laser structure is regarded as a weakly perturbed waveguide. Hence, the electromagnetic problem begins from frequency-domain equations imposing boundary conditions for monochromatic plane waves. Then, the slowly-varying approximation is applied. Time domain equations describe the evolution of the slowly-varying envelope of the electric fields and the evolution of the carrier densities. We assumed adiabatic elimination of the material polarization of the active material. The light-matter interaction is described through an optical susceptibility function. The details of this function, specially its frequency dependence and the nonlinear dependence with the carrier density, are important in dynamics occurring in a wide spectral range. For this reason in chapter 6 and 7, where we dealt with transverse mode dynamics of gain-guided VCSELs, the gain and refractive index spectra are included into the equations.

Even using simplified formulations of the physical models there not exist, in general, exact solutions and requires the use of numerical approaches. So, part of the work has required the use of advanced computational methods. A proper design of the laser is essential for improving its characteristics. Modeling should also be considered as an alternative to the trial-error approaches. The feedback between theoreticians and manufacturers is extremely important. For instance, the mesoscopic model of the VCSEL presented in the second part of the thesis can be used as a tool for VCSEL design. One of the major advantages of the model is its simplicity, and flexibility for incorporating additional modules. In its present form, the inconvenience is the lack of thermal and electrical modules and the use of self-consistent solutions. So, the work presented is not closed.

Are semiconductor lasers the technology of the future? This is a very difficult question to answer. In the case that they would be, the technology would demand low consume, miniaturization, and faster devices. Then, quantum effects and nonequilibrium processes would be every time more significative. One has to realize that the borderline defining the limits of validity of the semiclassical framework can be crossed. My personal belief about laser physics is that it constitutes a multidisciplinary branch of knowledge. Many fields of physics are involved, such as, electromagnetism, optics, quantum mechanics, electronics, solid state physics, nonlinear physics, etc. An irrefutable proof of such a sentence is the number of diverse applications of lasers ranging from industry, medicine, to nuclear fusion physics. In my opinion, the description of each of the processes occurring in a real laser may be a too ambitious goal. I consider that it is preferable a model that can be applied to a broad class of devices instead to a particular device. Then, some abstraction, simplification and hypothesis is always present in the modeling of semiconductor lasers. I hope that the work performed in the thesis provide a grain of sand to the understanding and development of semiconductor lasers.

Appendix A

Stability Analysis of LK Model

We apply a small perturbation to the steady state monochromatic solution (denoted by bars)

$$P(t) = \bar{P} + \delta P(t), \quad \phi(t) = \bar{\phi}(t) + \delta\phi(t), \quad D(t) = \bar{D} + \delta D(t). \quad (\text{A.1})$$

Upon linearizing the equations (2.30a)–(2.30c) for small fluctuations we arrive to the linear system involving time delays

$$\begin{aligned} \frac{d}{d(\kappa t)} \delta P(t) &= x \delta D(t) - s x \tilde{D} \delta P(t) + \bar{\kappa}_f \cos \Phi [\delta P(t - \tau) - \delta P(t)] \\ &\quad - 2\bar{\kappa}_f \bar{P} \sin \Phi [\delta\phi(t - \tau) - \delta\phi(t)], \end{aligned} \quad (\text{A.2a})$$

$$\begin{aligned} \frac{d}{d(\kappa t)} \delta\phi(t) &= -\frac{\alpha}{2} \tilde{a} [\delta D(t) - s \tilde{D} \delta P(t)] + \frac{\bar{\kappa}_f \sin \Phi}{2\bar{P}} [\delta P(t - \tau) \\ &\quad - \delta P(t)] + \bar{\kappa}_f \cos \Phi [\delta\phi(t - \tau) - \delta\phi(t)], \end{aligned} \quad (\text{A.2b})$$

$$\frac{d}{d(\kappa t)} \delta D(t) = -T [(1+x) \delta D(t) + \tilde{a} \tilde{D} \delta P(t)]. \quad (\text{A.2c})$$

where we have introduced the following definitions

$$\begin{aligned} \tilde{a} &\equiv \frac{a}{1+s\bar{P}}, \quad x \equiv \tilde{a}\bar{P}, \quad \tilde{D} \equiv \frac{\bar{D}}{1+s\bar{P}}, \\ \bar{\kappa}_f &\equiv \kappa_f/\kappa, \quad \Phi \equiv \bar{\eta}_s + \Omega_0\tau, \quad T \equiv \gamma_e/\kappa. \end{aligned}$$

We propose an exponential-like solution

$$\begin{bmatrix} \delta P(t) \\ \delta\phi(t) \\ \delta D(t) \end{bmatrix} = \begin{bmatrix} \delta P_\lambda \\ \delta\phi_\lambda \\ \delta D_\lambda \end{bmatrix} e^{\lambda\kappa t}. \quad (\text{A.3})$$

For any nontrivial solution, λ must obey a characteristic equation that reads

$$\lambda^3 + c_2(\lambda) \lambda^2 + c_1(\lambda) \lambda + c_0(\lambda) = 0, \quad (\text{A.4})$$

with

$$\begin{aligned} c_2 &= -2K(\lambda) \cos \Phi + (1+x)T + s\tilde{D}x \\ c_1 &= K^2(\lambda) + Tx\tilde{D}(1+s\bar{P}) - 2T(1+x)K(\lambda) \cos \Phi \\ &\quad + sx\tilde{D} \left[T - \sqrt{1+\alpha^2}K(\lambda) \cos(\Phi + \text{atan } \alpha) \right] \\ c_0 &= T(1+x)K^2(\lambda) - xT\tilde{D}[\tilde{a} + s(1+x)]\sqrt{1+\alpha^2}K(\lambda) \times \\ &\quad \cos(\Phi + \text{atan } \alpha) \\ K(\lambda) &= \frac{\kappa_f}{\kappa} [e^{-\lambda\kappa\tau} - 1]. \end{aligned}$$

Appendix B

Regimes of Operation

We present an asymptotic analysis of Eq. (5.16) for two different limits, i) small linear anisotropies and ii) large spin-flip rate. Proceeding along the lines described in [30], we summarize the behavior in each of these two regions. Some examples can be found in Fig. B.1, where we represent the regimes of operation in a current versus spin-flip portrait.

A. Small linear anisotropies

In this limit, the birefringence verifies that $\gamma_p \ll \gamma_e < \gamma_s < \kappa$, while for simplicity we take $\gamma_a = 0$. We recall that $\gamma_a = \gamma_p = 0$ describes a perfectly symmetric VCSEL, i.e., any linear polarization direction is allowed. The eigenvalues of Eq. (5.16), $\mathcal{D}(\lambda) = 0$, can be expanded in power series of γ_p , that at first order read

$$\begin{aligned}\lambda_0 &= -2\varepsilon\alpha\gamma_p, \\ \lambda_{1,2} &= \lambda_{1,2}^o + \varepsilon \frac{\alpha\gamma_p}{1 + \frac{\gamma_s + 2\gamma_e Q^2}{8\kappa\gamma_e Q^2} \lambda_{1,2}^o},\end{aligned}\tag{B.1}$$

with $\varepsilon = \pm 1$ for \hat{x} , \hat{y} -LP solutions. $\lambda_{1,2}^o$ are the two non-vanishing eigenvalues calculated at $\gamma_p = 0$

$$\lambda_{1,2}^o = -\frac{\gamma_s + 2\gamma_e Q^2}{2} \pm i\sqrt{4\kappa\gamma_e Q^2 - \frac{(\gamma_s + 2\gamma_e Q^2)^2}{4}}.$$

In the absence of birefringence, the eigenvalue $\lambda_0 = 0$ is associated with the arbitrariness in the polarization orientation. In the presence of small birefringence, this non-vanishing real eigenvalue determines the stability: the high frequency solution is stable (\hat{x} -LP if $\gamma_p > 0$). The direction of the eigenvector associated with λ_0 is the

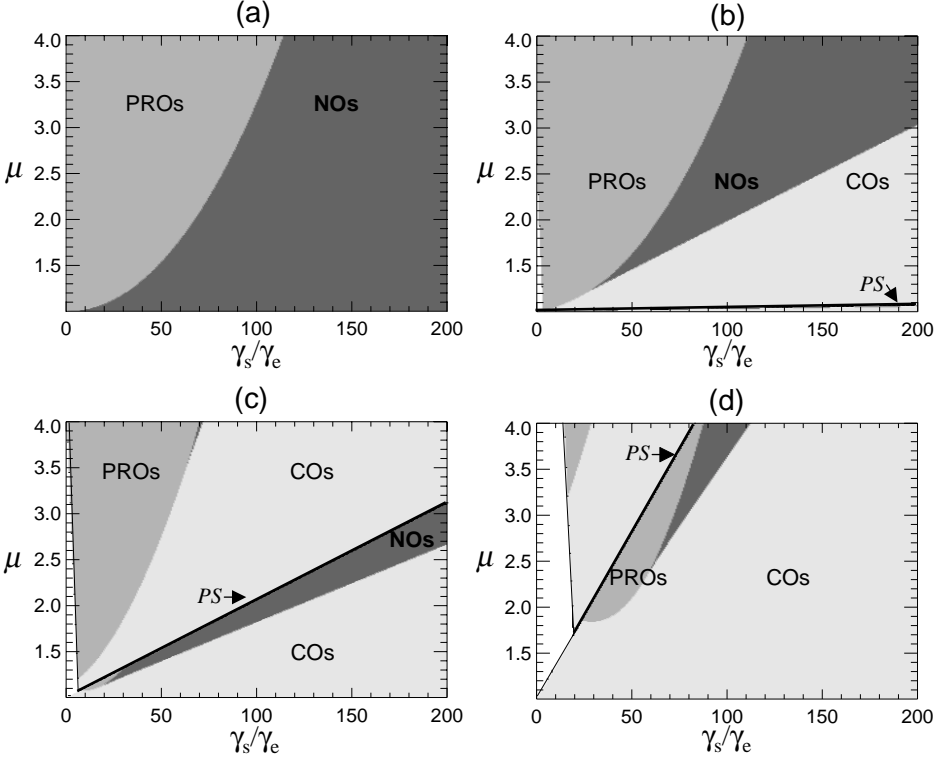


Figure B.1. Regions of operation represented in the phase diagram current versus spin-flip. The parameters are: $\alpha = 3$, $\gamma_e = 1 \text{ ns}^{-1}$, $\kappa/\gamma_e = 300$, $\gamma_p = \gamma_a = 0$ in panel (a). $\alpha = 3$, $\gamma_e = 1 \text{ ns}^{-1}$, $\kappa/\gamma_e = 300$, $\gamma_p/\gamma_e = 0.5$, $\gamma_a/\gamma_e = 0.1$ in panel (b). $\alpha = 1$, $\gamma_e = 1 \text{ ns}^{-1}$, $\kappa/\gamma_e = 150$, $\gamma_p/\gamma_e = 3$, $\gamma_a/\gamma_e = 0.1$ in panel (c). $\alpha = 1$, $\gamma_e = 1 \text{ ns}^{-1}$, $\kappa/\gamma_e = 150$, $\gamma_p/\gamma_e = 10$, $\gamma_a/\gamma_e = 0.1$ in panel (d). Meaning of the symbols: Polarization relaxation oscillations (PROs), coupled oscillations (COs), absence of polarization oscillations (NOs), polarization switching current from LF to HF solution (PS). Note also narrow white regions where no linearly polarized solution is stable.

polarization orientation angle and it decouples of the fluctuations of the ellipticity and carrier difference $d(t)$. The remaining eigenvalues $\{\lambda_{1,2}\}$ are complex when

$$\gamma_s < \gamma_s^c \equiv \sqrt{8\kappa\gamma_e(\mu - 1)} - \gamma_e(\mu - 1),$$

which implies small to moderate values of γ_s and injection currents relatively far from threshold. In such a case, $|\text{Im}\lambda_{1,2}|$ describes the oscillation frequency that undergo the ellipticity angle and $d(t)$, known as *polarization relaxation oscillations* (PROs). Similarly to ROs, the PROs frequency grows with the square-root of the distance to its threshold, $\sim (\mu - \mu^c)^{1/2}$. Finally, for larger spin-flip, $\gamma_s > \gamma_s^c$, the polarization fluctuations experience damped relaxation without any kind of oscillation.

B. Large spin-flip rate. Nonlinear anisotropies

Another interesting limit is when the spin-flip rate is large, i.e., $\gamma_e < \gamma_p < \kappa \ll \gamma_s$. There exists a pair of complex eigenvalues and a real one. The real eigenvalue is $\lambda_0 \approx -\gamma_s$ and describes the damped relaxation of $d(t)$. The two complex conjugated eigenvalues of Eq. (5.16), are expanded in power series of γ_s^{-1} . They have two different contributions

$$\lambda_{1,2} = \lambda_{lin} + \lambda_{non}.$$

The linear contribution λ_{lin} , that corresponds to the limit¹ $\gamma_s \rightarrow \infty$, reads $\lambda_{lin} = 2\varepsilon(\gamma_a \pm i\gamma_p)$. They represent oscillations whose damping and frequency are exclusively determined by the linear anisotropies. The nonlinear contribution λ_{non} is the result of a finite value of γ_s . It is common to define the nonlinear dichroism and nonlinear birefringence [160] as the real and imaginary parts of λ_{non} , i.e., $\lambda_{non} = \gamma_{non} \pm i\omega_{non}$. Finally, the complex pair reads

$$\lambda_{1,2} = 2\varepsilon(\gamma_a \pm i\gamma_p) - \frac{1}{\gamma_s} \gamma_e \kappa (\mu - D_0) [1 \mp i\alpha\varepsilon \text{sign}(\gamma_p)]. \quad (\text{B.2})$$

The imaginary part of these eigenvalues describes *coupled oscillations* (COs) of the polarization angles. The approximate expression for the COs frequency in the limit of large γ_s is then

$$\Omega_P \equiv |\text{Im}\lambda_{1,2}| = 2|\gamma_p| + \varepsilon \frac{\gamma_e}{\gamma_s} \alpha \kappa (\mu - D_0) + o\left(\frac{\gamma_e}{\gamma_s}\right)^2, \quad (\text{B.3})$$

where Ω_P increases (decreases) for the HF (LF) mode corresponding to the sign $\varepsilon = +(-)$. In contrast to ROs and PROs, the COs frequency varies linearly with the distance to threshold, i.e. $\sim (\mu - 1)$. From the last expression, the Ω_P frequency² can be identified with the birefringence splitting $2\gamma_p$ although modified by the nonlinearities. It can be seen that the nonlinear anisotropies obtained from the adiabatic elimination of $d(t)$ [160, 161] coincide, at first order in γ_e/γ_s , with those predicted by Eq. (B.2). Consequently, these previous works, based on the adiabatic elimination of $d(t)$ are unsuitable to describe the dynamical properties within the PROs region. In contrast to PROs, where the real eigenvalue determined the stability properties, the stability is now determined by the complex pair.

In the limit of the adiabatic elimination of $d(t)$, polarization switching is not present. When analyzing the real part of the eigenvalues [Eq. (B.2)], we go from a situation where only one polarization is stable to one of optical bistability when the

¹We note that the same result is obtained close to threshold, where Q^2 is treated as a small parameter, regardless of the magnitude of γ_s .

² Ω_P is also referred as effective birefringence splitting.

current is increased. Polarization switching occurs for moderate values of γ_s , reflecting itself in the expression of γ_{non} when orders $(\gamma_e/\gamma_s)^2$ are considered. Hence, in this work, we deal with the dynamics of $d(t)$ being capable to describe, without any restriction, the fluctuations in both PROs and COs regimes.

Appendix C

Langevin Equations

As a starting point, we consider that a complex dipole's amplitude σ , in absence of electric field and decaying at rate γ_{\perp} , is governed by the simple Langevin equation

$$\frac{d\sigma}{dt} = -\gamma_{\perp}\sigma + f(t), \quad (\text{C.1})$$

where $f(t)$ is a rapidly fluctuating random term. A mathematical formulation of such a highly irregular function, is that $f(t)$ and $f(t')$ are statistically independent when $t \neq t'$. Hence the correlation function $\langle f(t)f^*(t + \tau) \rangle = 2\mathcal{D}\delta(\tau)$, with \mathcal{D} the diffusion coefficient, is zero everywhere except at $\tau = 0$ where has the rather pathological result of an infinite variance. Furthermore, we also require that $f(t)$ has zero mean, i.e. $\langle f(t) \rangle = 0$, where $\langle \dots \rangle$ means average over different noise realizations. An object with these properties is known as (complex) white Gaussian noise. An efficient algorithm we use to generate these random numbers is based on the numerical inversion method developed in [61].

The formal solution of Eq. (C.1) can be expressed as

$$\sigma(t) = \sigma(0)e^{-\gamma_{\perp}t} + \int_0^t dt' f(t')e^{-\gamma_{\perp}(t-t')}. \quad (\text{C.2})$$

If one assumes that the initial condition is deterministic or Gaussian distributed, then mean value and variance of $\sigma(t)$ read

$$\langle \sigma(t) \rangle = \langle \sigma(0) \rangle e^{-\gamma_{\perp}t}, \quad (\text{C.3})$$

$$\begin{aligned} \text{var}\{\sigma(t)\} &= \langle \sigma(t)\sigma^*(t) \rangle - |\langle \sigma(t) \rangle|^2 = \\ &= \left(\text{var}\{\sigma(0)\} - \frac{\mathcal{D}}{\gamma_{\perp}} \right) e^{-2\gamma_{\perp}t} + \frac{\mathcal{D}}{\gamma_{\perp}}. \end{aligned} \quad (\text{C.4})$$

Making use of these results, the correlation function of $\sigma(t)$ can be expressed as follows

$$\langle \sigma(t)\sigma^*(t+\tau) \rangle = [|\langle \sigma(t) \rangle|^2 + \text{var}\{\sigma(t)\}] e^{-\gamma_{\perp}|\tau|}. \quad (\text{C.5})$$

In the case of a stationary process σ_s , being that in which statistical properties are time independent, we have

$$\langle \sigma_s(t)\sigma_s^*(t+\tau) \rangle = \lim_{t \rightarrow \infty} \langle \sigma(t)\sigma^*(t+\tau) \rangle = \frac{\mathcal{D}}{\gamma_{\perp}} e^{-\gamma_{\perp}|\tau|}, \quad (\text{C.6})$$

which describes an Ornstein-Uhlenbeck process that displays a more realistic correlation function when comparing with the white noise $f(t)$. Note however that the σ_s process tends to a white noise in the limit of large damping

$$\gamma_{\perp}^2 \langle \sigma_s(t)\sigma_s^*(t+\tau) \rangle \xrightarrow{\gamma_{\perp} \rightarrow \infty} 2\mathcal{D} \delta(\tau). \quad (\text{C.7})$$

The consistent semiclassical description of quantum noise must be formulated in such a way that the noise terms acting on the fields and dipoles always preserve the uncertainty relations of the corresponding quantum operators. Let us assume that at $t = 0$, $\text{var}\{\sigma(0)\} = \frac{1}{2}$. From Eq. (C.4), we assure that $\text{var}\{\sigma(t)\} = \frac{1}{2}$ only when the strength of noise verifies $\mathcal{D} = \gamma_{\perp}/2$. In dissipative systems, the loss of quantum noise must be compensated by a corresponding fluctuation of the time derivative. This rough justification can be rigorously presented in terms of the quantum mechanical fluctuation-dissipation theorem [180, 188], that determines

$$\langle f(t)f^*(t+\tau) \rangle = \gamma_{\perp} \delta(\tau). \quad (\text{C.8})$$

In the case of an ensemble of N_0 dipoles providing a macroscopic material polarization $P = \sum_i \sigma_i$, Eq. (C.8) is generalized to $\langle F(t)F^*(t+\tau) \rangle = \gamma_{\perp} N_0 \delta(\tau)$.

In many calculations, it is useful to define the Fourier transform of a white Gaussian noise $f(t)$ as

$$\tilde{f}(\omega) = \int_{-\infty}^{\infty} dt f(t) e^{i\omega t}. \quad (\text{C.9})$$

The Fourier transformed white Gaussian noise $\tilde{f}(\omega)$ has a correlation

$$\langle \tilde{f}(\omega)\tilde{f}^*(\omega') \rangle = 2\mathcal{D} \delta(\omega - \omega'). \quad (\text{C.10})$$

A more convenient way to describe a generic stationary noise process $G_s(t)$ is by means of the spectral density function at frequency ω [62]

$$S_G(\omega) \equiv \int_{-\infty}^{\infty} \langle \tilde{G}_s(\omega)\tilde{G}_s^*(\omega') \rangle d\omega' = \int_{-\infty}^{\infty} \langle G_s(t)G_s^*(t+\tau) \rangle e^{i\omega\tau} d\tau, \quad (\text{C.11})$$

where the second equality results from the Wiener-Khintchine theorem. In the case of a white noise, $G_s(t) = f(t)$, the spectral density function reduces to $S_f(\omega) = 2\mathcal{D}$, which implies that Langevin noise sources have a white (frequency-independent) spectrum. Finally, the spectral density of an Ornstein-Uhlenbeck process $\sigma_s(t)$ is a Lorentzian function

$$S_\sigma(\omega) = \frac{2\mathcal{D}}{\omega^2 + \gamma_\perp^2}. \quad (\text{C.12})$$

The generalization of Eqs. (C.11) and (C.12) to a linear system of n differential equations is given in Ref. [62]. For a review of stochastic processes and its application to physical systems the reader is address to Ref. [143].

Itô transformation

Let us concentrate in Eq. (5.6a) for the complex slowly-varying amplitude of the electric field

$$\begin{aligned} dE_\pm &= \{ \kappa(1 + i\alpha)[D \pm d - 1]E_\pm - (\gamma_a + i\gamma_p)E_\mp \} dt \\ &+ \sqrt{\beta_{sp}\gamma_e(D \pm d)} dW_\pm(t), \end{aligned} \quad (\text{C.13})$$

where we have introduced the complex Wiener process as $dW_\pm(t) \equiv \xi_\pm(t)dt$. We are interested to know the stochastic equations governing the amplitudes and phases of the electric field, $P_\pm(t)$ and $\phi_\pm(t)$, with $E_\pm(t) = \sqrt{P_\pm(t)}e^{i\phi_\pm(t)}$. For these purposes, we introduce an auxiliary variable $\rho_\pm = \frac{1}{2} \ln P_\pm$, then

$$d(\rho_\pm + i\phi_\pm) = d(\ln E_\pm) = \ln(E_\pm + dE_\pm) - \ln(E_\pm).$$

We expand the right hand of the above equation at first order in dt . Making use of the Itô rules for a generic real Wiener process $dW_a(t)$ [62, 143]

$$dW_a(t)^2 = dt, \quad dW_a(t)^{2+N} = 0 \quad \text{for } N > 0,$$

we arrive at

$$\begin{aligned} d\rho_\pm &= \kappa(D \pm d - 1)dt - (\gamma_a \cos \phi \pm \gamma_p \sin \phi) \sqrt{\frac{P_\mp}{P_\pm}} dt \\ &+ \sqrt{\frac{\gamma_e \beta_{sp}(D \pm d)}{P_\pm}} dW_{P_\pm} - \frac{1}{2} \frac{\gamma_e \beta_{sp}(D \pm d)}{E_\pm^2} [dW_{R,\pm} + i dW_{I,\pm}]^2, \end{aligned} \quad (\text{C.14})$$

$$\begin{aligned} d\phi_\pm &= \alpha\kappa(D \pm d - 1)dt - (\gamma_p \cos \phi \mp \gamma_a \sin \phi) \sqrt{\frac{P_\mp}{P_\pm}} dt \\ &+ \sqrt{\frac{\gamma_e \beta_{sp}(D \pm d)}{P_\pm}} dW_{\phi_\pm}, \end{aligned} \quad (\text{C.15})$$

with $\phi = \phi_+ - \phi_-$. It is worth noting that since $dW_{R,\pm}$ and $dW_{I,\pm}$, representing the real and imaginary parts of dW_{\pm} , are independent, the last term of Eq. (C.14) vanishes. The second remark is that the Wiener processes $dW_{P_{\pm}}, dW_{\phi_{\pm}}$, being defined through the orthogonal transformation

$$dW_{P_{\pm}}(t) = \cos \phi_{\pm} dW_{R,\pm}(t) + \sin \phi_{\pm} dW_{I,\pm}(t), \quad (\text{C.16})$$

$$dW_{\phi_{\pm}}(t) = -\sin \phi_{\pm} dW_{R,\pm}(t) + \cos \phi_{\pm} dW_{I,\pm}(t), \quad (\text{C.17})$$

are also independent. As a final step, we apply the Itô rules to the variable ρ_{\pm}

$$dP_{\pm} = d[e^{2\rho_{\pm}}] = e^{2(\rho_{\pm}+d\rho_{\pm})} - e^{2\rho_{\pm}} = 2P_{\pm} (d\rho_{\pm} + d\rho_{\pm}^2 + \dots).$$

Introducing Eq. (C.14) in to this last expression, we arrive at

$$\begin{aligned} dP_{\pm} = & 2\kappa(D \pm d - 1)P_{\pm}dt - 2(\gamma_a \cos \phi \pm \gamma_p \sin \phi) \sqrt{P_+ P_-} dt \\ & + 2\gamma_e \beta_{sp}(D \pm d) dt + \sqrt{4\gamma_e \beta_{sp}(D \pm d)} P_{\pm} dW_{P_{\pm}}, \end{aligned} \quad (\text{C.18})$$

that is nothing but Eq. (5.17a). The interesting result from this stochastic transformation, is the term $2\gamma_e \beta_{sp}(D \pm d)$ in Eq. (C.18), that accounts for the mean value of spontaneously emitted photons in each circular polarization. The remaining equations in Sec. 5.5 can be straightforwardly derived, by defining $\xi_{P_{\pm}} = dW_{P_{\pm}}/dt$ and $\xi_{\phi_{\pm}} = dW_{\phi_{\pm}}/dt$.

Appendix D

RIN Expressions

The following functions define the power spectra of the polarization components as was described in Eq. (5.30),

$$\begin{aligned} \mathcal{C}(\omega) &\equiv \mathcal{D}(i\omega)\mathcal{D}(-i\omega) = \\ &= [(\Gamma_s - 2\varepsilon_a)\omega^2 - \{(\varepsilon_a^2 + \varepsilon_p^2)\Gamma_s - b(\varepsilon_a - \alpha\varepsilon_p)\}]^2 \\ &\quad + \omega^2 [\omega^2 - \{\varepsilon_a^2 + \varepsilon_p^2 + b - 2\varepsilon_a\Gamma_s\}]^2. \end{aligned} \quad (\text{D.1})$$

$$\begin{aligned} \mathcal{A}_\phi(\omega) &= [\omega^2 - b \pm \varepsilon_a\Gamma_s]^2 + \omega^2 [\Gamma_s - \varepsilon_a]^2, \\ \mathcal{B}_\phi(\omega) &= \omega^2(\varepsilon_p + \alpha c)^2 + [\alpha b + \varepsilon_p\Gamma_s - c(\varepsilon_p + \alpha\varepsilon_a)]^2. \end{aligned} \quad (\text{D.2})$$

$$\begin{aligned} \mathcal{A}_\chi(\omega) &= \varepsilon_p^2(\omega^2 + \Gamma_s^2), \\ \mathcal{B}_\chi(\omega) &= \omega^2(\gamma_s - \varepsilon_a)^2 + (\omega^2 + \gamma_s\varepsilon_a + \alpha c\varepsilon_p)^2. \end{aligned} \quad (\text{D.3})$$

$$\begin{aligned} \mathcal{A}_\delta(\omega) &= (\varepsilon_p b)^2 / \kappa^2, \\ \mathcal{B}_\delta(\omega) &= [\{c(\varepsilon_a^2 + \varepsilon_p^2 - \omega^2) - b\varepsilon_a\}^2 + \omega^2(b - 2c\varepsilon_a)^2] / \kappa^2, \end{aligned} \quad (\text{D.4})$$

where for the sake of clarity we have defined these new quantities

$$\varepsilon_{a,p} \equiv 2\gamma_{a,p}, \quad \Gamma_s \equiv \gamma_s + 2\gamma_e Q^2, \quad b \equiv 4\kappa\gamma_e D_0 Q^2, \quad c \equiv 2\gamma_e Q^2.$$

These expressions are valid for an arbitrary \hat{x} -LP (HF solution). For a \hat{y} -LP (LF solution) the signs of ε_a and ε_p have to be changed.

In Chapter 5, we defined the power spectra of polarization fluctuations by means

$$S_\Xi(\omega) = \frac{\gamma_e \beta_{sp} D_0}{2Q^2} \left[\frac{\mathcal{A}_\Xi(\omega) + \mathcal{B}_\Xi(\omega)}{\mathcal{C}(\omega)} \right], \quad (\text{D.5})$$

where $\Xi = \phi, \chi, \delta$. The asymptotic behavior of the power spectra in the limit of large frequencies is

$$S_\phi(\omega) = S_\chi(\omega) = \left(\frac{\kappa}{c}\right)^2 S_\delta(\omega) \xrightarrow{\omega \rightarrow \infty} \frac{1}{1 + \left(\frac{\omega}{\Delta\omega}\right)^2}, \quad (\text{D.6})$$

that behaves like the spectra of an Ornstein-Uhlenbeck process [Eq. (C.12)] with correlation time

$$\tau^{-1} \equiv \Delta\omega = \sqrt{\Gamma_s^2 + 2(\varepsilon_a^2 - \varepsilon_p^2 - b)}.$$

Another interesting aspect is the shape of the fluctuations onto the Poincaré plane $\phi - \chi$. At low frequencies we find that

$$\begin{aligned} \left| \frac{S_\phi}{S_\chi} \right|_{\omega=0} &\approx \frac{b^2 + [\alpha b + \varepsilon_p \gamma_s]^2}{\varepsilon_p^2 [\Gamma_s^2 + \alpha^2 c^2]} \\ &\xrightarrow{\varepsilon_p \rightarrow 0} (1 + \alpha^2) \frac{b^2}{\varepsilon_p^2 \Gamma_s^2} \gg 1 \\ &\xrightarrow{\mu \rightarrow D_0} 1. \end{aligned}$$

Fluctuations display a circular shape in the $\phi - \chi$ plane close-to-threshold, while they preferably follow the ϕ -direction for small birefringence.

Appendix E

Optical Modes

We consider a cylindrical optical waveguide which physical properties are invariant along the propagation direction z . The electric and magnetic fields can be expressed as

$$\vec{E} = (\vec{e}_\perp + \hat{z}e_z)e^{i\beta z}, \quad (\text{E.1})$$

$$\vec{H} = (\vec{h}_\perp + \hat{z}h_z)e^{i\beta z}, \quad (\text{E.2})$$

\vec{e}_\perp , and \vec{h}_\perp are the projection of the fields onto the transverse plane, whereas e_z and h_z stand for their longitudinal components, and β the propagation constant. This structure resembles a VCSEL except for the unbounded propagation in z direction.

In absence of sources, the Maxwell's equations lead to

$$\{\nabla^2 + k_0^2 n^2 - \beta^2\} \vec{e}_\perp = -\vec{\nabla} \left\{ \vec{e}_\perp \cdot \vec{\nabla}_\perp \ln n^2 \right\}, \quad (\text{E.3})$$

$$\{\nabla^2 + k_0^2 n^2 - \beta^2\} e_z = -i\beta \vec{e}_\perp \cdot \vec{\nabla} \ln n^2, \quad (\text{E.4})$$

$$\{\nabla^2 + k_0^2 n^2 - \beta^2\} \vec{h}_\perp = (\vec{\nabla} \times \vec{h}_\perp) \times \vec{\nabla} \ln n^2, \quad (\text{E.5})$$

$$\{\nabla^2 + k_0^2 n^2 - \beta^2\} h_z = (\vec{\nabla} h_z - i\beta \vec{h}_\perp) \cdot \vec{\nabla} \ln n^2, \quad (\text{E.6})$$

with $k_0 = \omega/c$, and $n(\vec{r}_\perp)$ the transverse distribution in index of refraction. The right-hand term in Eqs. (E.3)–(E.6), mainly the term $\vec{\nabla} \ln n^2$, defines the polarization properties of the waveguide. This framework is suitable for the description of the vectorial modes in strong index-guided VCSELs (air-post or mesa structure). In gain-guided VCSELs, the variations in refractive index δn onto a background value n_e are generally small, and thus $\vec{\nabla} \ln n^2$ is a small term. In the weak guidance approximation [238], the bound modes of (E.3)–(E.6) and the propagation constant β are expanded in a power series of the small parameter $\Delta = \delta n/n_e \ll 1$, e.g.,

$$\vec{e}_\perp = \vec{e}_\perp^{(0)} + \vec{e}_\perp^{(1)} \Delta + \dots \quad (\text{E.7})$$

To lower order in Δ we obtain the scalar wave equation that reads

$$\left\{ \nabla_{\perp}^2 + k_0^2 n^2(\vec{r}_{\perp}) \right\} \Phi(\vec{r}_{\perp}) = \tilde{\beta}^2 \Phi(\vec{r}_{\perp}), \quad (\text{E.8})$$

where $\Phi(\vec{r}_{\perp})$ stands for either component of $\vec{e}_{\perp}^{(0)}$, and $\tilde{\beta}$ is the propagation constant neglecting polarization effects.

In the case of a radially-symmetric distribution of refractive index, the modes can be expressed as

$$\Phi(r, \theta) = F(r) e^{il\theta}, \quad (\text{E.9})$$

with $l = 0, \pm 1, \dots$ describing the angular order. Upon substitution of (E.9) into (E.8) we obtain the radial equation

$$\left\{ R^2 \frac{d^2}{dR^2} + R \frac{d}{dR} - l^2 + R^2 (V^2 f(R) - W^2) \right\} F(R) = 0. \quad (\text{E.10})$$

The radial coordinate is normalized with respect to the waveguide radius r_g with $R \equiv r/r_g$. We consider a refractive index distribution varying from n_c (core) to n_e (cladding). The waveguide number is $V \equiv k_0 r_g \sqrt{n_c^2 - n_e^2}$, the dimensionless propagation constant with respect to the cladding $W^2 \equiv r_g^2 (\beta^2 - k_0^2 n_e^2)$, and $f(R)$ is the normalized refractive index profile, varying from 1 (core) to 0 (cladding).

The refractive index profile is approximated by a truncated parabolic profile

$$f(R) = \begin{cases} 1 - R^2 & \text{if } R < 1 \\ 0 & \text{if } R \geq 1 \end{cases}, \quad (\text{E.11})$$

The modes of such a waveguide can be analytically expressed as a series expansion when $R < 1$ and read [238]

$$F_{ml}(R) = \begin{cases} \frac{\sum_{n=0}^{\infty} a_n R^{n+l}}{\sum_{n=0}^{\infty} a_n} & \text{if } R < 1 \\ \frac{K_l(W_{ml}R)}{K_l(W_{ml})} & \text{if } R \geq 1 \end{cases} \quad (\text{E.12})$$

where K_l is a second kind Bessel function of order l , and the coefficients a_n in Eq. (E.12) are given by the recursive relations

$$\begin{aligned} a_0 &= \text{arbitrary}, \\ a_2 &= -\frac{(V^2 - W_{ml}^2) a_0}{4(l+1)}, \\ a_{2n} &= \frac{1}{4n(n+l)} [V^2 a_{2n-4} - (V^2 - W_{ml}^2) a_{2n-2}] \quad \text{if } n \geq 2, \\ a_{2n+1} &= 0, \end{aligned} \quad (\text{E.13})$$

Figure E.1. Dependence of the dimensionless propagation constant W_{ml} with the waveguide parameter V for all the guided modes.

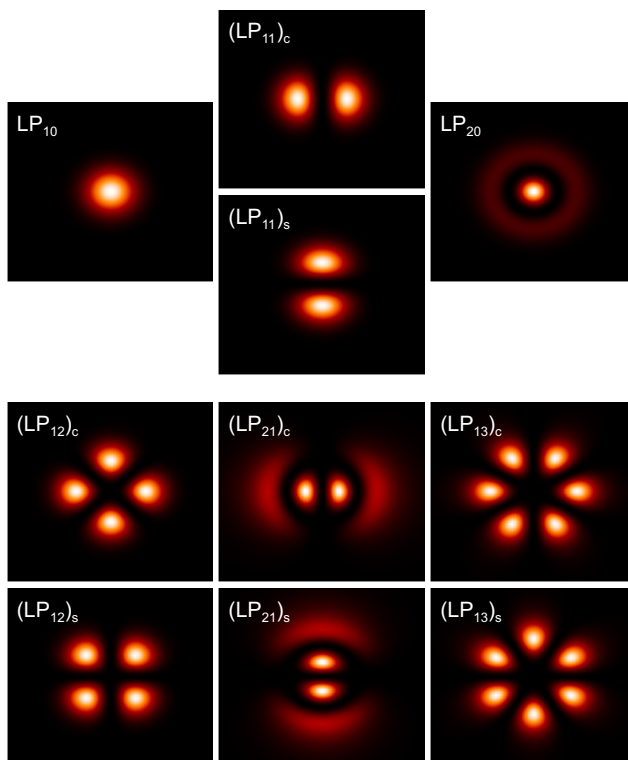
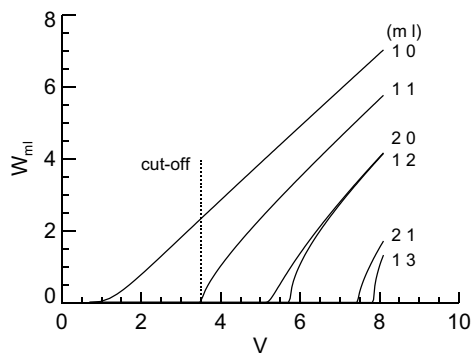


Figure E.2. Intensity distribution for the guided modes when $V = 7.91$. (c,s) represent modes cos, sin of Eq. (E.9).

The bound modes must verify $0 \leq W_{ml} \leq V$ being formally equivalent to propagation in a homogeneous medium with refractive index between the cladding and the core. Their propagation constants $\beta_{ml}^2 = (k_0 n_e)^2 + (W_{ml}/r_g)^2$ are obtained by imposing continuity at $R = 1$. This yields a transcendental equation for W_{ml}

$$W_{ml} \frac{K_{l+1}(W_{ml})}{K_l(W_{ml})} = - \frac{\sum_{n=0}^{\infty} n a_n}{\sum_{n=0}^{\infty} a_n}. \quad (\text{E.14})$$

These modes LP_{ml} are indexed with $m = 1, 2, \dots$ and $l = 0, \pm 1, \dots$. The mode profile has $(m - 1)$ zeros in the radial direction whereas $(2l)$ zeros are in the angular direction. LP_{10} is referred as the fundamental mode, LP_{11} the first-order transverse mode and the remaining as higher order transverse modes. An important property of Φ_{ml} in calculations is that represents a complete set of orthogonal eigenfunctions. It is worth recalling that these cavity modes and modal frequencies are polarization independent, and that the cavity anisotropies that may favor one linearly polarized state over the orthogonal one have been included through γ_a and γ_p .

Fig. E.1 depicts the dimensionless cladding propagation constant of all the guided modes as function of the V parameter. In a cylindric waveguide always supports at least one guided mode. Singlemode operation is possible below the cut-off $V \approx 3.518$, where only the fundamental mode $m = 1, l = 0$ is guided. Beyond this value, several modes are guided (multimode fiber). The intensity distribution of the modes $|\Phi(x, y)|^2$, for a fixed value of $V = 7.91$, are shown in Fig. E.2.

Appendix F

Integration Scheme

The equation (6.35a) is integrated by implementing a spectral method that treats the linear terms exactly, while the nonlinear terms are integrated within an accuracy $o(dt)$. Eq. (6.35a) can be formally expressed as

$$\begin{aligned}\partial_t A_{\pm}(\vec{r}_{\perp}, t) &= \hat{\mathbb{L}}A_{\pm} + \mathbb{N}_{\pm}(\vec{r}_{\perp}, t) + \sqrt{A\beta_{sp}D_{\pm}} \xi_{\pm}(\vec{r}_{\perp}; t), \\ \hat{\mathbb{L}} &= -\kappa + \frac{ic^2}{2\Omega n_e n_g} \nabla_{\perp}^2,\end{aligned}\quad (\text{E1})$$

$\hat{\mathbb{L}}$ being a position and time-independent linear operator whereas $\mathbb{N}_{\pm}(\vec{r}_{\perp}, t)$ contains the remaining terms of Eq. (6.35a). One starts the numerical integration from initial conditions for $A_{\pm}(\vec{r}_{\perp}, 0)$, taken as spontaneous emission distributions, and $D_{\pm}(\vec{r}_{\perp}, 0)$ that corresponds to the “off” state [See Eq. (6.41)]. The next step is to self-consistently obtain the instantaneous “frequency” $z_{\pm}(\vec{r}_{\perp}, t) \equiv \partial_t A_{\pm}/A_{\pm}$. From Eq. (6.35a) we have

$$z_{\pm} = \frac{ia\Gamma}{2} \chi_{\pm}(\Omega + iz_{\pm}, D_{+}, D_{-}) + \mathbb{G}_{\pm}(\vec{r}_{\perp}, t), \quad (\text{E2})$$

$$\mathbb{G}_{\pm}(\vec{r}_{\perp}, t) = \frac{1}{A_{\pm}} \left[i\hat{\mathcal{L}}A_{\pm} - (\gamma_a + i\gamma_p)A_{\mp} \right] - \kappa. \quad (\text{E3})$$

At each spatial point, for a given values of $A_{\pm}(\vec{r}_{\perp}, t)$ and $D_{\pm}(\vec{r}_{\perp}, t)$, we use Eq. (E3) to calculate the spatial distribution of \mathbb{G}_{\pm} . Then, Eq. (E2) has to be solved using Newton-Raphson iteration to obtain $z_{\pm}(\vec{r}_{\perp}, t)$. Proceeding in this way, now we have perfect knowledge of the nonlinear term $\mathbb{N}_{\pm}(\vec{r}_{\perp}, t)$ of the right-side of Eq. (E1). Following the approach used in [250], the circular components of the optical field are

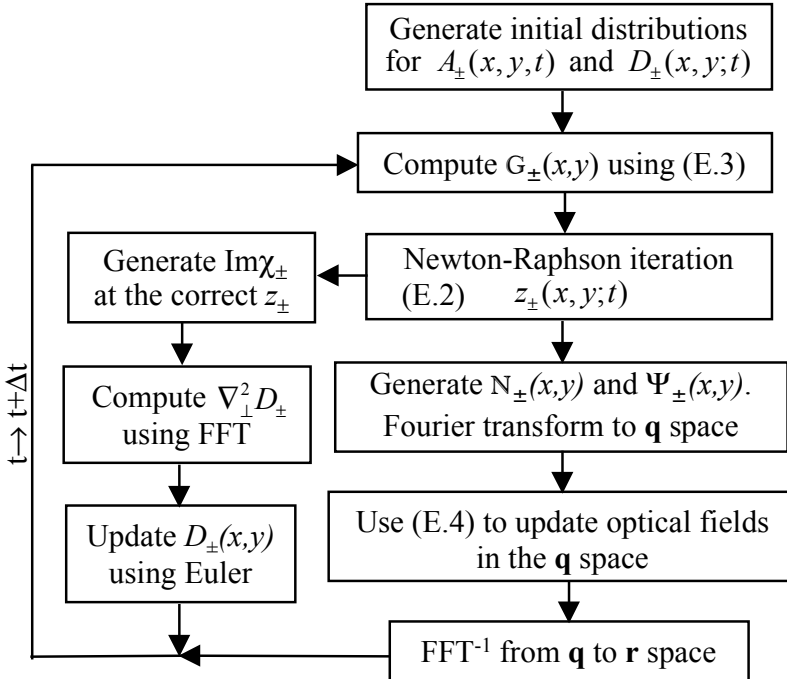
updated one time step in the Fourier space $\mathbf{q} = (q_x, q_y)$

$$\begin{aligned} \tilde{A}_{q\pm}(t + \Delta t) &= e^{-\alpha_q \Delta t} \tilde{A}_{q\pm}(t) + \frac{1 - e^{-\alpha_q \Delta t}}{\alpha_q} \tilde{\mathbb{N}}_{q\pm}(t) + \\ &\quad \sqrt{A\beta_{sp} \frac{(1 - e^{-2 \operatorname{Re} \alpha_q \Delta t})}{2 \operatorname{Re} \alpha_q}} \tilde{\Psi}_{q\pm}(t) + o(\Delta t^2), \end{aligned} \quad (\text{E.4})$$

$\tilde{A}_{q\pm}$, $\alpha_q \equiv \kappa - \frac{ic^2}{2\Omega n_e n_g} q^2$, $\tilde{\mathbb{N}}_{q\pm}(t)$ represent the discrete Fourier components (FFT) of $A_{\pm}(\vec{r}_{\perp}, t)$, $\hat{\mathbb{L}}$, and $\mathbb{N}_{\pm}(\vec{r}_{\perp}, t)$ respectively. $\Psi_{q\pm}(t)$ represents a white noise contribution at a transverse wavevector q obtained by Fourier transforming in space

$$\tilde{\Psi}_{q\pm}(t) = \text{FFT} \left\{ \sqrt{D_{\pm}(\vec{r}_{\perp}, t)} \xi_{\pm}(\vec{r}_{\perp}; t) \right\} \quad (\text{E.5})$$

Once the field variables have been updated, the carrier equations, being the slow variables in the problem, are integrated using an Euler method. The carrier diffusion in Eq. (6.35c), involving terms like $\nabla_{\perp}^2 D_{\pm}$, are calculated in the Fourier space.



Numerical iteration for the spatiotemporal model.

Notation

Symbol	Meaning
ξ	Attenuation coefficient
n_e	Background refractive index
B	Bimolecular recombination rate
N	Carrier density
$\gamma_e = A + BN$	Carriers decay rate
\mathcal{N}	Carrier number
κ	Cavity decay rate
L	Cavity length
W_{ml}	Cladding propagation constant
Γ	Confinement factor
$\vec{r} = (x, y, z)$	Coordinate vector
$\vec{r}_\perp = (x, y)$	Coordinate vector (in-plane)
κ_c	Coupling rate
G_N	Differential gain
$\gamma_s = 2\gamma_j + \gamma_e$	Electron spin-flip rate
\mathbf{k}	Electron's wavenumber
Ω_0	Emission frequency
κ_f	Feedback rate
$\tilde{f}(\omega) = \int_{-\infty}^{\infty} f(t)e^{i\omega t} dt$	Fourier transform (direct)
$f(t) = \frac{1}{2\pi} \int_{-\infty}^{\infty} \tilde{f}(\omega)e^{-i\omega t} d\omega$	Fourier transform (inverse)
$\xi(t)$	Gaussian random number
n_g	Group refractive index

Symbol	Meaning
$v_g = c/n_g$	Group velocity
$\nabla^2 = \partial_x^2 + \partial_y^2 + \partial_z^2$	Laplacian
$\nabla_{\perp}^2 = \partial_x^2 + \partial_y^2$	Laplacian (transverse)
α	Linewidth enhancement factor
Ω	Longitudinal mode frequency
\mathcal{P}	Material polarization
γ_{\perp}	Material polarization decay rate
A	Non-radiative recombination rate
\mathcal{E}	Optical electric field
χ	Optical susceptibility
q	Propagation constant
W	Quantum well thickness
R	Reflectivity (amplitude)
r	Reflectivity (field)
$E(t)$	Slowly varying electric field
β_{sp}	Spontaneous emission factor
$e = 1.60 \cdot 10^{-19} \text{ C}$	Absolute electronic charge
$k_B = 1.38 \cdot 10^{-23} \text{ J/K}$	Boltzmann constant
$\hbar = 1.05459 \cdot 10^{-34} \text{ J}\cdot\text{s}$	Reduced Planck constant
$c = 3 \cdot 10^8 \text{ m/s}$	Speed of light
$\mu_0 = 4\pi \cdot 10^{-7} \text{ T m/A}$	Vacuum permeability
$\epsilon_0 = 1/(\mu_0 c^2)$	Vacuum permittivity

Bibliography

- [1] H. Haken, *Light* (North-Holland, Amsterdam, 1985).
- [2] A. L. Schawlow and C. H. Townes, *Phys. Rev.* **112**, 1940 (1958).
- [3] T. H. Maiman, *Nature* **187**, 493 (1960).
- [4] R. N. Hall, G. E. Fenner, J. D. Kingsley, T. J. Soltys, and R. O. Carlson, *Phys. Rev. Lett.* **9**, 366 (1962).
- [5] T. Someya, R. Werner, A. Forchel, M. Catalano, R. Cingolani, and Y. Arakawa, *Science* **285**, 1905 (1999).
- [6] I. Esquivias, S. Weisser, J. D. Ralston, and D. F. G. Gallagher, *IEEE Trans. Electron Dev.* **39**, 2660 (1992).
- [7] M. Grundmann, *Physica E* **5**, 167 (1999).
- [8] J. Faist, F. Capasso, D. L. Sivco, C. Sirtori, A. L. Hutchinson, and A. Y. Cho, *Science* **264**, 553 (1994).
- [9] G. P. Agrawal, *Long-wavelength semiconductor lasers* (Van Nostrand Reinhold, N. Y., 1986).
- [10] G. P. Agrawal and N. K. Dutta, *Semiconductor lasers, 2nd edition* (Kluwer Academic Publishers, Massachusetts, 2000).
- [11] C. H. Henry and R. F. Kazarinov, *IEEE J. Quantum Electron.* **20**, 733 (1984).
- [12] K. J. Ebeling, “Analysis of vertical-cavity surface-emitting lasers diodes,” In *Semiconductor Quantum Optoelectronics*, A. Miller, M. Ebrahimzadeh, and D. Finlayson, eds., p. 295 (Institute of Physics, Bristol, 1999).
- [13] I. Fischer, G. H. M. van Tartwijk, A. M. Levine, Elsässer, E. Göbel, and D. Lenstra, *Phys. Rev. Lett.* **76**, 220 (1996).
- [14] G. H. M. van Tartwijk and G. P. Agrawal, *Prog. in Quantum Electron.* **22**, 43–122 (1998).
- [15] C. O. Weiss and R. Vilaseca, *Dynamics of Lasers* (VCH, Weinheim, 1991).
- [16] S. Balle, P. Colet, and M. San Miguel, *Phys. Rev. A* **43**, 498 (1991).
- [17] M. Yamada, *IEEE J. Quantum Electron.* **29**, 1330 (1993).
- [18] S. D. Brorson, S. Bischoff, J. Mørk, A. Møller-Larsen, and J. M. Nielsen, *IEEE Photonics Technol. Lett.* **8**, 1308 (1996).
- [19] H. Kawaguchi, *Appl. Phys. Lett.* **45**, 1264 (1984).
- [20] P. C. D. Jagher, W. A. V. d. Graaf, and D. Lenstra, *J. Opt. B: Quantum Semiclass. Opt.* **8**, 805 (1996).
- [21] G. H. M. V. Tartwijk and D. Lenstra, *J. Opt. B: Quantum Semiclass. Opt.* **7**, 87 (1995).
- [22] E. Hernández-García, C. R. Mirasso, M. San Miguel, and K. A. Shore, *IEEE J. Quantum*

- Electron. **30**, 241 (1994).
- [23] M. Homar, C. R. Mirasso, I. Esquivias, and M. San Miguel, IEEE Photonics Technol. Lett. **8**, 861 (1996).
- [24] G. H. M. van Tartwijk and M. San Miguel, IEEE J. Quantum Electron. **32**, 1191 (1996).
- [25] D. Lenstra, B. H. Verbeek, and A. J. den Boef, IEEE J. Quantum Electron. **21**, 674 (1985).
- [26] B. Tromborg and J. Mørk, IEEE J. Quantum Electron. **26**, 642 (1990).
- [27] C. Risch and C. Voumard, J. Appl. Phys. **48**, 2083 (1977).
- [28] R. Lang and K. Kobayashi, IEEE J. Quantum Electron. **16**, 347 (1980).
- [29] K. Iga and F. Koyama, "Surface-emitting lasers," In *Semiconductor lasers II. Materials and structures*, E. Kapon, ed., pp. 323–372 (Academic Press, San Diego, 1999).
- [30] M. San Miguel, "Polarization properties of vertical-cavity surface-emitting lasers," In *Semiconductor Quantum Optoelectronics*, A. Miller, M. Ebrahimzadeh, and D. Finlayson, eds., p. 339 (Institute of Physics, Bristol, 1999).
- [31] K. D. Choquette, D. A. Richie, and R. E. Leibenguth, Appl. Phys. Lett. **64**, 2062–2064 (1994).
- [32] J. Martín-Regalado, F. Prati, M. San Miguel, and N. Abraham, IEEE J. Quantum Electron. **33**, 765–783 (1997).
- [33] S. Balle, E. Tolkachova, M. San Miguel, J. Tredicce, J. Martín-Regalado, and A. Gahl, Opt. Lett. **24**, 1121–1123 (1999).
- [34] G. Verschaffelt, J. Albert, I. Veretennicoff, J. Danckaert, S. Barbay, G. Giacomelli, and F. Marin, Appl. Phys. Lett. **80**, 2248 (2002).
- [35] T. Ackemann, S. Barland, M. Cara, S. Balle, J. R. Tredicce, R. Jäger, M. Grabherr, M. Miller, and K. J. Ebeling, J. Opt. B: Quantum Semiclass. Opt. **2**, 406–412 (2000).
- [36] H. Li, T. L. Lucas, J. G. McInerney, and R. A. Morgan, Chaos, solitons and fractals **4**, 1619 (1994).
- [37] M. San Miguel, Q. Feng, and J. V. Moloney, Phys. Rev. A **52**, 1728–1739 (1995).
- [38] W. Nakwaski and M. Osinski, "Thermal properties of vertical-cavity surface-emitting lasers," In *Progress in Optics XXXVIII*, E. Wolf, ed., pp. 165–262 (Elsevier North-Holland, Amsterdam, 1998).
- [39] L. Borrueal, S. Sujecki, I. Esquivias, J. Wykes, P. Sewell, T. M. Benson, E. C. Larkins, J. Arias, and B. R. Herrero, Proc. SPIE **4646**, 335 (2002).
- [40] M. Born and E. Wolf, *Principles of optics* (Pergamon, Oxford, 1980).
- [41] H. Haug and S. W. Koch, *Quantum theory of the optical and electronic properties of semiconductors* (World Scientific, Singapore, 1993).
- [42] W. W. Chow, S. W. Koch, and M. Sargent III, *Semiconductor Laser Physics* (Springer-Verlag, Berlin, 1994).
- [43] W. W. Chow, H. C. Schneider, S. W. Koch, C.-H. Chang, L. Chrostowski, and C. J. Chang-Hasnain, IEEE J. Quantum Electron. **38**, 402 (2002).
- [44] A. Yariv, *Quantum electronics* (Wiley, New York, 1989).
- [45] B. Romero, J. Arias, I. Esquivias, and M. Cada, Appl. Phys. Lett. **76**, 1504 (2000).
- [46] Feature section on optical chaos and applications to cryptography, IEEE Journal Quantum Electron **38**, n. 9 (2002).
- [47] C. R. Mirasso, "Applications of semiconductor lasers to secure communications," In *Fundamental issue of nonlinear dynamics*, B. Krauskopf and D. Lenstra, eds., **548**, 112

- (American Institute of Physics, New York, 2000).
- [48] A. Hohl, A. Gavrielides, T. Erneux, and V. Kovanis, *Phys. Rev. Lett.* **78**, 4745 (1997).
 - [49] M. Mackey and L. Glass, *Science* **197**, 287 (1977).
 - [50] J.-L. Chern, K. Otsuka, and F. Ishiyama, *Opt. Comm.* **96**, 259–266 (1993).
 - [51] F. Rogister, A. Locquet, D. Pieroux, M. Sciamanna, O. Deparis, P. Mégret, and M. Blondel, *Opt. Lett.* **26**, 1486 (2001).
 - [52] S. Tang and J. M. Liu, *IEEE J. Quantum Electron.* **37**, 329–336 (2001).
 - [53] G. Giacomelli and A. Politi, *Phys. Rev. Lett.* **76**, 2686 (1996).
 - [54] C. Masoller, *Chaos* **7**, 455 (1997).
 - [55] G. Vaschenko, M. Giudici, J. J. Rocca, C. S. Menoni, J. R. Tredicce, and S. Balle, *Phys. Rev. Lett.* **81**, 5536 (1998).
 - [56] D. W. Sukow, T. Heil, I. Fischer, A. Gavrielides, A. Hohl, and W. Elsässer, *Phys. Rev. A* **60**, 667 (1999).
 - [57] F. Favre, *IEEE J. Quantum Electron.* **23**, 81 (1987).
 - [58] M. Giudici, T. Ackemann, S. Barland, J. R. Tredicce, and S. Balle, *J. Opt. Soc. Am. B* **16**, 2114 (1999).
 - [59] T. Heil, I. Fischer, W. Elsässer, and A. Gavrielides, *Phys. Rev. Lett.* **87**, 243901 (2001).
 - [60] M. Sargent III, M. O. Scully, and J. E. Lamb, *Laser physics* (Addison-Wesley, Massachusetts, 1974).
 - [61] R. Toral and A. Chakrabarti, *Comp. Phys. Commun.* **74**, 327 (1993).
 - [62] C. W. Gardiner, *Handbook of stochastic methods. 2nd Ed.* (Springer-Verlag, Berlin, 1995).
 - [63] G. H. M. van Tartwijk, A. M. Levine, and D. Lenstra, *IEEE J. Select. Topics Quantum Electron.* **1**, 446 (1995).
 - [64] J. Mørk, M. Semkow, and B. Tromborg, *Electron. Lett.* **26**, 609 (1990).
 - [65] D. Lenstra, *Opt. Comm.* **81**, 209 (1991).
 - [66] A. Ritter and H. Haug, *J. Opt. Soc. Am. B* **10**, 130 (1993).
 - [67] A. M. Levine, G. H. M. van Tartwijk, D. Lenstra, and T. Erneux, *Phys. Rev. A* **52**, 3436 (1995).
 - [68] K. Wada, T. Umeda, and Y. Cho, *Opt. Comm.* **109**, 93 (1994).
 - [69] T. Heil, I. Fischer, and W. Elsässer, *Phys. Rev. A* **58**, 2672 (1998).
 - [70] J. O. Alvarez, *The Nonlinear Journal* **2**, 58 (2000), see online at, <http://www.math.arizona.edu/~goriely>.
 - [71] K. Petermann, *Laser diode modulation and noise* (Kluwer Academic Publishers, Address, 1988).
 - [72] G. P. Agrawal, *IEEE J. Quantum Electron.* **20**, 468 (1984).
 - [73] M. V. Homar, “Semiconductor laser dynamics under feedback and modulation. Single and multimode operation,” PhD Dissertation, Universitat de les Illes Balears, 1997.
 - [74] R. W. Tkach and A. R. Chraplyvy, *J. Lightwave Technol.* **4**, 1655 (1986).
 - [75] C. R. Mirasso, P. Colet, and P. García-Fernández, *IEEE Photonics Technol. Lett.* **8**, 299 (1996).
 - [76] C. R. Mirasso, J. Mulet, and C. Masoller, *IEEE Photonics Technol. Lett.* **14**, 456 (2002).

- [77] J. Ye, H. Li, and J. G. McInerney, *Phys. Rev. A* **47**, 2249 (1993).
- [78] H. Li, J. Ye, and J. G. McInerney, *IEEE J. Quantum Electron.* **29**, 2421 (1993).
- [79] A. Ritter and H. Haug, *J. Opt. Soc. Am. B* **10**, 145 (1993).
- [80] C. H. Henry and R. F. Kazarinov, *IEEE J. Quantum Electron.* **22**, 294 (1986).
- [81] J. Mørk, B. Tromborg, and L. Christiansen, *IEEE J. Quantum Electron.* **24**, 123 (1988).
- [82] J. Sacher, W. Elsässer, and E. O. Göbel, *Phys. Rev. Lett.* **63**, 2224 (1989).
- [83] T. Sano, *Phys. Rev. A* **50**, 2719 (1994).
- [84] C. R. Mirasso, M. Mulder, H. J. W. Spoelder, and D. Lenstra, *Computers Phys.* **11**, 282 (1997).
- [85] G. Huyet, S. Hegarty, M. Giudici, B. De Bruyn, and J. G. McInerney, *Europhys. Lett.* **40**, 619 (1997).
- [86] G. Huyet, S. Balle, M. Giudici, C. Green, G. Giacomelli, and J. Tredicce, *Opt. Comm.* **149**, 341 (1998).
- [87] G. Huyet, J. K. White, A. J. Kent, S. P. Hegarty, J. V. Moloney, and J. G. McInerney, *Phys. Rev. A* **60**, 1534 (1999).
- [88] A. Hohl, H. J. C. van der Linden, and R. Roy, *Opt. Lett.* **20**, 2396 (1995).
- [89] M. Giudici, C. Green, G. Giacomelli, U. Nespolo, and J. R. Tredicce, *Phys. Rev. E* **55**, 6414 (1997).
- [90] D. W. Sukow, J. R. Gardner, and D. J. Gauthier, *Phys. Rev. A* **56**, 3370 (1997).
- [91] T. Heil, I. Fischer, W. Elsässer, J. Mulet, and C. R. Mirasso, *Opt. Lett.* **18**, 1275 (1999).
- [92] P. Bergé, Y. Pomeau, and C. Vidal, *Order within chaos. Towards a deterministic approach of turbulence* (John Wiley & Sons, Paris, 1986).
- [93] C. Grebogi, E. Ott, F. Romeiras, and J. A. Yorke, *Phys. Rev. A* **36**, 5365 (1987).
- [94] M. C. Eguía, G. B. Mindlin, and M. Giudici, *Phys. Rev. E* **58**, 2636 (1998).
- [95] M. C. Eguía and G. B. Mindlin, *Phys. Rev. E* **60**, 1551 (1999).
- [96] T. Heil, I. Fischer, and W. Elsässer, *Phys. Rev. A* **60**, 634 (1999).
- [97] J. Mulet and C. R. Mirasso, *Phys. Rev. E* **59**, 5400 (1999).
- [98] E. Ott, C. Grebogi, and J. A. Yorke, *Phys. Rev. Lett.* **64**, 1196 (1990).
- [99] G. Giacomelli, M. Giudici, S. Balle, and J. R. Tredicce, *Phys. Rev. Lett.* **84**, 3298 (2000).
- [100] J. M. Buldú, J. García-Ojalvo, C. R. Mirasso, M. C. Torrent, and J. M. Sancho, *Phys. Rev. E* **64**, 051109 (2001).
- [101] J. M. Buldú, J. García-Ojalvo, C. R. Mirasso, and M. C. Torrent, *Phys. Rev. E* **66**, 021106 (2002).
- [102] J. Mulet, "Statistics of power dropouts in semiconductor lasers with optical feedback and current modulation," Master Thesis, Universitat de les Illes Balears, 1998.
- [103] D. W. Sukow and D. J. Gauthier, *IEEE J. Quantum Electron.* **36**, 175 (2000).
- [104] J. S. Lawrence and D. M. Kane, *IEEE J. Quantum Electron.* **38**, 185 (2002).
- [105] G. Huyet, P. A. Porta, S. P. Hegarty, J. G. McInerney, and F. Holland, *Opt. Comm.* **180**, 339 (2000).
- [106] J. M. Mendez, R. Laje, M. Giudici, J. Aliaga, and G. B. Mindlin, *Phys. Rev. E* **63**, 066218 (2001).
- [107] K. Coffman, W. D. McCormick, and H. L. Swinney, *Phys. Rev. Lett.* **56**, 999 (1986).

-
- [108] C. Schäfer, M. G. Rosenblum, J. Kurths, and H. H. Abel, *Nature* **392**, 239 (1998).
- [109] U. Ernst, K. Pawelzik, and T. Geisel, *Phys. Rev. Lett.* **74**, 1570 (1995).
- [110] R. Roy, K. S. Thornburg, and Jr., *Phys. Rev. Lett.* **72**, 2009 (1994).
- [111] A. Pikovsky, M. Rosenblum, and J. Kurths, *Synchronization: a universal concept in non-linear sciences* (Cambridge University Press, New York, 2001).
- [112] L. M. Pecora and T. L. Carroll, *Phys. Rev. Lett.* **64**, 821 (1990).
- [113] T. Heil, J. Mulet, I. Fischer, C. R. Mirasso, M. Peil, P. Colet, and W. Elsässer, *IEEE J. Quantum Electron.* **38**, 1162 (2002).
- [114] T. Sugawara, M. Tachikawa, T. Tsukamoto, and T. Shimizu, *Phys. Rev. Lett.* **72**, 3502 (1994).
- [115] G. D. VanWiggeren and R. Roy, *Science* **279**, 1198 (1998).
- [116] G. D. VanWiggeren and R. Roy, *Int. J. Bif. Chaos* **9**, 2129 (2000).
- [117] H. G. Winful and L. Rahman, *Phys. Rev. Lett.* **65**, 1575 (1990).
- [118] V. Annovazzi-Lodi, S. Donati, and A. Scire, *IEEE J. Quantum Electron.* **32**, 953–959 (1996).
- [119] T. B. Simpson, J. M. Liu, A. Gavrielides, V. Kovanis, and P. M. Alsing, *Phys. Rev. A* **51**, 4181 (1995).
- [120] N. A. Olsson and W. T. Tsang, *IEEE J. Quantum Electron.* **20**, 332 (1984).
- [121] G. P. Agrawal, *IEEE J. Quantum Electron.* **21**, 255 (1985).
- [122] D. Marcuse, *IEEE J. Quantum Electron.* **21**, 154 (1985).
- [123] D. Marcuse and T.-P. Lee, *IEEE J. Quantum Electron.* **20**, 166 (1984).
- [124] L. A. Coldren and T. L. Koch, *IEEE J. Quantum Electron.* **20**, 671 (1984).
- [125] G. C. Dente, C. E. Moeller, and P. S. Durkin, *IEEE J. Quantum Electron.* **26**, 1014 (1990).
- [126] A. Hohl, A. Gavrielides, T. Erneux, and V. Kovanis, *Phys. Rev. A* **59**, 3941 (1999).
- [127] J. Mulet, C. R. Mirasso, T. Heil, and I. Fischer, *Proc. SPIE* **4283**, 293 (2001).
- [128] T. Heil, I. Fischer, W. Elsässer, J. Mulet, and C. R. Mirasso, *Phys. Rev. Lett.* **86**, 795 (2001).
- [129] H. Fujino and J. Ohtsubo, *Opt. Rev.* **8**, 351 (2001).
- [130] C. R. Mirasso, M. Kolesik, M. Matus, J. K. White, and J. V. Moloney, *Phys. Rev. A* **65**, 013805 (2002).
- [131] J. Mulet, C. Masoller, and C. R. Mirasso, *Phys. Rev. A* **65**, 063815 (2002).
- [132] J. Mulet, C. R. Mirasso, T. Heil, and I. Fischer, submitted for publication (2002).
- [133] J. K. White, M. Matus, and J. V. Moloney, *Phys. Rev. E* **65**, 036229 (2002).
- [134] A. A. Duarte and H. G. Solari, *Phys. Rev. A* **64**, 033803 (2001).
- [135] E. Hecht and A. Zajac, *Optics* (Addison-Wesley, Delaware, 1988).
- [136] M. Yousefi and D. Lenstra, *IEEE J. Quantum Electron.* **35**, 970 (1999).
- [137] M. G. Rosenblum, A. S. Pikovsky, and J. Kurths., *Phys. Rev. Lett.* **76**, 1804 (1996).
- [138] M. G. Rosenblum, A. S. Pikovsky, and J. Kurths, *Phys. Rev. Lett.* **78**, 4193 (1997).
- [139] M. Peil, T. Heil, I. Fischer, and W. Elsässer, *Phys. Rev. Lett.* **88**, 174101 (2002).
- [140] T. Heil, J. Mulet, I. Fischer, C. R. Mirasso, M. Peil, P. Colet, and W. Elsässer, *IEEE J. Quantum Electron.* **38**, 1162 (2002).
- [141] M. K. S. Yeung and S. H. Strogatz, *Phys. Rev. Lett.* **82**, 648 (1999).

- [142] G. Kozyreff, A. G. Vladimirov, and P. Mandel, *Phys. Rev. Lett.* **85**, 3809 (2000).
- [143] M. San Miguel and R. Toral, "Stochastic effects in physical systems," In *Procs. instabilities and non-equilibrium structures VI*, E. Tirapegui, J. Martínez, and W. Tiemann, eds., p. 35 (Kluwer academic, Dordrecht, 2000).
- [144] J. D. Jackson, *Classical electrodynamics* (Wiley, New York, 1975).
- [145] G. P. Agrawal, *Phys. Rev. A* **37**, 2488–2494 (1988).
- [146] F. Koyama, K. Morito, and K. Iga, *IEEE J. Quantum Electron.* **27**, 1410–1416 (1991).
- [147] K. H. Hahn, M. R. Tan, and S.-Y. Wang, *Electron. Lett.* **30**, 139–140 (1994).
- [148] D. V. Kuskonov, H. Temkin, and S. Swirhun, *Appl. Phys. Lett.* **67**, 2141–2143 (1995).
- [149] D. C. Kilper, P. A. Roos, J. L. Carlsten, and K. L. Lear, *Phys. Rev. A* **55**, R3323–R3326 (1997).
- [150] J.-L. Vey and W. Elsässer, *J. Opt. Soc. Am. B* **14**, 1299–1304 (1997).
- [151] J.-L. Vey and W. Elsässer, *Opt. Lett.* **23**, 721–723 (1998).
- [152] F. Marin and G. Giacomelli, *J. Opt. B: Quantum Semiclass. Opt.* **1**, 128–132 (1999).
- [153] G. Giacomelli, F. Marin, M. Gabrysch, K. H. Gulden, and M. Moser, *Opt. Comm.* **146**, 136–140 (1998).
- [154] J.-P. Hermier, A. Bramati, A. Z. Khoury, E. Giacobino, J.-P. Poizat, T. J. Chang, and P. Grangier, *J. Opt. Soc. Am. B* **16**, 2140–2146 (1999).
- [155] J. P. Hermier, A. Bramati, A. Z. Khoury, V. Josse, E. Giacobino, P. Schnitzer, R. Michalzik, and K. J. Ebeling, *IEEE J. Quantum Electron.* **37**, 87–91 (2001).
- [156] A. Valle, J. Sarma, and K. A. Shore, *IEEE J. Quantum Electron.* **31**, 1423–1431 (1995).
- [157] A. Valle and L. Pesquera, *Proc. SPIE* **3625**, 46 (1999).
- [158] J. Y. Law and G. P. Agrawal, *IEEE Photonics Technol. Lett.* **9**, 437–439 (1997).
- [159] M. P. van Exter, M. B. Willemsen, and J. P. Woerdman, *Proc. SPIE* **3946**, 58–68 (2000).
- [160] M. P. van Exter, M. B. Willemsen, and J. P. Woerdman, *Phys. Rev. A* **58**, 4191–4205 (1998).
- [161] M. P. van Exter, A. Al-Remawi, and J. P. Woerdman, *Phys. Rev. Lett.* **80**, 4875–4878 (1998).
- [162] M. B. Willemsen, M. P. van Exter, and J. P. Woerdman, *Phys. Rev. A* **60**, 4105–4113 (1999).
- [163] E. Goodbar, J. W. Scott, B. Thibeault, G. Robinson, Y. Akulova, and L. A. Coldren, *Appl. Phys. Lett.* **67**, 3697–3699 (1995).
- [164] M. Giudici, T. Ackemann, S. Barland, J. Tredicce, and S. Balle, *J. Opt. Soc. Am. B* **16**, 2114–2123 (1999).
- [165] C. Degen, J.-L. Vey, P. Schnitzer, and K. J. Ebeling, *Electron. Lett.* **34**, 1585–1587 (1998).
- [166] M. P. van Exter, M. B. Willemsen, and J. P. Woerdman, *J. Opt. B: Quantum Semiclass. Opt.* **1**, 637–645 (1999).
- [167] T. Erneux, J. Danckaert, K. Panajotov, and I. Veretennicoff, *Phys. Rev. A* **59**, 4660–4667 (1999).
- [168] M. B. Willemsen, M. P. van Exter, and J. P. Woerdman, *Phys. Rev. Lett.* **84**, 4337–4340 (2000).
- [169] J. Martín-Regalado, J. L. Chilla, J. J. Rocca, and P. Brusenbach, *Appl. Phys. Lett.* **70**, 3350–3352 (1997).
- [170] J.-P. Hermier, M. I. Kolobov, I. Maurin, and E. Giacobino, *Phys. Rev. A* **65**, 053825 (2002).
- [171] A. K. J. van Doorn, M. P. van Exter, and J. P. Woerdman, *Appl. Phys. Lett.* **69**, 1041–1043 (1996).

-
- [172] M. P. van Exter, A. K. Jansen van Doorn, and J. P. Woerdman, *Phys. Rev. A* **56**, 845–853 (1997).
- [173] L. Viña, *J. Phys.: Condens. Matter* **11**, 5929–5952 (1999).
- [174] A. Tackeuchi, T. Kuroda, S. Muto, Y. Nishikawa, and O. Wada, *Jpn. J. Appl. Phys.* **38**, 4680–4687 (1999).
- [175] H. Ando, T. Sogawa, and H. Gotoh, *Appl. Phys. Lett.* **73**, 566–568 (1998).
- [176] K. Panajotov, B. Ryvkin, J. Danckaert, M. Peeters, H. Thienpont, and I. Veretennicoff, *IEEE Photonics Technol. Lett.* **10**, 6–8 (1998).
- [177] M. P. van Exter, A. K. J. van Doorn, and J. P. Woerdman, *Phys. Rev. A* **56**, 845–853 (1997).
- [178] A. K. J. van Doorn, M. P. van Exter, and J. P. Woerdman, *Appl. Phys. Lett.* **69**, 1041–1043 (1996).
- [179] G. P. Agrawal and C. M. Bowden, *IEEE Photonics Technol. Lett.* **5**, 640–642 (1993).
- [180] H. F. Hofmann, “Quantum noise and spontaneous emission in semiconductor laser devices,” PhD dissertation, Institut für Technische Physik Stuttgart, 1999.
- [181] A. Valle and L. Pesquera, *IEEE Photonics Technol. Lett.* **13**, 272–274 (2001).
- [182] B. Ryvkin, K. Panajotov, A. Georgievski, J. Danckaert, M. Peeters, G. Verschaffelt, H. Thienpont, and I. Veretennicoff, *J. Opt. Soc. Am. B* **16**, 2106–2113 (1999).
- [183] M. San Miguel, S. Balle, J. Mulet, C. R. Mirasso, E. Tolkachova, and J. R. Tredicce, *Proc. SPIE* **3944**, 242–251 (2000).
- [184] J. Martín-Regalado, “Polarization properties of vertical-cavity surface-emitting lasers,” PhD dissertation, Universitat de les Illes Balears, 1997, online access <http://www.imedeia.uib.es/publicationsdbfiles/000280/>.
- [185] R. F. M. Hendriks, M. P. van Exter, J. P. Woerdman, L. Weegels, and A. Van Geelen, *J. Opt. Soc. Am. B* **16**, 832–834 (1999).
- [186] S. Ciuchi, M. San Miguel, and N. B. Abraham, *Phys. Rev. A* **57**, 3843–3857 (1998).
- [187] J.-L. Vey, C. Degen, K. Auen, and W. Elsässer, *Phys. Rev. A* **60**, 3284–3295 (1999).
- [188] C. W. Gardiner, *Quantum noise* (Springer-Verlag, Berlin, 1991).
- [189] K. D. Choquette, D. A. Richie, and R. A. Leibenguth, *Appl. Phys. Lett.* **69**, 2062–2064 (1994).
- [190] K. D. Choquette, R. P. Schneider, K. L. Lear, and R. A. Leibenguth, *IEEE J. Select. Topics Quantum Electron.* **1**, 661–666 (1995).
- [191] K. Panajotov, B. Ryvkin, J. Danckaert, M. Peeters, H. Thienpont, and I. Veretennicoff, *IEEE Photonics Technol. Lett.* **10**, 6–8 (1998).
- [192] J. Mulet, C. R. Mirasso, and M. San Miguel, *Phys. Rev. A* **64**, 023817 (2001).
- [193] D. Burak, J. V. Moloney, and R. Binder, *IEEE J. Quantum Electron.* **36**, 956–970 (2000).
- [194] S. Balle, E. Tolkachova, M. San Miguel, J. R. Tredicce, J. Martín-Regalado, and A. Gahl, *Opt. Lett.* **24**, 1121–1123 (1999).
- [195] G. R. Hadley, K. L. Lear, M. E. Warren, K. D. Choquette, J. W. Scott, and S. W. Corzine, *IEEE J. Quantum Electron.* **32**, 607–616 (1996).
- [196] D. Burak and R. Binder, *IEEE J. Quantum Electron.* **33**, 1205–1215 (1997).
- [197] H. Wenzel and H.-J. Wünsche, *IEEE J. Quantum Electron.* **33**, 1156–1162 (1997).
- [198] M. J. Noble, J. P. Loehr, and J. A. Lott, *IEEE J. Quantum Electron.* **34**, 1890–1903 (1998).
- [199] B. Demeulenaere, P. Bienstman, B. Dhoedt, and R. G. Baets, *IEEE J. Quantum Electron.*

- 35**, 358–367 (1999).
- [200] L. Raddatz, I. H. White, H. D. Summers, K. H. Hahn, M. R. Tan, and S.-Y. Wang, *IEEE Photonics Technol. Lett.* **8**, 743–745 (1996).
- [201] J. Law and G. P. Agrawal, *IEEE Photonics Technol. Lett.* **9**, 437–439 (1997).
- [202] J. Martín-Regalado, S. Balle, and M. San Miguel, *Opt. Lett.* **22**, 460–462 (1997).
- [203] J. Martín-Regalado, S. Balle, M. San Miguel, A. Valle, and L. Pesquera, *J. Opt. B: Quantum Semiclass. Opt.* **9**, 713–736 (1997).
- [204] T. Rössler, R. A. Indik, G. K. Harkness, J. V. Moloney, and C. Z. Ning, *Phys. Rev. A* **58**, 3279–3292 (1998).
- [205] C. Z. Ning and P. M. Goorjian, *J. Opt. B: Quantum Semiclass. Opt.* **16**, 2072–2082 (1999).
- [206] H. Haug and S. Schmitt-Rink, *Prog. Quantum Electron.* **9**, 3 (1984).
- [207] M. Lindberg and S. W. Koch, *Phys. Rev. B* **38**, 3342–3350 (1988).
- [208] M. Lindberg, S. An, S. W. Koch, and M. Sargent III, *Phys. Rev. A* **40**, 4415–4425 (1989).
- [209] H. Haug and S. W. Koch, *Phys. Rev. A* **39**, 1887–1898 (1989).
- [210] D. Burak, J. V. Moloney, and R. Binder, *Phys. Rev. A* **61**, 053809 (2000).
- [211] S. Balle, *Phys. Rev. A* **57**, 1304–1312 (1998).
- [212] C. M. Bowden and G. P. Agrawal, *Opt. Comm.* **100**, 147–152 (1993).
- [213] S. Balle, *Opt. Comm.* **119**, 227–235 (1995).
- [214] C. Z. Ning, R. A. Indik, and J. V. Moloney, *IEEE J. Quantum Electron.* **33**, 1543–1550 (1997).
- [215] A. Yariv, *Optical electronics* (Holt, Rinehart and Winston Inc., Philadelphia, 1991).
- [216] B. Mroziewicz, M. Bugajski, and W. Nakwaski, *Physics of Semiconductor Lasers* (North-Holland, Amsterdam, 1991).
- [217] G. P. Agrawal and N. K. Dutta, *Long-Wavelength Semiconductor Lasers* (Van Nostrand-Reinhold, New York, 1986).
- [218] L. A. Coldren and S. W. Corzine, *Diode Lasers and Photonic Integrated Circuits* (Wiley, New York, 1995).
- [219] F. Stern, *J. Appl. Phys.* **47**, 5382 (1976).
- [220] D. S. Citrin and Y.-C. Chang, *IEEE J. Quantum Electron.* **29**, 97–108 (1993).
- [221] T. Yamanaka, Y. Yoshikuni, K. Yokoyama, W. Lui, and S. Seki, *IEEE J. Quantum Electron.* **29**, 1609–1616 (1993).
- [222] W. L. Li, Y. K. Su, and D. H. Jaw, *IEEE J. Quantum Electron.* **33**, 416–423 (1997).
- [223] P. M. Enders, *IEEE J. Quantum Electron.* **33**, 580–588 (1997).
- [224] O. Hess and T. Kuhn, *Phys. Rev. A* **54**, 3347–3359 (1996), *ibidem*, pp. 3360–3368, 1996.
- [225] T. Makino, *IEEE J. Quantum Electron.* **32**, 493–501 (1996).
- [226] H. Ohno, *Science* **281**, 951 (1998).
- [227] W. H. Press, S. A. Teukolsky, W. T. Vetterling, and B. P. Flannery, *Numerical recipes in FORTRAN: the art of scientific computing* (Cambridge University Press, Cambridge, 1992).
- [228] N. K. Dutta, *J. Appl. Phys.* **65**, 1961–1963 (1990).
- [229] O. Buccafusca, J. L. Chilla, J. J. Rocca, P. Brusenbach, and J. Martín-Regalado, *IEEE J. Quantum Electron.* **35**, 608 (1999).

-
- [230] O. Buccafusca, J. L. A. Chilla, J. J. Rocca, C. Wilmsen, S. Feld, and R. Leibenguth, *Appl. Phys. Lett.* **35**, 185 (1995).
- [231] M. Giudici, J. R. Tredicce, G. Vaschenko, J. J. Rocca, and C. S. Menoni, *Opt. Comm.* **158**, 313 (1998).
- [232] W. Nakwaski and R. P. Sarzala, *Opt. Comm.* **148**, 63–39 (1998).
- [233] P. Colet, C. R. Mirasso, and M. San Miguel, *IEEE J. Quantum Electron.* **29**, 1624 (1993).
- [234] J. Mulet and S. Balle, *IEEE J. Quantum Electron.* **38**, 291–305 (2002).
- [235] J. L. Jewell, A. Sherer, S. L. McCall, Y. H. Lee, S. Walker, J. P. Harbison, and L. T. Florez, *Electron. Lett.* **25**, 1123 (1989).
- [236] W. W. Chow, K. D. Choquette, M. H. Crawford, K. L. Lear, and G. R. Hadley, *IEEE J. Quantum Electron.* **33**, 1810 (1997).
- [237] D. L. Huffaker, D. G. Deppe, K. Kumar, and T. J. Rogers, *Appl. Phys. Lett.* **65**, 97 (1994).
- [238] A. W. Synder and J. D. Love, *Optical waveguide theory* (Chapman and Hall, New York, 1983).
- [239] G. P. Bava, P. Debernardi, and L. Fratta, *Phys. Rev. A* **63**, 023816 (2001).
- [240] S. Riyopoulos, D. Dialetis, J. Inman, and A. Phillips, *J. Opt. Soc. Am. B* **18**, 1268 (2001).
- [241] A. Valle, J. Sarma, and K. A. Shore, *J. Opt. Soc. Am. B* **12**, 1741 (1995).
- [242] A. Valle and L. Pesquera, *Appl. Phys. Lett.* **79**, 3914 (2001).
- [243] J. J. Morikuni, P. V. Mena, A. V. Harton, K. W. Wyatt, and S.-M. Kang, *J. Lightwave Technol.* **17**, 95 (1999).
- [244] J. S. Gustavsson, J. A. Vukusic, J. Bengtsson, and A. Larsson, *IEEE J. Quantum Electron.* **38**, 203 (2002).
- [245] J. Tatum, D. Smith, J. Guenter, and R. Johnson, *Proc. SPIE* **3004**, 151 (1997).
- [246] J. A. Lehman and R. A. Morgan, In *Vertical-cavity surface-emitting lasers: Technology and applications*, J. Cheng and N. K. Dutta, eds., p. 133 (Gordon and Breach Sci. Publ., Amsterdam, 2000).
- [247] M. I. Cohen, A. A. Allerman, K. D. Choquette, and C. Jagadish, *IEEE Photonics Technol. Lett.* **13**, 544 (2001).
- [248] See http://content.honeywell.com/vcSEL/technical/006703_1.pdf.
- [249] A. Valle, J. Mulet, L. Pesquera, and S. Balle, *Proc. SPIE* **4649**, 10 (2002).
- [250] R. Montagne, E. Hernández-García, A. Amengual, and M. San Miguel, *Phys. Rev. E* **56**, 151–167 (1997).

List of Figures

1.1	Band structure of a semiconductor.	2
1.2	Energy band diagram of a heterostructure semiconductor laser.	3
1.3	Sketch of a heterostructure edge-emitting semiconductor laser.	5
1.4	Experimental time traces of a semiconductor laser with optical feedback.	6
1.5	Sketch of a vertical-cavity surface-emitting semiconductor laser.	7
1.6	Materials for VCSELs in a wide spectral band.	8
1.7	LI curve after projection on linear polarization states.	9
1.8	Nearfield images for an oxidized VCSEL.	10
1.9	Experimental (dashed lines) TE absorption spectra of a single quantum well (GaIn)As / (AlGa)As laser diode.	14
2.1	Edge-emitting laser with optical feedback from a distant reflector.	26
2.2	Operation regimes of a laser with optical feedback.	35
2.3	Characteristic dynamics of a laser with optical feedback under CC operation. . .	37
2.4	Characteristic dynamics of a laser with optical feedback under LFF operation. . .	38
2.5	Three dimensional representation of the LFF attractor (Sisyphus effect).	39
2.6	Probability distribution functions of the time between dropouts.	42
2.7	Return maps T_{n+1} vs. T_n for the time between dropouts.	43
2.8	Mean time between dropouts versus normalized current.	44
2.9	Optical spectrum of the DFB laser.	45
2.10	Time traces showing alternation between LFF and stable operation.	46
2.11	Probability density function $f(T)$ of the time interval T between LFF dropouts. .	47
2.12	Ln-ln plot of the average time interval between subsequent dropouts $\langle T \rangle$ versus the normalized injection current $\varepsilon_2 = p/p_{\text{LFF}} - 1$	48
2.13	Variation of PDFs and return maps on the modulation frequency.	49
2.14	Variation of PDFs and return maps on the modulation amplitude.	50
3.1	Sketch of two mutually coupled Fabry-Perot semiconductor lasers.	58
3.2	Frequency dependence of the transmittivity: a single Fabry-Perot cavity (a), a C^3 laser with $L_e = 0.42L$ (b), two distant coupled lasers with $L_e = 55L$ (c).	64
3.3	Frequency dependence of the gain of symmetric solutions.	66
3.4	Spectrum of the symmetric monochromatic solutions.	68
3.5	$\delta\mathcal{G}_1 - \delta\mathcal{G}_2$ diagram around an in-phase symmetric solution (\diamond).	69

3.6	Frequency shift $\delta\eta$ with respect to an in-phase symmetric solution.	69
3.7	Relative phase among the oscillation of the two electric fields.	70
3.8	Threshold analysis: The coupling time is $\tau = 0.1$ ns.	73
3.9	Threshold analysis: The coupling time is $\tau = 4$ ns.	73
3.10	Scheme of the experimental setup.	76
3.11	Numerical and experimental comparison of the maximum degree of correlation achieved as function of the coupling strength.	79
3.12	Numerical time traces of the laser intensities for injection current.	79
3.13	Experimental time traces of the intensity emitted by the two lasers when running under resonant conditions.	79
3.14	Subnanosecond synchronized dynamics between two consecutive power dropouts using time shifted series: numerical and experimental results.	80
3.15	Deterministic numerical simulation describing the destabilization of the isochronal solution.	81
3.16	Numerical and experimental crosscorrelation function.	82
3.17	Numerical and experimental generalized return plots.	82
3.18	Probability distribution function of the time shift between power dropouts.	82
3.19	Dynamics of the injection phases during the destabilization of the isochronal solution.	83
3.20	Statistical properties of the injection phases under symmetric operation of the lasers.	84
3.21	Comparison of the complete dynamical model and the phenomenological model for weak coupling.	88
3.22	Comparison of the complete dynamical model and the phenomenological model for strong coupling.	89
5.1	Intensity noise and cross correlation of the $5 \mu\text{m}$ device measured through a Glan-Thompson polarizer.	102
5.2	Sketch of a four level system in the SFM.	105
5.3	Linear stability of the linearly-polarized solutions in the $\mu - \gamma_p$ plane.	112
5.4	Typical polarization switching in the SFM from the low to the high frequency state.	112
5.5	Power spectra in arbitrary units for currents below PS and above PS.	117
5.6	Temporal trace of the intensity components and their respective probability density function.	118
5.7	Poincaré sphere.	121
5.8	Power spectra of the polarization fluctuations within a COs region.	123
5.9	Power spectra of the polarization fluctuations for weak linear anisotropies.	123
5.10	Study of the effect of γ_s in the absence of birefringence.	125
5.11	Study of the effect of γ_p for moderate values of γ_s	126
5.12	Normalized crosscorrelation of the circular components C_{+-} and the linear components C_{xy}	127
6.1	Temperature distribution and current flux in a top-emitting VCSEL.	133
6.2	Polarization of the field vector in the VCSEL cavity.	134

6.3	Scheme of the allowed transitions in the spin subbands of a strained QW.	142
6.4	Optical gain, refractive index, differential gain spectrum, and alpha factor.	144
6.5	Current-detuning linear stability diagram for the linearly polarized solutions.	148
6.6	Threshold curves for the fundamental and first-order transverse modes as function of the normalized detuning.	153
6.7	Lateral confinement factor of the transverse modes in a bottom-emitter VCSEL.	153
6.8	Threshold curves for the successive transverse modes in a top-emitter VCSEL.	155
6.9	Lateral confinement factor of the transverse modes in a top-emitter VCSEL.	155
6.10	Switch-on dynamics of the bottom emitter VCSEL.	158
6.11	Higher-order transverse mode selection for the top-emitter VCSEL.	159
6.12	Power spectra for the VCSEL <i>A</i> in both polarizations.	161
6.13	Power spectra for the VCSEL <i>B</i> in both polarizations.	161
6.14	Evolution of the modal power of each transverse mode and the total intensity for the VCSEL <i>A</i> , and <i>B</i>	163
6.15	Turn-on delay as function of the ‘on’ current.	164
6.16	Response to a current pulse of the bottom-emitter VCSEL of $15\mu\text{m}$	165
6.17	Polarization resolved optical spectra of the bottom-emitter VCSEL.	166
7.1	Turn-on and turn-off transients for strong lateral guiding conditions.	175
7.2	Disc contact: turn-on and turn-off transients for weak lateral guiding conditions.	176
7.3	Ring contact: turn-on and turn-off transients for weak lateral guiding conditions.	177
7.4	Optical profiles computed from the numerical integration of the spatiotemporal dynamics.	179
7.5	Evolution of the active-material susceptibility obtained from integration of the 2D model.	180
7.6	Secondary pulsations in a multimode VCSEL from the full spatiotemporal model.	181
7.7	Secondary pulsations in a multimode VCSEL from the modal expansion.	182
B.1	Regions of operation represented in the phase diagram current versus spin-flip.	192
E.1	Dependence of the dimensionless propagation constant W_{ml} with the parameter V for all the guided modes.	203
E.2	Intensity distribution of the guided modes for $V = 7.91$	203

Curriculum vitae

Josep Mulet was born in Lloseta, Mallorca, Spain, in 1975. He is currently an assistant professor at the Physics Department of the Universitat de les Illes Balears, Palma de Mallorca, Spain. His research topic is the physics and nonlinear dynamics of semiconductor lasers: lasers with optical feedback, mutually coupled lasers, synchronization, polarization and transverse mode dynamics in vertical-cavity surface-emitting lasers.

Personal Information

Date of birth: 20/1/1975
Place of birth: Lloseta
Country: Spain
Marital status: Single
Sex: Male
Private address: C./ Antoni Oliver 2, E-07360 Lloseta (Balears)
E-mail: mulet@imedea.uib.es
URL: <http://www.imedea.uib.es/~mulet>
Phone: +34 971 172 536
Fax: +34 971 173 426

Education

1993 - 1998 Master Degree in Physics
Universitat de les Illes Balears, Palma de Mallorca (Spain)
June 1998, qualification= excellent.
Master's thesis: "Statistics of power dropouts in semiconductor lasers with optical feedback and current modulation"

Current Position

- Assistant professor at the Departament de Física de la Universitat de les Illes Balears (since 1/10/2002).

- PhD student at the Cross-Disciplinary Physics Department, IMEDEA (Mediterranean Institute for Advanced Studies), Palma de Mallorca, Spain. Fellowship from the Spanish Ministerio de Educación y Cultura (1/1/1999)-(30/9/2002). Advisors: Prof. Maxi San Miguel and Dr. Claudio R. Mirasso.

Visit to Other Institutions

- Institute of Applied Physics, Darmstadt University of Technology. Darmstadt, (Germany). Under supervision of Dr. I. Fischer (One week, April 1999).
- Department of computer & electrical engineering. Colorado State University, Fort Collins, CO (USA). Under supervision of Dr. C. Menoni and Dr. J. Rocca. (Two weeks, October 2000).
- Instituto de Física de Cantabria. Under supervision of Dr. A. Valle and Dr. L. Pesquera. (One week, July 2001).

Schools

- *International summer school on semiconductor lasers*. 25-30 July 1999. Cork (Ireland). J. McInerney, S. Koch, W. Chow, P. Blood, J.V. Moloney.

Publications

1. J. Mulet and C. R. Mirasso, Phys. Rev. E **59**, 5400 (1999).
2. T. Heil, J. Mulet, I. Fischer, W. Elsässer and C. R. Mirasso, Opt. Lett. **24**, 1275 (1999).
3. J. Mulet, C. R. Mirasso, and M. San Miguel, Phys. Rev. A **64**, 023817 (2001).
4. T. Heil, I. Fischer, W. Elsässer, J. Mulet and C. R. Mirasso, Phys. Rev. Lett. **86**, 795 (2001).
5. J. Mulet and S. Balle, Phys. Rev. A **66**, 053802 (2002).
6. J. Mulet and S. Balle, IEEE J. Quantum Electron. **36**, 291-305 (2002).
7. J. Mulet, C. Masoller, and C. R. Mirasso, Phys. Rev. A **65**, 063815 (2002).
8. T. Heil, J. Mulet, I. Fischer, C. R. Mirasso, M. Peil, P. Colet, and W. Elsässer, IEEE J. Quantum Electron. **38**, 1162 (2002).
9. C. R. Mirasso, J. Mulet, and C. Masoller, IEEE Photon. Technol. Lett. **14**, 456 (2002).
10. A. Scire, J. Mulet, C. R. Mirasso, and M. San Miguel, Opt. Lett. **27**, 391 (2002).

-
11. A. Scire, J. Mulet, C. R. Mirasso, J. Danckaert, and M. San Miguel, Submitted for publication (2002).

Proceedings

1. M. San Miguel, S. Balle, J. Mulet, C. R. Mirasso, E. Tolkachova, and J. R. Tredicce, “*Combined effects of semiconductor gain dynamics, spin dynamics and thermal shift in polarization selection in VCSELs,*” Proc. SPIE **3944**, 242 (2000).
2. J. Mulet, C. R. Mirasso, S. Balle and M. San Miguel, “*Transverse and polarization mode selection in VCSELs,*” Proc. SPIE **4283**, 139 (2001).
3. J. Mulet, C. R. Mirasso, T. Heil and I. Fischer, “*Dynamical behavior of two distant mutually coupled semiconductor lasers,*” Proc. SPIE **4283**, 293 (2001).
4. A. Scire, J. Mulet, C. R. Mirasso, and M. San Miguel, “*Intensity and polarization self-pulsations in VCSELs,*” Proc. SPIE **4646**, 205 (2002).
5. A. Scire, J. Mulet, J. Danckaert, C. R. Mirasso, and M. San Miguel, “*Vectorial chaos synchronization and polarization encoding in self-pulsating VCSELs,*” Proc. SPIE **4646**, 227 (2002).
6. A. Valle, J. Mulet, L. Pesquera, and S. Balle, “*Diffusive turn-off transients in current-modulated multitransverse mode VCSELs,*” Proc. SPIE **4649**, 50 (2002).

Conference Presentations

1. T. Heil, J. Mulet, I. Fischer, and C. R. Mirasso, “*Low frequency fluctuations under single mode operation in DFB lasers,*” IEEE Lasers and Electro-Optics Society, Annual meeting Dec. (1998). [O]
2. J. Mulet, C. R. Mirasso, T. Heil, and I. Fischer, “*Numerical statistics of power dropouts in semiconductor lasers with optical feedback,*” European Semiconductor Laser Workshop, 24-26 September (1998), El Escorial, (Spain). [O]
3. J. Mulet, C. R. Mirasso, and M. San Miguel, “*Intensity and Polarization fluctuations in VCSELs,*” Quantum Optics X, 3-7 October (1999), Cala Vinyes (Spain). [P]
4. J. Mulet, C. R. Mirasso, S. Balle, and M. San Miguel, “*Fluctuations and Polarization Switching in VCSELs,*” TMR meeting: Microlasers and cavity QED, 13-17 October (1999), Schloss Reisenburg (Germany). [O]
5. J. Mulet, C. R. Mirasso, S. Balle, and M. San Miguel, “*Intensity and polarization fluctuations in VCSELs,*” COST 268 & VISTA workshop, 28-30 August (2000), Brussels (Belgium). [P]

6. J. Mulet, S. Balle, C. R. Mirasso, and M. San Miguel, “*Transverse and polarization mode selection in VCSELs*,” COST 268 & VISTA workshop, 28-30 August (2000), Brussels (Belgium). [O]
7. T. Heil, I. Fischer, W. Elsässer, J. Mulet, and C. R. Mirasso, “*Dynamical behavior of mutually coupled semiconductor lasers: Experimental Investigations*,” CLEO/IQEC Europe, 10-15 September (2000), Nice (France). [O].
8. J. Mulet, C. R. Mirasso, T. Heil, and I. Fischer, “*Dynamical behavior of mutually-coupled semiconductor lasers: modelling and simulations*,” CLEO/IQEC Europe, 10-15 September (2000), Nice (France). [P]
9. J. Mulet, S. Balle, C. R. Mirasso, M. San Miguel, E. Tolkachova, and J. R. Tredicce, “*Transverse and polarization mode selection in VCSELs*,” CLEO/IQEC Europe, 10-15 September (2000), Nice (France). [O]
10. J. Mulet, S. Balle, M. San Miguel, and C. R. Mirasso, “*Transverse and polarization mode selection in VCSELs*,” 17th IEEE International semiconductor laser conference, 25-28 September (2000), Monterey CA (USA). [P]
11. J. Mulet, C. R. Mirasso, T. Heil, and I. Fischer, “*Dynamical behavior of two distant mutually coupled semiconductor lasers*,” Physics and simulation of optoelectronic devices IX (2001), San José (USA). [O]
12. J. Mulet, C. R. Mirasso, S. Balle, and M. San Miguel, “*Transverse and polarization mode selection in VCSELs*,” Physics and simulation of optoelectronic devices IX (2001), San José (USA). [O]
13. J. Mulet, S. Balle, C. R. Mirasso, and M. San Miguel, “*Mesoscopic modelling of the transverse and polarization dynamics of VCSELs: Influence of thermal lensing*,” VISTA meeting, 11-13 June (2001), Paris (France). [O]
14. J. Mulet, S. Balle, C. R. Mirasso, and M. San Miguel, “*Transverse and polarization mode dynamics in VCSELs*,” CLEO/EQEC Focus Meeting, 19-22 June (2001), München (Germany). [O]
15. J. Mulet, “*Spin dynamics and light polarization state in vertical-cavity surface-emitting lasers*,” The Rank Prize Funds: Optical orientation and spintronics, 19-21 March (2002), Grasmere (UK). [O]
16. J. Mulet, S. Balle, A. Valle, and L. Pesquera, “*Transverse mode dynamics in VCSELs: Spatio-temporal versus Modal expansion*”, MidTerm VISTA Meeting, 24-27 May (2002), Como (Italy). [O]
17. A. Scire, J. Mulet, C. R. Mirasso, and M. San Miguel, “*Polarization properties of self-pulsating VCSELs*”, Summer Topical Meetings (LEOS Conferences), 15-17 July (2002), Mont Tremblant (Canada). [O]

-
18. J. Mulet and S. Balle, “*Characterizing transient dynamics in VCSELs*,” Summer Topical Meetings (LEOS Conferences), 15-17 July (2002), Mont Tremblant (Canada). [O]
 19. J. Mulet, C. R. Mirasso, C. Masoller, T. Heil, I. Fischer, and W. Elsässer, “*Synchronization properties of two mutually coupled semiconductor lasers*,” 2nd International Workshop on Dynamics of Nonlinear Optical Systems, 2-6 September (2002), Platja d’Aro (Spain). [O]
 20. J. Mulet, and S. Balle, “*Optical modelling of the large-signal dynamics in VCSELs: Full spatio-temporal versus modal descriptions*,” NUSOD-02, 25-27 September (2002), Zürich (Switzerland). [O]

[O] = Oral presentation, [P] = Poster presentation

Other Merits

- Laboratory teaching in Optoelectronics (Physics Department, and Polytechnical School of the Univ. Illes Balears). Academic years: 2000-2001, 2001-2002.
- Participation in research projects:
 - VISTA, Research Training Network, Improving the Human Research Potential Program of the European Commission, HPRN-CT-2000-00034.
 - Acciones integradas Hispano-Alemanas HA98-29.
 - The Spanish MCyT TIC99-0645-C05-02 and BFM2000-1108.
 - OCCULT No. IST-2000-29683 of the European commission.
- Referee of IEEE J. Quantum Electronics, and Phys. Rev. E.
- Working experience in: DOS, WINDOWS 9x'-NT-2000, UNIX, LINUX. Programming languages: FORTRAN, BASIC, IDL, HTML, \LaTeX .

Other Related PhD Thesis from IMEDEA and UIB

- Margarita V. Homar, “*Semiconductor Laser Dynamics under Feedback and Modulation. Single and Multimode Operation*,” Universitat de les Illes Balears (1995).
- Josep Martín-Regalado, “*Polarization Properties of Vertical-Cavity Surface-Emitting Lasers*,” Universitat de les Illes Balears (1997).
- Catalina Mayol, “*Nonlinear dynamics of laser systems: Lyapunov potentials and bifurcation diagrams*,” Universitat de les Illes Balears (2002).

This thesis is a contribution to the study of the nonlinear dynamics of semiconductor lasers. One of the major challenges is the identification of the physical mechanisms underlying the optical instabilities. In the first part, we explore the fascinating dynamical behavior caused by delayed optical feedback, and the mutual coupling of two edge-emitting semiconductor lasers. In the second part, we investigate spin dynamics, light polarization state, and transverse mode selection in vertical-cavity surface-emitting lasers.

